NASA/TM—2019–220139

Marshall Space Flight Center Faculty Fellowship Program

N.F. Six, Program Director
Marshall Space Flight Center, Huntsville, Alabama

G. Karr, Compiler
The University of Alabama in Huntsville, Huntsville, Alabama

November 2019

The NASA STI Program…in Profile

Since its founding, NASA has been dedicated to the advancement of aeronautics and space science. The NASA Scientific and Technical Information (STI) Program Office plays a key part in helping NASA maintain this important role.

The NASA STI Program Office is operated by Langley Research Center, the lead center for NASA's scientific and technical information. The NASA STI Program Office provides access to the NASA STI Database, the largest collection of aeronautical and space science STI in the world. The Program Office is also NASA's institutional mechanism for disseminating the results of its research and development activities. These results are published by NASA in the NASA STI Report Series, which includes the following report types:

- TECHNICAL PUBLICATION. Reports of completed research or a major significant phase of research that present the results of NASA programs and include extensive data or theoretical analysis. Includes compilations of significant scientific and technical data and information deemed to be of continuing reference value. NASA's counterpart of peer-reviewed formal professional papers but has less stringent limitations on manuscript length and extent of graphic presentations.

- TECHNICAL MEMORANDUM. Scientific and technical findings that are preliminary or of specialized interest, e.g., quick release reports, working papers, and bibliographies that contain minimal annotation. Does not contain extensive analysis.

- CONTRACTOR REPORT. Scientific and technical findings by NASA-sponsored contractors and grantees.

- CONFERENCE PUBLICATION. Collected papers from scientific and technical conferences, symposia, seminars, or other meetings sponsored or cosponsored by NASA.

- SPECIAL PUBLICATION. Scientific, technical, or historical information from NASA programs, projects, and mission, often concerned with subjects having substantial public interest.

- TECHNICAL TRANSLATION. English-language translations of foreign scientific and technical material pertinent to NASA's mission.

Specialized services that complement the STI Program Office's diverse offerings include creating custom thesauri, building customized databases, organizing and publishing research results…even providing videos.

For more information about the NASA STI Program Office, see the following:

- Access the NASA STI program home page at <http://www.sti.nasa.gov>

- E-mail your question via the Internet to <help@sti.nasa.gov>

- Phone the NASA STI Help Desk at 757–864–9658

- Write to:
  NASA STI Information Desk
  Mail Stop 148
  NASA Langley Research Center
  Hampton, VA 23681–2199, USA

NASA/TM—2019–220139

Marshall Space Flight Center Faculty Fellowship Program

N.F. Six, Program Director
Marshall Space Flight Center, Huntsville, Alabama

G. Karr, Compiler
The University of Alabama in Huntsville, Huntsville, Alabama

National Aeronautics and
Space Administration

Marshall Space Flight Center • Huntsville, Alabama 35812

November 2019

Acknowledgments

All are grateful to those who, through their diligence, brought the 2018 NASA Marshall Space Flight Center Faculty Fellowship program to completion. These professionals include Jody Singer, Larry Leopard, John Honeycutt, Gerald Karr, Brooke Graham, Mona Miller, Katie Hayden, Debora Nielson, Judy Drinnon, and Tammy Rowan.

TRADEMARKS

Available from:

NASA STI Information Desk
Mail Stop 148
NASA Langley Research Center
Hampton, VA 23681–2199, USA
757–864–9658

This report is also available in electronic form at
<http://www.sti.nasa.gov>

EXECUTIVE SUMMARY

The 2018 Marshall Faculty Fellowship Program involved 16 faculty in the laboratories and departments at Marshall Space Flight Center. These faculty engineers and scientists worked with NASA collaborators on NASA projects, bringing new perspectives and solutions to bear. This Technical Memorandum is a compilation of the research reports of the 2018 Marshall Faculty Fellowship program, along with the Program Announcement (Appendix A) and the Program Description (Appendix B). The research affected the following five areas:

(1) Materials
(2) Propulsion
(3) Spacecraft systems
(4) Vehicle systems
(5) Space science

The materials investigations includes Lunar Regolith for habitats, friction stir welding, and composite joints. Propulsion studies included cryogenic tank pressurization, transmitted torque in a cryogenic environment, and condensation in presence of noncondensables, Europa Lander Deorbit Stage, and catalyst development for a hybrid rocket. Spacecraft systems include wireless sensor networks and printed electronic inks. Vehicle systems studies were performed on Mars ascent vehicle analysis, architecture models, and Space Launch System manual steering. Space science studies included planetary lava flow. Our goal is to continue the Marshall Faculty Fellowship Program funded by Center internal project offices.

Faculty Fellows in this 2018 program represented the following minority-serving institutions: Alabama A&M University, Southern University, Delgado Community College, and Dillard University.

2018 Marshall Space Flight Center Faculty Fellowship

From Left to Right:

Front Row—Frank Six, Robert Amaro, Charles Yang, Aaron Adams, Leonard Petnga, Md Abdus Salam, Alakananda Bandyopadhyay, Gerald Karr

Back Row—Carlos Montalvo, Joshua Shive, Gennady Miloshevsky, Joanna Rivers, Charles Wu, Tomekia Simeon, Zhengtao Deng, Stephen Whitmore, Rachael Damiani

Not pictured—Seyed Ghiaasiaan, Christopher Hamilton, Jack Van Natta

TABLE OF CONTENTS

TABLE OF CONTENTS (Continued)

Chemical Sintering of Lunar Regolith for Space-Based Habitats

A.Adams[1]
Alabama A &M University, Department of Mechanical and Civil Engineering, Normal, AL 35762

W. Kaukler [2]
The University of Alabama Huntsville, Rotorcraft Systems Engineering & Simulation Center, Huntsville AL 35899

and

E. Fox.[3]
NASA, Marshall Space Flight Center, Alabama, 35812

Nomenclature

IL	=	Ionic Liquid
ISRU	=	In-Situ Resource Utilization
JSC-1A	=	Johnson Space Center Lunar Soil Simulant
MSFC	=	Marshall Space Flight Center
NASA	=	National Aeronautics and Space Administration
MLS-1	=	Minnesota Lunar Simulant
JSC-1	=	Johnson Space Center
ORBITEC	=	Orbital Technologies Corporation

I. Introduction

President Bush's declarations of the program "Moon-Mars and Beyond" in the early 2000's for a planned manned mission to the moon by 2020 has spawned researchers to develop In-Situ resource utilization for lunar missions. This ambitious campaign proposed crews of three or four astronauts to the moon for days and weeks at a time, building permanent bases and constructing tests beds for future missions to Mars and beyond. The establishment of these habitats on the lunar surface in preparation for further and future exploration of Mars and beyond will require astronauts to be able to "Live off the land" on the moon.[1] To accomplish this goal, In-Situ Resource Utilization (ISRU) of lunar materials will be essential for the development of a human settlement on the moon. One important aspect of completing this mission successfully is developing methods to deal with the geotechnical issues that are associated with lunar soils. The various engineering and material science studies that will be necessary for these missions to be successful will have to focus on the regolith (crushed rock) and the soil (<1 cm regolith) as the starting materials for the settlements. There were various samples collected during the Apollo, Luna Lunokhod, and Surveyor missions and are considered national treasures. Several tests have been conducted on these samples and have been published in various journals. They are generally protected from unnecessary usage and scientific study. [2] Due to this fact, researchers have developed various lunar simulates that have a similar chemical and elemental composition. These simulants include Minnesota Lunar Simulant (MLS-1), which is a lunar simulant that was developed at the University of Minnesota. The basaltic rock used in this simulant was mined from a quarry in Duluth, Minnesota. It contains plagioclase, olivine, pyroxene and ilmenite as some of its major minerals. The minerals and grain sizes resemble the chemistry of the Apollo 11 mare material. The Simulant Johnson Space Center Number One JSC-1 is a lunar regolith simulant that was developed in 1994 under the auspices of NASA and the Johnson Space Center. Its developers intended it to approximate the lunar soil of the Maria. Unlike MLS-1, it simulates a soil that is poor in titanium. It is a basaltic ash with high glass content. The simulant JSC-1A has the same composition as JSC-1 manufactured by Orbital Technologies Corporation (ORBITEC) however it is produced in three different grades, JSC-1AF is a fine simulant that has particles on the average size of 27um, JSC-1A is a simulant that has particles that are less than 1 mm in size, and finally JSC-1AC which is a simulant that is coarse in texture and has a particle size of greater then 5 mm. One unique property of JSC-1A is that it can geopolymerize in an alkaline solution resulting in a

[1] Assistant Professor, Mechanical and Civil Engineering, Alabama A&M University Normal, AL 35762
[2] Associate Professor, RSESC Center, University of Alabama Huntsville, Huntsville, AL
[3] Aerospace Polymeric Engineering, Materials and Processes Lab, EM22, MSFC, Al 35812

hard, rock-like material. This geopolymerizer has shown comparable compressive and flexural strength to that of conventional cement.[3] These simulants are being reacted with ionic liquids to form building structures for lunar settlements on the moon and beyond.[7] An ionic liquid is a salt in the liquid state that has been restricted to salts whose melting point is below an arbitrary temperature, such as 100°C. Comparing that to ordinary liquids such as water or gasoline, which are predominantly made up of electrically neutral molecules, ionic liquids are largely composed of ions and short-lived ion pairs. The substances are being called the liquid electrolytes, ionic melts, ionic fluids, fused salts, liquid salts or ionic glasses.[1][2][3] One of the first ionic liquids discovered in 1888 by S. Gabriel and J. Weiner was Ethanolammonium[9], another early ionic liquid that was able to exist in room temperatures was ethylammonium nitrate discovered by Paul Walden in 1914.[10] During the 1970's and the 1980's, ionic liquids based on alkyl substituted imidazolium and pyridinium cations, with a halide or tetrahalogenoaluminate anions, were developed as potential electrolytes in batteries.[11][12] In the 1970s and 1980s, ionic liquids based on alkyl for the imidazolium halogenoaluminate salts, their physical properties—such as viscosity, melting point, and acidity—could be adjusted by changing the alkyl substituents and the imidazolium/pyridinium, and halide/halogenoaluminate ratios.[13] Two major drawbacks for some applications were moisture sensitivity and acidity/basicity. Wilkes and Zawarotko obtained ionic liquids with 'neutral' weakly coordinating anions such as hexafluorophosphate (PF^-_6) and tetrafluoroborate (BF^-_4), allowing a much wider range of applications in the early 90's.[14] Although most ionic liquids are based on hexafluorophosphate and tetrafluoroborate salts, bistriflimide $[(CF_3SO_2)_2N]^-$are also frequently used. Ionic liquids have been called the "designer solvents" or "solvents of the future" and have been described as having many potential applications. Salts that are liquid at near-ambient temperature are important for electric battery applications and have been considered as sealants due to their very low vapor pressure. Any salt that melts without decomposing or vaporizing usually yields an ionic liquid. Sodium chloride (NaCl), for example, melts at 801 °C (1,474 °F) into a liquid that consists largely of sodium cations (Na^+) and chloride anions (Cl^-). Conversely, when an ionic liquid is cooled, it often forms an ionic solid—which may be either crystalline or glassy. The ionic bond is usually stronger than the Van der Waals forces between the molecules of ordinary liquids. For that reason, common salts tend to melt at higher temperatures than other solid molecules. Some salts are liquid at or below room temperature. Examples include compounds based on the 1-Ethyl-3-methylimidazolium (EMIM) cation and include: EMIM:Cl, EMIM dicyanamide, $(C_2H_5)(CH_3)C_3H_3N^+_2{\cdot}N(CN)^-_2$, that melts at −21 °C (−6 °F);[4] and 1-butyl-3,5-dimethylpyridinium bromide which becomes a glass below −24 °C (−11 °F).[5] Low-temperature ionic liquids can be compared to ionic solutions, liquids that contain both ions and neutral molecules, and in particular to the so-called deep eutectic solvents, mixtures of ionic and non-ionic solid substances which have much lower melting points than the pure compounds.[6] Using lunar simulant and an alkali/basic type of ionic liquids to react with the minerals in a coarse powered simulant to cause a chemical reaction the will bind the simulant, causing silicate to react and transfer into sodium silicate. After the reaction has occurred, the IL is recycled and able to be used to make another building block or brick for a lunar settlement. After the displacement of the IL, the silicate is reverted back to silica and hardens in the space between the simulant particles and helps improve the rigidity of the solid structure. On earth, rocks are bonded similarly using water, high temperatures, and pressure. In this process, the ionic liquid replaces the water and the pressure or temperature. This is unlike the usual way of binding regolith together which uses an adhesive or cement that flows and can be shaped and free formed into bricks or structural walls or floors. [8] Using ionic liquids, chemical sintering is possible which will bind the loose aggregate regolith by partially dissolving the regolith particles. These particles can be pressed together or slightly heated to dry and harden into any number of shapes. This differs from standard sintering which requires the regolith particles to be compressed tightly together and heated to a temperature near the melting point of the regolith 1100 to 1300 C, in a large furnace that would be energy intensive. There is also sometimes a binder needed to initiate the sintering process. If a binder is not used then the enormous pressure is required to form the compact before sintering can occur. The process of recovering the ionic liquid is best completed if the shape created is made into a simple shape like a brick or a tile, which could be accomplished using a mold for repeatability. These simple shapes allow the simplification of the addition and removal of the specific ionic liquids, which entails washing the sample with deionized water that displaces the ionic liquid used in the chemical sintering process. Using the process of chemical sintering very light pressure in need to form a building block since the regolith particle surface are chemically active which promotes bonded on the surfaces of the particles. This chemical sintering offers enormous benefits over traditional methods which use binders, cement, adhesives, and epoxies, which would be a weight penalty in the transportation of these items for the earth, the lunar settlement.

II. Experimental Method

The data was collected by processing JSC-1A-A (**Figure 5 & 6 below**) regolith in two different particles size distribution, a coarse sample based on a particles size of < 5 mm and fine based on a particle size of 27µm. An average of four grams of JSC-1A regolith was mixed with the four ionic liquids (listed below) that have been identified for this project. The experimental matrix was varied by the variables of strength of the ionic liquid in terms of concentration, the particle size of the JSC-1A regolith rather coarse of fine, the amount of time that the reaction was allowed to take place between the ionic liquid and the regolith, if the mixture was allowed to react at room temperature or at elevated temperatures of 80 to 100 °C. After the mixture of ionic liquid and regolith were done reacting the ionic liquid was recovered and the reacted regolith was rinsed with deionized water and then allowed to dry in some iterations of the experimental matrix and in other heated and pressed at a press of 3000 PSI and a temperature of 100 °C. If the samples looked favorable they were then set in epoxy, allowed to solidify, polished and examined.

Here is a list of the Ionic Liquids that are where used in the experiments to collect the data for this study

1) 1-ethyl-3methylimidazolium hydrogen sulfate **(Figure # 1 below)**
2) 1-[butyl-4-sulfonic acid]-3-methylimidazolium hydrogen sulfate aka 3-(butyl-4-sulfonic acid)-1-methylimidazolium hydrogen sulfate **(Figure # 2 below)**
3) Trimethylglycinium bis(trifluoromethanesufonimide) + 15% H_2O **(Figure # 3 below)**
4) Taurininium hydrogen sulfate **(Figure # 4 below)**

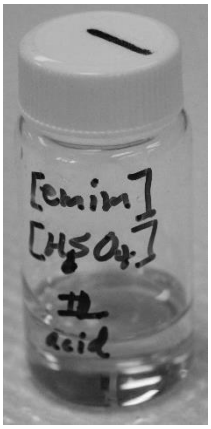

Figure 1 *Ionic Liquid #1*

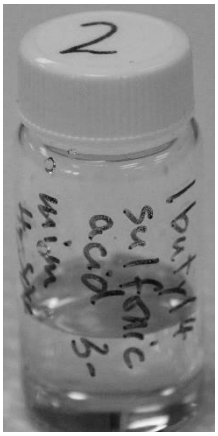

Figure 2 *Ionic Liquid #2*

Figure 3 *Ionic Liquid #3*

Figure 4 *Ionic Liquid #4*

Figure 5 *JSC-1A Lunar Simulant*

Figure 6 *JSC-1A Lunar Simulant 6x zoom*

Table 1: Composition (wt. %) of JSC-1A lunar regolith simulant powders

Composition (wt.%) of JSC-1A lunar regolith simulant powders (from orbitec) [56].

Oxide	Mineral Phase Compositions (%)					Overall Composition
	Plagioclase	Silica Glass	Ca-Pyroxene	Olivine	Titanomagnetite/Ilmenite	
SiO_2	**49.8**	**46.1**	**47.2**	**37.7**	1.9	46.7
Al_2O_3	**31.4**	14.9	5.6	0.6	6.1	15.8
Fe_2O_3	–	–	–	–	–	3.4 [57,66]
FeO	0.9[a]	12.7[a]	10.3[a]	**23.2**[a]	**65.4**[a]	7.6 [57,66]
TiO_2	0.1	2.8	2.5	0.2	14.4	1.7
MnO	<0.1	0.2	0.2	0.4	0.5	0.2
MgO	0.2	5.1	12.3	**36.1**	4.8	9.4
CaO	14.2	10.0	**20.3**	0.7	0.5	9.9
Na_2O	3.2	4.0	0.6	0.1	0.2	2.8
K_2O	0.1	1.4	<0.1	<0.1	<0.1	0.8
P_2O_5	<0.1	1.0	0.3	0.4	<0.1	0.7
Cr_2O_3	<0.1	<0.1	<0.1	<0.1	1.1	–

The compositions in bold indicate the majority (>20%) constituents of each mineral phase.
[a] Total Fe calculated as FeO.

Experiment 1

For the first experiment, the container of choice was a petri dish with the purpose of distinguishing how the ionic liquid #3 would react to the JSC-1A regolith at different partial sizes. The aluminum dish consisted of 0.554g of coarse regolith, 0.406g of fine regolith and 0.655g of mix coarse and fine regolith. After the different particle sizes of the regolith were separated in the petri dish, the ionic liquid #3 was poured onto them and allowed to react then followed by epoxy with the purpose of laminating the regolith **(Figure 7).** After 24 hours the epoxy was removed from the aluminum foil dish then transported to the polishing table where it was polished using 100µ, 50µ, and 10µ grit sandpaper and examined under a microscope.

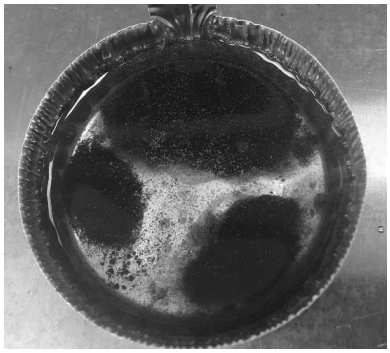

Figure 7 *JSC-1A Regolith in Three-Particle Sizes solidified in Epoxy*

Experiment 2

For experiment two, a decision was made to halt using the fine JSC-1A and only continue experiments using coarse JSC-1A. The coarse JSC-1A showed more promise of conglomeration while the fine JSC-1A did not. The container used for mixed changed from a petri dish to a 20mL glass bottle in order to have a homogenous mixture with the regolith and the ionic liquid #4 **(Figure 8).** The ionic liquid #4 was poured into the bottle that consisted of 1.642g of coarse regolith. The bottle was then shaken with the purpose of allowing all of the ionic liquid to come into contact with all of the regolith material. The mixture was allowed to rest for 24 hours to maximize the reaction time. After the 24 hour time period the mixture was placed into filter paper to extract the ionic liquid #4 **(Figure 9)**. After extracting all of the ionic liquid #4 that would freely separate from the reacted regolith mixture **(Figure 10),** ionized water was used to rinse the ionic liquid #4 that was still attached to the reacted regolith particles**.** The regolith was then allowed to dry for 20 hours at room temperature ~ 23 °C **(Figure 11).**

Figure 8 *1.6g of Coarse Regolith in 20mL Glass Bottle*

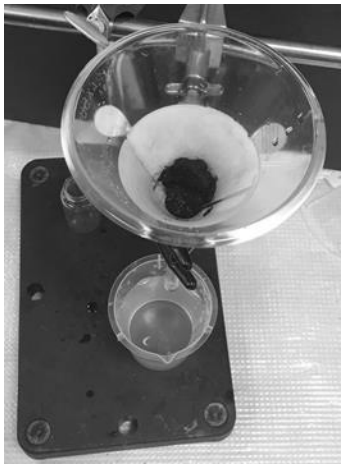

Figure 9 *Extraction of Ionic Liquid # 4 From Reacted Regolith*

Figure 10 *Collected Ionic Liquid #4 After One Reaction*

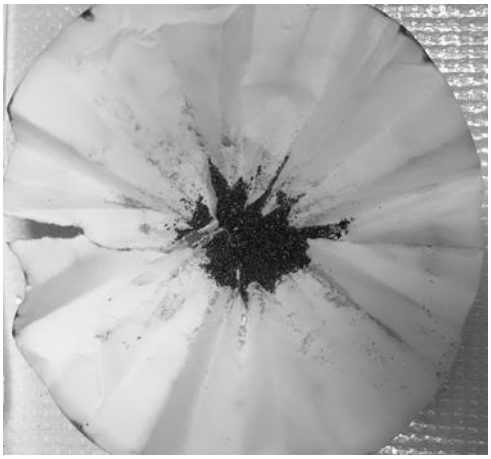

Figure 11 *Dried JSC-1A Regolith reacted with Ionic Liquid #4*

Experiment 3

For experiment three, the procedure remained the same as experiment two with the exception of 4.19g of coarse JSC-1A had been added to the glass bottle and the ionic liquid #1 had been diluted by 20 percent.

Experiment 4

From the first three experiments, the results concluded with the regolith not completely forming a solid structure **(Figure 12)**. After drying, the bottle was rotated 90° and the regolith crumbled into clumps of material. It was decided that the previous ionic liquids were too strong and did not allow full conglomeration of the particles. For experiment four, there were 4.76 grams of JSC-1A mixed with the ionic liquid #1 that had been diluted by 50%. This allowed full reaction between the ionic liquid #1 and the JSC-1A material. After turning the bottle 90° there were no large clumps of the JSC-1A breaking apart **(Figure 13).**

Figure 12 *Dried Regolith not Forming Completely Solid Structure*

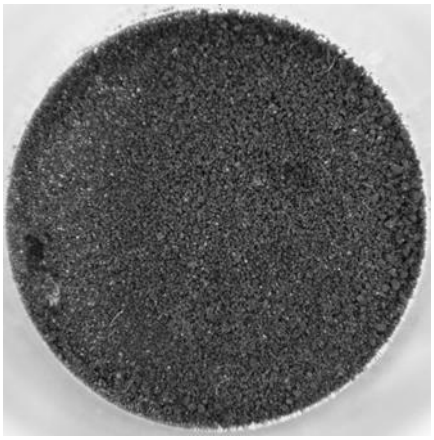

Figure 13 *Dried Regolith Forming Solid Structure*

Experiment 5

For experiment five, the 20mL glass bottle had been exchanged with a 100mL glass beaker**.** The belief was that due to the 20mL glass bottle having a small area, the ionic liquid was not allowed to come into contact with every JSC-1A particle, even after agitation. The large glass beaker would increase the area and thin out the JSC-1A material which would allow maximum contact between the mixture of the two. There were also difficulties removing the JSC-1A from the glass bottle without damaging the sample so increasing the area would allow ease of removing a sample. For this experiment, 3.96 grams of JSC-1A had been mixed with the ionic liquid #2 diluted by 20% and allowed to react for 4 hours. After the reaction time, the sample was removed from the beaker and washed five times with 35°C water until reaching a PH value of approximately 6. Without drying, the sample was placed into a press machine shown in Figure 14. The JSC-1A was pressed at 3000psi for 5 minutes while 100°C heat had been applied.

Figure 14 *Buehler SimpliMet 2 Hydraulic Specimen Mounting Press*

Figure 14 *Buehler SimpliMet 2 Hydraulic Specimen Mounting Press*

Experiment 6

For Experiment 6, the procedure remained the same as experiment 5 with the exception of the following:

- Mass of JSC-1A- 4.2927g
- 85% diluted ionic liquid #3 (10mL)
- 3 hours reaction time at ~23 °C

Experiment 7

For experiment 7, the procedure remained the same as experiment 5 with the exception of the following:

- Mass of JSC-1A – 6.6054 grams
- Ionic liquid #3 no dilution
- 1.5 hours reaction time at 75 °C
- 3000psi pressed for 5 minutes at 110 °C

Experiment 8

For experiment 8, the procedure remained the same as experiment 5 with the exception of the following:

- Mass of JSC-1A – 8.1 grams
- 85% diluted ionic liquid #3 (5mL)
- 3 hours reaction time at 79°C
- 3000psi pressed for 20 minutes at 100°C

Experiment 9

For experiment 10, the procedure remained the same as experiment 5 with the exception of the following:

- Mass of JSC-1A – 6.60 grams
- 25% diluted ionic liquid #3 (12mL)
- 15 hours reaction time under 75°C

Experiment 10

For experiment 11, the procedure remained the same as experiment 5 with the exception of the following:

- Mass of JSC-1A – 6.20 grams
- 20% diluted ionic liquid #2 (10mL)
- 20 hours reaction time

III. Results

These experimental results offer a better understanding of the complex parameters that are involved in the process of trying to chemical sinter lunar regolith. By changing the multiple variables (Mass of JSC-1A, temperature, pressure, reaction time, composition, container) we were able to witness the different reactions from the initial powder state to solid puck forms. For the first experiment, the fine JSC-1A had not properly bonded with the ionic liquid #3 however, the coarse JSC-1A had shown great promise of conglomeration after the reaction likely due to the coarse particles being larger in size which would allow them to engulf more of the ionic liquid. Experiment 2 led to changing the container from a petri dish to a 20mL glass bottle with the purpose of having the ability to create a more homogeneous mixture of ionic liquid and JSC-1A by shaking the mixture allowing maximum exposure. The results showed the conglomeration increase between the particles mixture however, there were still large imperfections such as large clumps of material which lead to experiment failure. Not knowing which variables affected the reaction between the ionic liquid and JSC-1A, the mass of JSC-1A was increase as well as change the ionic liquid to ionic liquid #1 and dilute it by 20% for experiment 3, **shown in Figure 15**, which resulted in the same conclusion as experiment 2. For experiment 4 the decision was made to keep the same amount of JSC-1A but dilute the ionic liquid #1 by 50% which led to maximum conglomeration and resulted in a nearly solid structure for experiment 4. The ionic liquid in that mixture completely reacted causing a composition change thus resulting in the particles being changed from black to white as shown in **Figure 16**.

Figure 15 *Pieces of partially comgomatate JSC-1A*

Figure 16 *JSC-1A with Composition Change*

Since this was the first experiment to show a high promise of a solid structure, the results were examined at a microscopic level to determine the precise amount of bonding that occurred. **Figure 17-Figure 19** shows the conglomeration of the JSC-1A that is reacted with the ionic liquid at the beginner phases of a solid structure being formed.

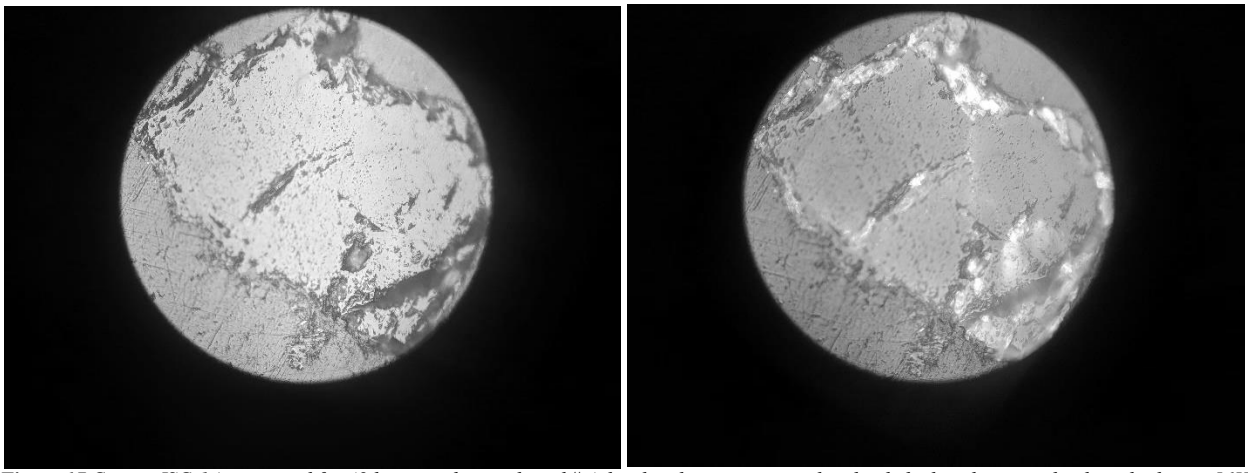

Figure 17 *Coarse JSC-1A processed for 48 hours with ionic liquid # 4 dried and cross-sectioned and polished, right crossed polars; high mag 56X obj 5X eyepiece*

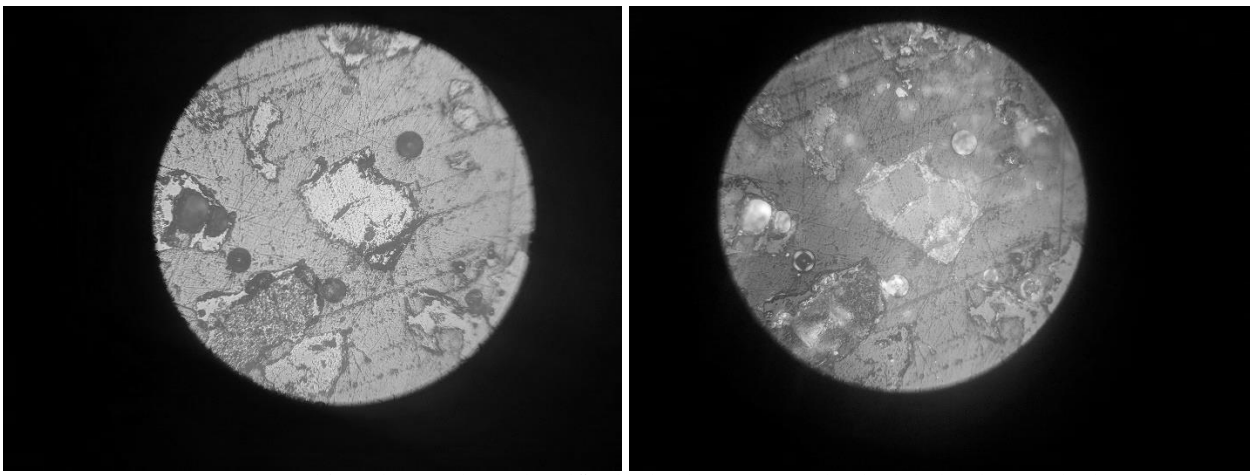

Figure 18 *Coarse JSC-1A processed for 48 hours with ionic liquid # 4 dried and cross-sectioned and polished, right crossed polars; med mag 20X obj 5X eyepiece*

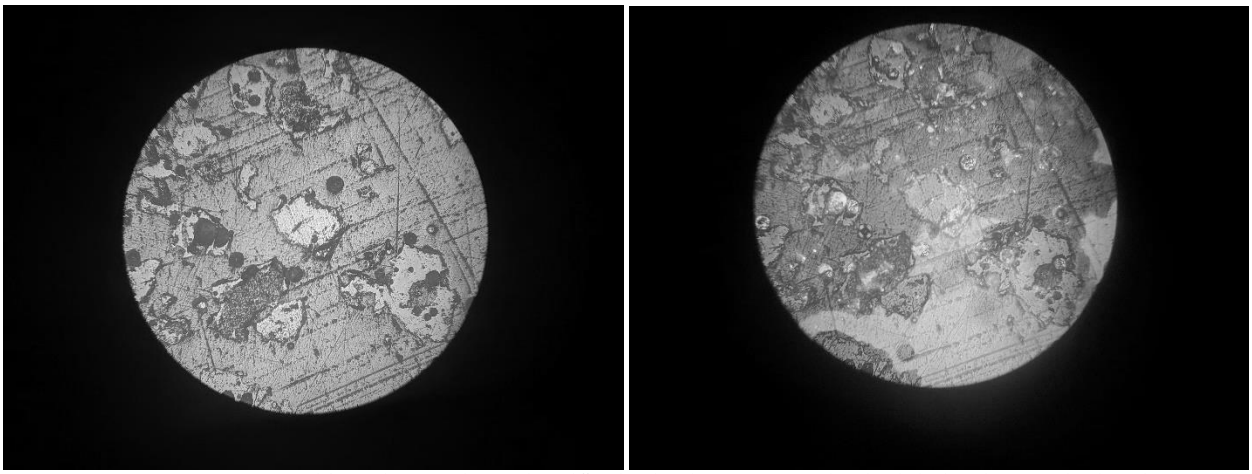

Figure 19 *Coarse JSC-1A processed for 48 hours with ionic liquid # 4 dried and cross-sectioned and polished, right crossed polars; low mag 12X obj 5X eyepiece*

The decision was made to increase the container area to produce the desired effect that would allow maximum contact between the JSC-1A and ionic liquid which led to using a 100mL beaker. For experiment 5, ionic liquid #2 was used while the mass of the regolith remained approximately the same as experiment 4. This resulted in a solid structure forming in the bottom of the beaker which showed promise as a viable solution for forming a structural building block. Due to the promising results of experiment 5, pressure and temperature were introduced which resulted in a puck formation that can be seen in **Figures 20-22**. After finally being able to create a solid structure, experiments 6-10 had been repeated with the same process as experiment 5 but adjusting different variables. Experiments 6-9 had disproportional ratios of fully reacted and partially reacted particles which let to the pucks shattering with minimum pressure applied shown in **Figure 23**. Experiment 10 resulted in the most promising results. 25% of the JSC-1A had fully reacted which resulted in the white particles while the other 75% had partially reacted which resulted in the grey particles. This 25-75 ratio allowed maximum conglomeration of the particles which resulted in **Figure 24** where the JSC-1A material had not shattered when pressure had been applied using a spatula.

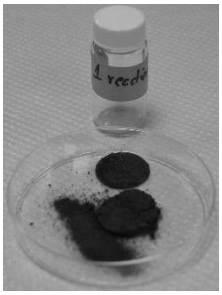

Figure 20 *Ionic Liquid #1*

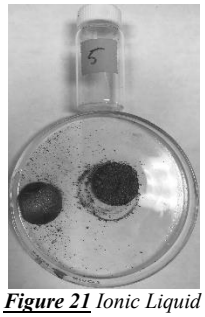

Figure 21 *Ionic Liquid #2*

Figure 22 *Ionic Liquid #3*

Figure 23 *Experiments # 6-9 Partially Conglomerated JSC-1A*

Figure 24 *Experiment #10 Fully Conglomerated JSC-1A*

IV. Conclusion

The concept of chemical sintering lunar regolith into usable building blocks for construction and sustain lunar settlement represents a new direction in the design of materials using ISRU. This report has provided preliminary experimental data to help define the correct parameters for this process to become reliable and repeatable. The parameters that have been verified are mass, reaction time, drying time, composition, type of container, pressure, and temperature and the experiments showed that with this variation of parameters, the process of using ionic liquids to perform ISRU building structures is still in the development phases. This method could be used for the in-situ fabrication of micro-truss structures for construction materials such as bricks, blocks or support materials for communication, energy, and transportation systems, as well as habitats on the Moon. The final experiments conducted showed promising results but still need to be improved upon to realize the true promise of chemical sintering using ionic liquids.

Acknowledgments

This work was done at NASA Marshall Space Flight Center and has been supported by the MSFC's Dr. Frank Six, director of the Office of University Affairs, Dr. Surendra Singhal director EM, Dr. Wayne Gamwell, Mrs. Erin Richardson, EM division. The United States Government retains, and by accepting the article for publication, the publisher acknowledges that the United States Government retains, a non-exclusive, paid-up, irrevocable, worldwide license to publish or reproduce the published form of this work or allow others to do so, for United States Government purposes.

The primary author would like to give a special thank you to the co-authors Dr. William Kaulker and Dr. Eric Fox, I would also like the thank the entire staff of NASA MSFC building 4464, for providing their expertise and access to their facilities, raw material, and equipment used in this study.

References

[1] *Thomas Welton (1999). "Room-Temperature Ionic Liquids". Chem. Rev.99: 2071 2084. doi:10.1021/cr980032t. PMID 11849019.*

[2] *F. Endres; S. Zein El Abedin (2006). "Air and water stable ionic liquids in physical chemistry". Phys. Chem. Chem. Phys.* ***8*** *(18): 2101–16. Bibcode:2006PCCP....8.2101E. doi:10.1039/b600519p. PMID 16751868.*

[3] *Freemantle, Michael (2009). An Introduction to Ionic Liquids. Royal Society of Chemistry. ISBN 978-1-84755-161-0.*

[4] *D. R. MacFarlane; J. Golding; S. Forsyth; M. Forsyth & G. B. Deacon (2001). "Low viscosity ionic liquids based on organic salts of the dicyanamide anion". Chem. Commun. (16): 1430–1431. doi:10.1039/b103064g.*

[5] *J. M. Crosthwaite; M. J. Muldoon; J. K. Dixon; J. L. Anderson & J. F. Brennecke (2005). "Phase transition and decomposition temperatures, heat capacities and viscosities of pyridinium ionic liquids". J. Chem. Thermodyn.****37*** *(6): 559–568. doi:10.1016/j.jct.2005.03.013.*

[6] *Mixture of nitrate salts with m.p. below 100 deg C*

[7] *R. M. Barrer (1943). "The Viscosity of Pure Liquids. II. Polymerised Ionic Melts". Trans. Faraday Soc. 39: 59–67. doi:10.1039/tf9433900059.*

[8] *Jones, R*, *Mechanics of Composite* Materials, *1st ed., McGraw–Hill, Washington D.C., 1983,*

[9]*Committee on Space-Based Additive Manufacturing, 3D Printing in Space, The National Academics Press, Washington D.C., 2014,*

[10] *G. Postiglione, G.Natale, G.Griffini, M.Levi, and S.Turri ., "Conductive 3D microstructures by the direct 3D printing of polymer/carbon nano tube nanocomposites via liquid deposition modeling," Journal of Composites, 2014 pp. 110-113.*

[11]*R.D. Goodridge, M.L. Shofner, R.J.M. Hague, M. McClelland , M.R. Schlea and R.B. Johnson,* C.J. Tuck., "*Processing of a Polyamide-12/carbon nanofiber composite by laser sintering," Journal of Polymer Testing Composites*, 2011 pp. 94-100.

[12]*C. I. Braga, et al., "Methodology for DSC calibration in high heating rates," J. Aerosp. Technol. Manag., 3(2), May-Aug. 2011, 179-192.*

[13] *Bara, J. E.; Camper, D. E.; Gin, D. L.; Noble, R. D. Room-Temperature Ionic Liquids and Composite Materials: PlatformTechnologies for CO2 Capture. Acc. Chem. Res. 2010, 43, 152−159.*

[14] *Wingard, D NASA Technical Briefing, 12-11-14*

On the Development of a Tool to Predict the Soundness of Friction Stir Welds in AA2219 Aluminum by use of Microhardness Measurements

Robert L. Amaro[1], Emma B. Burford[1], Kathryn V. Anderson[1], George Stubblefield[1], Omar L. Rodriguez[2], Jeffrey W. Sowards[2],
[1]Department of Mechanical Engineering, University of Alabama, Tuscaloosa, AL, 35487.
[2]NASA Marshal Space Flight Center

The self-reacting friction stir welding (SR-FSW) process is extensively used in the construction of NASA's Space Launch System (SLS) launch vehicle. The process metallurgically joins metals by use of large-scale inelastic shear and heat generation, all while maintaining a joint temperature below the parent materials' meting temperature. This solid-state joining process provides the benefit of reduced welding time, reduced warpage, and reduced residual stresses when compared to traditional fusion welding processes. Heat generation in the SR-FSW is primarily governed by the following weld parameters: tool rotational speed (ω), tool traverse speed (v), tool crown or plunge force (Fc), and tool root or reaction force (Fr). Closely controlling the SR-FSW process parameters enables the production of a sound weld, while minimizing the metallurgical transformation of the parent material induced by excessive heat. This work documents the progress of development of an analytical tool which provides insight to the health of a FSW joint in AA2219 aluminum. Specifically, the analytical tool predicts relative strength contributions from grain size/refinement/texture, solid solution strengthening, and precipitate strengthening for the FSW base material, heat affected zone, thermo-mechanically affected zone, and stir zone. Ultimately, once complete, the tool will provide insight to the temperatures experienced spatially within the FSW as a function of the remaining strength contribution from the precipitates post-weld.

Multi-node Modeling of Cryogenic Tank Pressurization

Alak Bandyopadhyay[1]
Alabama A & M University, Normal, AL 35762

And

Alok Majumdar.[2]
NASA Marshall Space Center, Huntsville, AL 35812

ABSTRACT

This paper presents a multi-node model of pressurization process in a cryogenic tank. The tank ullage was discretized into multiple nodes in radial and axial direction to allow the flow to recirculate due to natural convection. The model included heat transfer from ambient, heat transfer from wall to fluid and heat and mass transfer between ullage and propellant. The test results from a flight tank where liquid nitrogen was pressurized by gaseous nitrogen, has been used to verify the numerical predictions. Good agreement between test data and predictions are observed.

I. Introduction

Cryogenic Tanks are pressurized by inert gas such as Helium or Nitrogen to maintain the required pressure of the propellant delivered to the turbo-pump of a liquid rocket engine. Thermo-fluid system simulation tools are used to analyze the pressurization process of a cryogenic tank. Most system level codes (GFSSP and ROCETS) use single node [1] to represent ullage which is the gaseous space in the tank.. Ullage space in a cryogenic tank is highly stratified because the entering inert gas is at ambient temperature whereas the liquid propellant is at a cryogenic temperature. A single node model does not account for the effect of temperature gradient in the ullage. High fidelity Navier-Stokes based CFD model of Tank Pressurization is not practical for running a long duration transient model with thousands and millions of nodes. A possible recourse is to construct a multi-node model with system level code that can account for ullage stratification.

For the past several years, United Launch Alliance has been developing a propulsion system called Integrated Vehicle Fluids (IVF) to improve the functional and reliability limits of upper stages for long-duration space missions. IVF uses boil-off propellants to drive thrusters for the reaction control system as well as to run small internal combustion engines (ICEs). The produced thrust is used for maneuvering the vehicle and to settle propellants during coast flight. The ICE produces shaft power that is partly converted into electrical power and partly drives hydrogen and oxygen compressors. Also, the ICE releases exhaust gases and heat. The exhaust gases contribute to vehicle settling and attitude control while the heat is mainly absorbed by the recirculating coolant. The vented boil-off propellants are heated in heat exchangers that use the warm coolant as the hot fluid. Then, the propellant tanks are pressurized with the heated gases leaving the heat exchangers.

Figure 1 shows a simplified schematic of the IVF system. The pressurization system of the tank consists of a fluid loop with a compressor and heat exchanger instead of a helium tank in a conventional propulsion system. The compressor intakes propellant vapor from the tank ullage and drives it through a heat exchanger to heat it before it sends it back to the tank for pressurization. The heat exchanger receives heat from coolant of the ICE. The ICE provides power to the compressor and battery. The schematic does not include thrusters and the second propellant tank as this paper only focusses on numerical modeling of pressurization. Zegler[2] provides more details of the entire system. A flight tank has been tested at MSFC to understand the performance and optimize the design of the IVF system. The network flow solver program GFSSP[3] has been used to model the heat exchanger component and the complete IVF system by using one dimensional model (changing only in the tank axial direction) for temperature and pressure by LeClair et.al.[4] and Majumdar et.al.[5]. However both these models are unable to see any two dimensionally effect within the tank.

[1] Associate Professor, Electrical Engineering and Computer Science, Alabama A & M University.
[2] Aerospace Technologist, Thermal and Combustion Analysis Branch, NASA Marshall Space Flight Center

In the current work, a multi-node model is used to model the ullage space of the cryogenic tank. In the current model, the IVF loop is excluded; a multi-node computational model is used to simulate the pressurization of the tank due to propellant injection from the top of the tank and vent off after some time. The testing data were available with liquid Nitrogen; hence, in the current model liquid N_2 has been used as the working fluid. The model also considers the conjugate heat transfer in the tank wall.

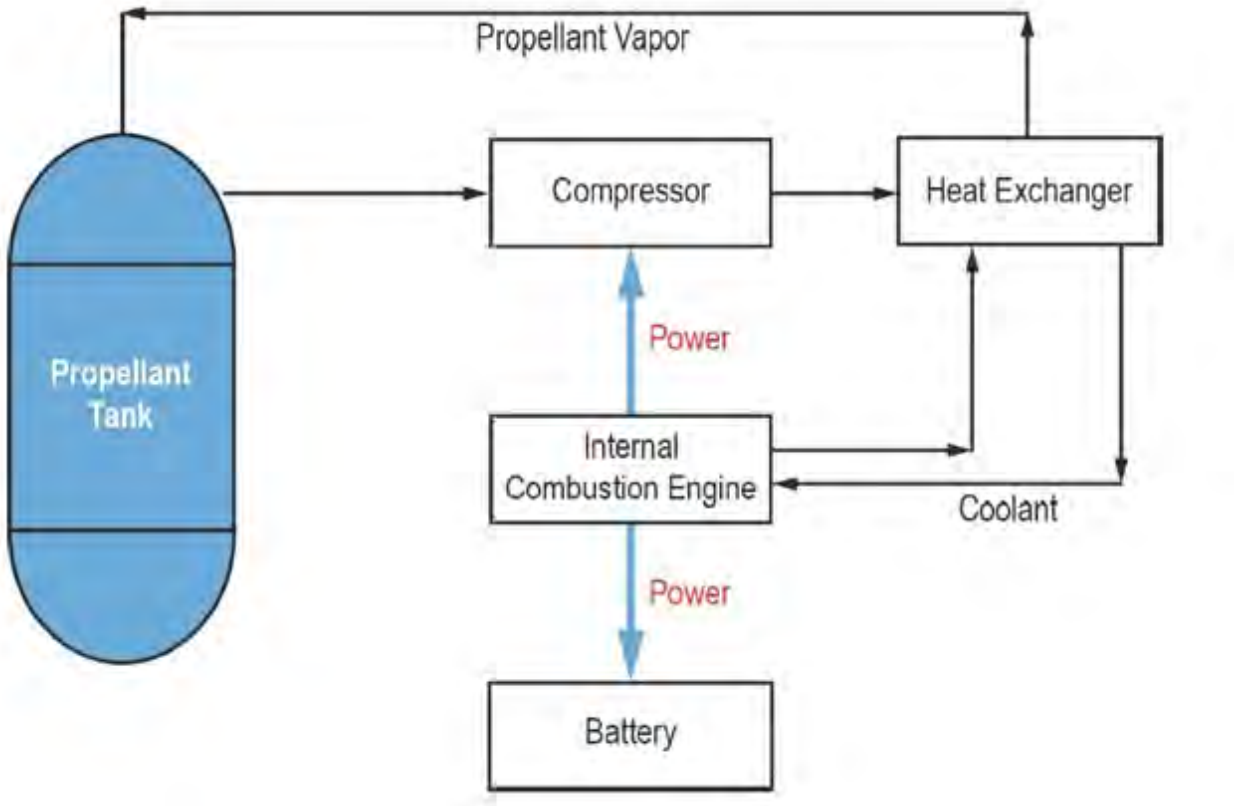

Figure 1. Simplified Schematic of IVF System

II. Problem Description and Computational Model

The Cryote3 tank is 10 ft. tall and core diameter is close to 10 ft. (119 inches) and the dome diameter at the top is 77 inches. The tank is assumed 75% filled with liquid N_2. The propellant is injected from the top under certain temperature and pressure conditions which varies with time and this is discussed later in the results and discussion section. The Cryote3 tank has been tested with liquid N_2. Hence in the current model liquid N_2 has been used as operating fluid. The computational model for the tank consists of the ullage space and tank wall. The interaction between ullage to liquid-vapor interface is modeled through the user sub-routine in GFSSP. Figure 2 shows the GFSSP model as given below.

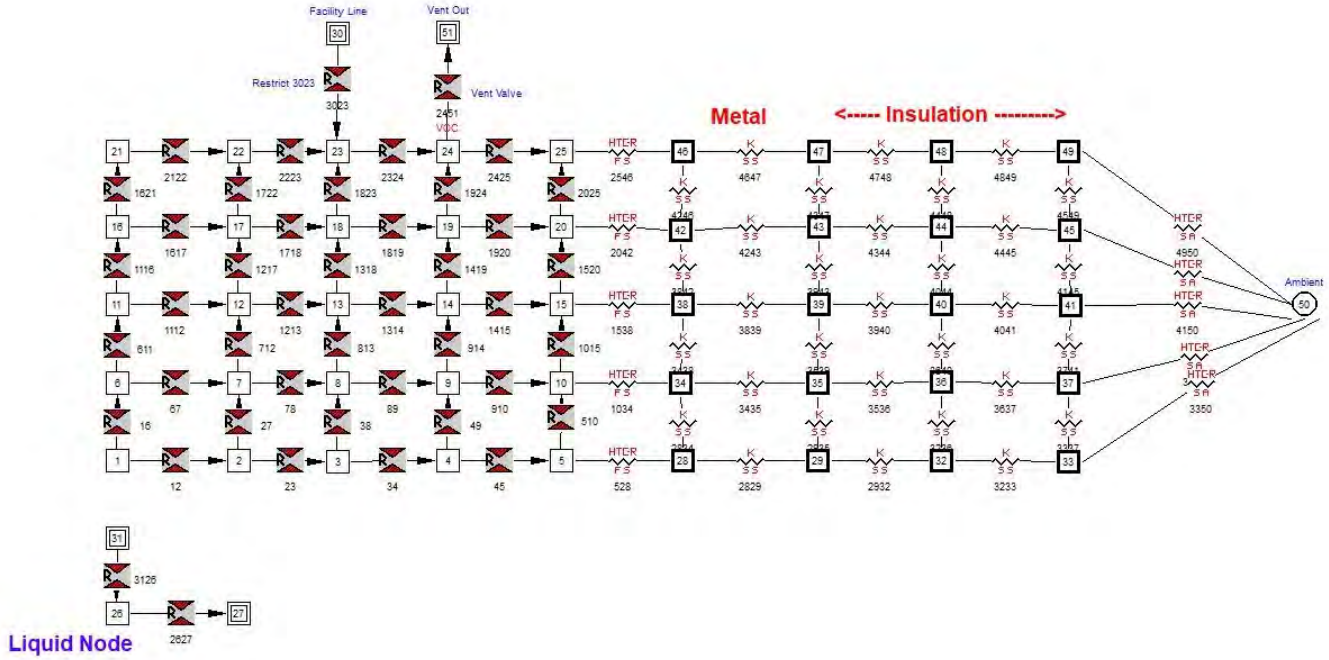

Figure 2. Computational Model for Cryote3 Tank using GFSSP

The tank ullage space is modeled with a total of 25 nodes (5 nodes in the horizontal or radial direction, at any elevation of the tank and a total of five vertical sections). Nodes 21, 22, 23, 24 and 25 are the nodes close to top of the tank (in the ullage space) and nodes 1, 2, 3, 4, 5 are fluid nodes close to the liquid surface. The left side of the figure 2 is close to center line of the tank. The model is assumed to be axisymmetric. The tank wall consists of stainless steel on the inside and surrounded by foam insulation on the outside. The ambient node is assumed to be at 86 F. In the current model, the governing differential equations (mass, momentum, energy) are solved in the ullage space with mass transfer between the liquid (represented by node 26) and the ullage through the user subroutine. The liquid-vapor interaction modeling for heat and mass transfer is described in detail by Majumdar et. Al[5]. Node 30 represents the propellant injection point at the top of the tank and node 51 represent the outside boundary representing the venting out of the propellant.

The heat transfer coefficient between the wall and ullage was computed from a natural convection correlation for a vertical plate[6]. The detailed formulation is given by Majumdar et al.[7], and hence is not discussed here. The natural convection heat transfer computation and implementation is carried out in the GFSSP user subroutine.

III. Results and Discussion

The pressure and temperature at which the propellant is injected at the tank top are shown as a function of time in Figure 3 as given below. The vent valve is open at about time 16300 sec and completely closed at about 17300 seconds. This is shown in Figure 4. The liquid temperature is at -315.2 F.

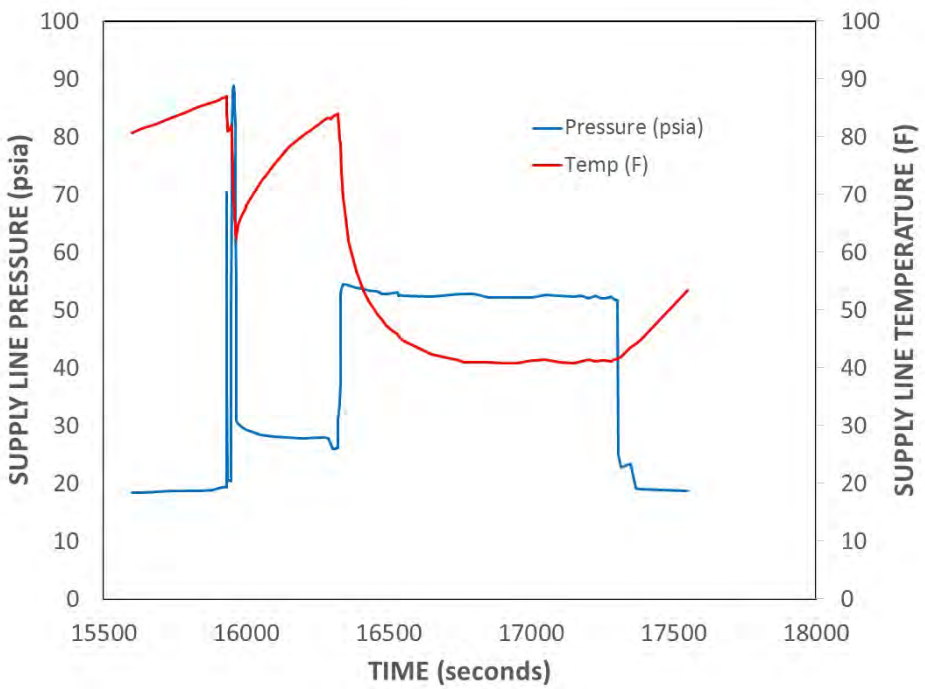

Figure 3. Pressure and Temperature at the supply line (propellant injection)

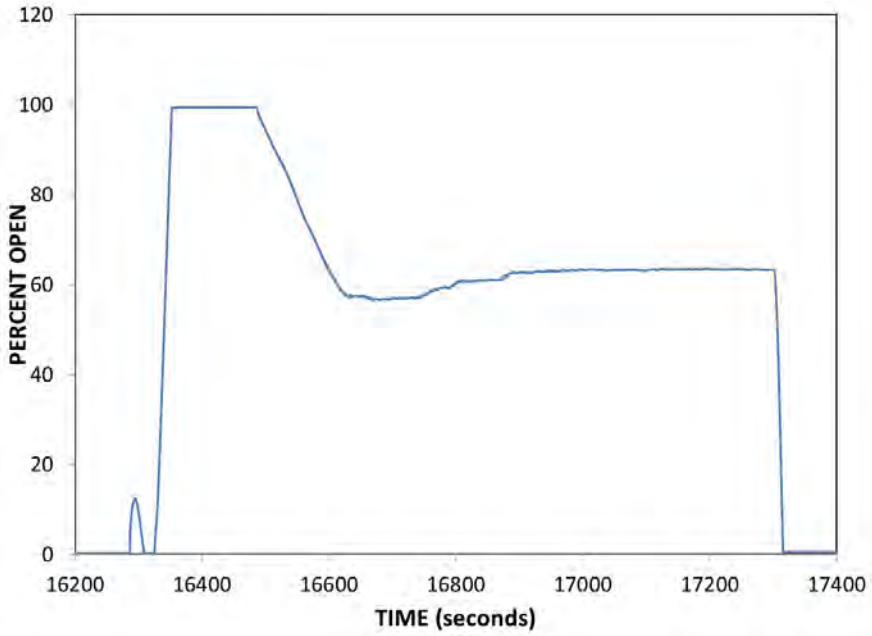

Figure4. Percentage of vent valve opening as a function of time.

The transient simulation has been carried out with a time step of 0.01 second with the operating conditions mentioned above. The results are converged with a convergence criteria of 1.e-4. It has been found that ullage pressure does not vary in either radial or axial direction of the tank, and hence the bulk pressure is plotted with the test data and figure 5 shows the comparison of the computed data with that of the test data. The agreement has been very good at the most of the points. The fluid temperature within the ullage space at node 18 (as the test data is available at that location) is plotted as a function of time and again very good agreement has been observed between the computed results and the test data, as shown in Figure 6.

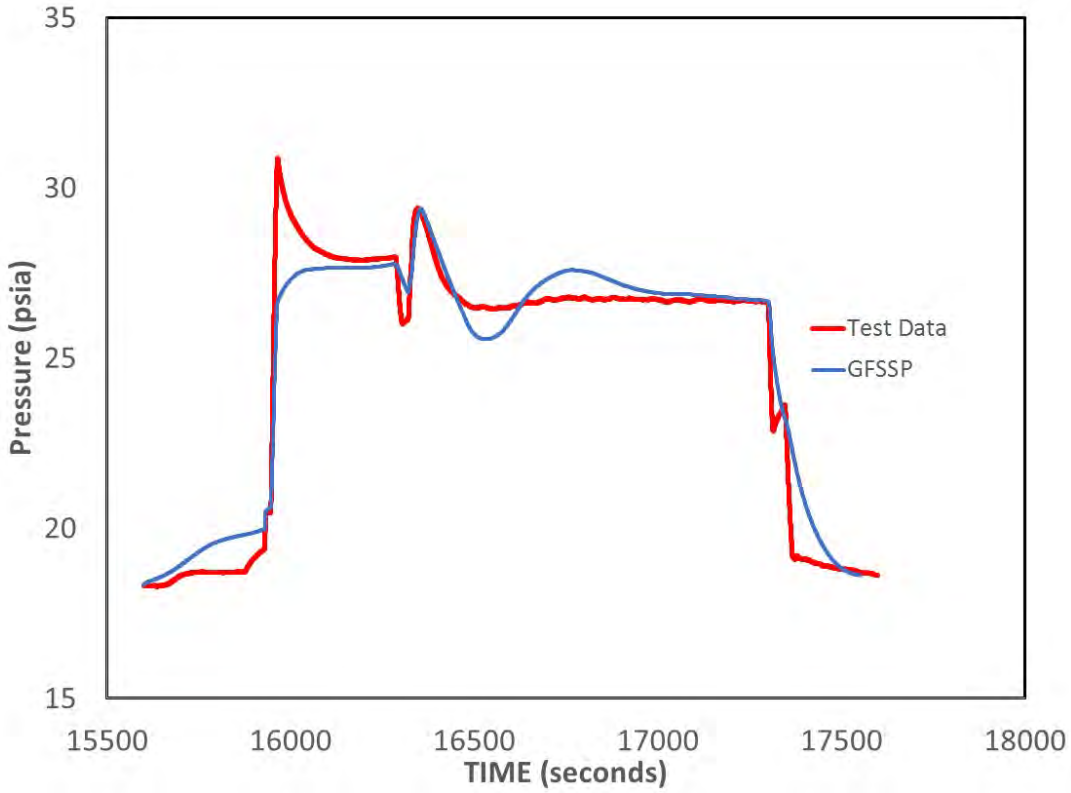

Figure 5. Comparison of computed ullage pressure with the test data.

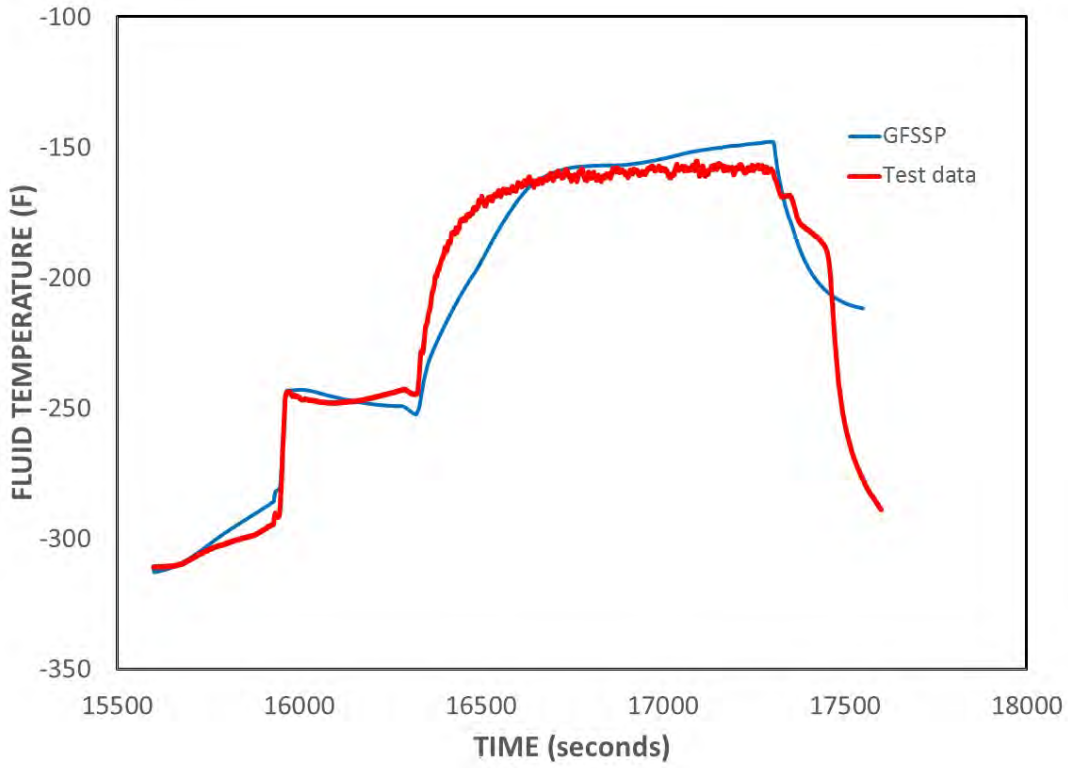

Figure 6. Comparison of computed ullage temperature with the test data.

In order to observe the two dimensional effect (i.e. variation both in the radial direction as well as along the vertical direction), the temperature distribution at nodes 1, 6, 11, 16, 21 (along vertical direction, close to center line of tank) and at nodes 5, 10, 15, 20, 25 (close to tank wall) are plotted as a function of time as shown in figure 7 below. It has been observed that the fluid is relatively at higher temperature near the wall as compared to center of the tank, which is expected and there is a rise of temperature of about 20 F from the center line towards the wall (as observed by considering any two nodes at the same height). In the vertical direction, there is a relatively sharp temperature gradient from liquid surface to the center of ullage space, but then the temperature does not change appreciably.

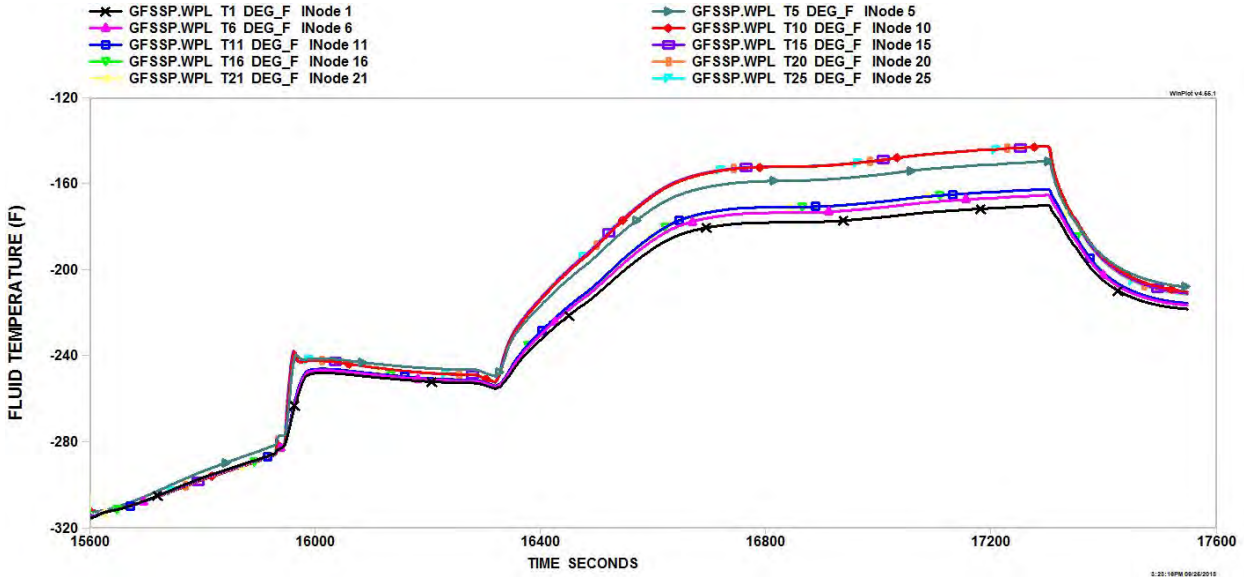

Figure 7. Temperature distribution in the ullage space.

Figure 8 shows the temperature distribution in the solid wall showing three nodes, node 39 in the stainless steel, and node 40 and 41 are in the insulation region.

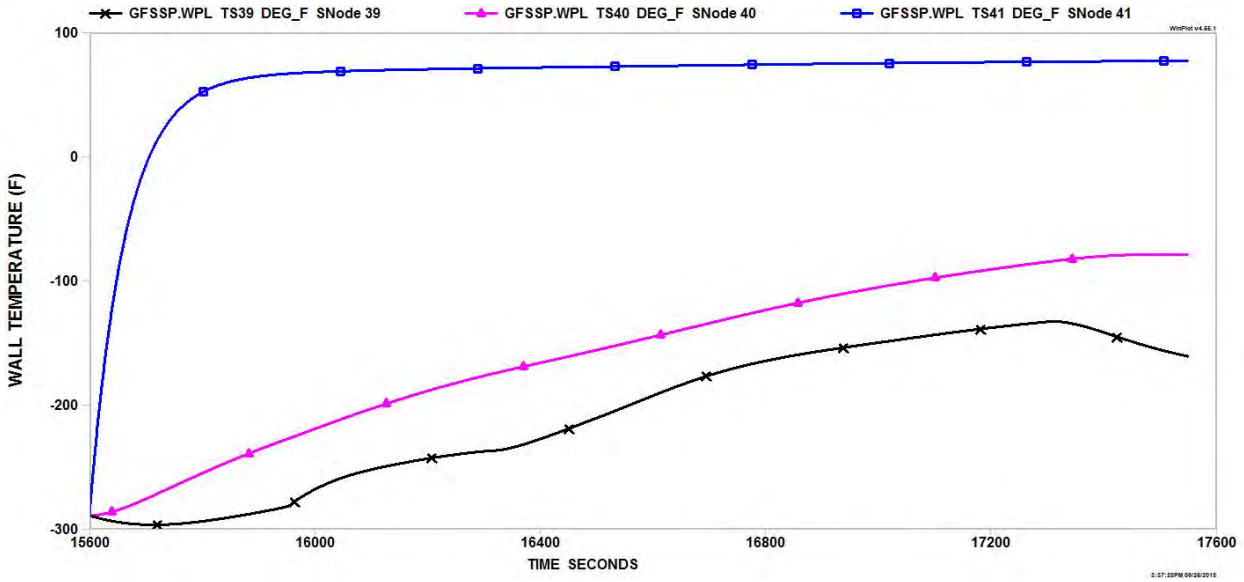

Figure 8. Radial temperature distribution along the tank wall.

Figure 9 shows the flow rate of the propellant that is injected into the tank and the flow rate of the vented out propellant. These distributions are comparable to test data, the pink line indicating the flow rate of the propellant injected into the tank and the black line indicating the vented flow out from the tank.

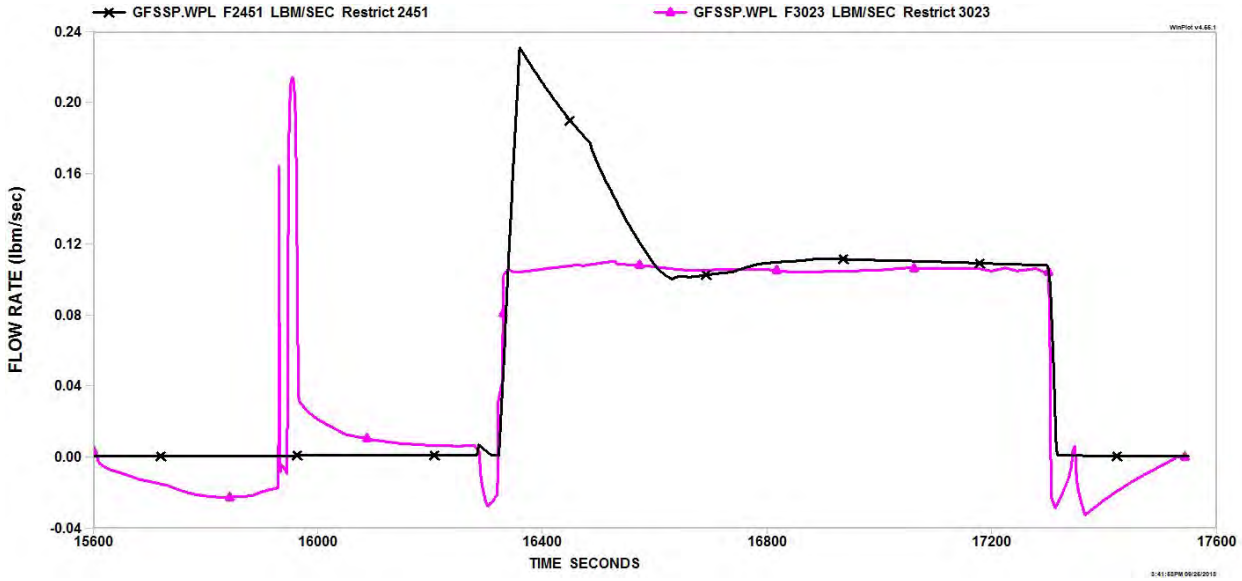

Figure 9. Flow Rate coming at injection and vent out.

IV. Conclusion

A multi-node axisymmetric model of Tank Ullage was developed to allow for flow recirculation and stratification caused due to free convection. The heat and evaporative mass transfer between liquid propellant and ullage was modeled assuming a saturated film at liquid-vapor interface. Numerical predictions of ullage pressure and temperature have been compared with test data from IVF experiments recently performed at NASA/MSFC. Good comparison has been observed between test data and predictions. The work needs to be further extended to compare additional test data from IVF experiments where ullage was pressurized using IVF loop.

Acknowledgments

This work was supported by a fellowship awarded to Dr. Alak Bandyopadhyay under the NASA Summer Faculty program. The work was conducted at MSFC, Huntsville, Alabama, in the ER43/Thermal Analysis Branch. The authors like to thank Dr. Andre LeClair of ER-43, Marshall Space Center for valuable inputs regarding the model and also Mr. Juan Valenzuela, testing Engineer, of ER-24 to support the work by providing test data and useful information about the testing details.

References

[1]Majumdar, Alok and Steadman, Todd, "Numerical Modeling of Pressurization of a Propellant Tank", Journal of Propulsion and Power, Vol 17, No.2. March – April, 2001.

[2]Zegler, F., "An Integrated Vehicle Propulsion and Power System for Long Duration Cryogen Spaceflight," AIAA 2011-7355, *AIAA SPACE 2011 Conference & Exposition*, September 27–29, 2011, Long Beach, CA, http://dx.doi.org/10.2514/6.2011-7355.

[3]Majumdar, A. K., LeClair, A. C., Moore, R., and Schallhorn, P. A., "Generalized Fluid System Simulation Program, Version 6.0," , *NASA/TP—2016–218218*, March 2016.

[4]Majumdar, A.K, LeClair, A.C. and Hedayat, A., "Numerical Modeling of Pressurization of Cryogenic Propellant Tank for Integrated Vehicle Fluid System", AIAA Propulsion and Engineering Forum, 52nd *AIAA/SAE/ASEE Joint Propulsion Conference*, July 25-27, 2016, Salt Lake City, UT, pp 1-18

[5]LeClair, A.C., Hedayat, A. and Majumdar A.K., "Numerical Modeling of an Integrated Vehicle Fluids System Loop for Pressurizing a Cryogenic Tank", AIAA Propulsion and Engineering Forum, 53rd *AIAA/SAE/ASEE Joint Propulsion Conference*, 10-12 July 2017, Atlanta, GA

[6]Rohsenow WM, Hartnett JP, Cho YI., *Handbook of heat transfer*. 3rd edition,, McGraw-Hill; 1998. p. 4.13.

[7]Majumdar, A., Valenzuela, J., LeClair, A. and Moder, J., "Numerical modeling of self-pressurization and pressure control by a thermodynamic vent system in a cryogenic tank", *Cryogenics*, 2016, vol. 74, pp 113-122.

Evaluation of Magnetic Coupling Tester Transmitted Torque in Cryogenic Environment

Z.T. Deng[1]
Mechanical Engineering, Alabama A&M University, Huntsville, AL 35762

Barry Battista[2], Jeremy Kenny[3], Alicia Turpin[4] and Stanley Tieman[5]
NASA Marshall Space Flight Center, Huntsville, Alabama

Abstract: The cryogenic fluid management technology is critical to the propulsion system for the success of the deep-space exploration. One of the technique to reduce the heat load of the pumping system in order to store and dispense cryogenic propellants is to position the pump motor outside the tank. The axial flux magnetic coupling, which may transmit torque magnetically through a non-magnetic containment barrier has been proposed to transmit the power required by the pump. The objective of this paper is to evaluate the axial-field magnetic coupling torque transmission mechanism in cryogenic environment. The influence of the tank wall magnetic permeability, the configuration of the permanent magnets on the transmitted torque from the proposed magnetic coupling tester were investigated. The minimum transmitted torque requirement was estimated in terms of the fluid friction and pump power. The transmitted torque analysis provides the critical design guideline for the magnetic coupling tester prototype.

I. Introduction

The NASA's manned exploration of deep-space and interplanetary travel require advanced Cryogenic Fluid Management (CFM) technology. The Exploration vision requires high performance propulsion systems for both human and robotic missions. The vision includes in-space propulsion stages, and In-Situ Resource Utilization (ISRU) for cryogenic propellant production and liquefaction of breathable gases [1]. Cryogenic propellants are gasses chilled to subfreezing temperatures and condensed to form highly combustible liquids, providing high-energy propulsion solutions critical to the long-term human exploration missions [2]. Liquid hydrogen is used in large volumes in the space program as a primary rocket fuel for combustion with oxygen, and as a propellant for nuclear powered rockets and space vehicles. Among the leading challenges associated with the CFM technology is the ability to store and dispense cryogenic propellants in space. On the surface of the earth, the gravitational force will separate the liquid and vapor inside a container. In space low-gravity environment, the fluid is not centered over the tank outlet, dispensing of the single-phased liquid propellant becomes a challenge. Dispensing the liquid hydrogen from a cryogenic propellant tank requires the gathering the liquid phase and the transferring of the liquid propellant from the tank. Liquid Acquisition Devices (LADs) of various types are frequently used to achieve a liquid distribution [3, 4].

A mechanical pump housed within the propellant tank was often used to pressurize the fluid and drive the fluid to desired location. The mixing process that is currently in use consists of electric motors directly couple to a pump inside the cryogenic tank that is submerged in the cryogen. However, the operation of the pump dissipated heat loads to the tank which may significantly increase the risk of cryogenic fluid boil-off. To reduce the heat load of the pump,

[1] Professor, Marshall Space Flight Center Faculty Fellow, Mechanical Engineering, Alabama A&M University.
[2] Thermal Analyst, Tecmasters, Collaborator, ER 43, NASA Marshall Space Flight Center.
[3] Acting Branch Chief, Collaborator, ER43, NASA Marshall Space flight Center.
[4] Branch Chief, Collaborator, ER 43, NASA Marshall Space Flight Center.
[5] Division Chief, Collaborator, ER 40, NASA Marshall Space Flight Center.

one can divorce the pump housing from the respective drive-motor or move the motor to a location external to the tank.

One of the potential pump concept is the Tesla pump. The Tesla pump is a centrifugal pump which is operated based on rotating parallel discs which are submerged in the fluid. If the rotating power or torque can be transmitted from outside of the tank, then it is possible to pump propellant without adding heat to it inside the tank. One of the key technology relies on the power transmission from motor to pump. Shafted connections are the norm but constitute thermal penetrations to the insulated tank wall. Moreover, the need to create a positive dynamic seal, capable of surviving cryogenic temperatures, renders this approach very difficult to implement. NASA has been investigating the possibility of driving a Tesla pump using an external motor in conjunction with a magnetic shaft coupling.

A magnetic coupling is a coupling that transfers torque from one shaft, but using a magnetic field rather than a physical mechanical connection. The basic working principle of the magnetic coupling device is to transmit torque magnetically through air or through a non-magnetic containment barrier. There are no contacting parts which allows for torque transmission through both angular and parallel misalignment. Atallah & Howe [5] presented a coaxial or concentric magnetic gear employing rare earth magnets that promised high torque densities and high torque transmission capability. Magnetic coupling can be used in the navy propulsion [6] for torque transmission between motor and propellers. Magnetic shaft couplings are most often used for liquid pumps and propeller systems, since a static, physical barrier can be placed between the two shafts to separate the fluid from the motor operating in air. Magnetic shaft couplings preclude the use of shaft seals, which eventually wear out and fail from the sliding of two surfaces against each another. Magnetic couplings are also used for ease of maintenance on systems that typically require precision alignment, when physical shaft couplings are used, since they allow a greater off axis error between the motor and driven shaft.

Most of the magnetic coupling system use either axial or radial flux topologies and both consists of two rotors with pre-configured array of permanent magnets. The two rotors are separated by an air gap. There are fundamentally four configurations of the axial magnetic flux coupling devices can be found [7]. As shown in Figure 1, the dark segments are magnetized upwards and light segments are magnetized downwards. In configuration #1, the driver rotor is extremely large and the driven rotor has a very small diameter. The number of magnet poles is arbitrary. In configuration #2, the coupling has same diameters for driver and driven rotors, spaced apart by a narrow gap. In configuration #3 a wider gap is presented. In configuration #4, the driver and driven rotors are in a ring shape, with polar magnets on it. None of the existing axial flux magnetic coupling system has been applied to the cryogenic environment with a separator wall for power transfer.

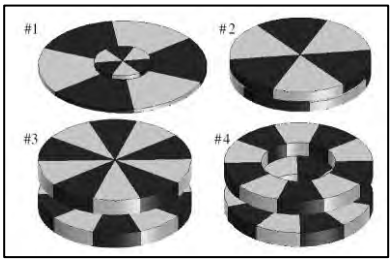

Figure 1. Typical configuration of the axial magnetic flux coupling adopted from [7].

The magnetic coupling device has the potential to be applied to the cryogenic tank fluid management. NASA engineers completed a simple battery of tests to determine the feasibility of using magnetic couplings to convey mechanical power across a metallic tank wall [8]. Although initial results were encouraging, much work remains to characterize the relationships between power, torque, and parameters such as magnetic field strength, separation distance, magnet placement and spacing, and tank wall characteristics (such as magnetic permeability) [9]. To apply the magnetic coupling torque transmission concept to the cryogenic tank fluid transfer, it is necessary to investigate the torque transfer mechanism and to understand the effects of cryogenic temperature effects on the performance of the magnetic coupling device.

The finite element modeling (FEM) is one of the most comprehensive and widely preferred technique [10, 11] to compute the Maxwell equations for the torque transmission of the magnetic couplings. Three-dimensional FEM allows a precise analysis of magnetic devices taking into account geometric details and magnetic nonlinearity. The

Maxwell stress tensor technique is normally used to calculate the torque of the magnetic gears. The FEM simulation indicated that the transmitted torque is sensitive to the number of magnetic poles, the sizes of the magnets, the air gap between rotors, the thickness of the magnetic rotors, and the relative angular offset of the two magnetic rotors. On the theoretical modeling side, the transmitted torque generated by an axial flux magnetic coupling has been modeled analytically based on the simplified two-dimensional approximation [12]. In these analytical modeling, the magnetic coupling has two identical opposing discs with polar shaped permanent magnets. The torque is created when the magnetic fields due to the two rotors are shifted by a load angle. The solution methodology replies on the linearization of the cylindrical topology which transform the three-dimensional field into two-dimensional field. By introducing the surface charge density, the simplified expression for the torque computation was derived for optimization of design purpose. The three-dimensional analytical technique [13, 14] for the modeling of permanent magnets axial flux magnetic couplings takes into account of the radial effects of the magnetic field. The influence of the air gap between rotors and number of permanent magnets pole pairs on the transmitted torque have been investigated in these analysis. However, the analytical modeling is limited to the simplified geometry and low permeability subdomains.

Axial magnetic flux magnetic coupling for potential application in cryogenic environment for power transmission has not be fully understood simply due to the fact that many fundamental physical control variables can influence the magnetic field distribution and torque transfer. In order to fully understand the potential of using axial flux magnetic coupling for power transfer in cryogenic tank application, NASA engineers proposed to build a magnetic coupling tester (MCT) and use it to conduct a series of experiment to determine empirical correlations between transmitted power and fundamental non-dimensional control variables. The MCT will identify the independent variables which determine the amount of power and torque that can be conveyed using a magnetic coupling, and characterize the specific relationship(s) among the transmitted torque/power and independent variables.

The first step towards understanding of the MCT prototype design criteria is to understand the influence of the MCT control variables on the transmitted torque. The parametric analysis has to be conducted before finalizing the MCT configuration. The objective of the current research is to evaluate the axial-field magnetic coupling torque transmission mechanism in cryogenic environment. Results of the analysis will provide the basic design guideline for the MCT prototype.

II. Modeling of Transmitted Torque for the Proposed MCT Configuration

Consider a MCT configuration [8,9] as shown in Figure 2. The MCT comprises a pair of opposing circular disc rotors, one of which is affixed to the output shaft of an unspecified prime mover and the other to a driven shaft inside the tank providing pumping power to the cryogenic fluid. Each of the discs retains a polar array of coin-type permanent magnets. The disc rotors are separated from one another, not only by some distance filled with air, fluid or vacuum, but by a solid media (i.e., a "separator wall"), representing the tank wall.

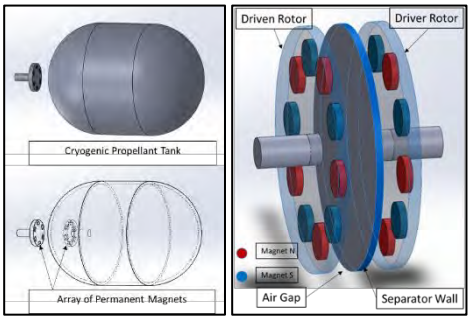

Figure 2. Conceptual sketch of a magnetic coupling device for power transmission in cryogenic tank.

The governing equations for the modeling of the MCT magnetic field distribution and its transmitted torque are the Maxwell's equations. For the general time-varying fields, the Maxwell's equations, written in differential forms, states the relationships between the fundamental electromagnetic quantities.

$$\nabla \times \vec{H} = \vec{J} + \frac{\partial \vec{D}}{\partial t}$$

$$\nabla \times \vec{E} = \frac{\partial \vec{B}}{\partial t}$$

$$\nabla \cdot \vec{B} = 0$$

$$\nabla \cdot \vec{D} = \rho_C$$

where $\vec{H}$ is the magnetic field intensity, $\vec{B}$ is the magnetic flux density, $\vec{E}$ is the electric field intensity, $\vec{J}$ is the current density, $\vec{D}$ is the electric flux density, ρ_C is the electric charge density. Another fundamental equation is the continuity equations, where,

$$\nabla \cdot \vec{J} = -\frac{\partial \rho_c}{\partial t}$$

Under the steady state condition, when the electric field is not presented, the Maxwell's equation can be simplified as

$$\nabla \times \vec{H} = 0 \quad \text{and} \quad \nabla \cdot \vec{B} = 0$$

To obtain a closed form solution of the Maxwell's equations, the constitutive relations that describing the macroscopic properties of the medium have to be provided. In a vacuum, $\vec{B}$ is proportional to the excitation magnetic field $\vec{H}$, and

$$\vec{B} = \mu_0 \vec{H}$$

The constant μ_0 is the magnetic permeability in a vacuum, also known as the magnetic constant or the permeability of free space, is a measure of the amount of resistance encountered when forming a magnetic field in a vacuum. In a material, the generalized form of the constitutive relations for the magnetic field is

$$\vec{B} = \mu_0 \mu_r \vec{H} + \vec{B}_r ,$$

and μ_r is the relative magnetic permeability, which is the ratio between the permeability of the materials μ and the permeability of the vacuum μ_0,

$$\mu_r = \mu / \mu_0$$

$\vec{B}_r$ is the remnant magnetic flux density, representing the magnetic flux output from the magnet, which is also the magnetic flux density when no magnetic field is present. In general, magnetic permeability of material is not a constant. In a nonlinear medium, the permeability may depend on the strength of the magnetic field. For example, in ferromagnetic materials, $\vec{B}$ is not a single value function of $\vec{H}$ and it exhibits hysteresis characteristics. Since the curl of $\vec{H}$ is zero, in a simply connected domain, $\vec{H}$ can be replaced by a magnetic scaler potential, φ, so that $\vec{H} = -\nabla\varphi$. Combining the magnetic scaler potential with the steady state condition and constitutive relations, the simplified Maxwell's equations can be written in terms of the magnetic scaler potential,

$$\nabla \cdot \left(-\mu_0 \mu_r \nabla\varphi + \vec{B}_r\right) = 0$$

In order to solve the above simplified Magnetic scaler potential equation, the boundary conditions have to be known, specifically, the magnetic flux density that penetrates outside the permanent magnets. The modeling has to include a larger domain (air or vacuum) outside the rotor discs with permanent magnets. The magnetic scaler potential at the far field boundary is a constant. The Maxwell's stress tensor is used in the calculation of forces and torques. The torque on a two-dimensional surface, can be numerically integrated using

$$\overrightarrow{\mathbb{T}} = \iint \overrightarrow{r} \times (\bar{\bar{\tau}} \cdot \overrightarrow{dA})$$

where $\bar{\bar{\tau}}$ is the Maxwell stress tensor, $\overrightarrow{dA}$ is the surface area element, $\overrightarrow{r}$ is the position vector where the force element is acted on. In Cartesian system, assume that $\vec{B} = \left(B_x B_y, B_z\right)$, then in air or vacuum, the element of the Maxwell stress tensor, $\bar{\bar{\tau}}$ can be expressed as $\bar{\bar{\tau}}_{ij}$, and

$$\bar{\bar{\tau}}_{ij} = \frac{1}{\mu_0} B_i B_j - \frac{1}{2\mu_0}\left(B_x^2 + B_y^2 + B_z^2\right)\Delta_{ij}, \qquad (i, j = 1,2,3)$$

where Δ_{ij} is an identity matrix. In three-dimensional space,

$$[\Delta_{ij}] = \begin{pmatrix} 1 & 0 & 0 \\ 0 & 1 & 0 \\ 0 & 0 & 1 \end{pmatrix}.$$

III. Torque Simulation Results and Discussion

The geometric parameters of the axial magnetic coupling, as sketched in Figure 3, includes the inner and outer disc rotor diameters, the gap (δ) between the rotor and the separator wall, the thickness of the separator wall (t), the diameter of the coin-type magnets (d), the diameter of the magnet array on the rotor discs (D), the distribution of the permanent magnets on the circular direction, the number of the permanent magnet pairs (N), the thickness of the rotor discs, the thickness of the embedded permanent magnets on both rotors.

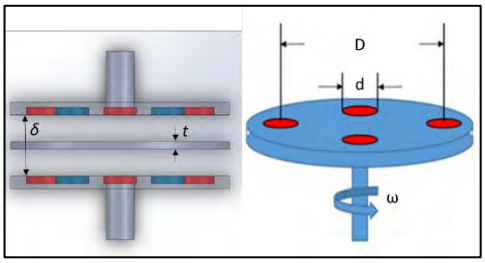

Figure 3. Schematic representation of a single rotor showing polar array of coin-type permanent magnets.

The maximum power transfer, P, across the coupling is a function of torque and rotational speed, and

$$P = f(\delta,\ t,\ T,\ \vec{B},\ \rho,\ \mu_w,\ d, D, N,\ \omega,\ t_1, t_2, \mu_{R1}, \mu_{R2}, \mu_F)$$

where, T is the absolute temperature, $\vec{B}$ is the magnetic flux density of the permanent magnets, ρ is the density of the separator wall material, μ_w is the magnetic permeability of the wall, ω is the rotational speed of the rotor, μ_{R1} is the magnetic permeability of the driver rotor disc material, μ_{R2} is the magnetic permeability of the driven rotor disc material, μ_F is the magnetic permeability of the fluid, $t_1$is the thickness of the driver rotor disc, and t_2 is the thickness of the driven rotor disc.

The COMSOL Multiphysics software with rotating machinery magnetic interface [15] is used to compute the Maxwell's equations for the magnetic field distribution and to obtain the transmitted torque. The computational domain includes the two rotors with identical size. The outer diameter of the rotor is 100mm, the inner diameter of the rotor is 60 mm. The two rotors are opposing (facing) each other with coin-size permanent magnets embedded on it. The rotors are connected to independent shafts. Both the driver and driven rotor discs have 5mm thickness. The rotor material is selected to be either lighter polymer materials such as ULTEM with relative permeability of 1 (very close to the permeability of the wood materials) or iron yokes which has a large relative magnetic permeability of 10. The two rotor discs are separated by air (vacuum) gap and a separator wall, which simulate the cryogenic tank wall. The tank wall has variable thickness ranging from 3 to 10 mm. The separator wall has the same diameter as the outer diameter of the rotor discs. The diameter of the coin-size permanent magnets range from 10mm to 16mm on the current MCT configuration. Five pairs of the north and south-pole magnets are alternatively and uniformly distributed and embedded on the opposing side of the two rotor discs. The thickness of the coin-type permanent magnet is 2mm. The center of each magnet is located concentrically on the rotor disc with a diameter of 80mm. The bore of the rotor disc is considered to be air. The entire rotor and magnet assembly is wrapped by air, with 20mm height away from each side of the rotors and 150 mm in diameter. The driver rotor has a rotational speed of 1000 RPM. Figure 4 shows the mesh system of the magnets, the rotor discs, and the air domain for the computation. To include the effect of the cryogenic tank wall materials on the transmitted torque, the relative permeability of the separator wall is selected to

range from 1 to 500, where 1 represents the wooden wall and 500 represents the steel wall. The relative permeability of the composite materials is about 1.0.

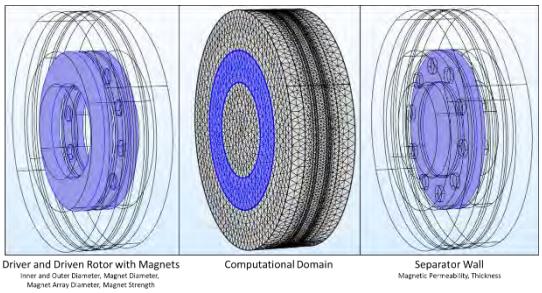

Figure 4. The computational domain and mesh for the MCT torque simulation.

The boundary condition for the permanent magnet specify the normal component of the magnetic flux density. For outward flux density (North-pole), the flux density is positive. For inward flux density (South-pole), the flux density is negative. For all simulations, the magnitude of the magnetic flux density of the coin-size permanent magnet is 1.42 Tesla. Figure 5 shows the configuration of the magnets.

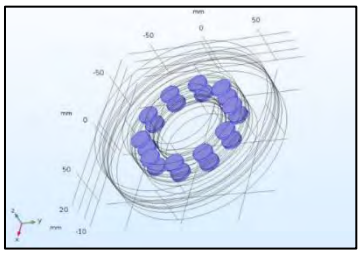

Figure 5. The magnet configuration on both driver and driven rotors.

A. Parametric Analysis:

The simulation started with the consideration of the influence of the magnetic property of the rotor disc and separator wall on the transmitted torque. The selected rotor discs materials are “iron wall” with relative magnetic permeability of 10 and “wood wall”, with relative magnetic permeability of 1. The separator wall materials are selected to “wood wall” with relative permeability of 1 and “steel wall” with relative permeability of 500. The control parameters are given in Table 1 for the parametric analysis.

The transmitted torque with respect to the magnets shifting angle (loading angle) was computed using COMSOL’s time-dependent rotating machinery magnetic module, with rotating mesh at 1000RPM. The magnets on the two opposing rotors are facing each other north to south, with attraction force at the beginning of the calculation. When the driver rotor rotates with 1000RPM, by keeping the driven rotor stationary, a shifting angle will be generated between the magnets on both rotors. As a result of the shift, the magnetic field distribution changes and in turn, the transmitted torque on driven rotor disc changes as a function of the shifting angle. Figure 6 shows the comparison of the transmitted torques among four configurations as listed in Table 1. The dimeter of the magnet is selected to be 10mm for all cases. The magnets are arranged on the surface of the rotor 36 degree a part circularly and alternating its poles. At zero degree shifting, the magnetic flux lines are focused on the axial direction of the rotors, and attracting force is maximum between the two rotors, there are no forces in the tangential direction of the rotor so the torque is approximately zero. When the shifting angle reaches 36 degrees, the north-pole magnets are facing the north-pole magnets creating repulsive force along the axial direction of the rotor, the torque again return to approximately zero. At 0.0148 second of rotation with 1000RPM speed, the shifting angle between magnets reaches 90 degree, the computed magnetic flux density distribution is shown in Figure 7. The flux lines are not focused on the axial direction, so the transmitted torque is not zero. The transmitted torque behaves like a sine function with respect to the shifting angles. For the “iron rotor-steel wall” configuration, the maximum transmitted torque is 0.0023 (Nm), for the “iron rotor-wood wall”, 0.0872 (Nm), for the “wood rotor-steel wall”, 0.0016 (Nm) and for the “wood rotor-wood wall” 0.0816 (Nm). Clearly, the permeability of the separator wall significantly affect the transmitted torque. The bigger the

permeability of the separator wall, the smaller the transmitted torque. On the influence of the rotor disc materials on the transmitted torque, the difference between "iron" and "wood" rotor materials is very small. The ratio between the percentage change of the maximum torque and the percentage change of the permeability of the separator wall, it was observed that

$$\frac{\Delta \mathbb{T}_{max}/\mathbb{T}_{max}}{\Delta \mu_w/\mu_w} = \begin{cases} -0.00195 & \text{for "iron rotor"} \\ -0.00196 & \text{for "wood rotor"} \end{cases}$$

Apparently, the influence on the transmitted torque from the rotor discs materials is very insignificant comparing to that of the separator wall materials.

Table 1 Simulation matrix for the influence of the rotor discs permeability

	Iron Rotor Steel Wall	Iron Rotor Wood Wall	Wood Rotor Steel Wall	Wood Rotor Wood Wall
Thickness Separator Wall t (mm)	5	5	5	5
Diameter of magnet d (mm)	10	10	10	10
Total Gap δ (mm)	11	11	11	11
Relative Permeability of the Driver Rotor μ_{R1} (N/mA)	10	10	1	1
Relative Permeability of the Driven Rotor μ_{R2} (N/mA)	10	10	1	1
Relative Permeability of the Separator Wall μ_w (N/mA)	500	1	500	1
Density of Driver Rotor Materials (kg/m^3)	7860	7860	750	750
Density of Driven Rotor Materials (kg/m^3)	7860	7860	750	750
Density of the Separator Wall (kg/m^3)	7860	750	7860	750

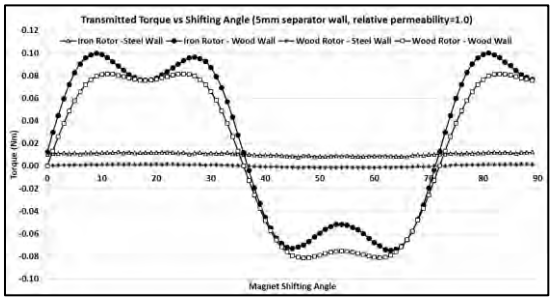

Figure 6. Comparison of the transmitted torque as a function of shifting angles for different rotor disc and separator wall materials.

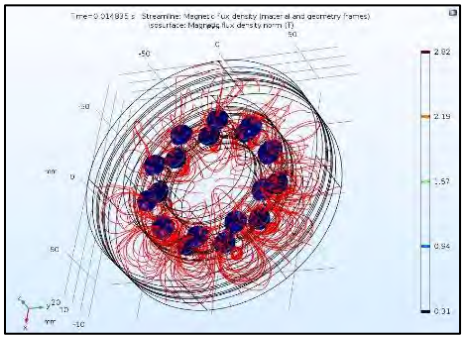

Figure 7. Magnetic flux density distribution at 90 degree shifting angle.

Figure 8 compares the effects of the permanent magnet size on the transmitted torque between the 10mm diameter magnets and 16mm diameter magnets. For both magnet configurations, the rotor material is "iron" so the relative permeability is 10, and the separator wall material is "wood", so the relative permeability is 1. The maximum torque generated by the 16mm diameter magnets is 0.5862 (Nm) which is much larger compared to the 10mm diameter magnets of 0.0872 (Nm). The effects of the separator wall permeability on the transmitted torque for large magnets

with a diameter of 16mm is shown in Figure 9. The relative permeability of the separator wall is selected to be 1 and 5, while keeping all other control variables the same for both cases. The maximum transmitted torques are 0.5892 (Nm) when $\mu_w = 1$, and 0.4750 (Nm) when $\mu_w = 5$. It is obviously observed that as the relative permeability of the separator wall decreases, the transmitted torque increases.

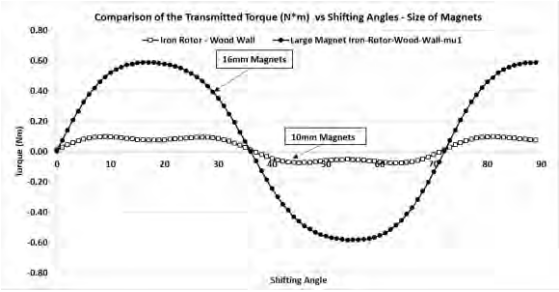

Figure 8. Comparison of the transmitted torque between 10mm and 16mm diameter magnets.

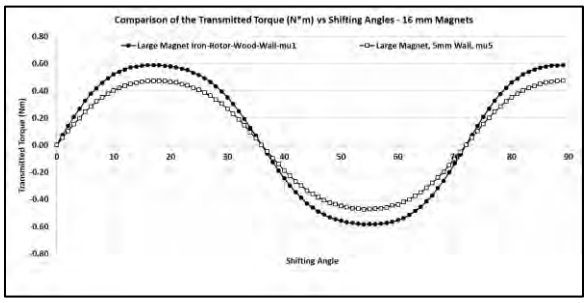

Figure 9. Effects of the separator wall relative permeability (μ_w =1 and μ_w =5) on the transmitted torque for 16mm magnet configuration.

The effects of the separator wall thickness on the transmitted torque is shown in Figure 10, for 10mm magnets (μ_w = 1) and 16mm magnets ($\mu_w = 5$). As the thickness of the separator wall increases, the transmitted torque decreases in both cases. This trend is the same for all wall permeability and all magnet diameters.

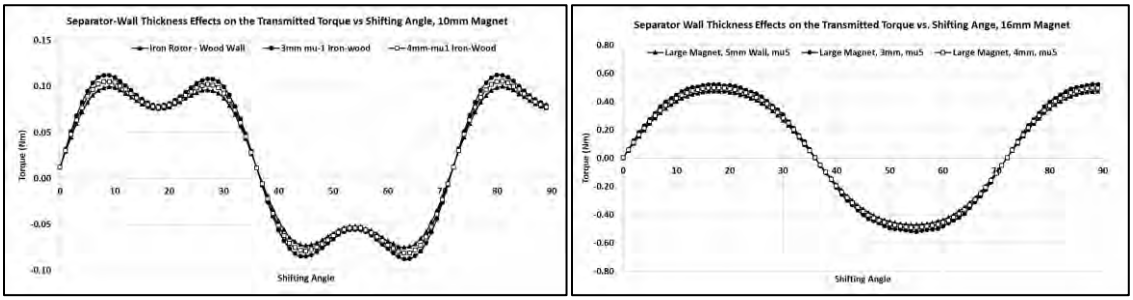

Figure 10. Separator wall thickness influence on the transmitted torque.

B. Non-dimensional analysis

It is obvious that there are a minimum of 15 parameters that affect the transmitted torque for the proposed MCT. It is critical to reduce the number of control variables so that a meaningful and well-controlled experiment can be conducted to investigate the feasibility of MCT prototype for cryogenic tank power transfer. Assuming that μ_{R1}, μ_{R2}, μ_F, t_1 and t_2 are pre-selected for the MCT, the independent variables will then reduce to 11. Using the Buckingham's Pi-theorem, a set of six dimensionless groups were developed [8] in terms of the 11 independent variables,

$$P = N \cdot \left[\frac{dD^2\omega B^2}{\mu_W}\right] \cdot f\left(\left[\frac{dD}{t\delta}\right], \left[\frac{T_s}{T}\right], \left[\frac{B^2}{\delta t \mu_W \rho_W \omega^2}\right], \left[\frac{d}{\delta}\right], \left[\frac{D}{\delta}\right]\right)$$

as shown in Table 2. It can be observed that the maximum torque, $\mathbb{T}=P/\omega$, increase with increases in the magnet diameter if the magnetic flux density is the same. The calculation results of the transmitted torque supported it. The results also support that the transmitted torque should decrease in response to an increase in μ_W, the magnetic permeability of the separator wall material.

Table 2. Value of non-dimensional groups calculated based on the parametric studies

Rotor - Wall	t(m)	δ (m)	d(m)	D(m)	μ_w	ρ_w (kg/m^3)	B(N/mA)	$\Pi_1=\frac{P\cdot\mu_W}{dD^2\omega B^2}$	$\Pi_2=\frac{dD}{t\delta}$	$\Pi_3=\frac{T_s}{T}$	$\Pi_4=\frac{B^2}{\delta t\mu_W\rho_W\omega^2}$	$\Pi_5=\frac{d}{\delta}$	$\Pi_6=\frac{D}{\delta}$	Torque (Nm)
Iron-Steel	0.005	0.011	0.010	0.08	500	7860	1.42	0.0112	14.5455	1	0.6769	0.9091	7.2727	0.0023
Iron-Wood	0.005	0.011	0.010	0.08	1	750	1.42	0.0008	14.5455	1	3547.1998	0.9091	7.2727	0.0872
Wood-Steel	0.005	0.011	0.010	0.08	500	7860	1.42	0.0078	14.5455	1	0.6769	0.9091	7.2727	0.0016
Wood-Wood	0.005	0.011	0.010	0.08	1	750	1.42	0.0008	14.5455	1	3547.1998	0.9091	7.2727	0.0816
Iron-Wood	0.003	0.011	0.010	0.08	1	750	1.42	0.0010	24.2424	1	5911.9997	0.9091	7.2727	0.1001
Iron-Wood	0.004	0.011	0.010	0.08	1	750	1.42	0.0009	18.1818	1	4433.9997	0.9091	7.2727	0.0934
Iron-Wood	0.005	0.011	0.016	0.08	1	750	1.42	0.0036	23.2727	1	3547.1998	1.4545	7.2727	0.5862
Iron-Wood	0.003	0.011	0.010	0.08	2	750	1.42	0.0019	24.2424	1	2955.9998	0.9091	7.2727	0.0969
Iron-Wood	0.004	0.011	0.010	0.08	2	750	1.42	0.0018	18.1818	1	2216.9999	0.9091	7.2727	0.0913
Iron-Wood	0.005	0.011	0.010	0.08	2	750	1.42	0.0017	14.5455	1	1773.5999	0.9091	7.2727	0.0866
Iron-Wood	0.003	0.011	0.016	0.08	5	750	1.42	0.0159	38.7879	1	1182.3999	1.4545	7.2727	0.5223
Iron-Wood	0.004	0.011	0.016	0.08	5	750	1.42	0.0150	29.0909	1	886.7999	1.4545	7.2727	0.4941
Iron-Wood	0.005	0.011	0.016	0.08	5	750	1.42	0.0144	23.2727	1	709.4400	1.4545	7.2727	0.4736

C. Start-Up Time and Slip Prediction

As illustrated in Figure 11, the torque and power requirement of the magnetic coupling device comes from the pump requirement of the CFM. The pump power is determined based on the fluid property, the tank geometry and the propellant mass flow rate.

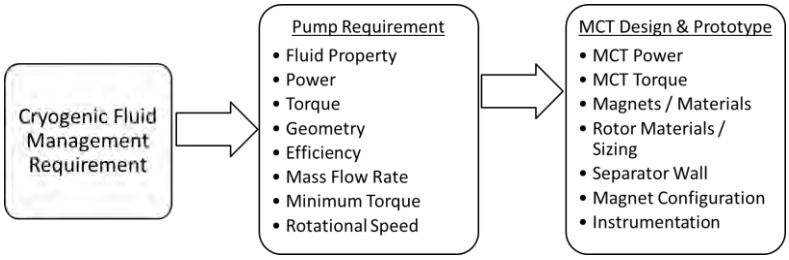

Figure 11. Key variables affecting the torque transmission of a magnetic coupler.

Due to the MCT bearing friction and the moment of inertia of the driven disc, the driven rotor will take time to synchronize with the driver disc rotor and accelerate to the required speed. As illustrated in Figure 12, for 10mm diameter magnets, the maximum transmitted torque exists when the shifting angle is abound 9 degree. For 16mm diameter magnets, the maximum torque exists when the shifting angle reaches 16 degree. At 1000 RPM rotational speed, the maximum transmitted torque can be reached between 0.0015 to 0.0026 seconds. Assume that the driven disc rotor is at rest in the beginning. The magnets on each rotor disc are configured north and south poles alternatively along the circumferential direction. The magnets on driver and driven rotor discs are opposing each other and aligned north to north through a separator wall. When the motor is turned on, the magnets are shifting its relative angle (loading angle), and the magnetic torque is generated. Through the separator wall, the torque is transmitted to the driven rotor. The transmitted torque increases as the shifting angle increases. If the transmitted torque reaches to the maximum, assuming there is no slip between rotors, then the driven disc rotor will synchronize with the driver disc rotor.

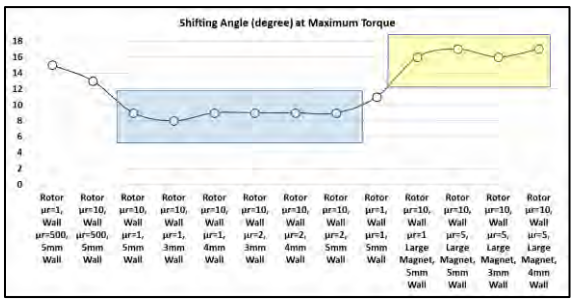

Figure 12. Magnet shifting angles when maximum torque reached.

Assume the driven disc rotor is made of polymer materials such as ULTEM. The moment of inertia of the disc rotor is I_z, the torque transmitted to the disc is $\mathbb{T}$, and the angular acceleration of the rotor is α. Then, based on the dynamics of the rotor, the transmitted torque $\mathbb{T}(t)$, as a function of the time t, can be expressed as

$$\mathbb{T}(t) = I_z \cdot \alpha(t)$$

If we integrate the angular acceleration with respect to time, from time zero to a final t_1, then

$$\int_0^{t_1} \alpha(t) \cdot dt = \int_0^{t_1} \frac{\mathbb{T}(t)}{I_z} dt$$

Note that the disc rotor moment of inertia, I_z, is a constant, and the integration of the angular acceleration with respect to time leads to the change of the angular rotational speed $\omega(t)$,

$$\omega(t_1) - \omega(0) = \frac{1}{I_z} \cdot \int_0^{t_1} \mathbb{T}(t) \cdot dt$$

If the disc rotor is at rest at $t=0$, then

$$\omega(t_1) \cdot I_z = \int_0^{t_1} \mathbb{T}(t) \cdot dt$$

Assuming the driven disc rotor is synchronized with the driver disc rotor under the maximum transmitted torque, $\mathbb{T}_{max}$, then the minimum time, t_1, required to reach maximum rotational speed RPM can be obtained from

$$t_1 = \frac{\left(2\pi \cdot \frac{RPM}{60}\right) \cdot (I_z)}{T_{max}}$$

Applying the moment of inertia principle for parallel axis, the moment of inertia of the driven disc rotor, as illustrated in Figure 13, can be calculated as

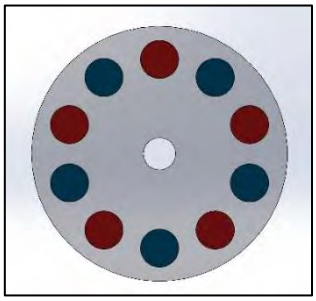

Figure 13. Configuration of the magnets on the disc rotor.

$$I_z = \left(\frac{1}{2} \cdot m_o \cdot R_o^2\right) - \left(\frac{1}{2} \cdot m_i \cdot R_i^2\right) + \left[\frac{1}{2} \cdot m_{mag} \cdot R_{mag}^2 + m_{mag} d^2\right] \cdot 10 - \left[\frac{1}{2} \cdot m_h \cdot R_h^2 + m_h d^2\right] \cdot 10$$

Where m_h is the removed hole inside the disc rotor, m_{mag} is the mass of the single magnet, which is measured at 0.006 kg.

$$m_o = \pi \cdot R_o^2 \cdot 0.008 \cdot \rho_{ultem} = \pi \cdot 0.05^2 \cdot 0.008 \cdot 1270 = 0.079796\ (kg)$$
$$m_i = \pi \cdot R_i^2 \cdot 0.008 \cdot \rho_{ultem} = \pi \cdot 0.03^2 \cdot 0.008 \cdot 1270 = 0.028727\ (kg)$$
$$m_h = \pi \cdot R_h^2 \cdot 0.003 \cdot \rho_{ultem} = \pi \cdot 0.005^2 \cdot 0.003 \cdot 1270 = 2.9924 \times 10^{-4} (kg)$$
$$m_{mag} = 0.006(kg)$$

So,

$$I_z = 2.7874 \times 10^{-4} \left(\frac{kg}{m^2}\right).$$

Therefore, for 16mm diameter magnets, t_1 can be estimated as

$$t_1 = \frac{2\pi \cdot 1000/60 \cdot 2.7874 \times 10^{-4}}{0.5862} = 0.050(s)$$

For 10mm diameter magnets, the minimum time required to reach 1000 RPM is

$$t_1 = \frac{2\pi \cdot 1000/60 \cdot 2.7874 \times 10^{-4}}{0.1001} = 0.292(s)$$

Comparing t_1 to the time required for the maximum torque to be reached against the shifting angle, 0.0015 ~ 0.0026 seconds, it is obvious that the motor has to be operated at the variable speed before it reaches the steady 1000 RPM. If no friction force or torque is applied to the disc rotor, it is only need a torque > 0 to rotate the system because there is no constraint that prevents the motion. Therefore, the designed magnets configuration will definitely rotate the rotor and provide power to the pump.

D. Minimum Torque Requirement Based on the Friction

The required transmitted torque depends on the cryogenic fluid viscosity. If the driven disc rotor is immersed in the cryogenic fluid, the liquid Hydrogen (LH2), the fluid will exert frictional torque to the rotational disc. The disc rotor will not rotate if the transmitted maximum torque is smaller than the resistance torque. Consider a single disc rotor as shown in Figure 14. The torque due to the viscosity shear stress on the surface of the rotor disc can be obtained as

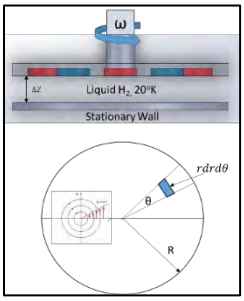

Figure 14. Sketch foe the frictional torque analysis.

$$\vec{\mathbb{T}} = \int \vec{r} \times d\vec{F}$$

and the magnitude of the torque is

$$\left|\vec{\mathbb{T}}\right| = \int_0^R 2\pi r^2 \sigma(r) dr,$$

where $\sigma(r)$ is the liquid shear stress on the surface of the rotor disc. Since the liquid hydrogen is between the rotor disc and a stationary wall, the shear stress can be obtained as

$$\sigma(r) = \mu_F \frac{dV}{dZ} = \mu_F \frac{\omega r}{\Delta Z},$$

where μ_F is the fluid viscosity. The frictional torque can be written as

$$\left|\vec{\mathbb{T}}\right| = 2\pi\mu_F \frac{\omega}{\Delta Z} \frac{1}{4} R^2,$$

In order to start the rotation, the transmitted torque on the rotor has to be higher than the frictional torque. It is known that the viscosity of the liquid hydrogen at 20K is about 1.354×10^{-5} $\left(\frac{kg}{ms}\right)$, the frictional torque as a function of rotational speed can then be plotted in Figure 15. Obviously, the transmitted torque from 10mm and 16mm magnet MCT configurations will provide enough torque.

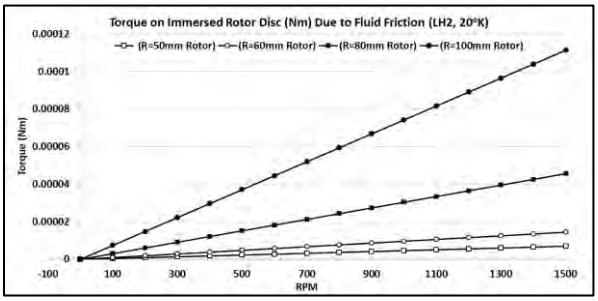

Figure 15. Frictional torque vs rotational speed.

E. Minimum Torque Requirement Based on the Pump Power

The required transmitted torque also depends on the cryogenic fluid pumping power. Assume the cryogenic tank fluid transfer can be simulated using one-dimensional incompressible fluid energy equation,

$$\frac{P_1}{\rho g} + \frac{V_1^2}{2g} + \frac{\dot{W}\eta_{pump}}{\dot{m}g} = \frac{P_2}{\rho g} + \frac{V_2^2}{2g} + h_L$$

where the power of the pump is, $\dot{W} = \mathbb{T} \times \omega$. The transferred power to the cryogenic fluid is $\dot{W}\eta_{pump}$. Assume the tank is large, so that $V_1 \approx 0$, neglect the pressure difference and head loss h_L, then the torque required to provide liquid hydrogen mass flow rate $\dot{m}$ can be obtained in terms of hydrogen density ρ and croess sectional area of the liquid transfer line, A.

$$\mathbb{T} = \frac{1}{2\omega}\frac{\dot{m}^3}{\rho^2 A^2 \eta_{pump}}$$

Assuming the efficiency of the pump, η_{pump}, is 50%, and cryogenic tank transfer line diameter is 1 inch, then the required torque as a function of the liquid hydrogen mass flow rate at various disc rotor rotational speed can be obtained as in Figure 16.

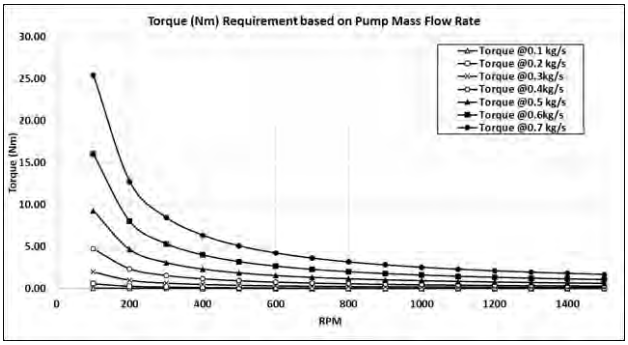

Figure 16. Torque requirement based on the propellant transfer requirement.

For the proposed MCT configuration, with the 16mm diameter magnets the MCT is capable of generate higher than 60W of power torque.

F. Effect of Cryogenic Temperature on Magnetic Materials

The critical temperature for Hydrogen to be liquid is 33 K. However, for hydrogen to be in a fully liquid state without boiling at atmospheric pressure, it needs to be cooled to 20.28 K. At this cryogenic temperature, the mechanical properties of the materials, include yield and ultimate strengths, fatigue strength, and hardness, all increases with decrease in temperature while the impact strength and the ductility of the materials decreases with decrease in temperature.

The understanding of the magnetic property at cryogenic temperature is a great design. Both of the magnetic property of the permanent magnets and the tank wall materials have to be considered in the cryogenic environment because the transmitted torque depends on the strength of the permanent magnets and the permeability of the tank wall. In the past, propellant tanks have been fabricated out of metals. Recent cryogenic tank development [2] uses composite materials which may dramatically reduce the weight of the tank. There are not enough experimental data for the magnetic property of the composite materials at cryogenic environment.

In general, all magnetic materials change its magnetic flux density as the temperature increases or decreases. The change of the magnetic permeability can be measured by the Reversible Temperature Coefficient of Induction, which is a measure for the average of the change in the value of $\vec{B}_r$ as a function of temperature. The reversible temperature coefficient (RTC) of magnetic flux density is defined as:

$$RTC = \frac{\Delta B_r}{B_r} \times \frac{1}{\Delta T} \times 100\%$$

where ΔB_r is the change of residual induction and ΔT is the change of temperature. The *RTC* indicates the reversible decrease of *Br*, based on normal room temperature (20°C) in percent per 1°C increase in temperature. *Br* can be calculated for any temperature within the measured range. Within the temperature range of 20°C to maximum temperature, the typical values of *RTC* for the major classes of permanent magnets are -0.2 %/°C for ceramic magnets, -0.12 %/°C for NdFeB, -0.04 %/°C for SmCo type magnets [16]. In temperatures ranging from -270°C up to 400°C Alnico magnet is very stable. Its temperature coefficient is as low as -0.03 to -0.02 %/°C [17]. This indicated that the magnetic flux density will increase for permanent magnet when temperature decreases.

However, the reversible temperature coefficient has four limitations: (1) on the high temperature side, if the Curie temperature of the material is reached then every magnet material loses its magnetism; (2) it is only suggested to work in given temperature range; (3) The reversible temperature coefficient is not a constant [18]. It may vary according to the temperature range that the measurement is conducted. The temperature coefficients of magnetization and coercive force in many instances do not give enough information about how a magnet will respond to temperature change; and most importantly (4) on the low temperature side, especially cryogenic temperature environment, the calculation of the *Br* is not reliable. There are not enough experimental data available for the magnetic property of composite materials.

At the cryogenic environment, it is expected that the magnetic properties of the materials can be determined based on the relative permeability. The relative magnetic permeability is influenced by the structure of materials and bonding energy levels. It indicates whether a material is attracted into or repelled out of a magnetic field, which in turn has implications for practical applications. Consider the three basic types of magnetic materials [19]: (1) diamagnetic materials ($\mu_r < 1$). In this materials, there is no net atomic or molecular magnetic moment. When magnetic field is applied, the materials create a magnetic field in opposition to an externally applied magnetic field thus causing a repulsive effect. When the field is removed, the effect disappears. Typical diamagnetic materials are silver, mercury, diamond, lead, and copper; (2) paramagnetic materials ($1 < \mu_r < 10$). In this materials, there is a net magnetic moment at the atomic level, but the coupling between neighboring moments is weak. When externally magnetic field is applied, the materials tend to create a magnetic field that align with the applied field, yielding a net magnetic moment causing materials to be attracted to the magnetic fields. When the external magnetic field is removed, the effect disappears; and (3) ferromagnetic materials ($\mu_r > 10$). In this materials, there is a strong coupling between neighboring moments. When external magnetic field is applied, the coupling gives rise to a spontaneous alignment of the moments. For ferromagnetic materials, such as Fe-Ni-Co alloys, magnetization is due to the contribution of the unpaired electron spins and coupling interactions causing magnetic moments of adjacent atoms to be parallel to an

applied magnetic field and parallel to each other. Thus, magnetization remains. At cryogenic temperature, the residual induction strength of ferromagnetic materials are expected to increase with decreasing temperature. For example the Fe-Ni alloys is more temperature sensitive than the Fe-Si alloys. Fe-Ni has large decrease in residual induction at low temperature [20]. The understanding of the magnetic property at cryogenic temperature remains a great challenge. It is critical to experimentally study the permanent magnet behavior at the cryogenic environment.

IV. Conclusion

The transmitted torque of an axial-field magnetic coupling was evaluated. The influence of the magnetic permeability of the tank wall, the thickness of the wall, and the configuration of the permanent magnets were analyzed. Results indicated that the larger the magnets, the larger the transmitted torque. The studied MCT transmitted larger torque with the smaller permeability wall, which indicated that the MCT is better suited for composite tank application. As the thickness of the tank wall increases, the transmitted torque decreases. The transmitted torque analysis provides the critical design guideline for the MCT prototype. The magnetic flux density of the permanent magnets may increase as temperature decreases, which indicated that the MCT will transmit larger torque at cryogenic temperature however it has not been confirmed by experimental measurements. In order to fully understand the MCT performance in the cryogenic environment, the magnetic property of the permanent magnet and composite materials have to be experimentally measured.

Acknowledgments

The author Z. Deng greatly thanks the support of NASA Marshall Faculty Fellowship Program for this research. Z. Deng also greatly thanks the excellent guidance and support of Barry Battista, Jeremy Kenny, Alicia Turpin, Stanley Tieman of ER 43 at NASA MSFC, Frank Six, the Director of NASA Marshall Faculty Fellowship Program, and Gerald Karr, Professor of the University of Alabama in Huntsville. The author would also like to thank the simulation support of Kiran Uppalapati from the COMSOL technical support team.

References

[1]Sheehy, J., "Cryogenic Fluid Management Investments Overview," Space Technology Mission Directorate, NASA, https://www.nasa.gov/sites/default/files/atoms/files/nac_jsheehy_cryo_nov2016_tagged.pdf, 2016.

[2]Steitz, D., McMahan, T., and Anderson J., "NASA Tests Game Changing Composite Cryogenic Fuel Tank," NASA News release, 13-205, https://www.nasa.gov/press/2013/july/nasa-tests-game-changing-composite-cryogenic-fuel-tank. 2013.

[3]Chato, D., "Cryogenic Fluid Transfer for Exploration," NASA/TM—2008-215286, 2008.

[4]Hastings, L., Tucker, Flachbart, R., Hedayat, A., Nelson, S., "Marshall Space Flight Center In-Space Cryogenic Fluid Management Program Overview," AIAA paper 2005-3561, 41st AIAA/ASME/SAE/ASEE Joint Propulsion Conference & Exhibit Tucson, Arizona, 2005.

[5]Atallah, K., and Howe, D., "A novel high-performance magnetic gear," Magnetics, IEEE Transactions on, vol. 37, pp. 2844-2846, 2001.

[6]Charpentier, J., Fadli, N. , and Jennane, J. , "Study of Ironless Permanent Magnet Devices Being Both a Coupling and an Axial Bearing for Naval Propulsion," *IEEE Transaction of Magnetics*, vol. 39, no. 5, pp. 3235–3237, May 2003.

[7]Ausserlechner, U., "The maximum torque of synchronous axial permanent magnetic couplings," *Progress in Electromagnetics Research B*, Vol. 40, 1-29, 2012.

[8]Battista, B., "Preliminary analysis of evaluation of magnetic shaft couplings for applications requiring transmission of mechanical work/power across the solid walls of cryogenic tank structures," Personnel communication with Alabama A&M university Magnetic Coupling Research team, November 2017.

[9]Battista, B., "Dimensional analysis of magnetic coupling," Presentation to Alabama A&M University Magnetic Coupling Research Meeting, March 2018.

[10]Mirimani, S.M., Vahedi, A., "Developing a 3D-FEM Model for Electromagnetic Analysis of an Axial Flux Permanent Magnet Machine," *J. Electromagnetic Analysis & Applications*, 2: 258-263, 2010

[11]Yang, Z., Zhao, H., "Torque Calculation and Analysis of Permanent-Magnetic Gears," https://www.ansys.com/-/media/ansys/corporate/resourcelibrary/conference-paper/2002-int-ansys-conf-77.pdf, 2002.

[12]Lubin, T., Smail, M., and Rezzoug, A., "Simple Analytical Expressions for the Force and Torque of Axial Magnetic Couplings," IEEE Transactions on Energy Conversion, Volume: 27, Issue: 2, June 2012.

[14]Dolisy, B., Lubin, T., Mezani, S., and Lévêque, J., "Three-Dimensional Analytical Model for an Axial-Field Magnetic Coupling," *Progress In Electromagnetics Research M*, Vol. 35, 173-182, 2014.

[14]Dolisy, B., Mezani, S., Lubin, T., Lévêque, J., "A new analytical torque formula for axial field permanent magnets coupling," *IEEE Transactions on Energy Conversion*, Volume: 30, Issue: 3, Sept. 2015.

[15]COMSOL Multiphysics 5.3a AC/DC Module User Guide, 2017.

[16]Permanent Magnet Stability, http://www.magmamagnets.com/magnets-technical-information/permanent-magnet-stability.

[17]IBS Magnet, "Permanent Magnets Materials and Magnet Systems," https://www.ibsmagnet.com/pdf/en/ibs_e.pdf.

[18]Constantinides, S., "Understanding and Using Reversible Temperature Coefficients," Presentation at the Magnetics 2010.

[19]Duthil, P., "Material Properties at Low Temperature," CAS - CERN Accelerator School: Course on Superconductivity for Accelerators, Erice, Italy, 24 Apr - 4 May 2013, pp.77-95 (CERN-2014-005).

[20]Gniewek, J. and Ploge, E., "Cryogenic Behavior of Selected Magnetic Materials," *Journal of research of the National Bureau of Standards-C*, Engineering and Instrumentation, vol. 69C, No.3, July- September 1965.

Modeling of Condensation in the Presence of Noncondensables in GFSSP

Michael R. Baldwin[1] and S. Mostafa Ghiaasiaan[2]
Georgia Institute of Technology, Atlanta, GA, 30332

and

Alok K. Majumdar[3] and Andre C. LeClair[4]
National Aeronautics and Space Administration, Marshall Space Flight Center, Huntsville, AL, 35812

The Generalized Fluid System Simulation Program (GFSSP) computer code is enhanced with the capability to model condensation in the presence of noncondensable gases. Condensation in the presence of noncondensables is modeled using the Couette flow film (stagnant film) model. Experimental data on the condensation of water vapor in downward flow of air-water vapor and helium-water vapor mixtures in vertical tubes are compared with the predictions of GFSSP. The comparisons show that with the implemented capability GFSSP can predict the experimental data well.

Nomenclature

A	=	area
$a_I^{"}$	=	interfacial area concentration
C_{Pv}	=	specific heat of vapor mixture
C_{PF}	=	specific heat of the liquid condensate
D	=	pipe diameter
$\boldsymbol{h_{fg}}$	=	specific enthalpy of vaporization
h_{FI}	=	liquid film-to-interphase heat transfer coefficient without the effect of mass transfer
$\dot{h}_{\mathrm{FI}}$	=	liquid film-to-interphase heat transfer coefficient with the effect of mass transfer
h_{GI}	=	gas mixture-to-interphase heat transfer coefficient without the effect of mass transfer
$\dot{h}_{\mathrm{GI}}$	=	gas mixture-to-interphase heat transfer coefficient with the effect of mass transfer
J	=	unit conversion factor (=778 ft-lb_f/Btu)
K_f	=	flow resistance coefficient
K_{GI}	=	gas mixture-to-interphase mass transfer coefficient for vapor
M_n	=	molar mass of the noncondensable
M_v	=	molar mass of the vapor
m	=	mass
$\dot{m}$	=	mass flow rate
$m^{"}$	=	condensation mass flux
$\dot{m}_G$	=	gas-vapor mixture mass flow rate
$\dot{m}_L$	=	liquid film mass flow rate
$m_{v,G}$	=	vapor mass fraction at the free stream mixture
$m_{v,s}$	=	vapor mass fraction at the condensate-gas mixture interphase
P	=	total pressure

[1] Graduate Student Assistant, Department of Mechanical Engineering, Georgia Institute of Technology.
[2] Professor, Department of Mechanical Engineering, Georgia Institute of Technology.

[3] Thermal Analysis Engineer, NASA Marshall Space Flight Center, ER43.
[4] Thermal Analysis Engineer, NASA Marshall Space Flight Center, ER43.

$\bar{T}_F$	=	condensate film mean temperature
$\bar{T}_G$	=	free stream gas-vapor mixture temperature
T_I	=	interfacial temperature
T_{SAT}	=	saturation temperature
u	=	velocity
$X_{v,s}$	=	vapor mole fraction at the condensate-gas mixture interphase
z	=	axial coordinate
α	=	void fraction
δ_F	=	condensate film thickness
Γ_{cond}	=	rate of condensation per unit mixture volume
ρ	=	density

I. Introduction

Condensation in the presence of noncondensables is a common phenomenon in nature and industry. Condensers in steam power cycles, for example, operate at low pressures and as a result are vulnerable to the inward leakage of air and the accumulation of air in the condenser flow passages. In large condensers the noncondensables preferentially accumulate in the parts of the condenser where the flow rate is low. Noncondensable-rich pockets can thus form in these parts of the condenser and lead to the air blanketing phenomenon, whereby rendering those condenser segments essentially ineffective. Even without noncondensable blanketing, the presence of noncondensables in the vapor, at a few percent mass fraction, leads to a significant reduction in the efficiency of the condenser. Condensation in the presence of noncondensables is also of particular interest when the recovery of water from steam-noncondensable gas mixtures is intended. Other applications of interest include but are not limited to moisture removal and in-situ propellant recovery for deep space missions.

The presence of small amounts of noncondensables reduces the condensation rate significantly. The flow of vapor towards the cold surface where condensation is to occur results in the accumulation of the noncondensables near the interphase between the gas-vapor mixture and the condensate. This forms a noncondensable-rich gas-vapor film. Consequently, the vapor will need to overcome a mass transfer resistance and diffuse through this noncondensable-rich film before it can condense at the interphase. The presence of noncondensables thus renders the condensation process into a combined heat and mass transfer process. A detailed discussion of condensation in general, and condensation in the presence of noncondensables can be found in Ghiaasiaan[1].

A widely-applied engineering method for modeling condensation in the presence of noncondensables is the Couette flow film model (also referred to as the stagnant flow film model). This technique has been shown to do well when applied to external as well as internal flow condensation processes. The model has also been successfully implemented in computer codes that apply the two-fluid modeling technique for the treatment of flow condensation[2,3]. More recent applications of the stagnant film model include condensation in the containment of nuclear reactors[4].

In this paper we report on the implementation of the Couette flow film model for condensation in the presence of noncondensables in the GFSSP computer code,[7] and its validation against experimental data.

II. Theory

A. General Remarks

GFSSP is a general purpose computer program that analyzes transient and steady state flow rates, pressures, temperatures, concentrations, and conjugate heat transfer in complex flow networks. It employs a finite volume formulation of the mixture mass, mixture momentum, and mixture energy conservation equations coupled with thermodynamic equations of state for real fluids. These systems of equations are solved using a hybrid numerical algorithm based on a combination of the Newton-Raphson and successive substitution methods. GFSSP contains a graphical user interface that allows the user to "point, drag, and click" various components of the model into place.

These components are divided into nodes, branches, and conductors which compute scalar properties, mass flow rates, and heat transfer rates, respectively. Fig. 1 provides a depiction of a typical counter-flow annular heat exchanger model displayed by GFSSP. The development of GFSSP at the NASA Marshal Space Flight Center started in 1994, and since then the program has been enhanced, and has been successfully verified through 30 example problems. Its ability to allow the implementation of user subroutines (using FORTRAN) greatly enhances its capacity to accommodate new sub-models and whereby simulate a vast variety of practical and specific applications.

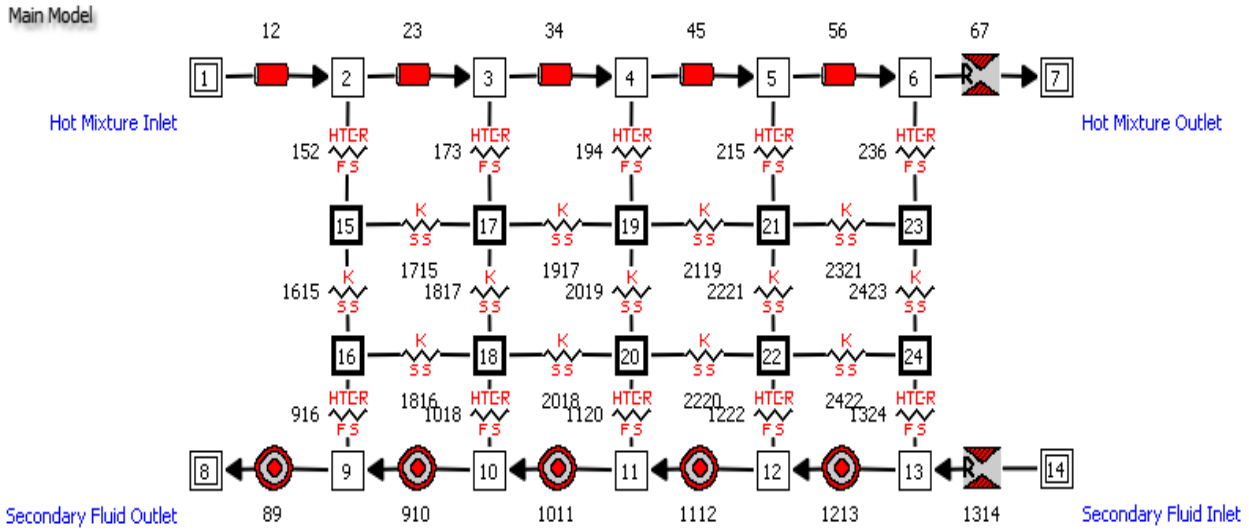

Figure 1: Counter flow heat exchanger model displayed in GFSSP.

Currently the condensation model has been implemented as a routine with one-way coupling to GFSSP. When condensation in a flow passage is of interest, for example, the condensation subroutine receives information about the pressure, flow rate, and flow properties at the inlet to the flow passage (i.e., the first node in the GFSSP model of the flow passage) from GFSSP, as well as the pressure and wall temperature at every node in the condensing flow passage. The wall inner surface temperature distribution can also be provided to the condensation subroutine as a user input. The condensation routine then solves the Couette flow film model equations (discussed below) at every node and every time step, thus calculating the condensation rate in each node. Although GFSSP rigorously keeps track of the mass conservation and concentration of vapor and noncondensables, the program does not currently separate the condensable species into vapor and liquid phases. To circumvent this issue, the condensation subroutine independently solves the mass conservation equations for the condensate, vapor, and the noncondensable, thus keeping track of the buildup of the noncondensable concentration along the condensation flow passage.

B. Couette Flow Film Model

Only the outline of the model is presented here, and a detailed discussion can be found in (Ref. 1). The implementation of the model follows Refs. (2, 3), where the model has been successfully implemented for the treatment of condensing two-phase flows in computer codes that are based on two-fluid modeling.

Fig. 2 depicts a schematic of the temperature and concentration profiles at the vicinity of the condensate-vapor/noncondensable mixture interphase during condensation on a cold surface, where for simplicity and convenience the condensate is depicted as a falling liquid film. Although a falling liquid film is the predominant flow regime for the condensate in most terrestrial condensation processes, the model to be described is general and can be applied to other flow regimes as well.

It is assumed that the noncondensable has essentially zero solubility in the condensate liquid. As mentioned earlier, a noncondensable-rich film of gas-vapor mixture forms next to the interphase and the vapor molecules need to diffuse through this layer before they can reach the interphase. The accumulation of the noncondensables near the interphase leads to the reduction of vapor pressure at the interphase. Because the interphase must be at saturation conditions with respect to the local vapor pressure, the interphase temperature will be reduced as well. The overall effect of the presence of noncondensables is often a significant reduction in the condensation rate, even when the concentration of the noncondensable in the vapor-noncondensable bulk is very small.

Application of energy and mass conservation to the interphase, and taking into account the effect of mass transfer on the convective heat and mass transfer processes (effect of transpiration), leads to the following set of six coupled equations that need to be solved simultaneously.

$$T_{\mathrm{I}} = T_{\mathrm{sat}}(X_{\mathrm{v,s}}P) \tag{1}$$

$$\dot{h}_{\mathrm{GI}}(\bar{T}_{\mathrm{G}} - T_{\mathrm{I}}) - \dot{h}_{\mathrm{FI}}(T_{\mathrm{I}} - \bar{T}_{\mathrm{F}}) + m^{"}\boldsymbol{h}_{\mathrm{fg}} = 0 \tag{2}$$

$$m^{"} = -K_{\mathrm{GI}} \ln \frac{1 - m_{\mathrm{v,G}}}{1 - m_{\mathrm{v,s}}} \tag{3}$$

$$m_{\mathrm{v,s}} = \frac{X_{\mathrm{v,s}}M_{\mathrm{v}}}{X_{\mathrm{v,s}}M_{\mathrm{v}} + (1 - X_{\mathrm{v,s}})M_{\mathrm{n}}} \tag{4}$$

$$\dot{h}_{\mathrm{GI}} = \frac{-m^{"}C_{Pv}}{\exp\left(\frac{-m^{"}C_{Pv}}{h_{\mathrm{GI}}}\right) - 1} \tag{5}$$

$$\dot{h}_{\mathrm{FI}} = \frac{m^{"}C_{PF}}{\exp\left(\frac{m^{"}C_{PF}}{h_{\mathrm{FI}}}\right) - 1} \tag{6}$$

In these equations h_{GI} and h_{FI} represent the interphase-mixture and interphase-film convective heat transfer coefficients, respectively, at the limit of vanishing mass transfer (i.e., vanishing condensation rate). The quantities $\dot{h}_{\mathrm{GI}}$ and $\dot{h}_{\mathrm{FI}}$ are defined similarly, but they account for the effect of mass transfer. The parameter K_{GI} represents the vapor mass transfer coefficient between gas-vapor bulk and the interphase, also at the limit of negligible mass transfer rate through the interphase. The unknowns in Eqs. (1 – 6) are $T_{\mathrm{I}}, m_{\mathrm{v,s}}, X_{\mathrm{v,s}}, m^{"}, \dot{h}_{\mathrm{GI}}$, and $\dot{h}_{\mathrm{FI}}$.

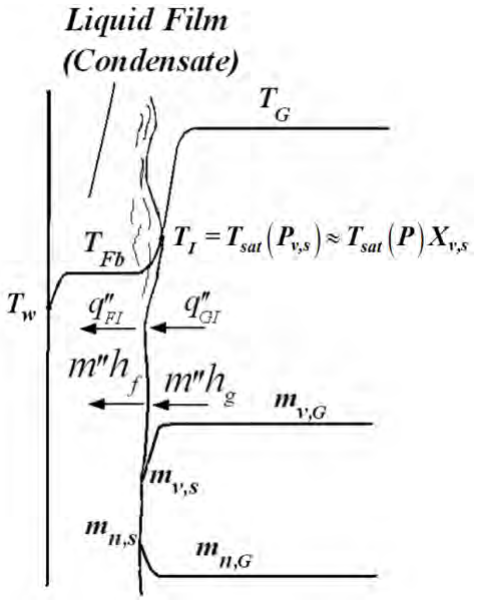

Fig. 2. Schematic of the temperature and species concentration profiles during condensation in the presence of a noncondensable.

C. Implementation in GFSSP

A discussion of GFSSP's mathematical formulation of the conservation and transport equations, and their numerical solution, can be found elsewhere, including Majumdar et al. (Refs. 8-10). GFSSP discretizes the thermofluid system to be analyzed into nodes, branches, and conductors. GFSSP applies a finite volume formulation of mass, momentum, species, and energy conservation equations in conjunction with the thermodynamic equations of state for real fluids as well as energy conservation equations for the solid. The system of algebraic equations describing the resulting fluid/solid network is solved by a hybrid numerical method that is a combination of the Newton-Raphson and successive substitution techniques. The scalar properties such as pressure, temperature, and concentrations are calculated at nodes, the flow rates are calculated at branches, and the heat transfer rates are computed in conductors.

The mass and momentum equations are simultaneously solved to calculate system respective pressures and mass flow rates. Next, the energy equation is solved for each species to compute enthalpies, and mixture temperatures can be extracted thereafter. GFSSP's conjugate heat transfer capabilities can then be utilized to solve for the inner wall temperatures needed for the condensation subroutine. Inner wall temperatures can also be specified by the user in a separate subroutine if desired. Currently GFSSP keeps track of the species conservation without differentiating between the liquid and gas phases. Therefore, the mass fraction (concentration) of the vapor and noncondensable in the gas-vapor mixture must be tracked within the condensation subroutine. Since the vapor in the free stream is always assumed to be saturated, the free stream nodal temperatures can be determined using the nodal pressures provided by GFSSP. The mixture mass flow rates in each branch are also receive from GFSSP by the condensation subroutine. Knowledge of the nodal pressures, mixture mass flow rates, and inner wall temperatures are thus sufficient to solve Equations (1-6).

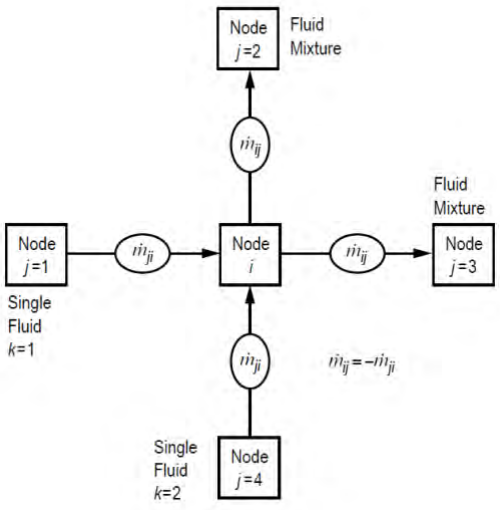

Figure 3: Indexing system for the mathematical formulation in GFSSP

The solving of Equations (1-6) thus lead to the calculation of the condensation mass flux at the condensate-vapor-noncondensable interphase. The condensation rate per unit mixture volume is then found from

$$\Gamma_{cond} = a_I'' m'' \tag{7}$$

where a_I'' represents interfacial area concentration (i.e., the interfacial area per unit two-phase mixture volume), which is flow regime dependent. As a result, in general, a flow regime map is needed for the calculation of the condensation flows. For an ideal annular flow in a circular pipe, assuming axisymmetric flow, we have

$$a_I'' = \frac{\sqrt{\alpha}}{D} \tag{8}$$

where α is the void fraction, and D is the tube inner diameter. The void fraction is related to the liquid film thickness according to

$$\alpha = 1 - \left(\delta_F / D\right)^2 \tag{9}$$

For a steady-state condensing flow in an axisymmetric circular pipe the following equations are solved independently by the condensation routine.

$$\frac{d}{dz}\dot{m}_L = Aa_I''m'' \tag{10}$$

$$\frac{d}{dz}\dot{m}_G m_{v,G} = -Aa_I''m'' \tag{11}$$

$$\dot{m}_G m_{n,G} = const. \tag{12}$$

Furthermore, as previously stated, the gas-vapor mixture is assumed to remain saturated, therefore

$$T_G = T_{sat}(x_{v,G}P) \tag{13}$$

Equations (1-6) are solved iteratively in every time step, and for every node where condensation is underway. These equations are solved using the method of repeated bisections. Equations (10-13) are discretized using the finite-volume technique, consistent with the solution method in GFSSP.

The general solution method for the method of repeated bisections is as follows. It is known that the mixture-film interface temperature (one of the six unknowns) must be bounded between the inner wall and mixture temperatures. Thus the condensation subroutine is first run twice, with an interface temperature guess as the wall temperature and the mixture temperature. Since the interface temperature is being provided, Equations (1-6) can be solved directly, and Equation (2) was chosen to act as a residual equation. A correct guess of the interface temperature would result in a zero residual, i.e., the left-hand and right-hand sides of Equation (2) would be equal. Our two initial guesses for the interface temperature are knowingly wrong but guarantee exactly one positive and one negative residual, ensuring a bounded solution. The condensation subroutine is then run a third time, and the interface temperature guess is now at the bisected temperature of the first two guesses. Based on the sign of the residual for this guess, it can be determine whether the guess was too high or too low. The just-guessed interface temperature then becomes either the new upper bound or new lower bound, respectively. The condensation subroutine is then run again at the new bisected temperature, and this process is repeated until the zero residual is found, to the desired accuracy.

III. Model Validation

A. Experimental Data

Experimental data of Siddique[5] and Ogg[6] are used for model validation. Selected test runs from these references were used in Refs. (2,3) for the validation of the Couette flow film model that had been incorporated in a two-fluid model for condensing two-phase flow. The important test section geometric characteristics of the experimental test rigs of Siddique[5] and Ogg[6] are summarized in Table 1. The test sections in these experiments were circular, vertical metallic tubes that had annular jackets. The condensing two-phase mixture flowed downward inside the circular tubes, while the tubes were cooled by a countercurrent flow of a liquid coolant that flowed in their annular jackets. The wall inner surface temperatures were measured at several points along the test sections. The reported wall inner surface temperatures for the tests of Siddique[5] and Ogg[6] are used as the flow passage boundary condition here.

The wall temperatures were measured at several points, as noted in Table 1. For the simulations interpolation was used for the estimation of wall surface temperature.

Test characteristic	Siddique[5]	Ogg[6]
Test section tube material	SS 304	SS 321
Total tube length [m]	2.54	5.2
Length of cooled segment of tube [m]	2.44	2.44
Inner diameter [m]	0.046	0.049
Wall thickness [m]	0.0024	0.00071
Temperature measurement location from test section entrance [cm]	10.0 and then at each 30.5 cm step	0.0 and then at each 5 cm step

Table 1. Important experimental test section geometric parameters

Source	Test no.	Pressure [kPa]	Mixture flow rate [kg s^{-1}]	Noncondensable mass fraction
Siddique[5]	6	133	0.00378	0.332
	26	233	0.00740	0.224
	41	213	0.00937	0.099
	56	157	0.00275	0.100
	63	466	0.00256	0.065
	74	465	0.00596	0.054
Ogg[6]	12-4	108	0.0131	0.179
	17-1	252	0.0203	0.017
	19-4	139	0.0111	0.018

Table 2. The test section inlet conditions for the experiments used for model validation.

B. Simulations

Fig. 4 depicts the GFSSP representation of the flow channels in the experiments. For the data of Siddique[5], the GFSSP model divides the flow channel into 25 nodes, with 26 branches that connect the adjacent nodes. All branches are 0.1 m long. GFSSP is capable of solving conjugate heat transfer problems, and the model depicted in Fig. 4 represents both the primary (condensing flow pipe) and secondary (the annulus) flows. The condensation model, however, runs parallel to GFSSP and currently is one-way coupled to GFSSP. The secondary side of the depicted GFSSP model is thus redundant and is included to facilitate the simulations. For the simulation of the experiments of Ogg[6], the flow channels is into 33 nodes and 34 branches, and each branch is 0.05 m long. As will be shown later, parametric calculations showed that the aforementioned nodalization was sufficient to ensure an acceptable grid-independence for the simulation results.

C. Results and Discussion

The grid-dependence of the model was investigated by parametric runs. The results of a typical test are shown in Figure 5, where the condensation rate along the test section of Siddique[5] for his Run 26 is calculated using nine nodes and 10 branches (the coarse node simulation), and 25 nodes and 26 branches (fine nodes), and the computed results are compared with experimental data. In the coarse nodes scheme, the first branch was 0.1 m long and the remainder of branches were all 0.3 m long. The scheme with fine nodes is used for all the forthcoming simulations representing the data of Siddique. This and other similar simulations indicated that the nodalization described in previous section is reasonable, and using more nodes and smaller branches will have a small effect on the results. It should also be mentioned that the wall temperatures were measured at finite distances during the simulated experiments. The wall

temperature readings provided in Siddique[5], for example, were spread 0.3 m apart such that either a coarse GFSSP model was required or linear interpolation of the inner wall temperatures from the data provided was required. The coarse model in Figure 5 thus assumes relatively large (0.3 m) segments of pipe contain constant thermal properties.

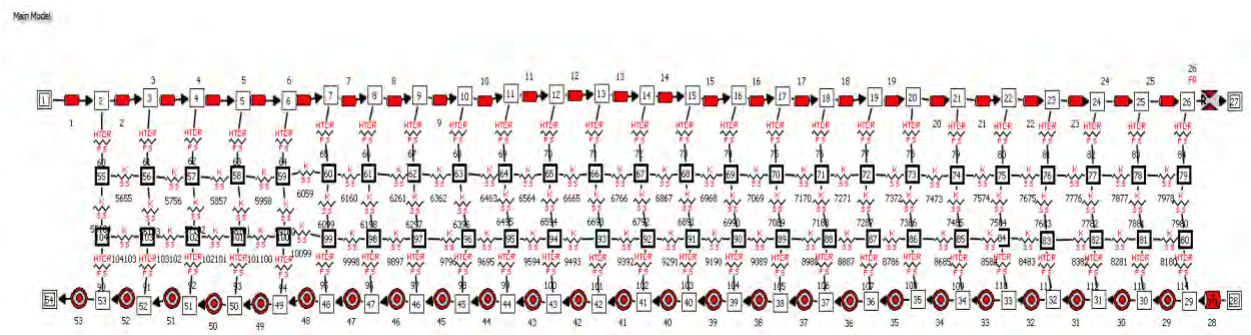

Figure 4. GFSSP model used to solve the Couette flow model condensation equations for the experiments of Sidduque[5].

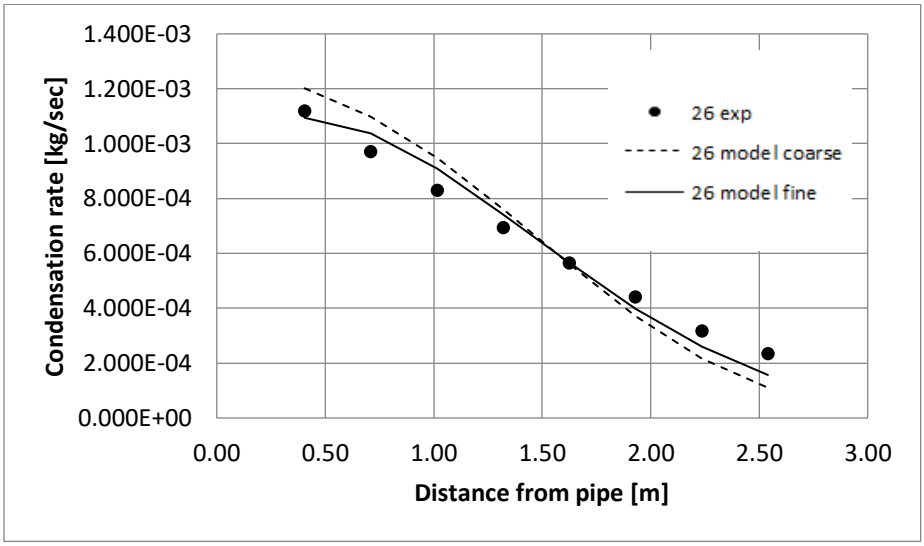

Figure 5. Grid-dependence test of the simulation results for Run 26 of Siddique (Ref. 5).

Figure 6 compares the GFSSP model predictions for air-steam mixtures with the experimental data of Siddique (Ref. 5). Figures 7 displays a similar comparison between model predictions and experimental data for Siddique's helium-steam mixtures. The experimental condensation rates in Figures 6 and 7 were reported in Siddique, where they had been calculated using locally measured vapor-noncondensable mixture temperatures and assuming that this mixture was everywhere saturated. Figure 8 compares the predictions of the model with the experimental data of Ogg (Ref. 6). The noncondensable mass fractions in the experiments of Ogg have also been calculated by using the the measured vapor-noncondensable mixture temperatures and assuming that the mixture was everywhere saturated. Figures 6 and 7 show that, overall, the model agrees with the experimental data of Siddique very well. The model deviates relatively slightly from the experimental data for run 41 in Figure 6. It is noted that, among the experimental runs simulated here, this run represented the lowest inlet mixture flow rate, as well as the lowest noncondensable mass fraction at inlet. In general, a source of discrepancy between model and experiments is the condensation process immediately downstream from the inlet, where the flow regime is rather chaotic and condensation rate is high. The model, however,

idealizes the process as filmwise condensation everywhere. The discrepancy between model and data is relatively small, however, and has a maximum value of about 20%. The agreement between model and data is also generally good for helium-steam experiments. For helium-steam mixtures, the model appears to systematically over predict the condensation rate. The over prediction is small in most cases, however, and has a maximum value of about 30% near the center of the test section for Run 74.

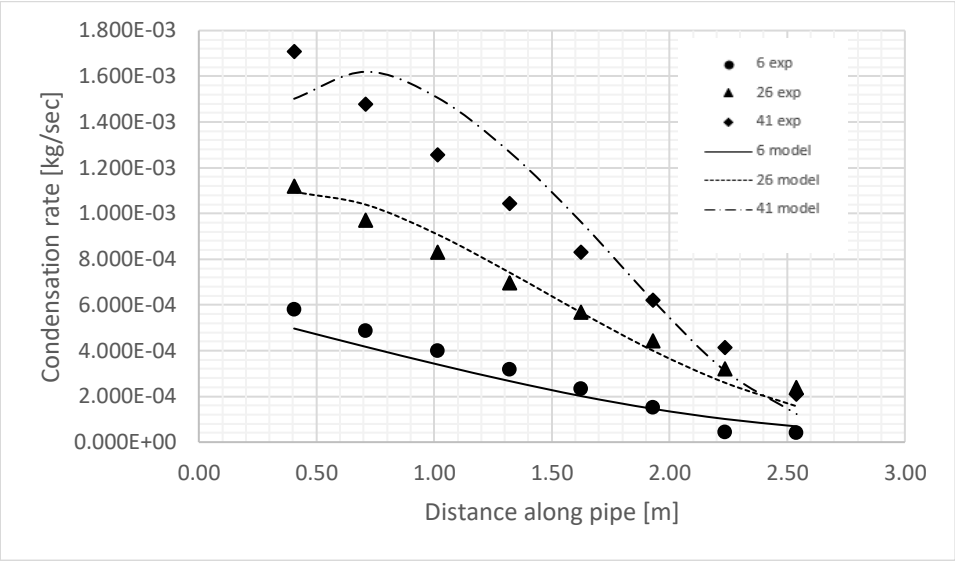

Figure 6. Comparison between model-predicted condensate rates with experimental data for air-steam experiments of Siddique[5].

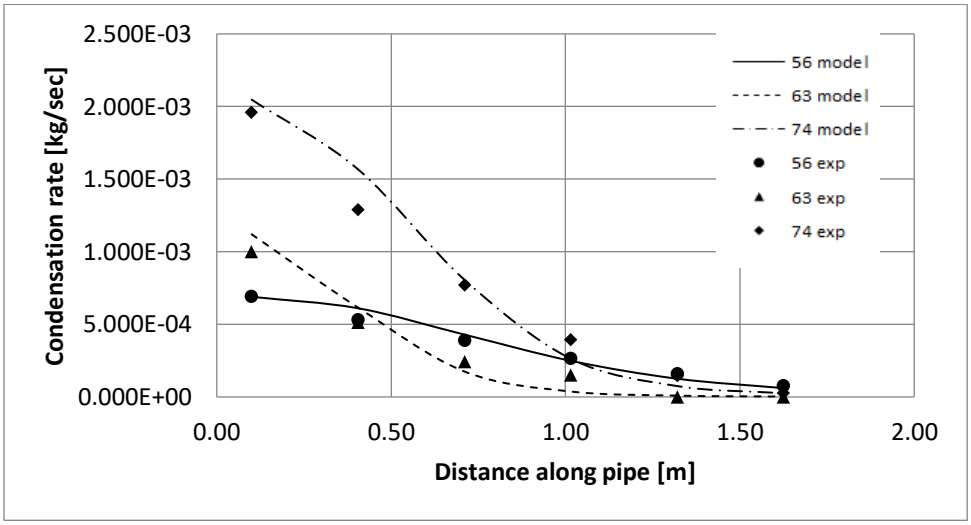

Figure 7. Comparison between model-predicted cumulative condensation rates (condensate flow rates) with experimental data for helium-steam experiments of Siddique[5].

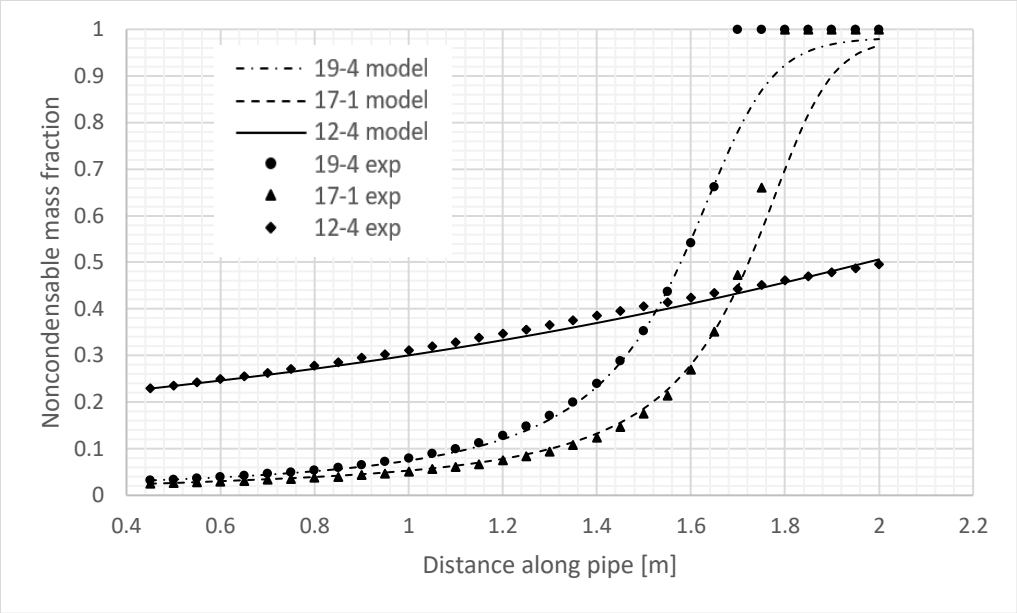

Figure 8. Comparison between model-predicted condensate rates with experimental data for air-steam experiments of Ogg[6].

Figure 8 also confirms that the model, overall, agrees with the data of Ogg[6] well. For Run 19-4 in Figure 8 the reported data suggest that near the test section exit the gas was essentially pure air. This is unlikely to occur in practice, however, and could have been caused by common measurement uncertainties and errors. The model, however, predicts an asymptotic approach to pure air near the exit, as expected. In Run 12-4 of Ogg the air mass fraction at inlet was high (17.9%). As a result the condensation rate was low throughout the length of the test section. The agreement between model and data is excellent for this run, confirming the suitability of the GFSSP-Couette flow film model for applications where extraction of water from medium and low-moisture content steam-noncondensable mixtures is of interest.

IV. Conclusions

A model for condensation in the presence of noncondensables, based on the Couette flow film (stagnant film) model, has been developed for implementation in the Generalized Fluid System Simulation Program (GFSSP) computer code. The developed computer routine is consistent with GFSSP and can be coupled to that code. The coupling with GFSSP is currently one way, whereby the condensation model receives information from GFSSP including the nodal pressure, temperature and mass concentrations, and calculates the condensation rate in each node. The model was validated against experimental data representing condensation of water vapor in downward flow of air-water vapor and helium-water vapor mixtures in vertical tubes, with good agreement between data and model predictions. The results confirm the suitability of the GFSSP-Couette flow film model for applications where extraction of water from medium and low-moisture content steam-noncondensable mixtures is of interest.

V. References

[1]Ghiaasiaan, S.M. *Two-Phase Flow, Boiling and Condensation in Conventional and Miniature Systems.* 2nd ed. Cambridge University Press, Cambridge, United Kingdom, 2017.

[2]Ghiaasiaan, S. M., Kamboj, B. K. and Abdel-Khalik, S. I., "Two-Fluid Modeling of Condensation in the Presence of Noncondensables in Two-Phase Channel Flows," Nuclear Science and Engineering, Vol. 119, 1995, pp. 1-17.

[3]Yao, G.F., Ghiaasiaan, S.M. and Eghbali, D.A., "Semi-Implicit Modeling of Condensation in the Presence of Noncondensables in the RELAP5/MOD3 Computer Code," Nuclear Engineering and Design, Vol. 166, 1996, pp. 277-291.

[4]Lee, J., Park, G.-C., and Cho, H.K., "Implementation of CUPID code for Simulating Filmwise Steam Condensation in the Presence of Noncondensable Gases," Nuclear Engineering Technology, Vol. 47, 2015, pp. 567-578.

[5]Siddique, M., "The Effects of Noncondensable Gases on Steam Condensation under Forced Convection Conditions," PhD Thesis, Massachusetts Institute of Technology, Department of Nuclear Engineering, Cambridge, Massachusetts, 1992.

[6]Ogg, D.G., "Vertical Downflow Condensation Heat Transfer in Gas-Steam Mixtures," MS Thesis, University of California, Department of Nuclear Engineering, Berkeley, CA, 1991.

[7]Generalized Fluid System Simulation Program, Version 6.0, A.K. Majumdar, A.C. LeClair, and R. Moore. Marshall Space Flight Center, Huntsville, Alabama.

[8]Majumdar, A.K., Bailey, J. and Sarkar, B., "A generalized system simulation program to model flow distribution in fluid networks", *33rd Joint Propulsion Conference and Exhibit*, 1997.

[9]Majumdar, A.K., and Schallhorn, P.A., "Implementation of finite volume based Navier Stokes algorithm within general purpose flow network code," *50th AIAA Aerospace Sciences Meeting Including the New Horizons Forum and Aerospace Exposition*, 2012.

[10]Majumdar, A.K., LeClair, A. C., Moore, R., and Schallhorn, P.A., "Generalized fluid system simulation program (GFSSP), version 6," *51st AIAA/SAE/ASEE Joint Propulsion Conference*, 2015.

"Fill and Spill" Lava Flow Emplacement: Implications for Understanding Planetary Flood Basalt Eruptions

Christopher W. Hamilton[1]
Lunar and Planetary Laboratory, University of Arizona, 1629 E. University Blvd., Tucson, AZ, 85721, USA

Basaltic flow types are traditionally viewed along a spectrum from pāhoehoe to ʻaʻā, with lobate pāhoehoe flows being indicative of low viscosity lavas emplaced at low shear strain rates, whereas channelized ʻaʻā flows imply higher viscosity lavas emplaced at higher strain rates. However, "transitional" flow types (e.g., platy, slabby, and rubbly lavas), do not fit well within this classification structure. Here, an alternative classification framework is proposed, which considers the stability/instability of the lava flow surface. This ternary system considers three types of lava crust: (1) stable; (2) continuously disrupted; and (3) episodically disrupted. Pāhoehoe exemplifies lava with a stable crust, whereas ʻaʻā surfaces are continuously disrupted. While these two lava types represent end-members in terms of crustal surface age, platy, slabby, and rubbly lavas can only be formed through the episodic disruption of an initially stable surface and, therefore, these lava types do not have a formation mechanism that lies directly along the pāhoehoe to ʻaʻā continuum. Using the December 1974 flow in Hawaiʻi as an example, the origin of transitional lavas are dominantly attributed to a "fill and spill" emplacement process, whereby an initially stable lava crust is formed as lava infills a topographically confined basin. This crust is then disrupted when the lava rapidly drains from its confinement during a dam-breaching event, leading to the formation of platy, slabby and rubbly lava types through the progressive fracturing of the initial lava surface. The characteristics of the December 1974 flow are also compared to flood basalt lava flows on Mars to demonstrate the importance of understanding the origin of transitional lava flow types as a local phenomenon that is not necessarily related to primary eruption conditions. Nonetheless, relative to more shallowly sourced magmas, high effusion rate eruptions sourced from the deep martian mantle will tend to favor the formation of transitional lavas because they are more likely to inundate basins and drain rapidly when they overtop their confinement. Fissure eruptions are also expected to favor the formation of transitional lavas because the successive opening of new fissure segments would cause effusion rates to pulsate. Similar eruption styles and lava types may also have formed on other planetary bodies, such as the Moon, Mercury, Venus, and Io.

Nomenclature

C	=	Lava crustal thickness
CTX	=	Context Camera
MRO	=	Mars Reconnaissance Orbiter
t	=	Time
τ	=	Maximum age of a lava flow surface before it cools to ambient temperature
$\bar{\tau}$	=	Mean age of a lava flow surface before it cools to ambient temperature

I. Introduction

Effusive volcanism involves the eruption of magma, which flows onto a planetary surface to become lava. Effusive volcanism is a fundamental component of the geologic history of terrestrial bodies and a dominant factor involved in the formation and modification of planetary crusts[1,2]. Volatiles released during large flood basalt eruptions can also influence climate and may have contributed to mass extinctions on Earth[3–5]. Volcanism has

[1] Assistant Professor, Lunar and Planetary Laboratory / Department of Planetary Sciences / Department of Geosciences, University of Arizona.

similarly had a profound effect on the interior, surface, and atmospheric history of Venus[6] and Mars[7,8], and mare-forming flood basalt eruptions may even have formed a transient atmosphere on the Moon[9]. Although volcanic activity in the inner Solar System has only been directly observed on the Earth, active silicate volcanism continues to occur in the outer Solar System on Jupiter's innermost Galilean satellite, Io[10]. Observations of Io—including the distribution of its volcanoes, styles of volcanic activity, and measurements of eruption temperatures—provide information about melt production and tidal heating processes within its interior[11]. Lava flows can therefore provide constraints on the thermal histories, interior structures, and eruption dynamics associated with a wide range of terrestrial bodies, and examining volcanic terrains addresses high priority goals within NASA's exploration program[12,13]. However, to correctly infer eruption parameters from observations of lava flow dimensions and morphologies, it is critical to understand how lava transport processes can affect local effusion rates and deposit characteristics. Additionally, it is important to understand how lava flow emplacement processes are related to the formation of internal structures, such as lava tubes, which are important targets for future robotic[14] and human[15] exploration on the Moon.

This study addresses issues related to effusive volcanism on planetary surfaces by first reviewing the characteristics and formation mechanisms of two end-member basaltic lava flow types: pāhoehoe and ʻaʻā. Then, counter-examples are considered that defy straightforward categorization into either of these two categories. These anomalous examples are associated with the transient storage and release of lava within a lava pathway, rather than changes in effusion rate at the vent. Distinguishing between the influences of eruption parameters (i.e., primary factors) and local effects on effusion rate (i.e., secondary factors) are thus critical for determining the magnitude and duration of effusive volcanic events on the Earth and other planetary bodies. This information, in turn, is vital for constraining magmatic ascent processes, and inferring the physical, chemical, and thermal state of planetary interiors.

II. Previous Work: A Traditional View of Lava Flow Types

Broadly speaking, there are two dominant lava flow types: pāhoehoe and ʻaʻā (Figure 1). Pāhoehoe tends to form thermally insulated lobate units at low shear strain rates, whereas ʻaʻā forms thermally inefficient channelized units at high shear strain rates[16,17]. The transition from pāhoehoe to ʻaʻā is often considered irreversible, due largely to cooling-induced increases in lava viscosity; however, Ref. 17 demonstrate that ʻaʻā can also change into pāhoehoe in response to a reduction in strain rate, which can occur where lava flows move from steep slopes onto more level ground. These transitions highlight important challenges in determining if a lava flow should be categorized as pāhoehoe or ʻaʻā. Specifically, is lava type determined by the geomorphological characteristics of the deposits, emplacement processes, or a combination of both criteria?

Figure 1. Examples of pāhoehoe (left) and ʻaʻā (right). Pāhoehoe tends to be emplaced as a series of lobes, with molten lava being transported to the flow front through thermally insulated internal pathways. In contrast, ʻaʻā tends to feed lava toward the flow front through thermally inefficient open channels that are maintained by continuous viscous tearing of the surface due to high shear strain rates.

Ref. 18 suggest that the terms pāhoehoe and ʻaʻā be restricted to describing solidified lava surfaces, whereas Ref. 19 expanded the use of these terms to include both fluid and crust. In contrast, Ref. 17 consider the transition to reflect a balance between shear strain rate and viscosity (Figure 2), whereas Ref. 20 consider the pāhoehoe to ʻaʻā transition to be a failure envelope where the crust begins to fragment, and Ref. 21 attribute the transition to a combination of crustal stability and rheology. While these factors are important for determining the conditions that

lead to transitions between pāhoehoe and ʻaʻā, Refs. 17, 20, and 21, all consider pāhoehoe and ʻaʻā flow types to be defined on the basis of preserved lava crusts, not on the state of the fluid.

More recently, Ref. 22 has advocated a descriptive (i.e., facies-based) classification system to categorize lava flow types on the basis of their surface morphology, vesicle type, flow-unit form, and breccia type—including clast character, size, and type. Although facies-based approaches provide a robust approach to categorizing terrestrial lava flows, internal structures such as vesicle distributions and fine-scale fracture patterns cannot be directly observed from orbital remote sensing data. This places increased emphasis on textures when classifying lava flow types on other planetary surfaces, but reliance on textural analysis can complicate interpretations of lava emplacement conditions because lava pathways evolve over time. For example, initially brecciated crusts can solidify into coherent layers, enabling lava channels to roof over to form lava tubes and even develop pāhoehoe-like inflation structures[22–27] within ʻaʻā[28] and transitional lava flows[29,30]. Thus, while lava texture can provide information about the state of the flow when its surface solidified, the processes of emplacement may continue to evolve through time. Transitional lava flows (e.g., platy,

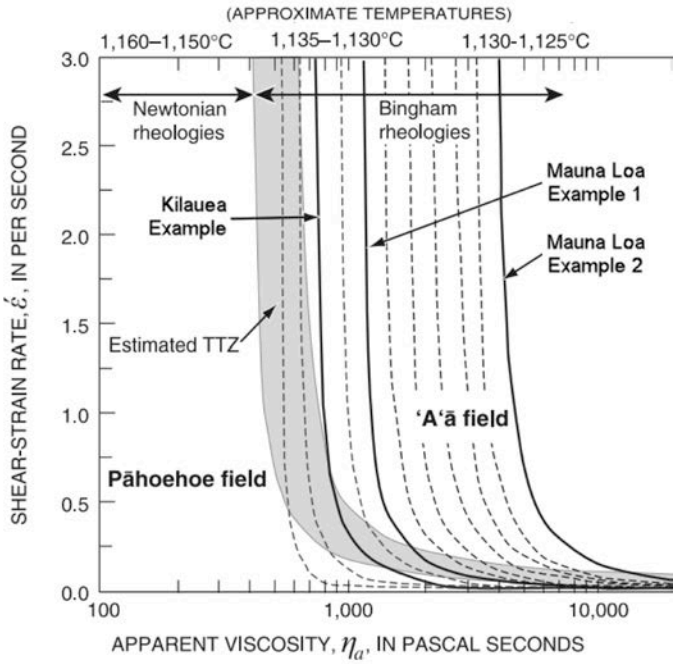

Figure 2. Diagram of shear strain rate versus apparent viscosity, with the shaded region showing the transition threshold zone (TTZ) between the stability fields for pāhoehoe (left) and ʻaʻā (right). Dashed lines illustrate a family of apparent viscosity curves for Hawaiian lavas. Black lines show specific curves for lavas erupted from Kīlauea and Mauna Loa. Figure adapted from Ref. 17.

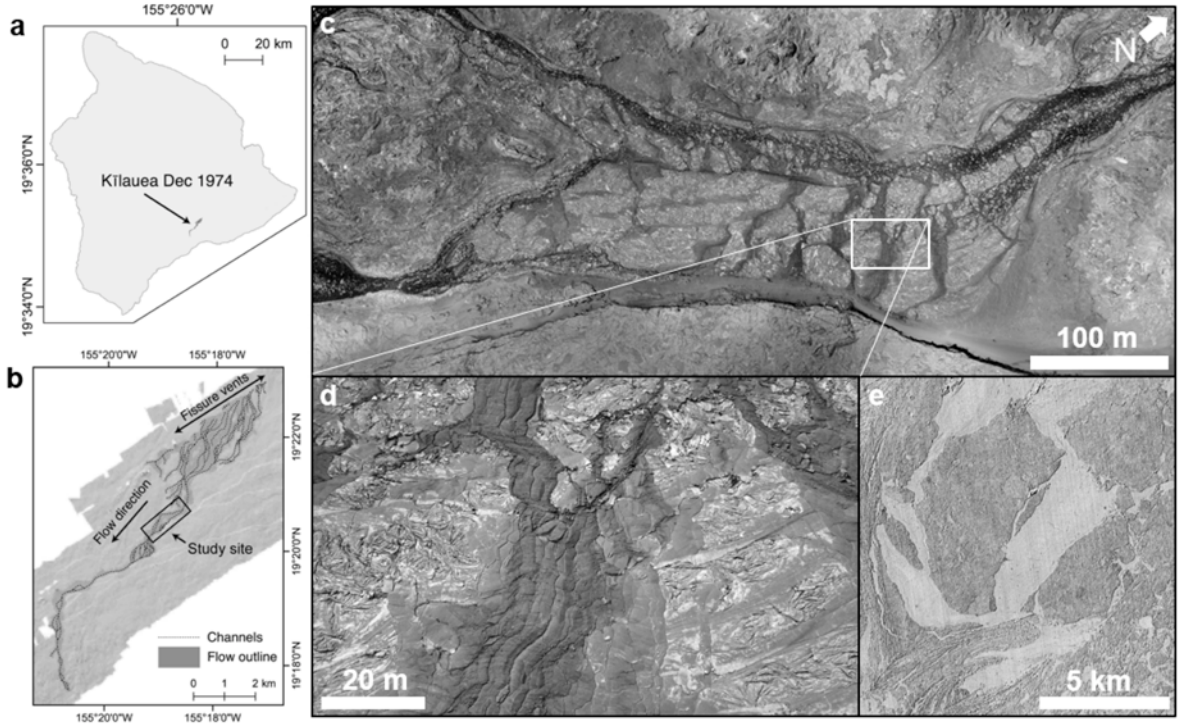

Figure 3. (a) Location of the December 1974 flow on the Big Island of Hawaiʻi, and (b) the study site. Panels (a) and (b) are adapted from Ref. 40. (c) Orthmosaic of a disrupted lava pond[42]. The white inset shown in (d) illustrates the formation of platy lava. (e) MRO CTX image showing platy lava in Elysium Planitia, Mars.

slabby, and rubbly lavas) provide particularly complicated cases where flows may be disrupted after their initial stage of emplacement to form surfaces that are neither traditional forms of pāhoehoe nor ʻaʻā (Figure 3).

In the Earth Sciences literature, transitional lava flow types have received relatively little attention, compared to pāhoehoe or ʻaʻā (see Ref. 22, and references therein). However, within a Planetary Sciences context, transitional flow types are prevalent on Mars[29,31–34] and perhaps Io as well[35], which raises important questions regarding their origin.

The "December 1974 flow", located in Kīlauea Volcano's Southwest Rift Zone on the Big Island of Hawai'i[36–40] provides one of the best terrestrial examples of well-preserved transitional surfaces, including platy, slabby, and rubbly lavas (Figure 3). The eruption took place over a six-hour period, beginning at 02:56 HST on December 31, 1974. The lava was an olivine-rich tholeiite, which is more mafic than most Kīlauean lavas[36], and Ref. 39 calculated that the maximum eruption temperature of the lava was approximately 1168°C, which is about 18°C hotter than other rapidly emplaced lava flows from Kīlauea Volcano, such as the July 1974 and 1823 Keaiwa flows. The December 1974 flow is also unusual in that it is a tributary channel system, in which multiple channels merged down-flow into a single-stem channel, rather than bifurcating as a distributary system[40]. This is important because most lava flows are distributary systems, with each branch in the lava pathway system leading to a decrease in the local effusion rate. In contrast, during the December 1974 eruption, lava from multiple fissure segments was funneled together into a single master pathway due to topographic confinement within Kīlauea Volcano's Southwest Rift Zone. This led to an increase in local effusion rate as each branch came together. However, rather than being directly due to the composition or thermo-rheology of the lava, Ref. 41 attribute the unusual nature of this flow's surface morphology to changes in local effusion rate due to ponding and release of stored lava in the transport system. Ref. 41 also suggests that "fill and spill" lava emplacement processes associated with the December 1974 flow are analogous to those operating on other planets, such as Mars (Figure 3e), which implies that the products of many flood basalt eruptions are neither pāhoehoe nor ʻaʻā, but rather an alternative flow type characterized by sudden changes in local effusion rate in response to local confinement and dam-breaching events. The following section explores the characteristics of transitional lavas and presents a new approach to considering these lava flow types in relation to pāhoehoe and ʻaʻā.

III. Innovation: A Novel Perspective on Lava Flow Types

A. Stable, Continuously Disrupted, and Episodically Disrupted Lava Crusts

An alternative perspective on lava flow types considers the timescale of crustal stability. From a thermal remote sensing perspective, Ref. 43 introduced the term τ to refer to the maximum age of a lava flow surface. The intuition behind this concept is that active lava flows can have surfaces that are being continuously formed and destroyed, with maximum surface ages ranging from zero to τ. This makes τ a measure of the vigor of volcanic activity[43]. If τ is longer than tens of minutes, it corresponds to more stable surfaces, such as very quiescent lava lakes, tube-fed flows, or very high lava fountains with long ballistic flight times. In contrast, surfaces characterized by τ on the order of a few seconds to minutes would apply to dynamic phenomena, such as the initial emplacement of pāhoehoe lobes, rapidly overturning lava lakes, pyroclasts with short flight times, or rapidly mixing ʻaʻā surfaces. Setting τ equal to a range of times, Ref. 43 calculated the blackbody spectra and expected brightness temperatures at different wavelengths for cooling lava surfaces ranging in age from 10 s to 10^4 s. However, they note that the model could be improved by considering distributions of τ, rather than using a single value to describe the wide distribution of ages and temperatures for lava flows and lava fountains. The concept of τ is revisited here to develop a novel perspective on lava flow types and place transitional flow morphologies into context. Within this framework, a parcel of lava representing a portion of a pāhoehoe surface will thicken as it cools according to the following relationship[24]:

$$C = 0.0779\sqrt{t}\,, \tag{1}$$

where C is the crustal thickness of the lava in meters, and t is the time in hours. Ref, 22 determined this relationship using cooling rate data collected from lava flows and lava lakes in Hawai'i. This cooling model considers the core of the lava flow to be isothermal, with an initial temperature of 1142°C, and uses the 1070°C isotherm to approximate the transition from the molten core to the viscoelastic layer (i.e., to define the maximum depth, or thickness of the crust). They also use the 800°C isotherm to mark the transition from the viscoelastic layer to the brittle portion of the crust. While these isotherms would be expected to similarly mark major rheological transitions within basaltic lava flows on other planetary surfaces, Eq. 1 is specific to environmental conditions in Hawai'i and has been revised by Ref. 44 to describe lava cooling rates on other planetary bodies. However, while the rate of cooling can vary, the

crusts of pāhoehoe-like flows and quiescent lava lakes all thicken over time according to a square root of time relationship. However, this assumes that the lava crust is overturned or otherwise disrupted and that there remains both an available supply of molten lava below the crust and that the core remains directly coupled with the crust. If these conditions are met, then τ will continue to increase with t—though to account for the range of ages associated with a lava flow's surface, it is more appropriate to refer to mean τ, or $\bar{\tau}$. In contrast, recycling of ʻaʻā crusts will cause $\bar{\tau}$ to remain significantly less than t. Transitional flow types (e.g., platy, slabby, and rubbly lavas) represent part of a continuum between pāhoehoe and ʻaʻā in terms of their increasing degree of surface disruption (Figure 4), but $\bar{\tau}$ does not decrease monotonically in these cases because the crust fractures during episodic events. These episodic disruptions lead to sudden decreases in $\bar{\tau}$ as new surfaces are exposed, followed by a gradual increase in $\bar{\tau}$ as the crust reforms and continues to age.

Figure 4. Examples of lava types with increasing degrees of surface disruption. The maximum surface age $\bar{\tau}$ does not monotonically decrease moving from pāhoehoe and ʻaʻā because the "transitional" types (e.g., platy, slabby, and rubbly lavas) form through episodic fracturing events, not as a continuous process.

Platy, slabby, and rubbly lavas thus represent increased stages of disruption, or autobrecciation, but they do not exist along a continuum between pāhoehoe and ʻaʻā end-members because they are not formed by a continuous process. Instead, platy lava forms where the surface of a sheet-like lava flow or a lava pond begins to crack, with older surfaces being rafted apart and separated by newer upwellings of lava that are exposed within the growing fractures (Figures 3c and 3d). The plates generally have a jigsaw fit and are not up-tilted or inclined with respect to the lava flow's surface. In the context of the December 1974 flow (Figure 5), Ref. 41 interpret the cause of the initial disruption to be a decrease in the level of lava in a dammed reservoir once the perched lava pond overtopped its confinement and drained through a spillway to the southwest. This caused the initial lava crust to break apart into plates, which gradually rafted toward the spillway. However, within other flows in Hawaiʻi, Ref. 45 documented the formation of "shatter rings" in association with pulses of lava moving though confined lava pathways (i.e., tubes), leading to cyclic vertical movements and the fragmentation of the crust into rubble. Thus, while crustal disruption and initial plate formation may be due to a decrease in lava level during a drainage event, it is also possible that a pulse of lava can pressurize the molten core of a lava flow, leading to uplift and fracturing of the overlying crust.

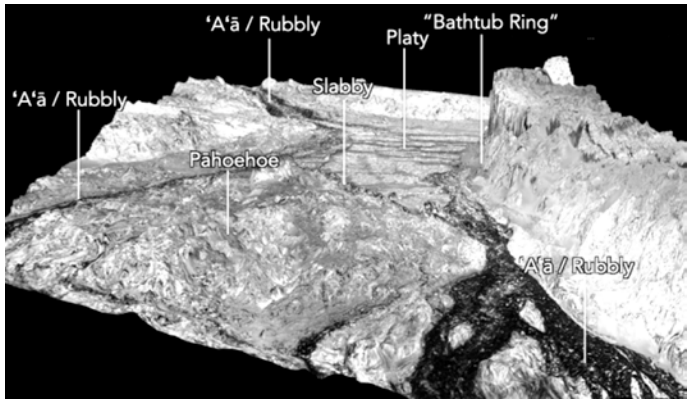

Figure 5. Perspective view of the study site within the December 1974 flow[41,42] (see Figure 2 for location). The rendering is shown with eight times vertical exaggeration facing approximately northeast. The flow direction was toward the southwest. Locations of various lava types are shown. The "bathtub ring" corresponds to the lava high-stand deposits preserved along the Koaʻe Fault scarp, providing evidence of the lava level within the perched pond before it drained.

After the initial formation of lava plates, slabby lava can develop as segments of the brittle crust detach from the underlying flow, producing inclined slabs with an original surface preserved on one side and viscous deformation features formed on the opposite side (i.e., the detachment surface). Within the December 1974 flows, slabby lava is most prevalent at the southern end of the partially-drained lava pond, where plates of lava collided against the margins of older lava flows,

which formed high-standing topographic obstacles near the breach point of the pond. Slabs tend to be thin (i.e., centimeters to tens of centimeters thick), and form imbricated deposits where slabs were progressively thrust on top of one another.

Rubbly lava is produced by the continued auto-brecciation of crustal slabs into smaller blocks of material through mechanical collisions between the slabs during transport. This rubble differs from ʻaʻā clinker in that the margins of the rubble show evidence of brittle fracturing. In contrast, clinker clasts are formed via viscous tearing of molten lava, which produces unconsolidated deposits with spiny surfaces on all sides. Within the December 1974 flow rubbly lava and ʻaʻā, both occur within the spillway channels feeding into and out of the lava pond. In these regions the channelized flows would have had higher shear strain rates, leading to rafted slabs fracturing into rubbly blocks and viscous tearing of freshly exposed molten lava.

Considering these examples, lava types can be related to crustal stability/instability (Figure 6). For instance, pāhoehoe lava is an example of a stable crustal surface, which thickens steadily through time, whereas ʻaʻā is an example of a continuously disrupted lava flow surface. Platy lava is more similar to pāhoehoe than it is to ʻaʻā because it forms after a period of stable crustal growth when the lava pathway is shocked, either by a drainage event, or by a pulse-like influx of molten lava, which could be related to either lava transport processes or changes in eruption activity at the vent. Rubbly lava is closely associated with ʻaʻā in that the surface is approaching a continuous state of disruption, but it cannot be formed by directly moving from pāhoehoe to ʻaʻā along an end-member spectrum. Instead, it requires the initial formation of lava slabs, which requires the formation of plates, which requires the formation of a stable crust.

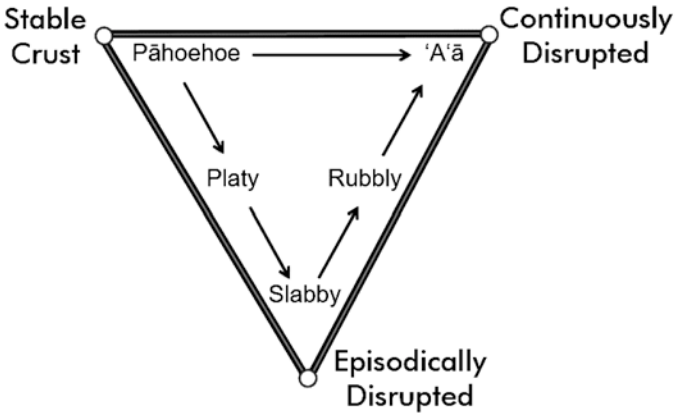

Figure 6. Diagram illustrating relationships between lava flow types and the stability of the lava crust. Transitional lava types (platy, slabby, and rubbly) are not simply located along an end-member spectrum between pāhoehoe an ʻaʻā, they are the product of episodic crustal disruption.

Thus, the key to understanding the formation of transitional lava flows is to recognize an alternative formation mechanism involving episodic disruption of a lava flow's crust. A single disruption event can produce platy lava, but continued disruption is required to separate the plates to form inclined crustal slabs. However, if the process of disruption becomes more frequent and approaches being a continuous process, the slabs will be broken down into rubble that may be mixed with ʻaʻā as fresh sources of lava are viscously torn into clinker.

B. Implications for Planetary Exploration

A fundamental issue in planetary volcanology relates the eruption of magma and its relationship to the chemical and thermodynamic state of planetary interiors. Magma effusion rates, compositions, temperatures, eruption styles and durations thus provide critical information about regions of melt within planetary bodies and the processes of magma ascent[46]. For instance, during the Noachian Period, early in martian history, the planet's crust would have been thinner and the mantle would have been more enriched in volatiles, producing voluminous high-SiO_2, low-Th, shergottite-like magmas[47]. However, during the intermediate Hesperian Period, the upper mantle would have become depleted in volatiles, favoring more isolated eruptions of low-SiO_2, high-Th magmas[47]. Then, during the more recent Amazonian Period, episodic entrainment of hydrous material from the deeper mantle may have led to the resumed production of shergottite-like magma, while the upper dehydrated mantle produced nakhlite-like magmas[47]. These changes in magma composition, volatile content, and crustal thickness led to changes in the distribution and style of volcanism on Mars through time.

On Mars, given probable magma compositions and density profiles, Ref. 46 show that lower gravity relative to the Earth (3.7 m/s^2 vs. 9.8 m/s^2) would be expected to lead to an increase in martian dike widths by a factor of approximately two (i.e., 1.4 times wider and 1.8 times longer), with effusion rates higher by a factor of five for laminar flows, or a factor of three for turbulent flows. This will tend to lead to much larger eruption volumes on Mars than on Earth with associated lava flows being more energetic. However, this assumes that the magma is erupted from a deep reservoir (i.e., a magmatic source located at least 10s of kilometers beneath the planet's surface). If instead martian magmas are erupted from shallow reservoirs (i.e., from magma chambers located within the upper several kilometers of crust), then effusion rates should be similar to those on Earth[46]. Additionally,

magmatic processes driven by positive or negative buoyancy (e.g., diapir ascent, or crystal settling, respectively), will be slower on Mars due to the lower gravity, which requires larger diapir volumes for magma to rise to an equivalent depth in the crust because magmatic heat loss by conduction would be similar on both planets[46]. Martian magma chambers are also expected to have neutral buoyancy depth of about 11 km, which is approximately four times deeper than on Earth, but this neutral buoyancy depth is sensitive to magmatic volatile content[46], which has changed significantly on Mars through time (Figure 7).

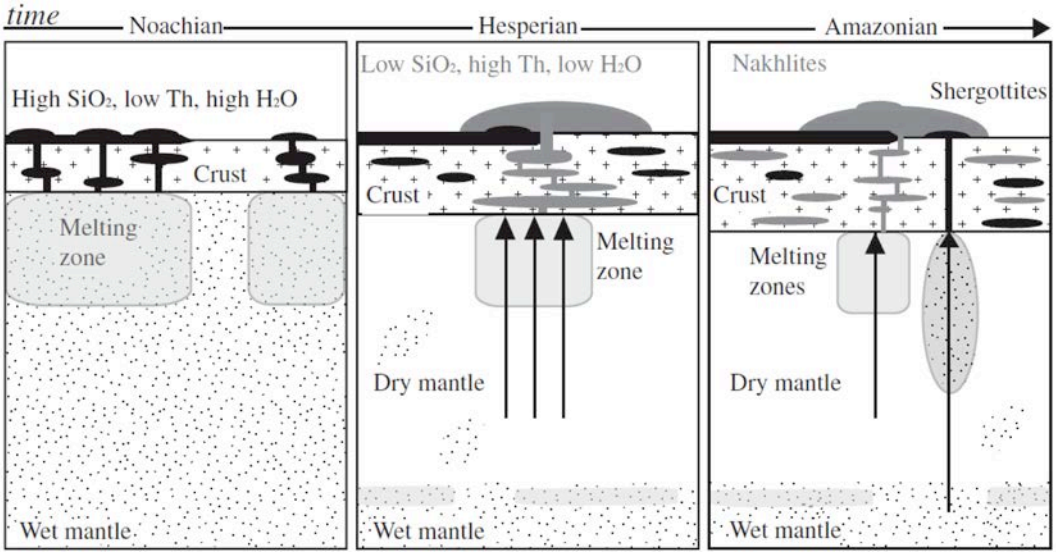

Figure 7. Schematic history of martian magmatism. During the Noachian Period on Mars, the "wet" (i.e., volatile-rich) mantle produced voluminous and widespread eruptions of primitive (i.e., mafic and ultramafic) magma. During the Hesperian Period isolated upwellings in the "dry" (i.e., volatile-poor) mantle generated more focused magma production beneath a thicker crust. During the Amazonian Period, hydrous material from the deeper mantle may have been occasionally entrained into upwelling zones, favoring the eruption of more primitive magma in addition to eruptions from shallow sources. Figure adapted from Ref. 47.

Changing magmatic source depths and compositions (including volatile contents) would favor a transition from widespread eruptions of mafic to ultramafic lava on early Mars to more focused extrusions of magma over time. This in turn would have contributed to the growth of major volcanic edifices, like Olympus Mons in the Tharsis Volcanic Province. However, during the Amazonian Period, episodic upwellings of deeply sourced magmas may have fed enormous flood basalt eruptions, like the Athabasca Valles Flood Lava[33], while other shallow intrusions of magma may have fed smaller volcanic fields[48,49] at lower effusion rates. If so, large, potentially turbulent, lava flows erupted during the Amazonian Period may imply deep magmatic source regions, rapid ascent rates, and high effusion rates—like the Noachian[50] and Hesperian[51] plains-forming flows—and these events would be fundamentally different than the smaller eruptions that would be fed by shallower crustal magma chambers at much lower rates of effusion. Consequently, shallow intrusions may favor more terrestrial-like effusive eruptions compared to highly energetic eruptions sourced by magma that rapidly ascends from the deep mantle.

For example, the Athabasca Valles Flood Lava has a total volume of 5000–7500 km^3 and the bulk of this magma may have been emplaced over a period of only a few weeks to months[33]. If so, molten lava may have inundated large valleys and basins, like Cerberus Palus, leading to the development of large ponded reservoirs that were disrupted into platy, slabby, and rubbly lavas as the lava overtopped topographic barriers and drained catastrophically during dam-breaching events. In contrast, lobate flow units near Hrad Vallis have continuous surface crusts resembling terrestrial pāhoehoe flows and, based on cooling relationships[44], may have been emplaced over the course of decades. These two end-member styles of lava emplacement imply vastly different eruption timescales and magmatic source regions. For instance, high effusion rate eruptions, like the one that produced the Athabasca Valles Flood Lava, may have been sourced by rapidly ascending magma from the deep portion of the primitive mantle on Mars, whereas the lobate flows near Hrad Vallis, may have been erupted at lower effusion rates from magma chambers that stalled within the crust at shallow depths. This observation also has important implications for magma–water interactions on Mars because large, shallow magma chambers stalled at neutral buoyancy depths would have the potential to melt surrounding ground ice. Consequently, major outflow channels—like Hrad

Vallis—may be a result of large magmatic intrusions that melted ice within the overlying cryosphere, generating catastrophic aqueous floods as the meltwater was released to the surface[52,53]. If so, this would imply a genetic relationship between pāhoehoe-like lava flow units and aqueous floods, as both would be related to shallow crustal intrusions.

IV. Conclusion

Large lava flows erupted on Mars during the Amazonian Period appear to have three dominant morphologies: (1) lobate flow units[58–60], resembling terrestrial pāhoehoe[22,61] and implying the formation of stable surface crusts; (2) channelized flow units[62,63], resembling terrestrial ‘a‘ā[22,61] and implying continuous surface disruption; and (3) transitional lava[29,31,34] resembling platy, slabby, and rubbly lava types on Earth and implying episodic disruption of lava flow surfaces[41]. However, given the complex geological history of major volcanic provinces like Tharsis[54–57] and Elysium[34,57], how can lava volumes and effusion rates be reliably inferred for individual eruptions? Conventional wisdom would suggest that disrupted lava flow surfaces (e.g., Figure 3e) are caused by high shear strain rates in association with high effusion rate eruptions, but if these textures are related to episodic disruption events—like those observed in association with the December 1974 flow—are these textures really indicative of source eruption parameters, or simply local processes? The first step in addressing these issues is to recognize that lava flow types do not exclusively lie along a continuum between pāhoehoe and ‘a‘ā end-members and that the temporary storage and release of lava within a lava transport system can result in tremendous changes in local effusion rate, which may be unrelated to conditions at the vent. Applications of terrestrial analogs to planetary volcanism therefore provide valuable information about the formation and significance of effusive eruption products on Mars and other planetary bodies, and recognition of transitional lava flow types as a consequence of episodic disruption is vital for distinguishing between the effects of primary (i.e., eruption parameters) and secondary (i.e., local) processes.

Acknowledgments

C.W.H. thanks Dr. Caleb Fassett and Dr. Debra Needham for constructive discussions related to planetary volcanism and the NASA Marshall Space Flight Center’s Faculty Fellowship Program for enabling this work.

References

[1]Self, S., Keszthelyi, L., and Thordarson, T. “The importance of pāhoehoe,” *Annual Review of Earth and Planetary Sciences*, Vol. 26, No. 1, 1998, pp. 81–110.

[2]Wilson, L., “Volcanism in the Solar System,” *Nature Geoscience*, Vol. 2, 2009, pp. 389–397.

[3]Thordarson, T., and Self, S. “The Laki (Skaftár Fires) and Grímsvötn eruptions in 1783–1785,” *Bulletin of Volcanology*, Vol. 55 No. 4, 1993, pp. 233–263.

[4]Thordarson, T., and Self, S., “Atmospheric and environmental effects of the 1783–1784 Laki eruption: A review and reassessment,” *Journal of Geophysical Research: Atmospheres*, Vol. 108, No. D1, 2003, 4011.

[5]Rampino, M. R., “Mass extinctions of life and catastrophic flood basalt volcanism,” *Proceedings of the National Academy of Sciences*, Vol. 105, No. 14, 2010, pp. 6555–6556.

[6]Taylor, F. W., Svedhem, H., and Head III, J. W., “Venus: The atmosphere, climate, surface, interior and near-space environment of an Earth-like planet,” *Space Science Reviews*, Vol. 214, No. 35, 2018, pp. 1–36.

[7]Greeley, R., and Supdis, P. D., “Volcanism on Mars,” Reviews of Geophysics, Vol. 19, No. 1, 1981, pp. 13–41.

[8]Halevy, I., and Head III, J. W. “Episodic warming of early Mars by punctuated volcanism,” *Nature Geoscience*, Vol. 7, 2014, pp. 865–868.

[9]Needham, D. H., and Kring, D. A., “Lunar volcanism produced a transient atmosphere around the ancient Moon,” *Earth and Planetary Science Letters*, Vol. 478, 2017, pp. 175–178.

[10]Lopes-Gautier, R., McEwen, A. S., Smythe, W. B., Geissler, P. E., Kamp, L., Davies, A. G., et al., “Active volcanism on Io: Global distribution and variations in activity,” *Icarus*, Vol. 140, No. 2, 1999, pp. 243–264.

[11]Hamilton, C. W., Beggan, C. D., Still, S., Beuthe, M., Lopes, R. M., Williams, D. A., Radebaugh, J., and Wright, W., “Spatial distribution of volcanoes on Io: implications for tidal heating and magma ascent,” *Earth and Planetary Science Letters*, Vol. 361, 2013, pp. 272–286

[12]National Research Council, *Vision and Voyages for Planetary Science in the Decade 2013–2022*, The National Academies Press, Washington, D.C., 2011, pp. 1–398.

[13]MEPAG, “Mars scientific goals, objectives, investigations, and priorities: 2015,” edited by V. Hamilton, *Mars Exploration Program Analysis Group (MEPAG)*, URL: http://mepag.nasa.gov/reports.cfm [cited 28 July 2018].

[14]Kerber, L., Nesnas, I., Keszthelyi, L., Head, J. W., Denevi, B., Hayne, P. O. et al., “Moon Diver: A Discovery mission concept for understanding the history of the mare basalts through the exploration of a lunar mare pit,” *49th Lunar and Planetary Science Conference*, The Woodlands, Texas, March 19–23, 2018, Abstract 1956.

[15]Angelis, D. G., Wilson, J. W., Clowdsley, M. S., Nealy, J. E., Humes, D. H., and Clem, J. M., "Lunar lava tube radiation safety analysis," *Journal of Radiation Research*, Vol. 43, 2002, pp. S41–S45.

[16]Rowland, S. K., and Walker, G. P. L., "Pahoehoe and aʻa in Hawaii: Volumetric flow rate controls the lava structure," *Bulletin of Volcanology*, Vol. 52, No. 8, 1990, pp. 615–628.

[17]Hon, K., Gansecki, C., and Kauahikaua J., "The transition from ʻaʻā to pāhoehoe crust on flows emplaced during the Puʻu ʻŌ ʻō-Küpaianaha Eruption," *U.S. Geological Survey Professional Paper*, Vol. 1676, 2003, pp. 89–103.

[18]MacDonald, G. A., "Pahoehoe, aa, and block lava," *American Journal of Science*, Vol. 251, 1953, pp. 169–191.

[19]Peterson, D. W., Holcomb, R. T., Tilling, R. I., and Christiansen, R. L., "Development of lava tubes in light of observations at Mauna Ulu, Kilauea Volcano, Hawaii," *Bulletin of Volcanology*, Vol. 56, No. 5, 1994, pp. 343–360.

[20]Kilburn, C. R. J., "Surfaces of aa flow-fields on Mount Etna, Sicily: morphology, rheology, crystallization and scaling phenomena," *Lava flows and domes: Emplacement mechanisms and hazard implications*, edited by J. H. Fink, Springer-Verlag, Berlin, pp. 129–156.

[21]Cashman, K. V., Thornber, C., and Kauahikaua, J. P., "Cooling and crystallization of lava in open channels, and the transition of Pāhoehoe Lava to ʻAʻā," *Bulletin of Volcanology*, Vol. 61, 1999, pp. 306–323.

[22]Harris, A. J. L., Rowland, S. K., Villeneuve, N., and Thordarson, T., "Pāhoehoe, ʻaʻā, and block lava: an illustrated history of the nomenclature," *Bulletin of Volcanology*, Vol. 79, No. 7, 2017, pp. 1–34.

[23]Walker, G. P. L., "Structure, and origin by injection of lava under surface crust, of tumuli, "lava-rises", "lava-rise pits", and "lava-inflation clefts" in Hawaii," *Bulletin of Volcanology*, Vol. 53, No. 7, 1991, pp. 546–558.

[24]Hon K., Kauahikaua, J., Denlinger, R., and MacKay, R., "Emplacement and inflation of pahehoe sheet flows: Observations and measurements of active lava flows on Kilauea Volcano, Hawaii," *Geological Society of America Bulletin*, Vol. 106, No. 3, 1994, pp. 351–370.

[25]Walker G. P. L., "The endogenous growth of pahoehoe lava lobes and morphology of lava-rise edges," *Studies in Volcanology—The Legacy of George Walker*, edited by T. Thordarson, S. Self, G. Larsen, S. K. Rowland, and A. Hoskuldsson Special publications of the International Association of Volcanology and Chemistry of the Earth's Interior No. 2. Geological Society, London, pp. 17–32.

[26]Hoblitt, R. P., Orr, T. R., Heliker, C., Denlinger, R. P., Hon, K., and Cervelli, P. F., "Inflation rates, rifts, and bands in a pāhoehoe sheet flow," *Geosphere*, Vol. 8, No. 5, 2012, pp. 179–195.

[27]Hamilton, C. W., Glaze, L. S., James, M. R., and Baloga, S. M., "Topographic and stochastic influences on pāhoehoe lava lobe emplacement," *Bulletin of Volcanology*, Vol. 75, No. 756, 2013, pp. 1–16.

[28]Duncan, A. M., Guest, J. E., Stofan, E., Anderson, S. W., Pinkerton, H., and Calvari S., "Development of tumuli in the medial portion of the 1983 aa flow-field, Mount Etna, Sicily," *Journal of Volcanology and Geothermal Research*, Vol. 132, 2004, pp. 173–187.

[29]Keszthelyi, L., McEwen, A. S., and Thordarson, T., "Terrestrial analogs and thermal models for Martian flood lavas," *Journal of Geophysical Research: Planets*, Vol. 105, 2000, pp. 15027–15049.

[30]Kolzenburg S., Jaenicke, J., Münzer, U., and Dingwell, D. B., "The effect of inflation on the morphology-derived rheological parameters of lava flows and its implications for interpreting remote sensing data – A case study on the 2014/2015 eruption at Holuhraun, Iceland," *Journal of Volcanology and Geothermal Research*, Vol. 357, 2018, pp. 200–212.

[31]Keszthelyi, L., Thordarson, T., McEwen, A., Haack, H., Guilbaud, M. N., Self, S., and Rossi, M. J., "Icelandic analogs to martian flood lavas," *Geochemistry, Geophysics, Geosystems*, Vol. 5, No. 11, 2004, pp. 1–32.

[32]Jaeger, W. L., Keszthelyi, L. P., McEwen, A. S., Dundas, C. M., and Russell, P. S., "Athabasca Valles, Mars: A lava-draped channel system," *Science*, Vol. 317, No. 5845, 2007, pp. 1709–1711.

[33]Jaeger, W. L., Keszthelyi, L. P., Skinner, J. A. Jr., Milazzo, M. P., McEwen, A. S., Titus, T. N., et al., "Emplacement of the youngest flood lava on Mars: A short, turbulent story," *Icarus*, Vol. 205, No. 1, 2010, pp. 230–243.

[34]Voigt, J. R. C., and Hamilton C. W., "Investigating the volcanic versus aqueous origin of the surficial deposits in Eastern Elysium Planitia, Mars," *Icarus*, Vol. 309, 2018, pp. 389–410.

[35]Keszthelyi L., Self, S., and Thordarson, T. "Flood lavas on Earth, Io and Mars," *Journal of the Geological Society*, Vol. 163, No. 2, 2006, pp. 253–264.

[36]Lockwood, J. P., Tilling, R. I., Holcomb, R. T., Klein, F., Okamura, A. T., and Peterson, D. W., "Magma migration and resupply during the 1974 summit eruptions of Kilauea Volcano, Hawaii," *U.S. Geological Survey Professional Paper*, Vol. 1613, 1999, pp. 1–37.

[37]Decker, R. W., and Christiansen, R. L., "Explosive eruptions of Kilauea volcano, Hawaii," in *Explosive Volcanism*, edited by The National Research Council, The National Academies of Science, Washington, D.C., 1984, pp. 122–132.

[38]McPhie, J., Walker, G. P. L., and Christiansen, R. L., "Phreatomagmatic and phreatic fall and surge deposits from explosions at Kilauea volcano, Hawaii, 1790 A.D.: Keanakakoi Ash Member," *Bulletin of Volcanology*, Vol. 52, 1990, pp. 334–354.

[39]Soule, S. A., Cashman, K. V., and Kauahikaua, J. P. "Examining flow emplacement through the surface morphology of three rapidly emplaced, solidified lava flows, Kilauea Volcano, Hawai'i," Bulletin of Volcanology, Vol. 66, 2004, pp. 1–14.

[40]Dietterich, H. R., and Cashman K. V., "Channel networks within lava flows: Formation, evolution, and implications for flow behavior," *Journal of Geophysical Research: Earth Surface*, Vol. 119, 2014, pp. 1704–1724.

[41]Hamilton, C. W., Scheidt, S. P., Bleacher, J. E., Irwin III, R. P., and Garry, W. B., ""Fill and spill" lava emplacement associated with the December 1974 flow on Kilauea Volcano, Hawaii, USA," *46th Lunar and Planetary Science Conference*, The Woodlands, Texas, March 16–20, 2015, Abstract 1072.

[42]Scheidt, S. P., and Hamilton, C. W., "Generation of ultrahigh spatial resolution digital terrain models for a martian lava flow analog from Kilauea Volcano, Hawaii," *46th Lunar and Planetary Science Conference*, The Woodlands, Texas, March 16–20, 2015, Abstract 1055.

[43]Keszthеyi L., and McEwen, A. "Thermal models for basaltic volcanism on Io," *Geophysical Research Letters*, Vol. 24, No. 20, 1997, pp. 2463–2466.

[44]Keszthelyi L. P., "Rate of solidification of silicate melts on the Earth, Moon, Mars, and beyond," *43rd Lunar and Planetary Science Conference*, The Woodlands, Texas, March 19–23, 2012, Abstract 2547.

[45]Orr, T. R., "Lava tube shatter rings and their correlation with lava flux increases at Kīlauea Volcano, Hawai'i," *Bulletin of Volcanology*, Vol. 73, 2010, pp. 335–346.

[46]Wilson, L., and Head III, J. W., "Mars: Review and analysis of volcanic eruption theory and relationship to observed landforms," *Reviews of Geophysics*, Vol., 32, No. 3, pp. 221–263.

[47]Balta, J. B., and McSween Jr., H. Y., "Water and the composition of Martian magmas," Geology, Vol. 41, No. 10, 2013, pp. 1115–1118.

[48]Bleacher, J. E., Greeley, R., Williams, D. A., Cave, S. R., and Neukum, G., "Trends in effusive style at the Tharsis Montes, Mars, and implications for the development of the Tharsis province," *Journal of Geophysical Research: Planets*, Vol. 112, No. E9, 2007, pp. 1–15.

[49]Richardson, J. A., Wilson, J. A., Connor, C. B., Bleacher, J. E., and Kiyosugi, K., "Recurrence rate and magma effusion rate for the latest volcanism on Arsia Mons, Mars," *Earth and Planetary Science Letters*, Vol. 458, 2017, pp. 170–178.

[50]Rogers, D. A., and Nazarian, A. H., "Evidence for Noachian flood volcanism in Noachis Terra, Mars, and the possible role of Hellas impact basin tectonics," *Journal of geophysical Research Planets*, Vol. 118, 2013, pp. 1094–1113.

[51]Head III, J. W., Kreslavsky, M. A., and Pratt, S., "Northern lowlands of Mars: Evidence for widespread volcanic flooding and tectonic deformation in the Hesperian Period," *Journal of geophysical Research Planets*, Vol. 107, No. E1, 2002, pp. 3-1–3-29.

[52]Mouginis-Mark, P. J. "Volcano/ground ice interactions in Elysium Planitia, Mars," *Icarus*, Vol. 64, No. 2, 1985, pp. 265–284.

[53]Wilson, L., and Mouginis-Mark, P. J., "Phreatomagmatic explosive origin of Hrad Vallis, Mars," *Journal of Geophysical Research*: *Planets*, Vol. 108, No. E8, 5082, 2003, pp. 1–18.

[54]Hauber, E., Brož, P., Jagert, F., Jodłowsk, P., and Platz, T., "Very recent and wide spread basaltic volcanism on Mars," *Geophysical Research Letters*, Vol. 38, No. 10, 2011, pp. 1–5.

[55]Crown, D. A., and Ramsey, M. S., "Morphologic and thermophysical characteristics of lava flows southwest of Arsia Mons, Mars," *Journal of Volcanological and Geothermal Research*, Vol. 342, 2017, pp. 13–28.

[56]Richardson, J. A., Bleacher, E., Connor, C. B., and Glaze, L. S., "Trends in distributed volcanism across Tharsis Province, Mars," *49th Lunar and Planetary Science Conference*, The Woodlands, Texas, March 19–23, 2018, Abstract 2045.

[57]Vaucher, J., Baratoux, D., Toplis, M. J., Pinet, P., Mangold, N., and Kurita, K., "The morphologies of volcanic landforms at Central Elysium Planitia: Evidence for recent and fluid lavas on Mars," *Icarus*, Vol. 200, 2009, pp. 39–51.

[58]Hamilton C. W., "Flood lavas associated with the Cerberus Fossae 2 unit in Elysium Planitia, Mars," *44th Lunar and Planetary Science Conference*, The Woodlands, Texas, March 18–22, 2013, Abstract 3070.

[59]Bleacher, J. E., Orr, T., R., de Wet, A. P., Zimbleman, J. R., Hamilton, C. W., Garry, W. B., Crumpler, L.S., and Williams, D. A., "Plateaus and sinuous ridges as the fingerprints of lava flow inflation in the Eastern Tharsis Plains of Mars," *Journal of Volcanology and Geothermal Research*, Vol. 342, 2017, pp. 29–46.

[60]Hamilton, C. W., Mouginis-Mark, P. J., Sori, M. M., Scheidt, S. P., and Bramson, A. M., "Episodes of aqueous flooding and volcanism associated with Hrad Vallis, Mars," *Journal of Geophysical Research: Planets*, Vol. 123. No. 6, 2018, pp. 1484–1510.

[61]Gregg, T. K. P. "Patterns and processes: Subaerial lava flow morphologies: A review," *Journal of Volcanology and Geothermal Research*, Vol. 342, 2017, pp. 3–12.

[62]Baloga, S. M., Mouginis-Mark, P. J., and Glaze, L. S., "Rheology of a long lava flow at Pavonis Mons, Mars," *Journal of Geophysical Research: Planets*, Vol. 108, No. E7, 5066, 2003, pp. 1–10.

[63]Glaze, L. S., Baloga, S. M., Garry, W. B., Fagents, S. A., and Parcheta, C., "A hybrid model for leveed lava flows: Implications for eruption styles on Mars," *Journal of Geophysical Research: Planets*, Vol. 114, No. E0, 7001, 2009, pp. 1–15.

Electron Deposition and Charging Analysis for the Europa Lander Deorbit Stage

Gennady Miloshevsky[1]
Purdue University, West Lafayette, Indiana, 47907

Jarvis A. Caffrey[2]
NASA Marshall Space Flight Center, Huntsville, Alabama, 35812

The radiation environment of Jupiter includes high-energy electrons, which deposit ionizing dose and electric charge in the materials of spacecraft, thus representing a significant hazard for a Europa Lander deorbit stage (EDOS). The deposited charge creates an electric field, which grows to an equilibrium state that may exceed the dielectric strength of the material resulting in an electrostatic discharge. A three-dimensional model has been developed and applied for evaluation of the electric field strength in a multi-layer configuration of the EDOS solid rocket motor as a function of the radiation environment, dielectric material properties, and temperature. The internal charging of materials was studied and results are reported for spectral energy distributions and monoenergetic beams of electrons, gammas, and X-rays, representing both space environment and ground experiment configurations.

Nomenclature

φ = electric potential
ρ = charge density
ε = dielectric constant
ε_r = relative permittivity
$\boldsymbol{E}$ = electric field vector
T = temperature
$\boldsymbol{J}$ = electric current vector
$\dot{\rho}$ = charge density rate (CDR)
σ = electrical conductivity
$\dot{D}$ = dose rate (DR)
σ_{RIC} = radiation induced conductivity (RIC)
k_{RIC} = coefficient of RIC
σ_d = dark conductivity

I. Introduction

The space radiation environment of the Jovian magnetosphere is characterized by extremely intense fluxes of ionizing radiation.[1, 2] The harsh trapped radiation environment in the vicinity of Europa,[3-5] one of Jupiter's moons, is far more severe than that of the Earth's radiation belts. The risks of damage due to ionizing radiation dose, charging, and electronic upsets are a serious concern for all missions destined for Jupiter's moons, including NASA's planned Europa Lander mission concept.[6, 7] The Europa lander mission would place a lander on the surface of Europa. Due to the very high approach velocity and thin atmosphere of Europa,[8] a large impulse of rocket thrust is required to shed horizontal velocity before approaching the surface for the delicate landing operation. A solid rocket motor (SRM) is assumed as a likely candidate for this deorbit braking operation due to its high thrust-to-weight ratio and long-term reliability. Electrons with the energy in excess of 100 MeV can penetrate the outer metallic casing of such a braking

[1] Associate Professor, School of Nuclear Engineering, 400 Central Drive, Purdue University.
[2] Nuclear and Radiological Engineer, Propulsion Research (ER24), NASA MSFC.

motor and deposit their kinetic energy (ionizing dose) and electric charge in the insulator (I), liner (L) and propellant (P) materials (the I-L-P slab configuration). As a result, the proper evaluation of Jovian radiation dose rates, charge density deposition rates, and induced high electric fields (E-fields) that can produce internal electrostatic discharge (iESD) are crucial factors for success of a Europa Lander mission.

The physical phenomenon of internal charging[9] represents the buildup of charge inside the insulating or dielectric materials of a deorbit stage due to the deep penetration of high energy (MeV) electrons. The amount of charge accumulating inside internal dielectric materials or cable insulators depends on the space radiation environment, stage component shielding, dielectric material geometry, and especially the conductivity of irradiated materials.[10] The conductivity of insulating materials is a very important characteristic. When the conductivity is very low, the rate of charge deposition may exceed the rate of charge leakage from the dielectric. In this case, the strength of E-fields inside the dielectric increases and may reach that material's electric breakdown threshold. iESD may occur leading to physical damage of stage components. Therefore, prevention or mitigation of deep dielectric charging is of great importance.[11] It is important to note that for the purposes of this work, the material-specific parameters were estimated in a variety of ways, often measured from surrogate materials or estimated roughly based upon knowledge of other similar materials. Those same parameters were applied uniformly across the various analytical methods to confirm analytical performance and test the methods developed in this work, but this report should not be considered as a source for material properties.

The numerical modeling of spacecraft internal charging is a challenging problem. The 1D computer codes such as NUMIT[12] and DICTAT[13] have been developed and widely used to simulate the internal charging of dielectric and insulating materials. The slab layers of materials and approximate analytical models are implemented in these codes for describing the charge deposition. The recent trend is to combine the 3D Monte Carlo (MC) radiation transport models and highly accurate numerical methods for solving the system of electrostatic equations.[14, 15] The MC model provides accurate 3D distributions of the dose rate (DR) and charge density rate (CDR) which are used as input in the solver for electrostatic problem.

In this report, we present the Modeling Ionizing Radiation Deep Insulator Charging (MIRDIC) code that is developed and applied for investigating the internal charging of multi-layer materials of a solid rocket motor under the impact of electrons and photons. The DR and CDR distributions in slab materials are calculated using MIRDIC-GEANT4. These are used then as input in the MIRDIC-OpenFOAM code that solves the electrostatic problem and predicts the strength of the radiation-induced E-field. This report is organized as follows: In Section II, the developed MIRDIC-GEANT4 and MIRDIC-OpenFOAM computer codes are described. The contribution of secondary electron-hole pairs to the CDR is discussed. The charging of a standard SRM propellant (P_{std}) by a monoenergetic electron beam is presented in Section III. Section IV contains a discussion of the results on the charging of multi-layer materials by monoenergetic electrons, gammas, and X-rays. The depth-dose profiles produced by Jovian electrons and X-rays with spectral energy distributions are reported in Section V.

II. MIRDIC-GEANT4 and MIRDIC-OpenFOAM Computational Models

The MIRDIC code implements open source GEANT4 and OpenFOAM software toolkits and solves the radiation transport and dielectric charging problems.

A. MIRDIC-GEANT4 Model

GEANT4 is an open source C++ toolkit for 3D Monte Carlo modeling of the transport of radiation in materials.[16, 17] It can treat a variety of different particles within a wide range of energies providing several physics models for describing interactions between particles and target atoms. The electromagnetic interactions of electrons and photons are tracked down to zero residual range (energy), which is extremely useful for studies of the charging of insulating and dielectric materials. The tracking of charged particles to zero energies enables accurate prediction of their transport and deposited charge distributions. Production thresholds for secondary particles expressed in terms of range cutoffs r_c allow a control of the number of secondaries, thus leading to more accurate charging analysis using small values of r_c. The low energy Livermore model is used to describe the electromagnetic physics processes for photons and electrons such as the photo-electric effect, Compton scattering, Rayleigh scattering, gamma conversion, bremsstrahlung, impact ionization, fluorescence and Auger electron emission.

The MIRDIC code based on GEANT4 libraries was written in C++. The main stages implemented in MIRDIC-GEANT4 are as follows: (1) The set-up of geometry and selection of materials, primary incident particles, and physics models for interaction processes is implemented in mirdicDetectorConstruction() and mirdicPrimaryGeneratorAction() functions. (2) The C++ function mirdicRunAction() sets the MC run, creates histogram bins for DR and CDR, post-processes, and writes data in file formats suitable for reading by the MIRDIC-

OpenFOAM code. Histograms with equal, grading, and logarithmic bin spacing are implemented. (3) The collection of information on a particle's energy at the end of each MC step and binning DR into histograms is accomplished by mirdicSteppingAction() function. (4) The C++ function mirdicTrackingAction() identifies the end of electron's trajectories and bins the CDR into histograms.

B. Contribution of Secondary Electrons and Holes to CDR

Irradiation of insulating and dielectric materials with electrons results in the deposition of electron charges. The depth-CDR distribution of deposited charge by primary electrons in ammonium perchlorate (AP) is shown in Fig. 1a. The negative charge density (CD) is created at the surface with the CD peak at ~0.15 cm and nearly zero CD beyond ~0.25 cm. The effect of the electron range cutoff r_c on the CDR profiles is illustrated. Small variations of CDR at the

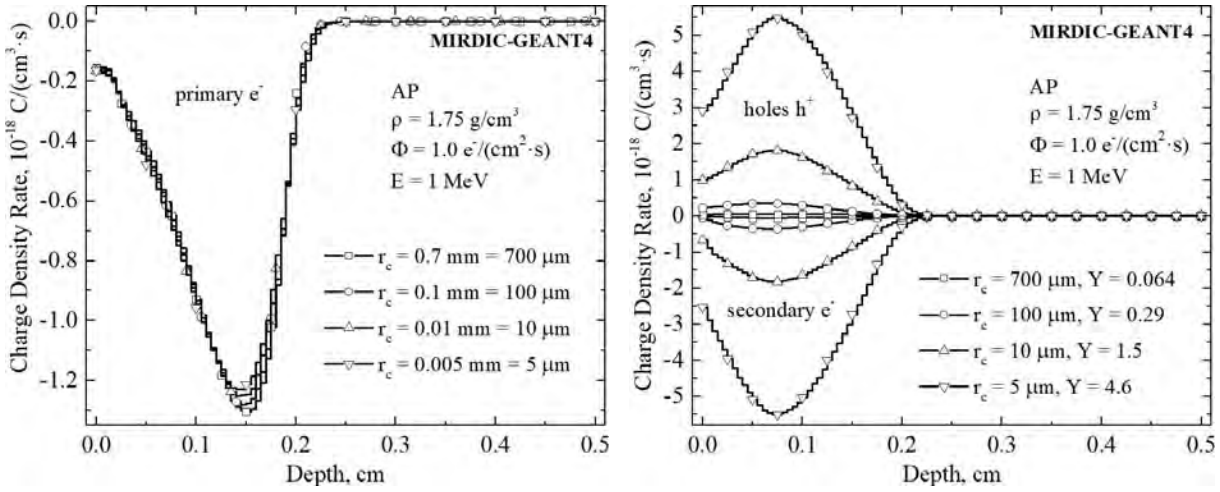

a) Primary electrons **b) Secondary electrons and holes**

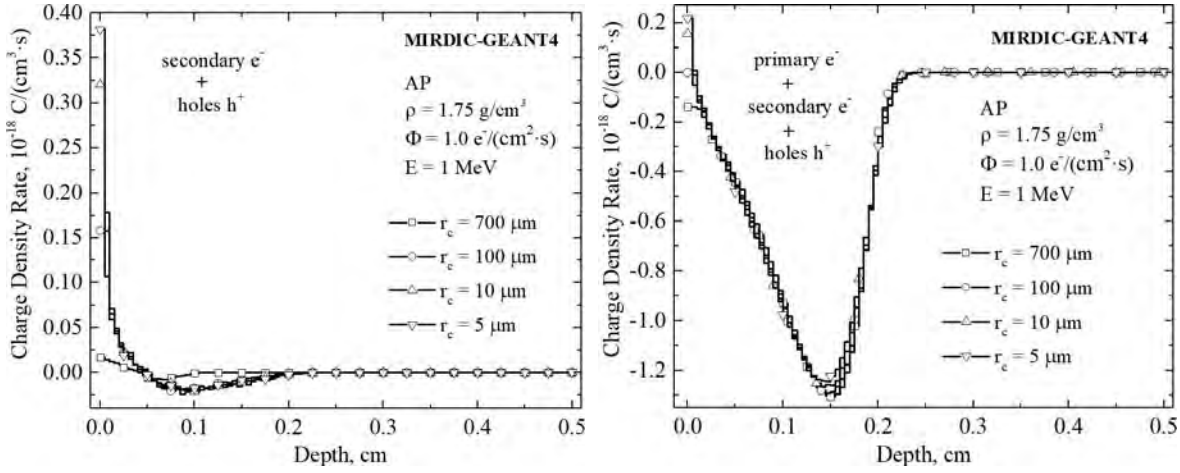

c) Net CDR due to secondary electrons and holes **d) Total CDR due to electrons and holes**

Figure 1. Depth-CDR in AP produced by primary and secondary electrons and holes.

peak and slight increase in the penetration depth of electrons are caused by the decrease of r_c. The transport of primary electrons in dielectric materials leads also to the generation of secondary electron-hole pairs[18] due to the electron impact ionization. The positively charged holes (note that here the term 'hole' is used to refer to any positive charge carrier induced by an electron vacancy) remain in the insulating material, since there is no free electrons to recombine with them.[19] The depth-CDR negative e^- (due to electrons) and positive h^+ (due to holes) profiles are shown in Fig. 1b. There is the e^- negative (h^+ positive) CD at the surface with the e^- negative (h^+ positive) CD peak at ~0.7 mm, and nearly zero CD beyond ~2.3 mm. The range cutoff r_c has the strong effect on the magnitude of CDR. It is seen that the secondary e^- and h^+ yields (Y) and generated CDR increase greatly with reducing r_c. More careful examination of

e^- and h^+ profiles in Fig. 1b reveals the asymmetry. There is *more positive CD* (h^+-holes) at the surface compared to *negative CD* (e^--electrons). The net CDR profiles due to both secondary e^--electrons and h^+-holes are shown in Fig. 1c. The main features are the large positive CD at the surface, shallow negative CD well at ~1 mm, and nearly zero CD beyond ~2.3 mm. This positive charging of the surface was also revealed in the previous work.[19] The physical mechanism of a strong positive charging of the near-surface regions involves the emission (backscattering) of secondary electrons escaping from the front surface of the AP sample and leaving the uncompensated h^+ charge.[19] This issue of secondary electron yield was actually recognized in the course of development of the AF-NUMIT code, but not implemented.[20] The total depth-CDR profiles shown in Fig. 1d demonstrate a positive CD at the surface due to the h^+-holes, large negative well at ~1.5 mm due to the primary electrons, and nearly zero CD beyond ~2.5 mm. The charge state of the surface is also affected by the choice of r_c as it is seen in Fig. 1d. The electron range cutoff r_c ~ 5 μm is found to be small enough to properly produce the reliable CDR profiles.

C. MIRDIC-OpenFOAM Model

The charge densities and internal E-fields in insulators and dielectrics due to irradiation by electrons or photons can be evaluated from the system of 3D differential equations. The electric potential $\varphi(x,y,z,t)\ [V]$ generated by a given charge density distribution $\rho(x,y,z,t)[C/m^3]$ is described by the Poisson equation

$$-\nabla\cdot(\varepsilon(T,x,y,z,t)\ \nabla\varphi(x,y,z,t)\ ) = \rho(x,y,z,t) \tag{1}$$

where $\varepsilon(T,x,y,z,t) = \varepsilon_0\cdot\varepsilon_r(T,x,y,z,t)$ is the dielectric constant, $\varepsilon_0 = 8.854\times10^{-12}\ [C/(V\cdot m)]$ is the permittivity of free space, and $\varepsilon_r(T,x,y,z,t)$ is the relative permittivity of a material. The variables depend on the three spatial coordinates (x,y,z) and time t. The relative permittivity can be affected by temperature T, thus varying in the space and time when the temperature is not constant. The E-field $\boldsymbol{E}(x,y,z,t)\ [V/m]$ is related to potential by

$$\boldsymbol{E}(x,y,z,t) = -\nabla\varphi(x,y,z,t) \tag{2}$$

The continuity equation describing the transport of charge is

$$\frac{\partial\rho(x,y,z,t)}{\partial t} + \nabla\cdot\boldsymbol{J}(x,y,z,t) = \dot{\rho}(x,y,z,t) \tag{3}$$

where $\dot{\rho}(x,y,z,t)\ [C/(m^3\cdot s)]$ is the CDR of charge generation by the radiation and $\boldsymbol{J}(x,y,z,t)\ [A/m^2]$ is the electric current density. The CDR distribution is evaluated by the MIRDIC-GEANT4 code. The electric current density is related to the E-field by the Ohm's law

$$\boldsymbol{J}(x,y,z,t)\ = \sigma(E,T,x,y,z,t)\boldsymbol{E}(x,y,z,t) \tag{4}$$

where $\sigma(E,T,x,y,z,t)\ [\Omega^{-1}\cdot m^{-1}]$ is the electrical conductivity that depends in general on the magnitude of E-field E and temperature T. For insulators and dielectrics, the electrical conductivity is comprised of two parts

$$\sigma(E,T,x,y,z,t) = \sigma_d(E,T,x,y,z,t) + \sigma_{RIC}(T,x,y,z,t) \tag{5}$$

where $\sigma_d(E,T,x,y,z,t)$ is the dark conductivity in the absence of exposure to radiation and $\sigma_{RIC}(T,x,y,z,t)$ is the radiation induced conductivity. The 3D system of Eqs. (1-5) is solved using numerical methods. Additionally, the electric energy density $\mathcal{E}(x,y,z,t)\ [J/m^3]$ can be easily evaluated as

$$\mathcal{E}(x,y,z,t)\ = \frac{1}{2}\varepsilon_0|\boldsymbol{E}(x,y,z,t)|^2 \tag{6}$$

The total electrostatic energy $\mathcal{E}_{tot}(t)\ [J]$ can be calculated by integrating or summing over the volume as

$$\mathcal{E}_{tot}(t) = \frac{1}{2}\varepsilon_0\sum_{volume}|\boldsymbol{E}(x,y,z,t)|^2 \tag{7}$$

D. Model of Dark Conductivity

The Adamec and Calderwood model[21] is used to describe the E-field and temperature dependence of $\sigma_d(E,T,x,y,z,t)\cong\sigma_{ET}$ as

$$\sigma_{ET} = \sigma_T\ \frac{1}{3}\ \frac{2kT}{eE\delta}sinh\left(\frac{eE\delta}{2kT}\right)\left[2+cosh\left(\frac{\sqrt{e^3E}}{2kT\sqrt{\pi\varepsilon_r\varepsilon_0}}\right)\right] \tag{8}$$

where $k = 1.38\times10^{-23}\ [J/K]$ is the Boltzmann constant, $e = 1.6\times10^{-19}\ C$ is the electron charge, and $\delta\approx1\ nm$ is the jump distance of charge carriers. The Arrhenius model is used to describe the temperature-activated electrical conductance σ_T as

$$\sigma_T = \sigma_d \frac{kT_d}{kT} exp\left[\left(\frac{E_a}{kT_d} - \frac{E_a}{kT}\right)\right] \quad (9)$$

where T_d is the temperature ($T \sim 293\ K$) at which σ_d was measured and E_a is the activation energy of conductance.

E. Model of RIC

The electric conductivity is enhanced by the absorbed dose. This effect is described by the Fowler model[22]

$$\sigma_{RIC}(T,x,y,z,t) = k_{RIC}(T)\dot{D}(x,y,z,t)^{\Delta(T)} \quad (10)$$

where $\dot{D}(x,y,z,t)$ $[Gy/s]$ is the dose rate (DR), $k_{RIC}(T)$ $[(A^2 \cdot s^6)/(kg \cdot m^5)]$ is the temperature-dependent coefficient of RIC expressed as

$$k_{RIC}(T) = k_{RIC0} \cdot {k_{RIC1}}^{\Delta(T)} (T/T_{RIC})^{3/2-2\Delta(T)} \quad (11)$$

and the T -dependent exponent $0.5 < \Delta(T) < 1$ associated with the energy distribution of electron trapping states is

$$\Delta(T) = [1 + T/T_{RIC}]^{-1} \quad (12)$$

The constants k_{RIC1}, k_{RIC0} $[(A^2 \cdot s^6)/(kg \cdot m^5)]$ and T_{RIC} $[K]$ are specific for each insulating material. The DR distribution $\dot{D}(x,y,z,t)$ is evaluated by the MIRDIC-GEANT4 code. The dose deposition enhances the electric conductivity, thus mitigating the charging of insulating materials.

The OpenFOAM C++ libraries[23, 24] are used to numerically solve the system of 3D electrostatic equations. The implementation of partial differential equations is accomplished through a natural language of equation mimicking with a few lines of code. OpenFOAM contains a collection of robust numerical schemes that can be selectively assigned to various operators (gradient, divergence, laplacian, etc.) in differential equations providing fast convergence and solution stability. Therefore, the OpenFOAM framework gives opportunity to implement new high-fidelity computational models, and the MIRDIC-OpenFOAM code was developed to integrate with those features. The main stages of MIRDIC-OpenFOAM include (1) the setup of initial fields for φ, ρ, ε and reading MIRDIC-GEANT4 calculated fields for $\dot{\rho}$ and $\dot{D}$; and (2) the time-iterations to numerically solve the Poisson's equation and determine new φ with ρ as a source, to calculate E-field $\boldsymbol{E}$, magnitudes of E and $\mathcal{E}$, and to solve the charge continuity equation and determine new ρ.

III. Charging of Propellant Slab by Electrons

A. Charge Density, Electric Potential, and E-field Strength

The charging of a standard SRM propellant (P_{std}) slab by 1.4 MeV electron beam at normal incidence is investigated to evaluate the effects that may be observed during a ground-based irradiation test. The flux of electrons is 5.62×10^9 $e^-/(cm^2 \cdot s)$. The dark conductivity of propellant is estimated as $\sigma_d = 1.25 \times 10^{-11}$ $\Omega^{-1} \cdot m^{-1}$. No dependence of σ_d on T and E-field is considered. The worst case scenario with $\sigma_{RIC} = 0$ and $\varepsilon_r = 1$ is modeled to evaluate the E-field magnitude in a propellant slab. The CDR profile (not shown) produced by MIRDIC-GEANT4 is found to be very similar to that illustrated in Fig. 1d. Since σ_{RIC} is set to zero, the DR profile is not used. The boundary condition of grounded and floating potential was used at the back and front sides of slab, respectively. The boundary condition of zero gradient was set for charge density at both sides. The conditions together with $\sigma_{RIC} = 0$ and $\varepsilon_r = 1$ provide the highest E-fields in the propellant slab.

The profiles of E-field magnitude in a SRM propellant slab are shown in Fig. 2a for different times. It is seen that the E-field inside a slab raises with the irradiation time reaching the equilibrium state after two seconds. The magnitude of E-field also increases along the slab's depth approaching a maximum E-field value and saturating beyond ~0.3 cm. That portion of propellant near the grounded back side is subject to the electrical breakdown (discharge), since the created E-field is close to the estimated dielectric strength of propellant. Fig. 2a suggests that there is a severe E-field spike and dip near the surface. To clarify the origin of this apparent spike, the MIRDIC-OpenFOAM calculation was performed using the CDR profile created only by the primary electrons (see Fig. 1a). The E-field magnitude plotted in Fig. 2b does not show a spike at the surface. This is because the apparent E-field spike is due to the positive charge near the surface which transitions to negative charge deeper in the material, but the plot represents only the absolute magnitude of the resulting field. The severe dip is thus the physical location of that polarity change. The equilibrium profile of E-field magnitude with charging time of 5 seconds is found to be in a good agreement with the NUMIT result with charging time of 338 minutes. However, the strength of E-field spike predicted by both NUMIT and MIRDIC-OpenFOAM is different due to different electron-photon transport models used for the evaluation of charge

deposition. The NUMIT data on the CDR profile are not available. However, it is obvious that the NUMIT's CDR profile does include a portion with the positive charge at the surface in order to produce the E-field spike.

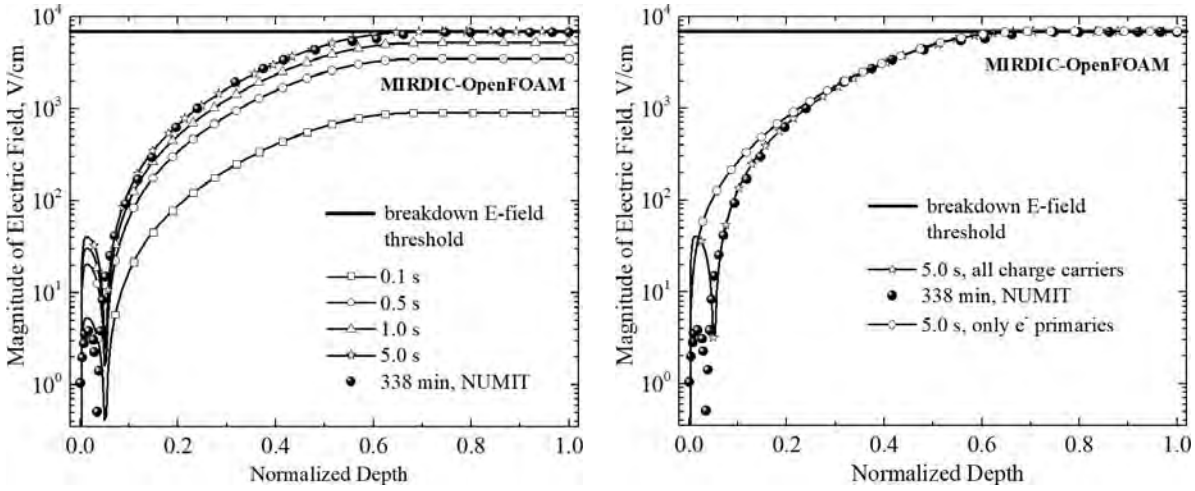

a) E-field magnitude due to total charge **b) Comparison to E-field due to e^- primaries**

Figure 2. Time evolution of E-field magnitude and comparison with the NUMIT data.

B. Temperature Dependence of E-field Strength

The dependence of the dark conductivity on temperature and its effect on the strength of E-field is investigated. It is assumed that the value of $\sigma_d = 1.25 \times 10^{-11}\ \Omega^{-1}\cdot m^{-1}$ for propellant was estimated at $T_d = 20\ ^0C$. When the environment temperature $T = T_d$, Eq. (9) yields $\sigma_T = \sigma_d$, showing no dependence on the activation energy E_a. However, the dependence of σ_{ET} on temperature and E-field magnitude (Eq. (8)) is still remaining for this specific case. This effect is demonstrated in Fig. 3 (compare curves with squares and circles). The strength of E-field (curve with circles) is

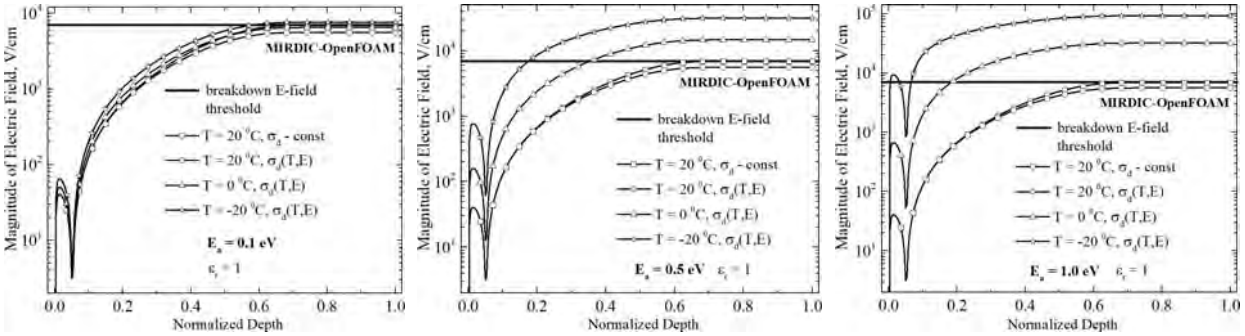

a) E_a = 0.1 eV **b) E_a = 0.5 eV** **c) E_a = 1.0 eV**

Figure 3. Effect of the value of activation energy E_a on the strength of E-field in P_{std}.

slightly reduced due to the influence of E-field on σ_d. The MIRDIC-OpenFOAM calculations are performed using $\varepsilon_r = 1$. The profiles of E-field magnitude are shown in Fig. 3 for three temperatures (20 ^{0}C, 0 ^{0}C and -20 ^{0}C), and the effect of the value of activation energy E_a on the E-field strength (Figs. 3a-3c) is illustrated. The value of E_a is unknown for propellant and should be measured in future experiments for various temperatures. The available measurements of E_a for pure AP provide a value of ~0.12 eV at 25 ^{0}C.[25] However, this value could be different, since SRM propellant includes other compounds. It can be seen in Fig. 3 that there is a significant increase in the strength of E-field with increasing E_a, reaching about an order of E-field magnitude for E_a = 1 eV. The magnitude of E-field exceeds the assumed dielectric strength of propellant at $T < 0\ ^0C$ and $E_a > 0.5$ eV, which could result in ESD.

Fig. 4 shows the depth profiles of E-field strength for three values of E_a (Figs. 4a-4c), affected by the choice of dielectric constant ε_r. It is normally expected that E-field should be reduced with increasing the value of ε_r. However, it is seen in Fig. 4 that the magnitude of E-field is significantly increased with increasing ε_r. The E-field dependence on ε_r seems to be nonlinear at high values of E_a (Fig. 4c). This behavior is caused by a nonlinear dependence of σ_{ET} on ε_r (see Eq. (8)). The scenario with $\varepsilon_r = 1$ is not a worst case as assumed before. The measurement of ε_r for some

propellants reported by JPL yields $\varepsilon_r \sim 5$.[26] This value could be different for the assumed SRM propellant. It should be noted that ε_r is temperature dependent implying that measurements of ε_r will be needed at various temperatures.

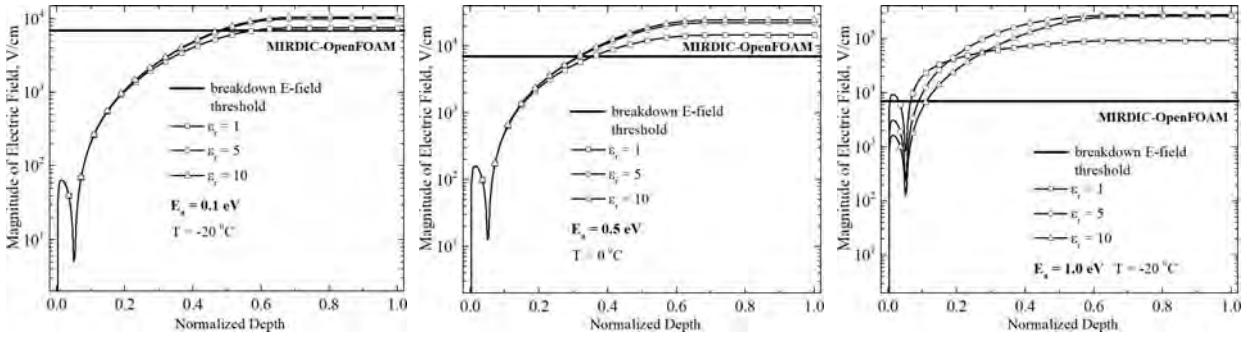

a) E_a = 0.1 eV **b) E_a = 0.5 eV** **c) E_a = 1.0 eV**

Figure 4. Effect of the value of dielectric constant of P_{std} on the strength of E-field for different E_a.

IV. Charging of 3-Slab System

A. Charge Density, Electric Potential, E-field, and Current Density

A study was performed using MIRDIC-GEANT4 and MIRDIC-OpenFOAM codes to investigate the charging of three-layer slab configuration composed of an insulator, liner, and propellant by 1.8 MeV electrons at their normal incidence on the insulator. This investigation is relevant for planned laboratory experiments at MSFC. The electron flux of 2.184×10^9 $e^-/(cm^2 \cdot s)$ was slightly lower compared to that used for one-slab case (see previous section). The dark conductivities of I and L materials are 2.3×10^{-14} $\Omega^{-1} \cdot m^{-1}$ and 2.0×10^{-8} $\Omega^{-1} \cdot m^{-1}$. The I and L dielectric constants are $\varepsilon_r = 3.4$ and $\varepsilon_r = 1$, respectively. The parameters used for propellant (P) are the same as in the previous one-slab case. Again, no dependence of σ_d on temperature and E-field strength is considered. The value of RIC was set to zero in all materials.

The distribution of E-field strength inside the I-L-P slab configuration is illustrated in Fig. 5a for different charging times. It can be seen that apparent E-field spike discussed in Section III (shown in Fig. 2) is now present in the I-slab. The E-field strength is very low in the L-slab and of intermediate value in the P-slab. This behavior is governed by

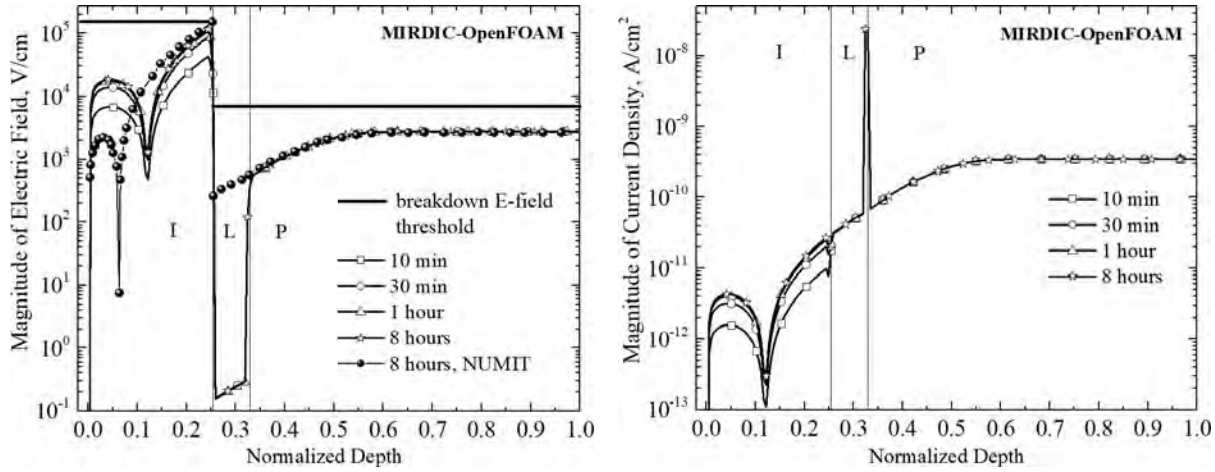

a) E-field **b) Electric current density**

Figure 5. Time evolution of E-field and electric current density magnitudes in 3-slab system.

the values of dark conductivity (low, high, and intermediate σ_d) in each of the I-L-P slabs. The profile of E-field is found to be in a good agreement with the NUMIT data near the I-L interface and inside the P-slab. However, the E-field spike inside the I-slab evaluated from MIRDIC-OpenFOAM is of a higher magnitude and larger width compared to that predicted by NUMIT. The strength of E-field inside the L-slab was not properly evaluated by NUMIT due to the problem with the stability of numerical solution. Much lower value of σ_d was used for the L-slab (to match the P-

slab) in NUMIT to get a stable solution (Fig. 5a). However, the E-field strength within the L-slab calculated by MIRDIC-OpenFOAM using a more realistic large σ_d is seen to be orders of magnitude lower than NUMIT's result. The E-field analysis matched NUMIT's result for the L-slab when using the P-slab's smaller σ_d in MIRDIC-OpenFOAM. In general, the use of lower values of σ_d inside a particular slab increases the strength of E-field, and also affects other properties within that slab (potential, energy, current, etc). However, it is observed that quantities of neighboring slabs are not significantly influenced. The evolution of the magnitude of electric current density with the irradiation time inside the I-L-P slab system is shown in Fig. 5b. The interesting features are the polarity-switching spike of current inside the I-slab, small perturbation of current at the I-L interface, large peak of current at the L-P interface, and increasing then constant current inside the P-slab. The z-component of L-P current peak is found to be negative and its physical origin should be further investigated. Finally, it should be noted that the charging time needed to reach equilibrium state is on the order of ~1 hour 5 for the I-slab, and several minutes for the L and P slabs.

B. Comparison of E-field Induced by Monoenergetic Electrons, X-rays and γ-rays

Except the electron beams, the other sources of radiation such as X-rays or γ-rays can be used in the laboratory experiments for irradiating multi-layer slabs of insulating materials and analyzing their ESD properties. The goal of this particular study is to compare the profiles of various electric quantities in the I-L-P slab system due to irradiation by monoenergetic electrons, X-rays, and cobalt-60 gammas. The charge, dose, and electric profiles produced by electrons and presented in the previous section are compared to those produced by 320 keV X-rays representing a peak photon energy from a particular X-ray irradiator system (true X-ray spectrum evaluated separately in the following section) and 1.25 MeV γ-rays representing the average gamma energy emission of the Co-60 double peak. The unit flux for all incident particles was used in the MIRDIC-GEANT4 calculations. It is discovered that the scaling of all charging profiles is possible by a constant value of the flux. This is a quite important finding allowing one-time calculation of the E-field and other electric quantities for the unit incident flux and then scaling them to a flux value of interest. The photon-induced CDR profiles (not shown) are found to be qualitatively different from the electron CDR because of the absence of the negative CD well created by the primary electrons (Fig. 1a). The amount of positive CD at the surface of the I-slab is also observed to be much smaller than that created by the electrons.

The magnitude of E-field generated in the I-L-P slab configuration by three different sources of radiation per unit incident flux after 8 hours of charging are compared in Fig. 6a. It can be seen that the E-field profiles are qualitatively

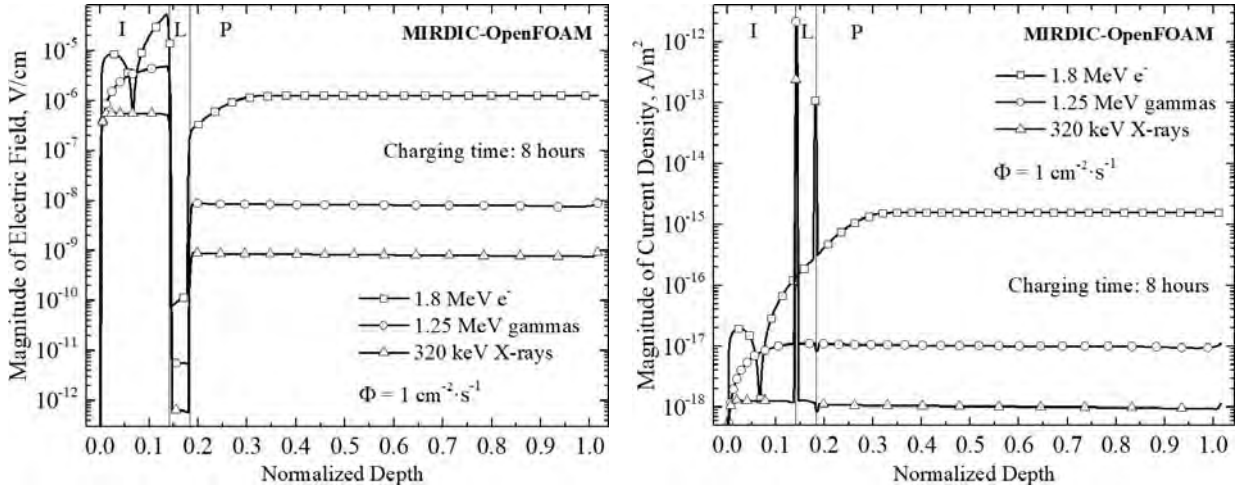

a) E-field **b) Electric current density**

Figure 6. Comparison of magnitude of E-field and electric current density produced by e^-, gammas and X-rays in the 3-slab system.

similar in the shape (highest, lowest and intermediate E-field in the I-, L- and P-slabs). However, the E-field strength induced by photons is in general lower in all slabs by order(s) of magnitude. The scaling by higher photon flux or using higher energy gammas can match the E-field strength produced by the electrons. The E-field spike created by the MeV electrons inside the I-slab is not reproduced by the photons. The profiles of current density magnitude are shown in Fig. 6b. The current induced by the photons inside the I-slab is lower than that due to the electrons. There is a large peak of electric current produced by the photons at the I-L interface that is different from that much smaller one generated by the electrons at the L-P interface. It should be noted according to the analysis of z-components of

electric current density that the positive photon- and negative electron-induced currents flow in different z-direction. The electric current in the P-slab produced by the photons is much lower than that due to the electrons.

V. X-ray Spectrum used to Model Space Radiation Effects

Modeling of the space radiation environment effects on the materials in laboratory experiments are of a great practical interest. The evaluation of depth-dose and deposited charge distributions in multi-layer slab configurations by electrons, protons and photons with their spectral energy fluxes is required. One way of simulating space radiation environment is to use an X-ray tube generating X-rays with spectral energy distribution of flux shown in Fig. 7a. The energy of X-rays is in the range ~4 - 320 keV with an appreciable X-ray flux ~10^{10} - 10^{11} photons/(cm^2·s). The CDR distribution inside the I-L-P slab configuration (not shown) reveals a positive CD at the surface and at the I-L and P-

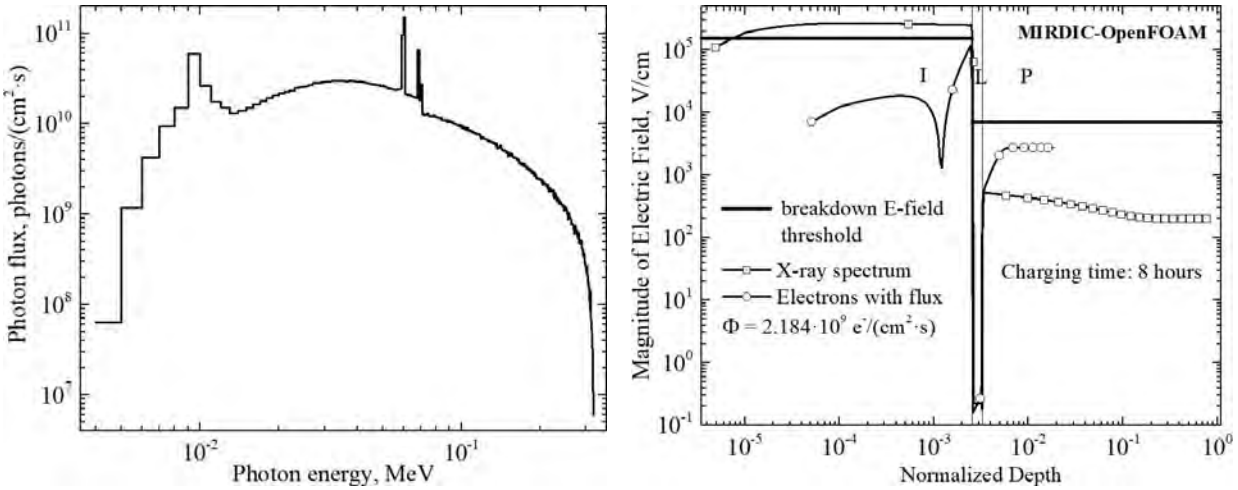

a) X-ray spectrum **b) E-field magnitude**

Figure 7. Comparison of magnitude of E-field induced in 3-slab system by X-ray with spectral energy distribution and 1.8 MeV electrons with incident flux of 2.184·10^9 e$^-$/(cm^2·s).

L interfaces, and a negative CD at the L-I and L-P interfaces. The profiles of E-field strength induced in the three-slab system by X-ray spectrum and monoenergetic electrons are compared in Fig. 7b. The E-field inside the I-slab is observed to (1) exceed the assumed breakdown strength of the insulator; and (2) differ in shape and be higher magnitude than that produced by the electrons with E = 1.8 MeV and flux of Φ = 2.184x10^9 e$^-$/(cm^2·s). The E-field inside the L-slab is seen to be very low and well matching the magnitude of E-field produced by the electrons. The E-field inside the P-slab is found to be well below the assumed breakdown strength of propellant and lower in the magnitude than that produced by the electrons.

The depth-dose distributions originated from the impact of Jovian electrons on multi-layer materials (a layer of Ti alloy shielding layers of insulator, liner and SRM propellant) were previously investigated using the MONSOL code.[27] The JPL time-integrated electron flux (fluence) through the entire Europa Lander mission was used in those studies. The depth-dose distribution predicted by MONSOL in the four-layer system irradiated by Jovian electrons is shown in Fig. 8. The depth-dose profile was reevaluated using the MIRDIC-GEANT4 code. A very good agreement can be seen between the depth-dose distributions calculated using MONSOL and MIRDIC-GEANT4. The irradiation of a four-layer slab target with the X-ray spectrum (Fig. 7a) was then modeled using MIRDIC-GEANT4. The irradiation time of ~2.8

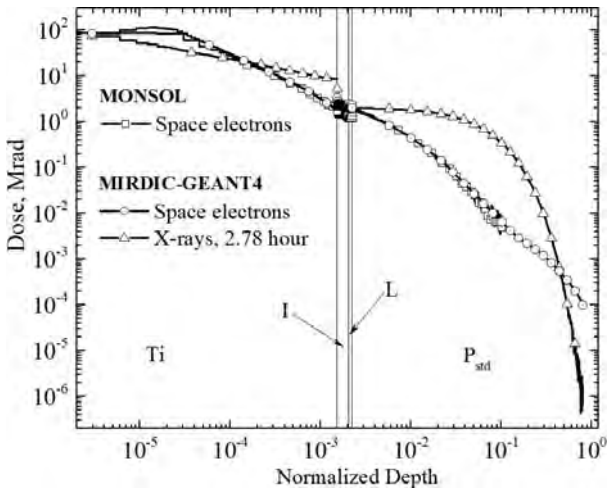

Figure 8. Comparison of depth-dose distributions produced by space environment electrons and X-rays with spectral energy distribution in four-slab system.

hours would be required to achieve approximately the same level of dose in the Ti, I, and L slabs (Fig. 8) as that caused by Jovian electrons. It can be seen that X-rays produce a large overdose in propellant within ~40-50 cm (curve with triangles). The shape of the X-ray induced depth-dose profile can be adjusted by manipulating the spectrum of X-rays using filtration and a multi-energy irradiation schedule, which requires further research. The MIRDIC-OpenFOAM code can be then applied for evaluating the E-field strength in the I-L-P slabs with the grounded front face of Ti sheet.

VI. Future Applications

There are several applications where the developed MIRDIC code can be directly used for future work: (1) modeling of the spectral energy flux of electrons *isotropically* incident on the surface of spacecraft components; (2) modeling of the charge deposition and the E-field strength inside the multi-layer slab configurations under the Jovian radiation environments with *the electron flux changing in time*; (3) modeling of realistic, *3D geometric configurations* of materials in order to evaluate 3D charging effects such as the strength of E-field at edges and corners.

VII. Conclusion

The evaluation of internal charging and dielectric breakdown under high radiation fluxes requires solving both radiation transport and electrostatic problems. The MIRDIC computer code based on GEANT4 and OpenFOAM open source C++ toolkits is developed. The 3D transport of electrons and photons in insulators is modeled using the MIRDIC-GEANT4 code, and the DR and CDR are calculated. These data are used as input in the MIRDIC-OpenFOAM code developed to numerically solve the 3D electrostatic equations.

The CDR distribution calculated by the MIRDIC-GEANT4 model includes the contribution from primary electrons, secondary ionization electrons, positively-charged holes (vacancies), and all secondary charge produced in photon-electron interactions (photo-electrons, Auger-electrons, etc.). The deep negative charge density well is found to be caused by the deposition of primary electrons. However, the positive charge density was also revealed in the near-surface region due to the backscattered secondary electrons leaving the uncompensated, positively-charged holes.

The E-field spike at the front surface of electron-irradiated propellant slab is found to be created by the positive charge. The magnitude of E-field spike calculated by NUMIT and MIRDIC-OpenFOAM is different due to different models used in these codes for the evaluation of charge deposition. However, the profile of E-field strength in the equilibrium state is found to be in a very good agreement with the NUMIT result. The charging time of propellant samples is about 3 seconds before reaching equilibrium. The E-field strength in the propellant slab is found to be significantly affected by temperature through its dependence on the dark conductivity, which is strongly influenced by values of activation energy and dielectric constant. These properties are not well known for components of the I-L-P slabs and they should be measured in future experiments.

The E-field strength induced by monoenergetic electrons in the I-L-P slabs is investigated. The profile of E-field strength is observed to be in a good agreement with NUMIT result near the I-L interface and within the P-slab. The E-field within the L-slab calculated using the realistic (large) L-slab's conductivity is found to be orders of magnitude lower than NUMIT's result, which was determined using an artificially reduced value of conductivity to stabilize the NUMIT solution method. The charging time needed to reach equilibrium is on the order of ~1 hour for the I-slab, and much shorter for the L and P slabs.

The profiles of E-field strength in the I-L-P slabs induced by monoenergetic 1.8 MeV electrons, 1.25 MeV gammas, and 320 keV X-rays are found to be qualitatively similar demonstrating highest, lowest and intermediate E-field strength in the I-, L- and P-slabs, respectively. The E-field spike induced by the electrons in the I-slab was not reproduced by the photons. Photons with higher flux can be used to match the E-field strength induced by the electrons.

The E-field strength induced by X-rays with spectral energy distribution in the I-L-P slabs is predicted. The E-field inside the I-slab is found to exceed the assumed breakdown strength at the flux used for this analysis, and it differs in shape and magnitude compared to that produced by the electrons. The E-field inside the L-slab was well-aligned with that produced by the electrons. The E-field inside the P-slab was well below the breakdown strength of propellant and lower in the magnitude than that produced by the electrons. It is concluded that the spectrum of X-rays can be adjusted to produce the depth-dose profiles similar to those created by space environment electron fluxes.

Acknowledgments

G. Miloshevsky thanks the NASA MSFC Summer Faculty Fellow Program managers and staff for supporting this research that allowed him the opportunity to closely collaborate with MSFC engineers and scientists.

References

[1]Bolton, S. J., Janssen, M., Thorne, R., Levin, S., Klein, M., Gulkis, S., Bastian, T., Sault, R., Elachi, C., Hofstadter, M., *et al.*, "Ultra-relativistic electrons in Jupiter's radiation belts," *Nature*, Vol. 415, 2002, p. 987.

[2]Bolton, S. J., Thorne, R. M., Bourdarie, S., de Pater, I., and Mauk, B. "Jupiter's inner radiation belts," *In: F. Bagenal, T. Dowling, and W. McKinnon, Editors. Jupiter: The Planet, Satellites and Magnetosphere*. Cambridge Univ. Press, 2004, pp. 671-688.

[3]Kivelson, M. G., Khurana, K. K., and Volwerk, M. "Europa's interaction with the Jovian magnetosphere," *in Europa, The Univ. of Arizona Space Sci. Ser., edited by R. T. Pappalardo, W. B. McKinnon, and K. K. Khurana*. Univ. of Ariz. Press, Tucson, Ariz., 2009, pp. 545-570.

[4]Paranicas, C., Mauk, B. H., Khurana, K., Jun, I., Garrett, H., Krupp, N., and Roussos, E., "Europa's near-surface radiation environment," *Geophysical Research Letters*, Vol. 34, No. 15, 2007, p. L15103.

[5]Paranicas, C., Cooper, J. F., Garrett, H. B., Johnson, R. E., and Sturner, S. J., "Europa's radiation environment and its effects on the surface," *in Europa, The University of Arizona space science series, edited by R. T. Pappalardo, W. B. McKinnon, K. K. Khurana, and R. Dotson (University of Arizona Press, Tucson)* 2009, pp. 529-544.

[6]Team, E. S. "Europa Study 2012 Report: Europa Lander Mission." Tech. Rep. JPL D-71990, Jet Propulsion Laboratory, May 2012.

[7]Coleman, N. M., and Coleman, F. A. "Mission to Europa - Lander and Orbiter Capabilities to Support the Search for Extant Life," *48th Lunar and Planetary Science Conference, held 20-24 March 2017, at The Woodlands, Texas. LPI Contribution No. 1964, id.2354*.

[8]Prockter, L., Hibbard, K., Magner, T., and Bolt, J. "Exploring Europa: Science from the Jupiter Europa Orbiter - A Future Outer Planet Flagship Mission." Vol. 30, Johns Hopkins APL Technical Digest, 2011, pp. 72–84.

[9]Garrett, H. B., and Whittlesey, A. C., "Spacecraft charging, an update," *IEEE Transactions on Plasma Science*, Vol. 28, No. 6, 2000, pp. 2017-2028.

[10]Lai, S. T., Cahoy, K., Lohmeyer, W., Carlton, A., Aniceto, R., and Minow, J. "Chapter 16 - Deep Dielectric Charging and Spacecraft Anomalies," *Extreme Events in Geospace*. Elsevier, 2018, pp. 419-432.

[11]Lai, S. T., "A critical overview on spacecraft charging mitigation methods," *IEEE Transactions on Plasma Science*, Vol. 31, No. 6, 2003, pp. 1118-1124.

[12]Jun, I., Garrett, H. B., Kim, W., and Minow, J. I., "Review of an Internal Charging Code, NUMIT," *IEEE Transactions on Plasma Science*, Vol. 36, No. 5, 2008, pp. 2467-2472.

[13]Rodgers, D. J., Ryden, K. A., Wrenn, G. L., Latham, P. M., Sørensen, J., and Levy, L. "An Engineering Tool for the Prediction of Internal Dielectric Charging." 6th Spacecraft Charging Technology Conference, AFRL-VSTR-20001578, September 2000.

[14]Kim, W., Chinn, J. Z., Katz, I., Garrett, H. B., and Wong, K. F., "3-D NUMIT: A General 3-D Internal Charging Code," *IEEE Transactions on Plasma Science*, Vol. 45, No. 8, 2017, pp. 2298-2302.

[15]Sarrailh, P., Paulmier, T., Dirassen, B., Rodgers, D., Santin, G., Cipriani, F., and Payan, D., "Validation Through Experiments of a 3-D Time-Dependent Model of Internal Charging," *IEEE Transactions on Plasma Science*, Vol. 45, No. 9, 2017, pp. 2566-2572.

[16]Allison, J., Amako, K., Apostolakis, J., Arce, P., Asai, M., Aso, T., Bagli, E., Bagulya, A., Banerjee, S., Barrand, G., *et al.*, "Recent developments in Geant4," *Nuclear Instruments and Methods in Physics Research Section A: Accelerators, Spectrometers, Detectors and Associated Equipment*, Vol. 835, 2016, pp. 186-225.

[17]"https://geant4.web.cern.ch/."

[18]Sessler, G. M., Figueiredo, M. T., and Ferreira, G. F. L., "Models of charge transport in electron-beam irradiated insulators," *IEEE Transactions on Dielectrics and Electrical Insulation*, Vol. 11, No. 2, 2004, pp. 192-202.

[19]Touzin, M., Goeuriot, D., Guerret-Piécourt, C., Juvé, D., Tréheux, D., and Fitting, H. J., "Electron beam charging of insulators: A self-consistent flight-drift model," *Journal of Applied Physics*, Vol. 99, No. 11, 2006, p. 114110.

[20]Beecken, B. P. "Development and Application of NUMIT for Realistic Modeling of Deep-Dielectric Spacecraft Charging in the Space Environment." Air Force Research Laboratory Report No. AFRL-RV-PS-TR-2014-0181, April 2014.

[21]Adamec, V., and Calderwood, J. H., "Electrical conduction in dielectrics at high fields," *Journal of Physics D: Applied Physics*, Vol. 8, No. 5, 1975, p. 551.

[22]Fowler, J. F., "X-ray induced conductivity in insulating materials," *Proceedings of the Royal Society of London. Series A. Mathematical and Physical Sciences*, Vol. 236, No. 1207, 1956, pp. 464-480.

[23]Weller, H. G., Tabor, G., Jasak, H., and Fureby, C., "A tensorial approach to computational continuum mechanics using object-oriented techniques," *Computers in Physics*, Vol. 12, No. 6, 1998, pp. 620-631.

[24]"https://www.openfoam.com/."

[25]Ohanian, M. G. "Electrical Conductivity and Thermodynamic Parameters of Ammonium Perchlorate." Ph.D. thesis, University of Miami, 1974.

[26]Strand, L. D., Shultz, A. L., and Reedy, G. K. "Determination of Solid Propellant Transient Regression Rates Using a Microwave Doppler Shift Technique." Technical Report 32-1569, Jet Propulsion Laboratory, Pasadena, California, October 15, 1972.

[27]Miloshevsky, G., Caffrey, J. A., Jones, J. E., and Zoladz, T. F. "Materials Degradation in the Jovian Radiation Environment," *NASA/TM-2017-219848 Technical Report*. December 2017, pp. 114-124.

Mars Ascent Vehicle Sensitivity Analysis

Carlos Montalvo*
University of South Alabama
150 Jaguar Dr, Shelby Hall Rm. 3106
Mobile, AL USA, 36688
John Rakoczy†
NASA Marshall Space Flight Center
Huntsville, AL

1 Introduction

Traveling such large distances from Earth is always challenging but the reward is often cutting edge research or game-changing knowledge. From the time the first stargazers looked up to the stars and noticed that certain "blinky" lights were in fact other planets, humans have been curious of these other worlds.[1] Mars being our closest neighbor and most similar in the Solar System has often been a source of exploration. Early historians record ancient Egyptian astronomers and Chinese who first noticed Mars.[2] It wasn't until Galileo Galilei made the first telescopic observation of Mars that humans really looked at this planet in detail.[3] Almost 300 years later in the 1960s, the Soviets began launching probes to Mars with the first successful flyby completed by NASA's Mariner 4 in 1965.[4] It wasn't long before the Mars 2 and Mars 3 probes landed on Mars followed by NASA's successful Viking 1 and 2 programs that transmitted the first color panoramic photos of Mars[5].[6] Fast forward to the present and the Curiosity rover is still alive and transmitting data everyday. It touched down in 2012. It has exceeded expectations.[7] Through all of these flybys, orbits and soft landings as well as ground rover explorations, no program has been able to secure samples and return those samples to Earth for study.

Such is the Mars Sample Return Mission which has been studied since the early 1980s.[8] The goal now is to send a rover and collect some samples that will be loaded into a lander complete with a Mars Ascent Vehicle (MAV). The MAV will then reach a stable circular orbit above Mars. Another mission will rendezvous with the Mars Ascent Vehicle and return the samples to Earth. The research presented here focuses on the Mars Ascent Vehicle, specifically on modeling orbital insertion. The sections that follow describe the dynamic model as well as numerous trade studies performed using the software codenamed MAnTiS (MAV Analysis Tool in Simscape).

*Assistant Professor, Department of Mechanical Engineering, cmontalvo@southalabama.edu, 251-460-7458
†Chief, Control Systems Design & Analysis Branch, NASA MSFC, john.m.rakoczy@nasa.gov, 256-544-1512

2 MAV Analysis Tool in Simspcape (MAnTiS)

The analysis tool created for the MAV is built in Simscape. The entire Simscape model is broken up into many different subsystems to ensure that anyone with mild understanding of guidance control and dynamics can follow the model. The overall block diagram is shown below with many common subsystems such as the guidance block as well as sensor feedback and actuator dynamics. The plant dynamics contain as many models as possible to ensure the simulation is as high fidelity as possible within reason for a quick 10 week turn around. The plant contains the following models: aerodynamics, thrust, mass, standard atmosphere and gravity models. The guidance block uses a two stage guidance law based on a chi table to orient the spacecraft and a boundary value solution for the second stage.

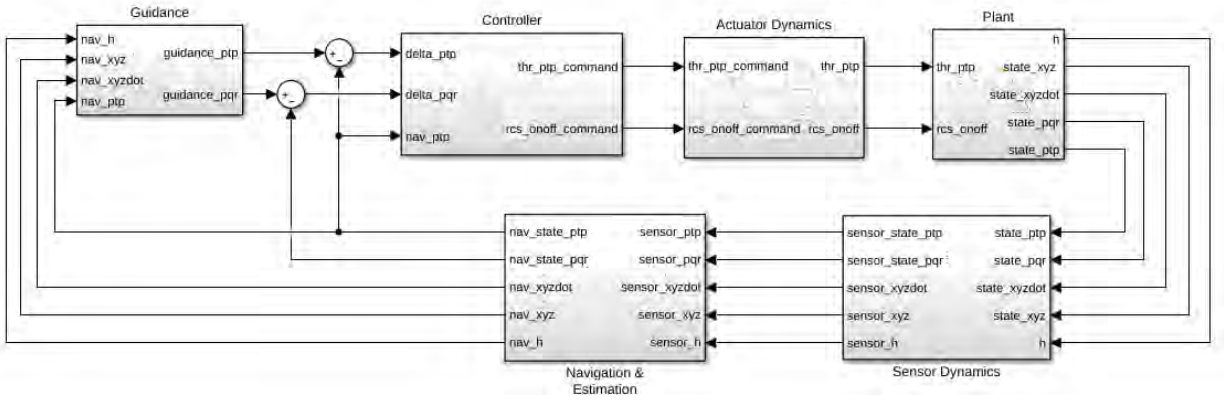

Figure 1: Overall Simscape Model

3 Nominal Simulation

The nominal simulation is created to model the Mars Ascent Vehicle with as much fidelity as possible. The mass of the payload and avionics is set to 24.3 kg, the RCS system is 9 kg with a dry mass of 5 kg. The 1st stage is 245 kg with a dry mass of 38 kg. The 2nd stage is 81 kg with a dry mass of 29 kg. The total mass is 359.3 kg. The payload center of mass is 0.25 m from the nose while the RCS system is 0.7 m from the nose. The 1st and 2nd stages are 2.37 m and 1.29 m from the nose respectively. The center of mass of the rocket is then 1.94 m at prelaunch and 1.42 m at MECO. After separation the center of mass is 1.02 m and 0.82 after 2nd stage cutoff. This can be seen graphically in Figure 2. The first and second stages have an Isp of 291 seconds with the distance from the nose to the first stage set to 3 meters and the second stage set to 1.91 meters. The first stage has a burn time of 43 seconds with a coast of about 508 seconds. The second stage has a burn time of only 23 seconds. The RCS system has 16 thrusters all positioned 0.25 meters from the nose of the spacecraft. The thrust of each thruster is 2.5 N with an Isp of 306 sec. The rise time is set to 30 ms with a duration and delay of 100 ms. The TVC actuators are set to have a rise time of 0.03 seconds with the estimation block set to 0.1 sec. The sensor rise times for the rate gyro and accelerometer are set to 0.03 seconds. The simulation time is set to 700 seconds with a timestep of 0.01 seconds. The aerodynamics for this vehicle are defined using three different methods namely a standard taylor series expansion, an empirical formula and some tabular data.[9] Overall the reference diameter of the rocket is set to 0.57 m with a stationline center of pressure of 1.65 m from the nose. The tabular data interpolates this value and thus it changes over time. Note that in some configurations this causes the spacecraft to be unstable since the center of mass is positioned at 1.94 m. The nominal atmosphere is set to zero with no turbulence or gusts. The nominal initial conditions are set to just on the surface of Mars with the vehicle pointing straight up.

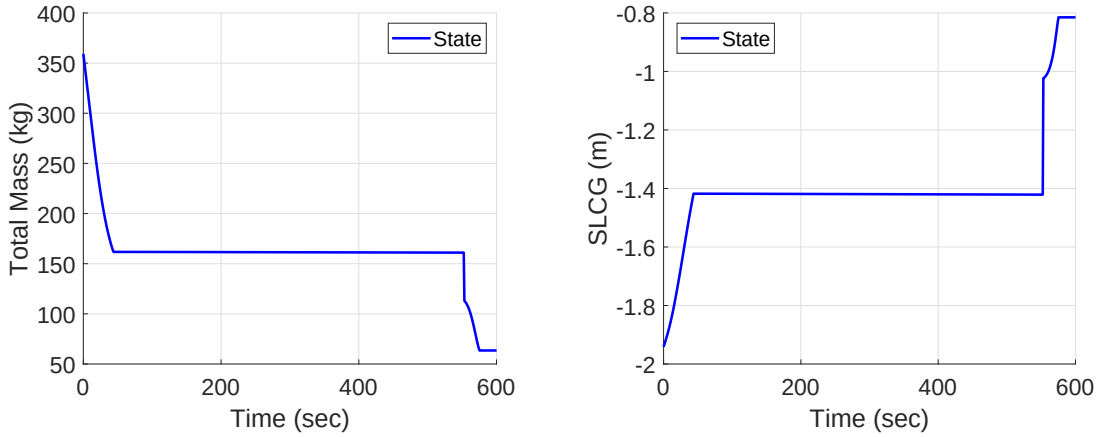

Figure 2: Mass (kg) and CG Location (m) vs. Time (sec) for Nominal Simulation

In order to utilize the maximum amount of orbital assist, the spacecraft is placed at a latitude and longitude of 0 degrees and commanded to insert into a 0 deg inclination orbit. The pitch over manuever is then a yaw maneuver simply due to the coordinates chosen (Planet centered Inertial - PCI). The pitch over manuever with aerodynamics turned off can be seen in Figure 3 (left).Here the phases include a 1 second altitude hold followed by a 4 second pitch over of 12.394 deg/s. During the remainder of the first stage (∼38 seconds), the vehicle pitches over at a rate of 0.289 deg/s. During coast, the pitch rate is set to 0.03554 deg/s. After second stage burnout (∼575 seconds), RCS is turned off to save mass and the spacecraft begins to tumble. A large spike at the beginning of the second stage (∼552) is due to the solution to the Boundary Value Problem which tries to get the spacecraft into a stable orbit. Using this pitch over maneuever, the orbital velocity and orbit can be seen in the figures below. The rocket successfully reaches a suitable orbit and velocity and is well outside the atmosphere of the planet as shown by the dashed line. The 1e-7 atmosphere line is 150 km above the surface of Mars where the density is less than 1e-7 kg/m^3. The Mars Atmosphere is taken from the Glenn Research Center.[10]

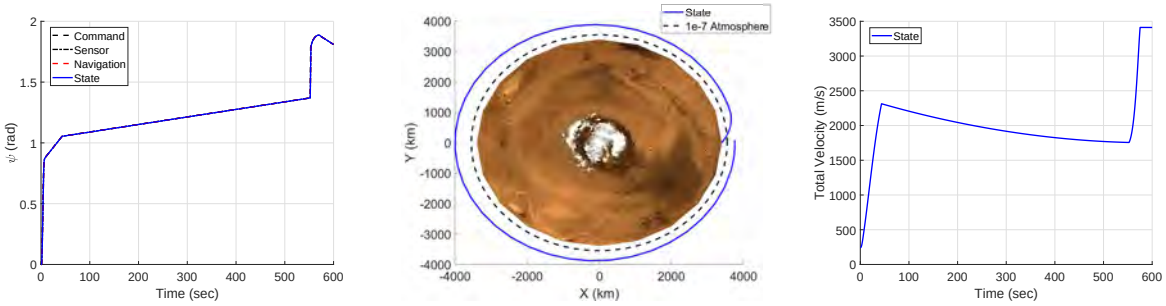

Figure 3: Successful Orbit and Orbital Velocity - No Aerodynamic Forces Present

Unfortunately, with aerodynamic forces present, apogee occurs much sooner than the open loop time computed by OTIS. Figure 4 (lower left) shows the apogee occuring a bit sooner than 552 seconds which is when OTIS computes is the best time for the second stage to fire. Thus, the guidance block can be altered to compute apogee and fire the second stage at apogee rather than waiting for a specific time. The second stage nominally fires at 552 seconds or 508 seconds after MECO. In reality, apogee without aerodynamic

forces occurs around 600 seconds or 558 seconds after MECO. With Aerodynamic forces present, apogee occurs around 510 seconds or 466 after MECO. For ease of comparison between aerodynamic forces on and off, plots of altitude, total velocity, heading angle and orbit are plotted simultaneously for both cases with aerodynamic forces on and off. Figure 4 shows these 4 states. The legend indicates a 0 for no aerodynamic forces and a 1 for the simulation with aerodynamic forces present. In these plots it is clear that the second stage fires at around 510 seconds with aerodynamic forces present but around 600 seconds without these forces. As previously stated, apogee occurs much sooner when aerodynamic forces are present and thus with the adaptive second stage rolled into the guidance module, the spacecraft fires as soon as apogee is detected.

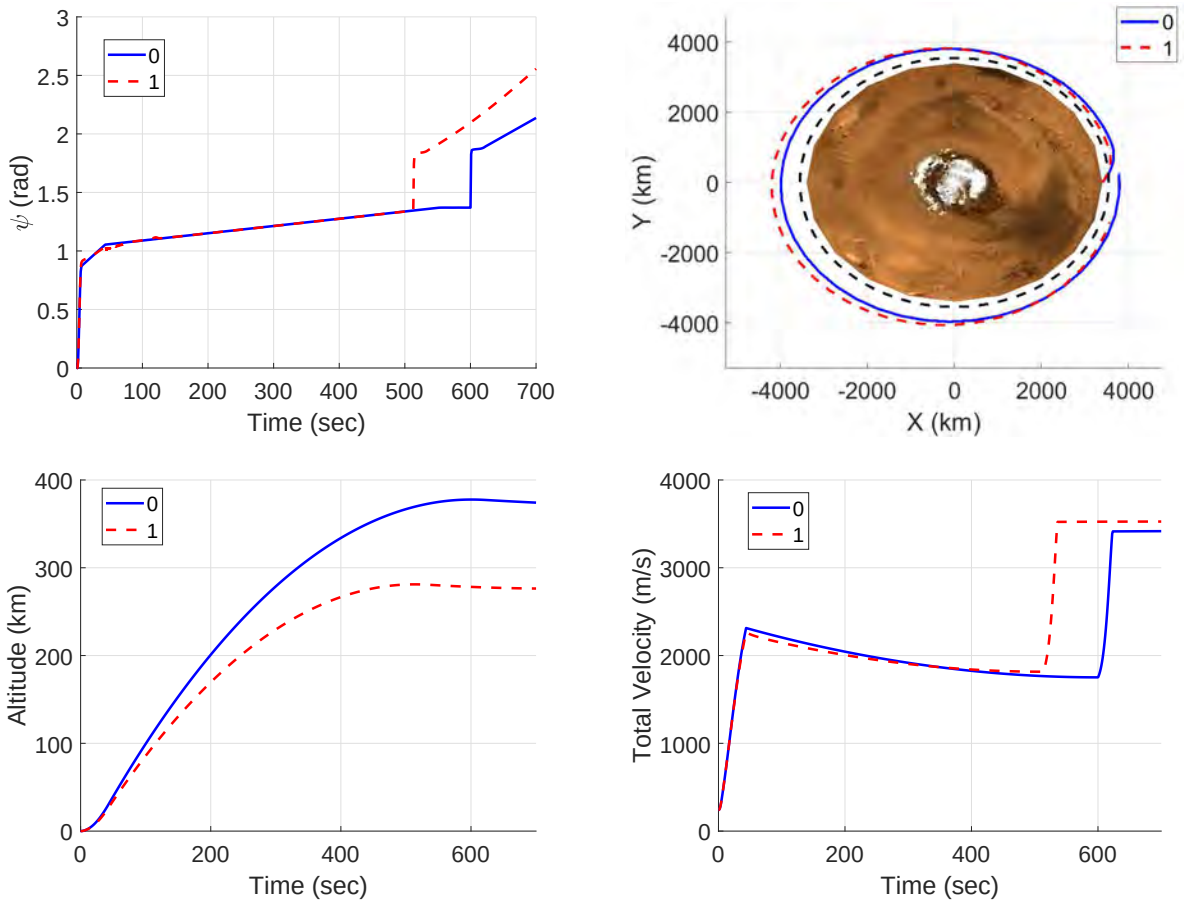

Figure 4: Equatorial Orbit with and without Aerodynamic Forces with Adaptive Second Stage

4 Trade Studies

Numerous trade studies are run from the nominal case. For the sections that follow, one nominal parameter is varied by a constant plus or minus delta Plots similar to Figure 4 are shown with all simulations plotted. Unfortunately, not all trade studies are included for brevity; thus, only a select few are included.

4.1 Stationline Center of Pressure

Stability of the system is largely governed by the static margin of the system which is defined as the stationline center of pressure minus the stationline center of mass. To investigate this issue, the Nominal case is simulated but the center of pressure is varied from by plus or minus 35% which corresponds to about 2.23 meters and 1.08 meters. The 2.23 m case will have a static margin that is always stable while the nominal 1.65 m case will have a static margin that is stable for a portion of the flight and then stable for the remainder of the flight. The 1.08 meter case will have a static margin that is always unstable. When the center of pressure is 2.23 m behind the nose, the static margin is always negative. Due to this fact, the TVC angle is also negative indicating that it is working with the aerodynamics rather than fighting it. When the SL_{CP} is 1.08 m the static margin is always positive and the TVC system is always fighting the system. After 43 seconds, the TVC system shuts down and the RCS takes over. As shown in the Figures below, the RCS is incapable of stabilizing the system and the system tumbles when the static margin is positive. Note that in the nominal case, the static margin conveniently becomes positive right before MECO. This occurs right around 40 seconds as can be seen in Figure 2.

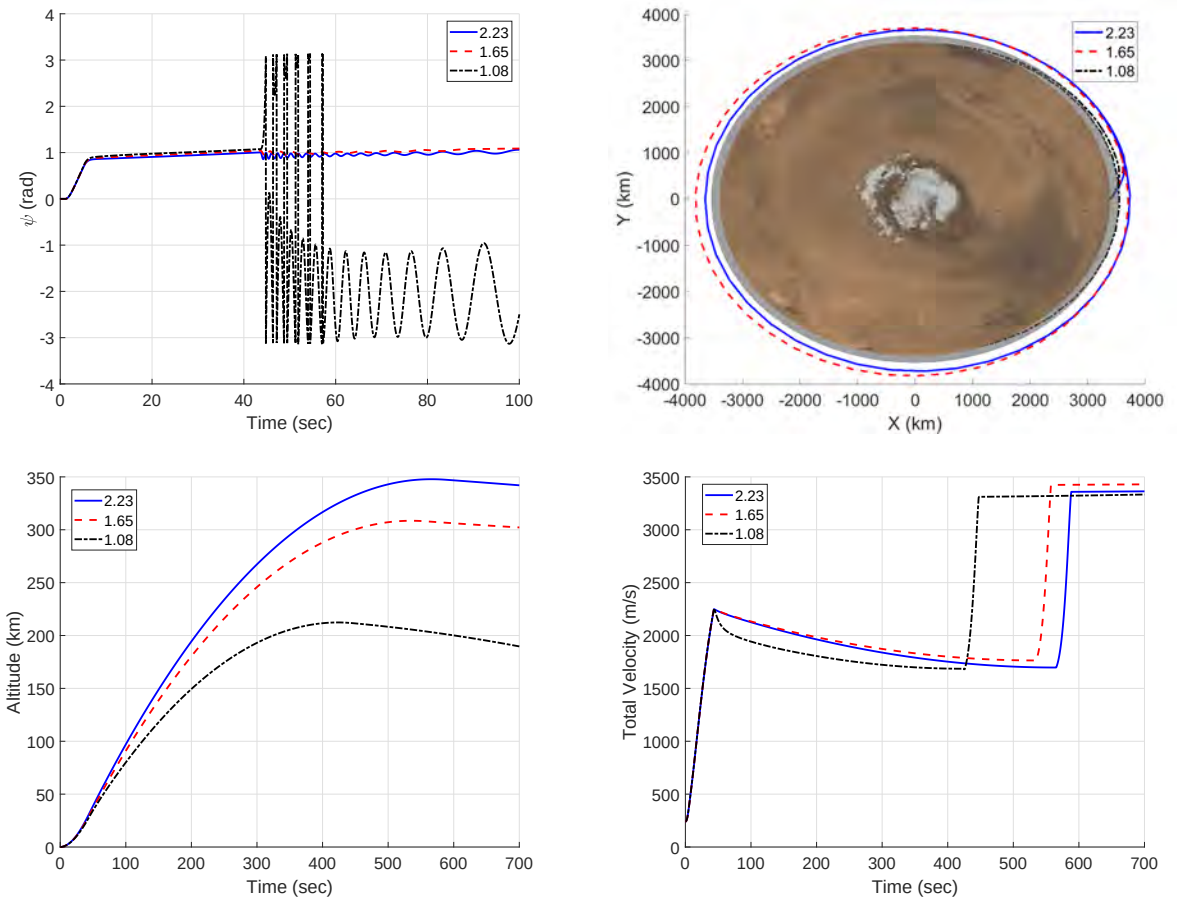

Figure 5: Stationline Center of Pressure Trade Study - Trajectory

Since the spacecraft tumbles right after MECO, the system does not reach a stable orbit. Apogee is reached around 400 seconds and although the second stage fires, the spacecraft is not pointing in the right direction and the orbit collapses into the planet.

4.2 First and Second Stage Thrust Variation

Many people say the phrase that too much of a good thing is a bad thing. The amount of thrust in this case falls into this category. Although more thrust may help get a body into orbit, it can also throw the spacecraft into the wrong orbit with either the wrong eccentricity or the wrong altitude. The simulation below increases and decreases the two main stages by 5% which corresponds to about 800 N of thrust for the first stage. The results for this trade study are shown below. Figure 6 (left) shows the thrust for all three cases. The biggest difference is the change in second stage burn. Clearly with less or more thrust, apogee occurs at a different time and thus the thrust trace is completely different. Figure 6 (right) shows the orbit. When the thrust variation is reduced by 5% the spacecraft fails to reach a stable orbit. On the other hand, with the thrust increased by 5%, a stable orbit is reached but the eccentricity is very high.

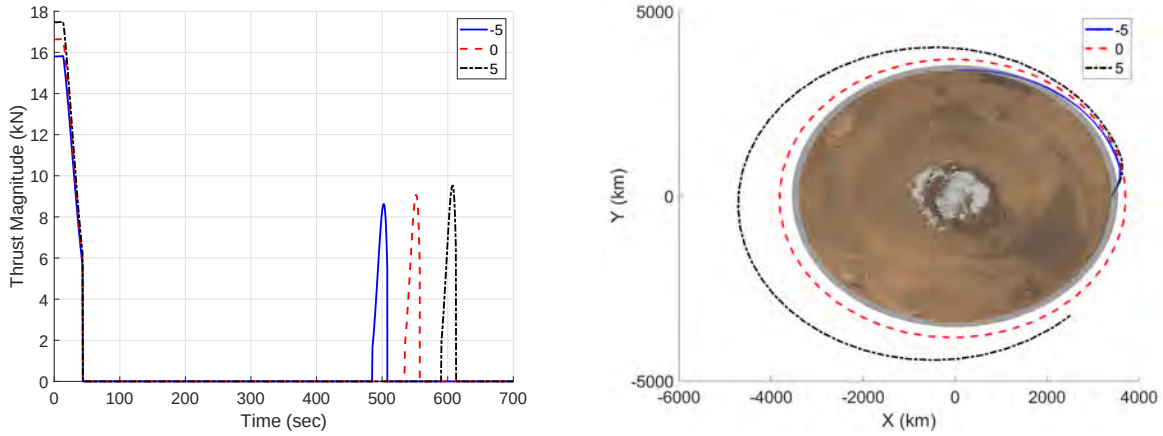

Figure 6: Thrust Variation Trade Study

4.3 TVC Misalignment

It can be shown that the TVC system is robust to perturbations in the pitch and yaw angle. This assumes that the TVC system itself is perfectly aligned with the body frame. If instead, uncertainty is added such that the TVC reference frame is offset by a few degrees from the body frame, the system does not perform very well. Figure 7 shows the result of this trade study. In order to run this trade study, the rotation matrix from the body frame to the thrust reference frame is randomized by a standard deviation from 1 to 3 degrees using a uniform random number generator. Since every simulation would be different, 10 runs are completed for each uncertainty value and Figure 7 is simply plotting the average of the 10 runs. As shown, a standard deviation of 2 degrees is enough to throw the spacecraft completely out of alignment and the orbit fails.

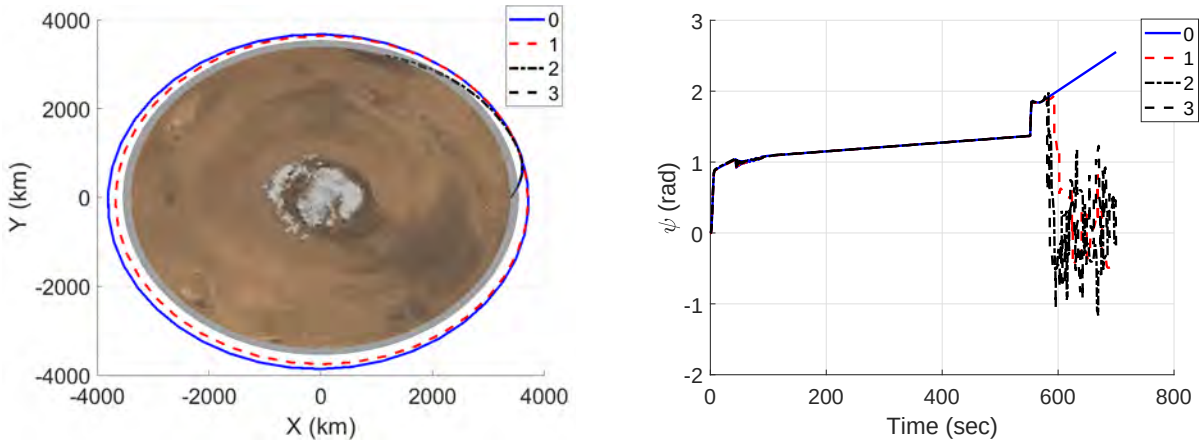

Figure 7: TVC Misalignment Trade Study

The reason for this failure in orbital insertion is due to the rather large thrust to weight ratio. During the initial boost phase, the thrust of the main engine is 16 kN. If the TVC reference frame is off by even 2 degrees, the off normal component of thrust will be around 550 N. For comparison, the aerodynamic force at maximum dynamic pressure is 500 N. Thus, a small deviation in angle with such a large thrust places a very large moment on the system. With out a robust control system to handle this type of uncertainty the entire system fails. This isn't to say that every scenario fails. It's possible that the offset is set up in such a way that the orbit succeeds. However, over 10 runs even 2 degrees is too much for the current system to handle.

4.4 Number of RCS Thrusters

The nominal simulation uses 16 RCS thrusters to control roll, pitch and yaw during the coast phase. Roll control is utilized for the entire duration of the flight while pitch and yaw are only controlled during the coast phase. With 16 thrusters there is alot of redundancy with some room for GLOM savings. The nominal simulation currently utilizes 8 thrusters for roll control, 4 for pitch and 4 for yaw for a total of 16. For a pure couple to be present, 4 thrusters are need per axis for a minimum of 12 thrusters for 3 pure couples. This means that there are 4 extra roll thrusters than needed. If these 4 thrusters used for roll control are removed, the total number of thrusters drops to 12. However, it is possible to further remove 2 thrusters per axis and only have 2 thrusters per axis for a total of 6 thrusters. Doing this would remove the pure couple and instead impart forces on the spacecraft but for simulation purposes this is a simple thing to do and interesting to study. The total mass of RCS system is placed at 9 kg. This corresponds to about 0.56 kg per thruster. If 10 thrusters are removed, the mass savings could be 5.6 kg which is about 1.5% of GLOM. Not very much but as shown previously, the system is highly sensitive to thrust and mass or really acceleration. The results of this simulation are shown in the Figure below.

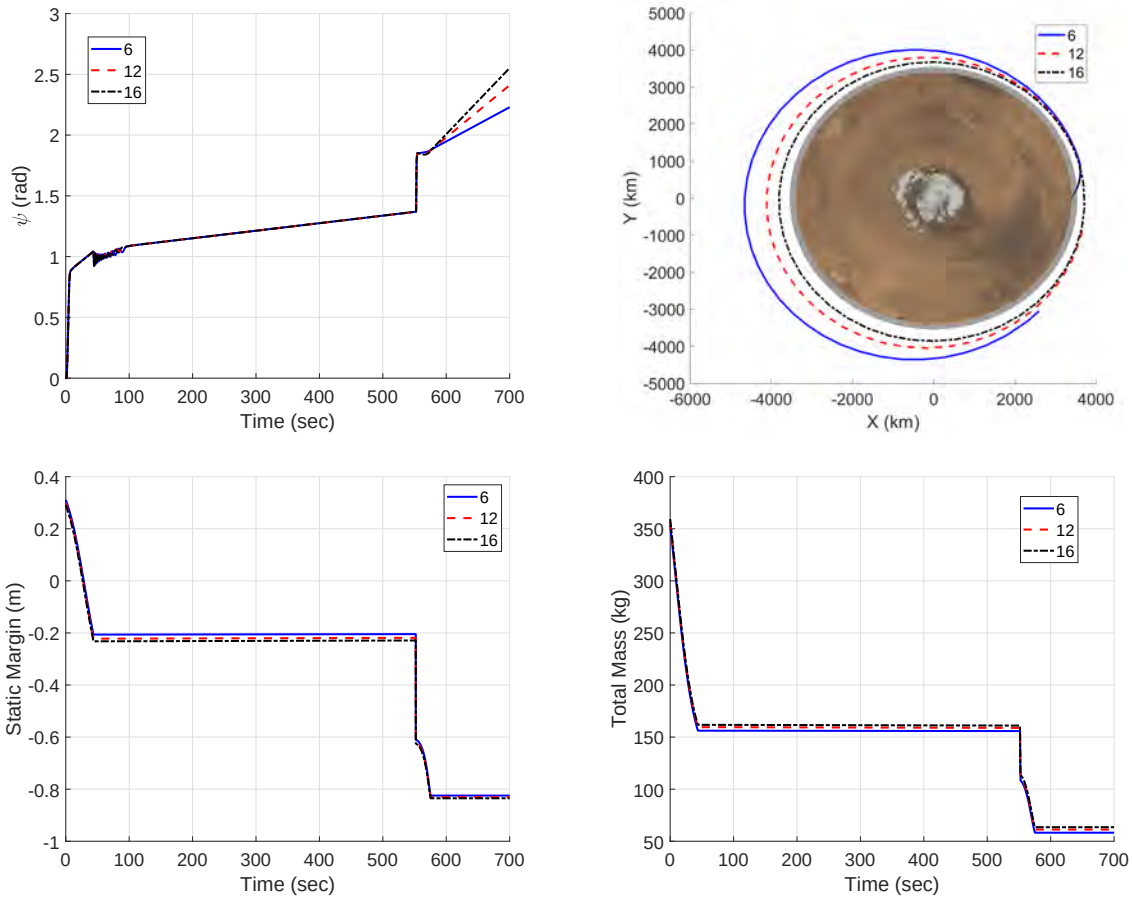

Figure 8: Number of RCS Thrusters Trade Study

Figure 8 (upper right) shows the heading angle which is largely unchanged except for a few perturbations. During the coast phase, the RCS system has no problem controlling the spacecraft in any of the situations simulated. As expected, the static margin becomes a bit more positive as the center of mass shifts backwards due to a loss in mass. It is not by very much however and this system is still controllable. The total mass pictured in Figure 8 (lower right) also shows the small decline in mass. Still, even with this small change in mass, the orbit changes by quite a bit as can be seen in Figure 8 (upper right). Another interesting point to make is the fact that the total amount of propellant expelled during coast is also diminished. In this case, the nominal case (16) has the most mass at the beginning of coast and it expels the most mass. The slope of the line is larger in this case. Thus, with more thrusters comes more mass and more mass means more thrust and more complexity. Note that no work on pointing performance in orbit was done and this must be further investigated before the decision to remove thrusters is conducted.

5 Conclusions

An in depth look at the Mars Ascent Vehicle from a dynamics perspective has been presented here. A primary goal of this work was to determine some trade offs and performance chracteristics of the MAV as well as some sensitivities. The software developed in Simscape is aptly named the MAV Analysis Tool in

Simscape (MAnTiS) which is actually an acronym within an acronym since MAV itself is also an acronym. The simulation contains all standard Control Systems blocks including the Plant (G), Sensors (H) and Control (C). Any graduate of engineering will be familiar with these standard blocks from their system dynamics and controls class. With the goal of trying to create a high fidelity model, the simulation contains as many piece parts as possible including, Gravity, Standard Atmosphere, Aerodynamics, Actuator Dynamics, Thrust and Mass models for the plant. The sensor model includes standard white noise, bias and a delay associated with a rise time of the sensor. The GNC block contains a two stage guidance law with inputs from a state estimation routine that is combined to form error signals to compute TVC and RCS commands. The end result is a visually appealing and easy to use software for trade studies and small monte carlo simulations.

Numerous trade studies have been run to investigate the effect the parameter has on the trajectory and performance of the spacecraft and how sensitive the spacecraft is to that particular parameter. From a bird's eye view, simulations have revealed that the spacecraft, given it's large T/W ratio, is highly sensitive to acceleration and thus thrust, mass and aerodynamics. These are the largest drivers for failed performance. In order to highlight these trade offs, a table has been created showing all trade studies performed and whether or not the trajectory is sensitive or not to this parameter.

Table 1: Trade Study Sensitivity Results

High Sensitivity	Low Sensitivity
Aerodynamics	
Aerodynamic Coefficients	Density Models
Center of Pressure	Atmospheric Winds
Propulsion	
Thrust	Coast Time
TVC Misalignment	
Trajectory Perturbations	
	Take off Angle
	Tip off Moments
RCS	
Number of RCS Thrusters	RCS Thrust
	RCS Misalignment
Sensors	
Angular Velocity Bias	Accelerometer Bias
Angular Velocity Noise	Accelerometer Noise

This analysis is further broken into 5 categories. Aerodynamic forces and moments can alter the trajectory by quite a bit and thus the aerodynamic coefficients and the center of pressure is a large driver for its trajectory. On the other hand, the atmopsheric wind models chosen only impart about 50 m/s of disturbances which is about 2.5% of the total velocity after the second stage. In addition, the two density models (GRC and MarsGRAM) did not differ by very much causing a low sensitivity to these parameters. Propulsion is largely governed by the high T/W ratio. The coast time is not as important as the thrust itself. Even a 5% change in thrust will cause the entire orbit to fail. Ensuring thrust within this tolerance may be difficult. Furthermore, any misalignment creates large side forces from the 16 kN of thrust during the first boost stage. Trajectory perturbations studied here seem to not affect the spacecraft due to it's high controllability. When TVC is active, the system responds robustly to disturbances. This would be different if the disturbance occurred during the coast phase when TVC is deactivated. The RCS system is a potential place for weight savings by reducing the number of thrusters from 16 to 12 or even 6 if a pure couple is not completely

necessary. Redundancy is important though so at least 12 is advised. The important and surprising result is that outside the atmosphere, the spacecraft responds pretty well to any uncertainty in RCS misalignment and thrust. Sensor bias and noise can wreak havoc on the system since double integration is performed but the spacecraft is more sensitive to the angular velocity measurement given that all commands are based on the orientation of the spacecraft. The accelerometer is important for second stage pointing but is not as important as knowing what direction the spacecraft is pointing. It is important to pour over these sensitivities for small programs like this especially in the beginng stages of these projects. If care is taken to choose the most optimal and robust configuration, it is highly likely that the 21st century will see the first ever samples returned from another planet.

References

[1]B. Novakovic. Senenmut: an ancient egyptian astronomer. *Publications of the Astronomical Observatory of Belgrade*, 85:19–23, October 2008.

[2]Liu Ciyuan. Ancient chinese observations of planetary positions and a table of planetary occultations. *Earth, Moon, and Planets*, 40(2):111–117, February 1988.

[3]Charles E Hummel. *The Galileo connection: resolving conflicts between science and the Bible*. InterVarsity Press, 1986. 35-38, ISBN:0-87784-500-X.

[4]J. R. Jokipii and Paul J. Coleman. Cosmic-ray diffusion tensor and its variation observed with mariner 4. *Journal of Geophysical Research*, 73(17):5495–5503, September 1968.

[5]M.Ya. Marov and G.I. Petrov. Investigations of mars from the soviet automatic stations mars 2 and 3. *Icarus*, 19(2):163 – 179, 1973.

[6]S. L. Hess, R. M. Henry, C. B. Leovy, J. A. Ryan, and J. E. Tillman. Meteorological results from the surface of mars: Viking 1 and 2. *Journal of Geophysical Research*, 82(28):4559–4574, September 1977.

[7]Paul R. Mahaffy, Christopher R. Webster, Sushil K. Atreya, Heather Franz, Michael Wong, Pamela G. Conrad, Dan Harpold, John J. Jones, Laurie A. Leshin, Heidi Manning, Tobias Owen, Robert O. Pepin, Steven Squyres, Melissa Trainer, and . Abundance and isotopic composition of gases in the martian atmosphere from the curiosity rover. *Science*, 341(6143):263–266, 2013.

[8]J. R. French, Jr. Mars sample return: mission. In D. B. Reiber, editor, *The NASA Mars Conference*, pages 303–321, 1988.

[9]Carlos Montalvo and Mark Costello. Effect of canard stall on projectile roll and pitch damping. *Proceedings of the Institution of Mechanical Engineers Part G: Journal of Aerospace Engineering*, 225(9):1003–1011, Feb 2011.

[10]NASA. Mars atmosphere model. https://www.grc.nasa.gov/www/K-12/airplane/atmosmrm.html, accessed: 8/6/2018.

Data-driven Quality Assessment of System Architecture Models

Leonard Petnga[a]
University of Alabama in Huntsville, Huntsville, AL, 35899

Abstract

We introduce a semi-automatic Data-driven approach to the Analysis of System Architecture Models (DASAM). This framework is suitable for exploration and quality assessment models developed with the System Modeling Language (SysML) at any stage of development and maturity throughout the system development lifecycle. Types of defects and insights are identified and categorized, then, used to guide and support the assessment process. The latter is supported by the core of the DASAM approach in which architecture model data is extracted and stored in **data models then, used to construct a network model mirroring the pillars of the modeling language. Queries enable the user to probe the model for answers to increasingly complex questions related to various types of defects including incompleteness, incorrectness, inconsistencies or general insights on the model structure and behavior. A prototype implementation of the DASAM approach on the requirement subset of a spacecraft architecture model is under development and preliminary results are promising.**

Nomenclature

CAD = *Computer-Aided Design*
DASAM = *Data-driven approach to the Analysis of System Architecture Models*
MBE = *Model-based Engineering*
MBSE = *Model-based Systems Engineering*
OMG = *Object Management Group*
SIPOC = *Suppliers, Inputs, Process, Outputs, and Customers*
SysML = *System Modeling Language*
UML = *Unified Modeling Language*
UPDM = *Unified Profile for DoDAF/MODAF*
WCC = *Weakly Connected Components*

I. Introduction

Advances in material science, computing, software and artificial intelligence have enabled the emergence of new engineering systems from drones to autonomous vehicles and smartphones. Upgrade of existing systems and their integration with new ones have increased the complexity of modern engineering systems. However, as systems are growing complex so is their development process, especially in a context driven by a push for reduced time to market, lower development and operational costs, higher performance and safety, and increasing demand for social responsibility. Model-based Engineering (MBE) and Model-based Systems Engineering (MBSE) have emerged as a way forward. In these approaches, models - as simplified representations a concept, phenomenon, relationship, structure or system - are integral part of the technical baseline. In the context of MBSE, the latter includes among others, behavioral analysis, system architecture, requirement traceability, performance analysis, simulation, test across throughout the acquisition/system life cycle. MBSE formalizes the application of modeling to support each and all of these activities[1].

[a] Assistant Professor, Industrial and Systems Engineering Department, University of Alabama, Huntsville, AL

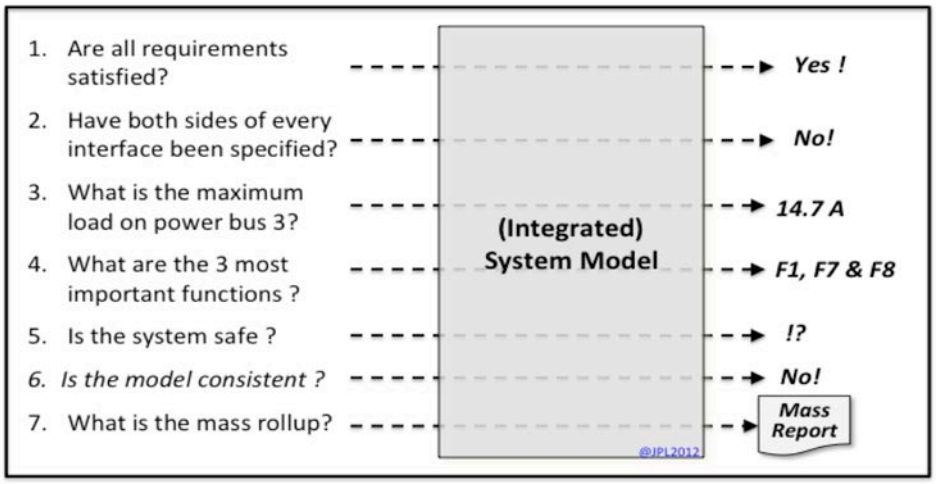

Figure 1. Illustration of the model analysis problem. *In order for a system model to achieve its objectives of, (1) facilitating understanding, (2) aiding in decision making with 'what if' scenarios and, (3) explaining, controlling, and predicting events, models need to be able to answer increasingly complex (engineering) questions.*

At the heart of MBSE is the move of the record of authority from documents to digital models of all types, managed in a data rich environment. Domain specific and general-purpose languages (and tools) have emerged or evolved to enable the systematic development of architecture models (e.g., system modeling language or SysML), physical representation/rendering (e.g., ECAD suite) or mathematical modeling (e.g., Matlab). As organizations have been making such transitions over the last decade, they aim to empower their engineering teams with increasing capability to understand design change impacts, communicate the design intent and analyze a system design before it is built. However, the issue of the quality of (architecture) models remains a matter hindering their usefulness and must be addressed[2,3]. Beside the lack of agreed upon definition of "quality" for MBSE models (and criteria), the size and complexity of the model (and modeling language) as well as the complexity of the domain knowledge contribute to making the task of checking model defects (completeness, correctness and consistency) an uphill undertake as the design project progresses through its lifecycle.

Both academia and industry have recognized the need to automate the process, at least partially, via the development of commercial and prototype software platforms[4,5]. Although these approaches produce encouraging results, they appear limited in scope, especially when it comes to untangling the complexity of the model as well as enabling its exploration and gaining insight beyond the identification of predefined defects or defect types. For architecture models to significantly contribute to closing the gap between modeler's intend and user's perceived meaning, there is a need to enable them to answer increasingly complex questions for review (see Figure 1) - before and after submission - and integration across multiple domains. Thus, we aim to develop solutions that enable a system analyst a full circle view and understanding of the architecture model under development across layer of abstractions and domains and enable its assessment beyond defect checks to provide insights into uncovering hidden patterns and relationships.

Our main contributions are twofold. First, measurable model quality assessment parameters (beyond defects count) are identified, defined and categorized with examples in the context of system architecting. Second, a systematic, semi-automatic procedure for assessing architecture models through above defined parameters is introduced and described. Even though the scope of this work is focused on assessing architecture models produced in SysML, the methodology can be applied to models created with the Unified Modeling Language (UML) and Unified Profile for DoDAF/MODAF (UPDM) as well. A (partial) SysML model of a spacecraft is used to illustrate our approach.

II. Background and literature review

This section gives a brief background information and insight in two core areas supporting the research described in this work: system architecting with SysML and quality assessment of models developed with that language.

A. System Architecting with the System Modeling Language (SysML)

SysML is a general purpose system modeling language developed and maintained by the Object Management Group (OMG)[6]. It's currently the leading language for system architecting. SysML is based on UML from which it borrows a subset of version 2.0 (UML4SysML) and defines its owns extensions[7]. SysML modeling paradigm revolves around reusable blocks (instead of classes in UML) that can represent people, product, processes, data or systems including software, hardware using nine (09) diagrams organized in four connected pillars as shown in

Figure 2. SysML reuses UML2 Sequence, State Machine, Use Case and Package Diagrams. Block Definition, Internal Block and Activity Diagrams are modified to properly capture complexity in system composition (structure) of and action/execution (behavior). Finally, Requirement and Parametric diagrams are specific extensions allowing the modeling of system requirements and (physical) constraints. The diagrams provide different views (and knowledge) of the system model stored in a single repository. However, not all model entities and connections would appear in diagram views. Thus, assessing the quality of the model will require understanding and untangling the web of connections encoded in the model itself.

B. Quality of SysML models

SysML is increasingly used at all stages of system development – form early concept of operation[8] to maintenance operations late in the system lifecycle [9]. However, a look into the manner in which it is used from project to project or from one system engineer to another within the same project (and even same task) shows a wide difference in the outputs. In the absence of standardized or agreed upon quality assessment criteria and metrics it becomes almost impossible to assess the quality of SysML models specially at reviews along the system/program development lifecycle. Quality assurance for UML models has gained most of researchers' attention thanks to the wide use of UML as de facto standard for modeling software systems since the mid 90's[10]. The bulk of researchers' effort has been on identifying and resolving defects in software models. Thus, methods for inconsistency detection (and resolution) have been investigated, including the representation of models as sequences of primitive construction operations[11] or through graph transformation rules[4]. Some researchers have proposed to build on these foundations and exploit similarities between UML and SysML to expand the scope of work to include completeness and correctness and apply the techniques to SysML models as well [2,3]. Early industry effort has led to software tools for model completeness and inconsistency review that have now fanned out[5]. Defects diagnostic and resolution is still not a standard feature in most current MBSE tools[12]. Most provide little to no assistance with defect checking and or help understanding the model in its complexity[13].

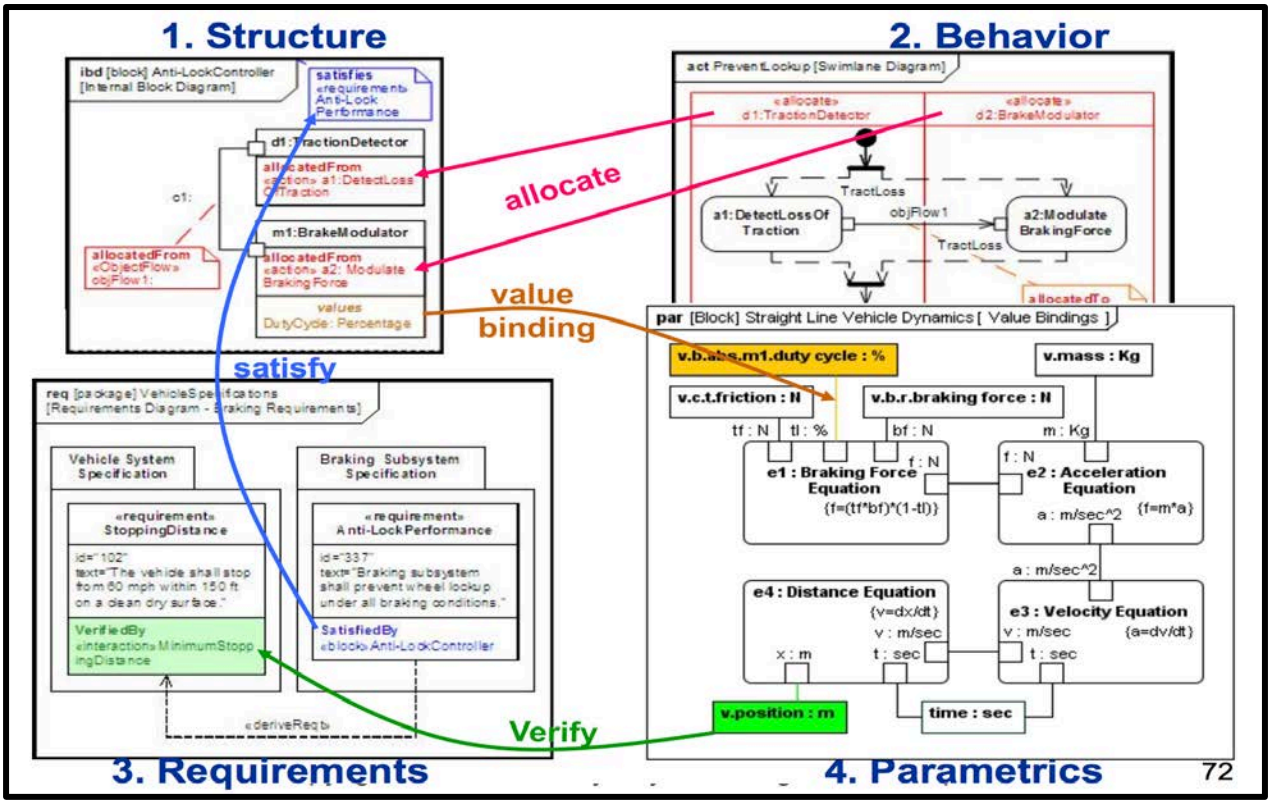

Figure 2. The Four pillars of SysML and sample connections. *Cross-cutting connections between model elements link the pillars together and help convey the intended meaning of the model as a whole.*

III. Understanding and Gaining Insight from SysML Models

Finding and resolving defects in the model earlier in the design process is cot only critical in ensuring the gap between the model intend and actual meaning is insignificant, but also in keeping the development cost and timeline in check. It's estimated that the cost of fixing model defects grows exponentially with its lifetime[10]. Thus the sooner defects are discovered and resolved, the better and smoother the development process will be. Also, inconsistencies can be induced by untracked or unanalyzed changes in the model, especially in requirements[14]. Thus, gaining insight on propagation of changes throughout the model as well as the relevant importance of model elements (and requirements) in the model are very important to improve both the communication capability of models but also their quality.

We identify and organize potential defects and insights in several groups as shown in Table 1. Categories and types of defects and insights are introduced along with illustrative examples in the context of system architecting. Incorrectness is added to the traditional two types of defects, independently from inconsistency. This is done to highlight the critical importance of capturing and representing system domains with respect to the related rules. For instance, let's consider example (1) for incorrectness: if both the "Chassis" and the "Electric subsystem" are represented as blocks, with a "composition" relationship, this will be consistent with SysML semantic and syntax but inconsistent with the vehicle domain knowledge thus, incorrect to that regard.

Direct queries into the model can allow the analyst to get answer to simple questions such as #3 and #7 in Figure 1. Advanced queries might be needed for questions # 1and #2. Gaining deeper insight requires the ability to probe the model for more difficult questions (e.g., #4). Thus, the model as a whole or a specific subset should be considered. Thus, we define three graph-based types of insights to that aim. Centrality measures help determine the relative importance and role of model elements in the network of connections they form with others. Community-based insights evaluate how a group of model elements is clustered or partitioned, as well as its tendency to strengthen or break apart. Path finding insights help find the shortest path (e.g., for traceability) or evaluate the availability and quality of connections (routes) between model elements.

Category	Type	Example (observation/query)
Defects	Incompleteness	(1)Missing "satisfied" or/and "verified" relationship for a given requirement ; (2) Elements of different types (e.g., Requirement and Diagram) assigned the same name.
	Inconsistency	(1) Two different requirements (by Ids) with the same name ; (2) A "Verify" relationship between two structural elements; (3) Undefined type for an operation's parameter
	Incorrectness	In a vehicle architecture model, (1) a chassis is modeled as a component of the electric subsystem and, (2) the "steer vehicle" function is allocated to the headlight component.
Insight	Query	List the requirements that are currently "satisfied" and count the number of model elements that contribute to that aim
	Centrality	(1) Estimate the relative importance of distinct components in the system model through the number and quality of connections to it; (2) Find the requirements on the containement path whose change or modification will impact the others the most.
	Community	(1) Find the clusters of heterogeneous model elements that are tightly connected; (2) Identify the community of connected model elements that help satisfy most requirements
	Path Finding	(1) Find the minimum (maximum) spanning tree of the requirement graph; (2) Determine the traceability path (across components of different types) between a requirement and a given model element

Table 1. Simplified categorization and illustration of potential defects and insights for SysML Model analysis. *Two quality assessment categories are defined with respectively three and four types of defects and insights. Examples illustrate scenarios and situation of occurrence involving system architecture models.*

IV. Data-driven Analysis of SysML-based Architecture Models

A. Overview of the Approach

We leverage graph theoretical foundations and the power of software engineering to develop a Data-driven approach to the Analysis of System Architecture Models (DASAM). It's a step-by-step procedure to analyze architecture models through a series of transformations and queries on model data and graph with the main objective of uncovering defects and insights identified in Table 1. The architecture of the DASAM is pictured in Figure 3. It follows a suppliers, inputs, process, outputs, and customers (SIPOC) system in which references (e.g., from standards, customer needs or the organization) constraint the process. Questions from users, reviewers or stakeholders are inputs that are applied to a graph model to answer the questions via query and interpretation of results as outputs. The graph model itself results from the process of extraction, processing and organizing the architecture model of interest data as per the specification of the architecture language and needs of the a given analysis. Verification and validation loops are used to ensure the quality (completeness, consistency and correctness) of each transformation.

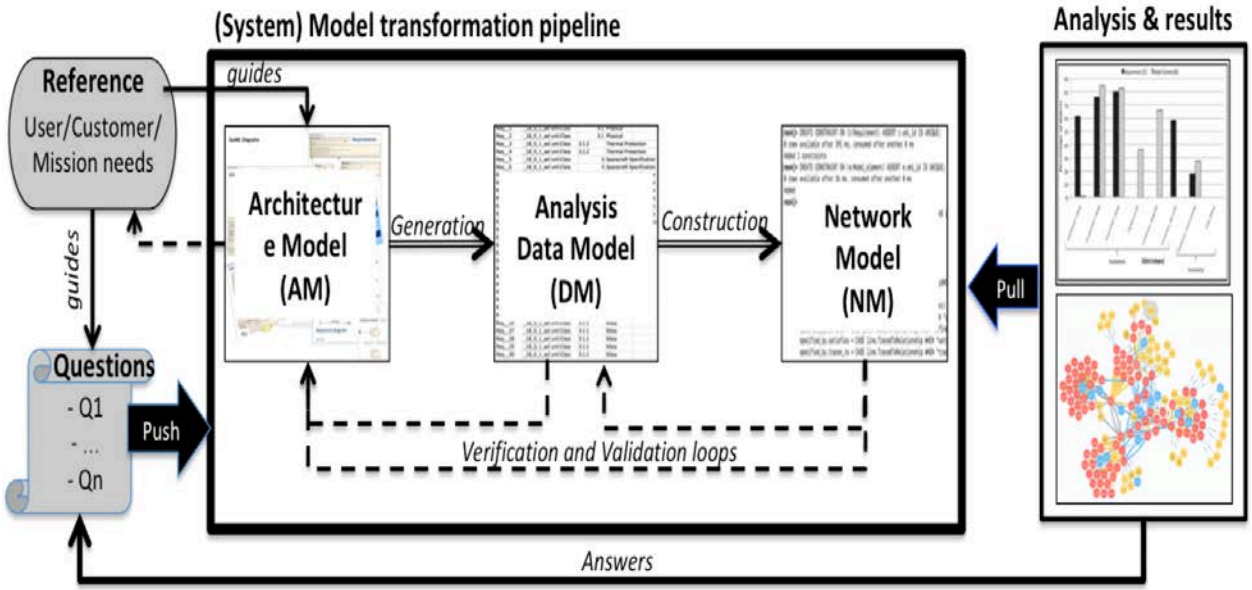

Figure 3. Overview of the Data-driven approach to the Analysis of System Architecture Models (DASAM). *The three nodes graph-like architecture features a series of transformations of the initial architecture model to expose underlining structures and connections needed to answer stakeholder, user or reviewer' questions.*

B. Problem analysis and Inputs/Outputs

The multiplicity and diversity of stakeholders, viewpoints and concerns throughout the MBSE-driven development lifecycle makes the range, number and complexity of questions to be answered by the system models extremely large. This generally requires system architecture model to integrate with a variety of specialty models including software, mechanical, CAD or even Program/project management models. Thus, an analysis of the problem at hand is required to sort out those of the questions to be answered by architecture models. This also ensures that the scope of the analysis is properly defined, especially given the evolving nature of the model throughout the development lifecycle. However, the list of questions has to be anchored to the purpose of the model, which is encapsulated in a heterogeneous set of references made of standards, customer needs and practices. Analyses are conducted and the results provide answers to specific questions accordingly, which closes the loop back to the input of the process. The format (tables, graphs, etc.) of the outputs is dependent on the analyst needs and capability of the supporting implementation platform.

C. Analysis Data Model (DM)

The analysis data model is generated from the architecture model of the system of interest. In order to ensure (and check for) consistency and correctness of the extracted data with respect to the input model being studied, we espouse and maintain the data representation structure of the modeling language of the model i.e., SysML in this

case. Therefore, records of model content for each of the main pillars (and necessary content) identified in Figure 2 will be needed for a full capture of relevant system and model information. The scope, type and level of data to be collected will depend on the goal of the analysis. For instance, if the set of questions to answer would require a 360^0 view of the requirements, then the main information on each and single requirement (i.e., id, name, text) will need to appear for each requirement record. Also, the identity and name of diagrams in which the requirement is shown as well as associated model elements unique id and name must be extracted from the architecture model for each record. The records must be cleaned of invalid entries to ensure the validity of results. This exercise effectively ensures that the data needed for processing and analysis, with respect to the questions at hand, is available.

D. Network Model (NM)

Data in the DM is partitioned and organized according to specific viewpoints as per the four pillars identified above. This structure is certainly not set in stone but as indicated previously, it allows for effectiveness in the data extraction process. However, the ability of the model to answer increasingly complex questions resides in the type and quality of connections among its elements. Thus, we need to create a network model capturing those connections relevant to the analysis as well as retrieved model data. Property graphs provide a suitable formalism to support such task as they perfectly espouse object models with entity relationship diagram paradigm of SysML. Figure 4 presents a simplified network model for the analysis of system model requirements. The "Requirement" node encapsulates the problem domain and is central to the network while the "ModelElement" node captures the solution domain. "Diagrams" are treated as a separate node to enable a 360^0 view of requirements and "ReqRecord" node enables traceability and consistency with the analysis data model. Node attributes are used to store collected data from the DM and Relationships provide directed, named, semantically relevant connections between two node-entities including self. One should note that Relationships between requirements and requirements and model element are consistent with SysML semantics. We also note that relationships can have properties of their own and labels can be added to nodes to represent their different roles in the system or modeling domain. With this infrastructure in place and the data loaded fed into the network model, answer to questions is obtained by queries and algorithmic operations on the graph.

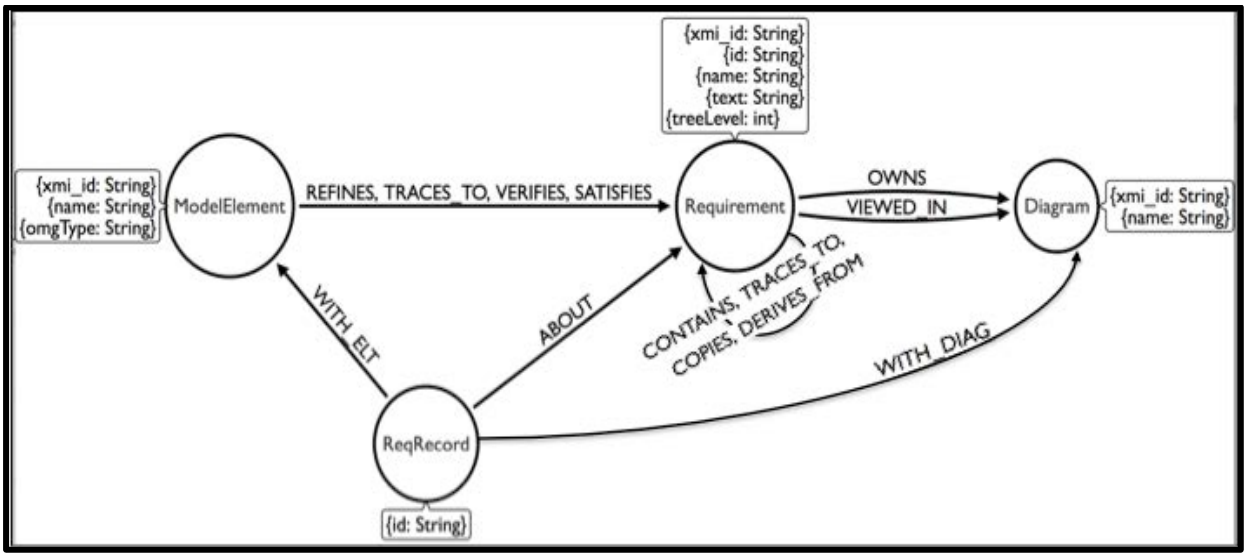

Figure 4. Simplified Data Network Model (with node attributes) for analysis of SysML requirements. *This metagraph is a map of metadata on model data for the viewpoint of interest and their relationships, properties, and more.*

V. Prototype implementation and Preliminary Results

A. Analysis of a Spacecraft Model Requirements

We illustrate the core concepts of the DASAM framework introduced in this paper in a simplified problem of analyzing requirements in a spacecraft architecture model. The model has been created with NoMagic's Cameo System Modeler (CSM) tool to support an introductory MBSE approach and illustrate how to model a system using SysML[15]. This is a work in progress thus, our focus is on uncovering and counting the classes of defects defined in

section III in requirements and, gaining some insights in (a subset of) the model. Thus, we first explore the model in CSM and trim it down to its core i.e., the Spacecraft Mission Context. It's organized into three layers of abstraction from the mission to subsystems, each covering multiple dimensions of the design, form requirement to verification and testing through behavior and structure. A software code is written to parse, extract and store the requirement data (id, name, text, associated diagrams, model element, relationships, etc.) into a predefined data model. The result is inspected for missed or improperly extracted data in records along with associations and consistency with the views in the original model (for diagrams especially). A graph database implementing the network model in Figure 4 is created and the data is sucked into it. Incomplete requirement records and undefined relationships are kept out of the database to prevent incompleteness and inconsistencies in queries. Questions are translated into queries that are applied directly to the database and results are interpreted accordingly. We summarize our finding as follows.

B. Preliminary Results

General statistics. Table 2 shows some global (a) and local (b) statistics obtained from the network model graph. With 593 nodes, the graph is of average size. In reality, it's smaller considering the fact that 60 of those nodes are completely disconnected from the rest. The diameter, i.e., the longest shortest path of the graph is 6, linking 7 nodes

Count/value					
Nodes	Relationships	WCC*	Triangles	ACC**	Diameter
593	379	436	219	0.0863	6

*WCC = weakly connected components

**ACC = Average clustering coefficient

(a)

	Degree			
	Average	Std_dev.	Max.	Mini.
Graph(all)	1.28	3.46	26	0
Requirements	4.06	4.37	26	0
Model_elements	0.70	0.60	2	0
Diagrams	12.88	8.24	24	1
Req. - CONTAINS ->	1.36	2.41	20	0
Model_elt. - SATISFIES ->	0.15	0.36	1	0

(b)

Table 2. Graph statistics: (a) Global statistics on the requirement submodel graph and, (b) Local statistics on the main requirement subgraph and various components. *Nodes count includes requirements nodes (not connected to the graph) while nodes degree characterize the connectivity of a node in the subgraph under consideration.*

(all are requirements) between the "Functional and Performance" requirement and the "Mission Availability" requirement. Links between nodes include "Contains" and "Derived_from" relationships.

Local statistics (Table 2. (b)) Show that the average degree, i.e., the number of *in* and *out* edges (relationships) of nodes is the highest for Diagrams, consistent with the nature of the relationship ("viewed_in") linking the diagrams and requirements in Figure 4. With an average of 0.70 and a maximum of 2 degrees, Model elements are not that connected to rest of the graph. This trickles down to the "Satisfies" relationship, which shows an average of 0.15 degree and a maximum of only 1 degree of connectivity. Requirements on the other hand have an average of 4.06 degree of connectivity and they drive the degree of the graph maximum degree at 26. Containment relationships are the ones powering the requirement node degree with an average of 1.36 and a maximum of 20 "Contains" relationships.

Defects. Figure 5 shows a summary of percentage of inconsistency and incompleteness defects types as introduced in Table 1. From the plot, it clearly appears that the submodel considered is incomplete. Unlike Model elements, up to 60% of the 91 requirements in the model are undefined i.e., they lack either a name of a full textual description. Even higher percentages of requirements are either unsatisfied (75%) or unverified (80%). Conversely, 85% (82%) of the 80 model elements do not satisfy (verify) any requirement. This can be explained by the fact that model elements may comprise entities (e.g., action, state, blocks) that are not directly linked to requirements. Checking the model for inconsistency yielded no loop but, an almost 20% (30%) rate of duplicated names for requirements (model elements) in the model.

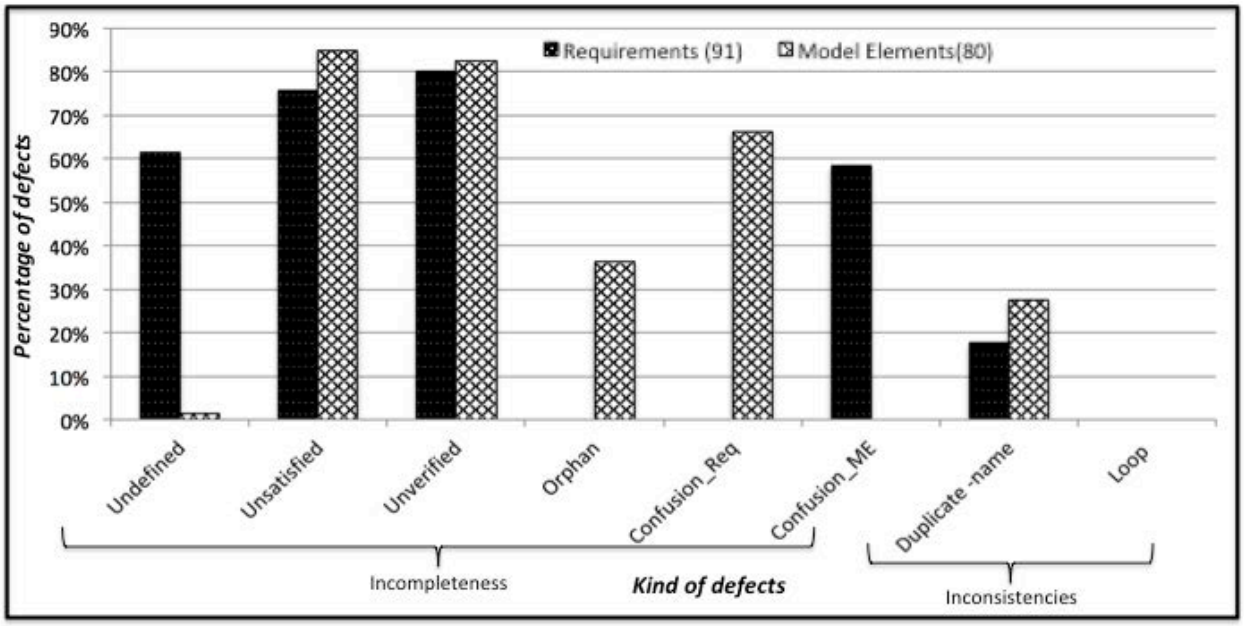

Figure 5. Percentage of selected defects in the reduced Spacecraft SysML Model (requirements). *The model is clearly incomplete with few inconsistencies. Incomplete definition of requirements is pervasive and the proportions of orphan and confusing model elements definition are high and need to be addressed.*

Insight: community. A preliminary look at communities in our model has uncovered 219 triangles and 436 weakly connected components (as nodes in the graph) as shown in Table 2 (a). The relatively high gap between the number of WCCs, i.e., the sets of connected nodes where each node is reachable from any other node in the same set and the total number of nodes can be explained by the presence of both unconnected nodes inside the model but also unconnected Requirement record nodes created to support our analysis. More than a third (37%) of the nodes in the graph are connected as triangles, mostly involving requirements and diagrams. This highlights the role views play as main vehicle of conveying the message about requirements in this submodel. A modularity-based search of communities in the graph as a whole yielded 5 clusters with between 5 and 75 nodes and averaging 32 nodes in size. Surprisingly, the largest cluster is 'led' by node 4 "Thermal Protection", a level 3 requirement! The explanation of this result is not obvious from the graph view of this node and its immediate vicinity. Further investigation is required to better understand the selection process of the community "leader".

VI. Conclusion and Future Work

In this work, we have introduced DASAM, a Data-driven approach to the Analysis of System Architecture Models (DASAM). The framework describes a step-by-step procedure to analyze architecture models through a series of transformations and queries on model data and graph with the main objective of uncovering defects in the context of quality assessment of the model and gaining insight in the model inner structure and behavior. A prototype implementation of the process has demonstrated the capabilities of the approach on a 360^0 exploration and assessment of requirements in a spacecraft architecture model. The results are promising. However, more work is needed to enable the framework to scale up to multiple, interrelated and complex pillars of the architecture languages such as the SysML and full automation of this novel approach. Exploration of Machine Learning techniques and architecture-specific graph algorithms are needed to support and enable these goals.

Acknowledgments

The author is grateful to the NASA MSFC Summer 2018 Faculty Fellowship program for supporting this research. The author acknowledges and thanks Mr. Joseph Hale, MSFC-EE11 - Systems Engineering Office, who was the project collaborator on this fellowship.

References

[1]International Council on Systems Engineering (INCOSE), "INCOSE SE Vision 2020", *INCOSE-TP-2004-004-02*, September 2007

[2]Hause M., " "Are we there yet?" Assessing Quality in Model Based Systems Engineering", *INCOSE International Symposium*, pp. 510-522, Denver, CO, 2011

[3]Hummell J. and Hause M., "Assessing Quality in Model Based Systems Engineering", *23rd Systems and Software Technology Conference (SSTC)*, Salt Lake City, UT, 2011

[4]Mens T., Van Der Straeten R., and D'Hondt M., "Detecting and Resolving Model Inconsistencies Using Transformation Dependency Analysis", *International Conference on Model Driven Engineering Languages and Systems MODELS 2006: Model Driven Engineering Languages and Systems* , pp 200-214

[5]McConnel T., "SOFTWARE TOOLS - Artisan Studio Reviewer for UML, SysML, UPDM released", *EE Times*, 10/15/2009, Available at : https://www.eetimes.com/document.asp?doc_id=1201288, Retrieved 07/14/2018

[6]Object Management Group (OMG), "What is SysML?", *SysML official webpage*, Available at : http://www.omgsysml.org/, Accessed 07/18/2018

[7]Finance G., "SysML Modeling Language explained", *Object Direct*, 10/07/2018, Available at : http://www.omgsysml.org/SysML_Modelling_Language_explained-finance.pdf, Retrieved 07/14/2018

[8]Gans H. D., "Development of a Space Vehicle CONOPS Using SysML and the Unified Profile for DoDAF and MoDAF(UPDM)", *AIAA SPACE and Astronautics Forum and Exposition*, September 12, 2017

[9]Durugbo C., Hutabarat W., Tiwari A. and, Alcock J. R., "SysML for the analysis of Product-Service System Requirements", *CIRP ISP2 conference*, 2010

[10]Chaudron M., "Quality Assurance in Model-Based Software Development: Challenges and Opportunities", *Lecture Notes in Business Information Processing*, January 2012

[11]Blanc X., Mougenot A., Mounier I., and Mens T., "Incremental Detection of Model Inconsistencies based on Model Operations", *International Conference on Advanced Information Systems Engineering (CAiSE): Advanced Information Systems Engineering*, pp 32-46, 2009

[12]Vitech Corporation, "Auto-Checking with Model Diagnostics", *CORE Online Help*, Available at www.vitechcorp.com, Accessed 07/15/18

[13]International Business Machine (IBM), "PM28132: Inconsistent behavior with respect to custom checks", *IBM Suppor*t, 10/12/03, Available at www.-01.ibm.com, Accessed 07/15/18

[14]Ten Hove D., Goknil A., Kurtev I., Van den Berg K. and, De Goed K., "Change Impact Analysis for SysML Requirements Models based on Semantics of Trace Relations", *Fifth ECMDA Traceability Work-shop (ECMDA-TW 2009)*, Enschede, the Netherlands, pp. 17–28, 2009

[15]Friedenthal S. and Oster C., "Architecting Spacecraft with SysML: a Model-Based System Engineering Approach", *Friedenthal & Oster*, 2017

Understanding Residual Strain in Friction-Stir Welds Using EBSD

J. Rivers
Delgado Community College, New Orleans, Louisiana 70119

G.Jerman[1]
Marshall Space Flight Center, Huntsville, Alabama

Dr. S. Gorti[2]
Marshall Space Flight Center, Huntsville, Alabama

The Space Launch System's fuel tank provides NASA with several design challenges. In order to meet the complex geometric welding requirements, NASA has implemented self-reacting friction stir welding (SRFSW) and switched from Aluminum Alloy 2195 (AA 2195) to Aluminum Alloy 2219. AA 2219 has experienced some low properties in some SRFSW joints. This paper reports the results of studying residual strain and grain structure of samples taken from weld regions with both high and low tensile properties using electron back scatter diffraction microscopy. Grain average misorientation was calculated and compared to ultimate tensile strength, yield strength and elongation of test panels at failure.

[1] Assistant Branch Chief, Materials Science and Metallurgy Branch EM31
[2] Team Lead, Materials and Failure Analysis Team EM31

Protocol Development and Data Visualization for Wireless Sensor Networks

Md A. Salam[1]
Southern University, Baton Rouge, Louisiana, 70813

And

Kosta Varnavas[2]
NASA Marshall Space Flight Center, Huntsville, Alabama, 35812

Abstract

Prolonging network lifetime is one of the challenging issues of Wireless Sensor Networks (WSN). Many techniques have been proposed to achieve a longer battery life of the sensor nodes. In this report, we focus on the routing technique to improve the battery life to extend the network lifetime and data visualization for the sensor networks. Our protocol is based upon the two existing protocols, namely, LEACH (Low-Energy Adaptive Clustering Hierarchy) and PEGASIS (Power Efficient Gathering in Sensor Information Systems). By extracting the fundamental working principles of these two routing techniques, we propose a new protocol, which provides increase network lifetime compared to these existing basic protocols. The sensor networks data visualization is simulated using Python programming to visualize the deployed environment.

Nomenclature

WSN = Wireless Sensor Network
LEACH = Low Energy Adaptive Clustering Hierarchy
PEGASIS = Power Efficient Gathering in Sensor Information Systems
BS = Base Station
CH = Cluster Head
MN = Member Nodes
TDMA = Time Division Multiple Access
RF = Radio Frequency
NASA = National Aeronautics and Space Administration
MSFC = Marshall Space Flight Center
EEPROM = Electrically Erasable Programmable Read-Only Memory

I. Introduction

This report integrates the protocol development and data visualization techniques for wireless sensor networks. Applications of wireless sensor networks are expanding tremendously. Wireless sensors are deployed in many places, such as security and surveillance, environmental monitoring, industries, precision agriculture, disaster response, automotive vehicular, health (body area network), underwater sensor networks, space crafts, and many more [1], [2]. Moreover, wireless sensor technology will reduce the cost and weight of the space craft [3].These sensor nodes collect useful information from the field. This information could range from audio data, seismic data, and video. These sensor nodes collaborate to perform high level of task in the deployed environment. Wireless sensor networks may be composed of hundreds or thousands of tiny sensor nodes depending upon the nature of the application and size of the networks. Each sensor node has a sensor and each sensor has the sensing, computing, and communicating capability [4]. These sensor nodes have the capability of communicating among themselves and the base station directly. These sensor nodes are powered by batteries and have limited energy source. It is very important that we keep the battery alive as long as possible to enhance the network lifetime. Many network protocols have been developed to increase the network lifetime [5]. The network lifetime has a high impact on the degree of performance and energy efficiency of the network [6]. It is necessary to design communication

[1] Professor, Department of Computer Science, Southern University
[2] Space Systems Department, Electronic Design Branch/ES36

protocols that will maximize node's lifetime [7], minimize bandwidth utilization by collaborating among the neighboring nodes, and tolerate nodes failure [8].

In this paper, we have considered two fundamental protocols, namely, LEACH and PEGASIS, which are the basic building blocks for our proposed algorithm. In the following sections, we will give a brief description of these two protocols, our proposed protocol and data visualization for wireless sensor networks.

II. Basic Protocols

A. LEACH Protocol

Low Energy Adaptive Clustering Hierarchy (LEACH) protocol was developed at the MIT Lab by Heinzelman and et al. [9]. Since the publication of LEACH, there have been many attempts by many researchers to enhance it and make it better including the developers of LEACH protocol itself who later on published another version of it called LEACH-C (Centralized). There are different versions of LEACH protocol available, such as energy-LEACH and multihop-LEACH [10]. Energy-LEACH improves the cluster head selection method whereas multihop-LEACH improves the communication mechanism between cluster heads and the base station. In [11], Tong and Tang have proposed another improved version of LEACH protocol, called LEACH-B (Balanced). In their protocol, at each round they have introduced two cluster heads concepts. The first cluster head is selected based on LEACH protocol and the second cluster head is chosen based on the node's residual energy. This way they have improved the network lifetime compared to LEACH protocol.

Now, lets us give a brief description of the basic LEACH protocol. LEACH is an adaptive self-organizing clustering hierarchy based protocol. It has two phases of operation, namely, setup and data transmission. In the setup phase of LEACH, sensor nodes are divided into an optimal number of clusters and the member nodes (MN) of each cluster elect their own cluster head (CH) based upon sensor node's energy level in a random fashion. After the cluster setup phase is over, the CH forms a TDMA (Time Division Multiple Access) protocol to communicate among the member nodes of that cluster. Figure 1 shows about 27 sensor nodes with five clusters. The dark circle represents cluster head (CH) and white circles represent member nodes (MN) of a cluster. The CH in a particular cluster rotates among the member nodes of that cluster after a certain round of data transmission. The CH performs data aggregation before it transmits to the base station (BS) to minimize energy dissipation and maximize network lifetime. Transmission of more data will require more energy consumption. After a round is over, the cluster is reformed among the remaining alive sensor nodes in a similar manner and the process continues until all the nodes in the network die.

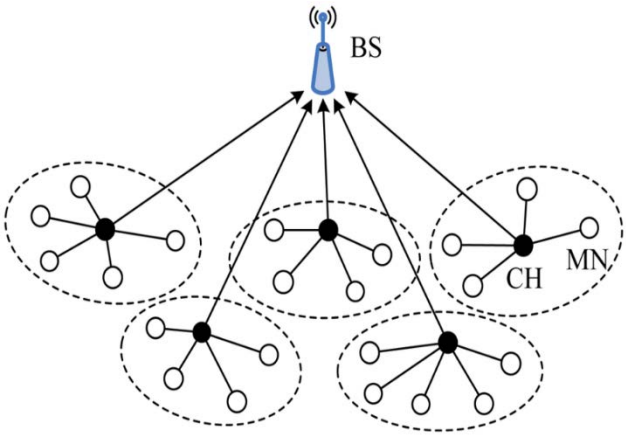

Figure 1. LEACH protocol architecture [12].

LEACH protocol outperforms direct communication protocol significantly. In direct protocol, nodes transmit data directly to the base station. Therefore, nodes farther from the base station die quickly compared to the nodes closer to the base station because of the energy dissipation due to longer distance.

B. PEGASIS Protocol

PEGASIS (Power Efficient Gathering in Sensor Information Systems) is proposed after the LEACH protocol to improve the network lifetime [13]. Like LEACH, since the development of PEGASIS, many scientists have been working to improve PEGASIS protocol as well. There are various improved version of PEGASIS available. In [14], Li et al. has proposed an ant colony algorithm to form the chain instead of greedy algorithm. Feng et al. has proposed another improved version of PEGASIS, which they named IEEPB (Improved Energy-Efficient PEGASIS-Based Protocol) [15]. IEEPB protocol assigns

each node a weight and uses weighting mechanism to select the transmitter node. They claimed that their modified version balances energy consumption and improves network lifetime compared to PAGASIS protocol.

Now, let us provide a brief description of PEGASIS. In each round, all sensor nodes' data needs to be collected and transmitted to the base station to make a decision about the deployed environment. In PEGASIS, the sensed information of the deployed environment is gathered by forming a chain among the sensor nodes (Fig. 2). The chain formation is done by using the greedy algorithm where each node will receive and transmit data to the nearest neighbor. It is assumed that all nodes have the global knowledge of the network and the base station has the knowledge about the geographic location of each sensor node. The farthest node from the base station will be the first node in the chain, i.e. the chain formation starts from the farthest node. Each node performs data fusion with its own sensed data and received data from the neighbor. The fused data is then transmitted to another neighboring node. Each node takes turn to be a transmitter to the base station.

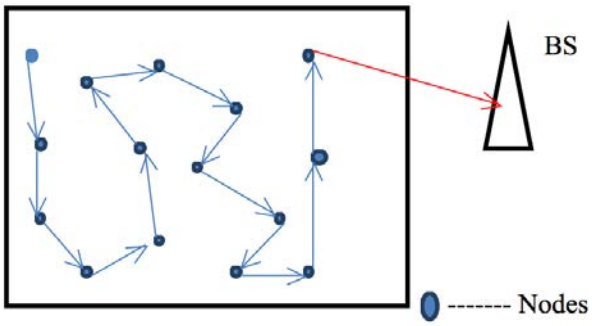

Figure 2. PEGASIS protocol architecture.

This way energy dissipation is distributed among all the nodes. Priority is given to the higher energy possessed nodes to be a transmitter. This way the transmission distance is minimized. PEGASIS protocol outperforms LEACH by approximately 2x the number of rounds when 1%, 20%, 50%, and 100% of nodes die for a 50m x 50m network [13].

III. Proposed Protocol

A. Architecture of the Proposed Protocol

Our proposed algorithm is based on the LEACH and PEGASIS algorithms. In the proposed algorithm, as shown in Fig. 3, the entire network is divided into clusters based on the LEACH protocol and in each cluster the nearest node to the base station is considered as the cluster head. The white circles represent member nodes and the black circles represent a cluster head. In each cluster the base station will calculate the distance of each node and the chain formation will start from the farthest node in cluster based on the PEGASIS protocol. The following steps describe the proposed algorithm.

Step-1: It is assumed that BS has the knowledge of the entire network and it will calculate the distance from each node in the network.

Step-2: Formation of clusters is based on the LEACH protocol.

Step-3: In each cluster the node that is nearer to BS will consider as cluster head.

Step-4: The base station will calculate the distance of each node in the cluster and the farthest node in the cluster is consider as initial node and from there the chain formation is done based on PEGASIS protocol.

Step-5: Once all the chain formation is done in each cluster, the BS will calculate the distances of all the cluster heads and the farthest cluster head is selected as initial node and from that cluster head the chain formation is done to the neighboring cluster heads based on PEGASIS protocol.

Step-6: The final cluster head in the chain will be considered as a transmitter and send the data to the BS.

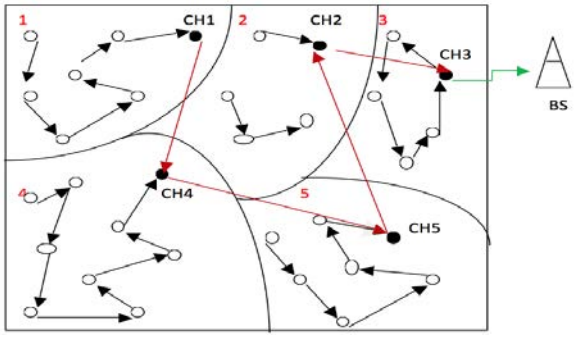

Figure 3. Proposed protocol architecture.

As shown in the Fig. 3, the entire network is divided into five clusters based on the LEACH protocol. The cluster heads CH1, CH2, CH3, CH4, and CH5 are chosen based on their distances from the base station. In each cluster the formation of the chain is based on the greedy algorithm, which we use in PEGASIS. The cluster head will be the base node in the chain in each cluster. First, the chain formations are done in each cluster. Second, the base station will calculate the distances of each cluster head and the farthest node i.e., in our case CH1 is chosen as the initial node and from that node (CH1) chain formation between each cluster head like CH1 to CH4, CH4 to CH5, CH5 to CH2, CH2 to CH3 are done. The transmitter node i.e., CH3 will transmit the data to the base station.

B. Simulation of the Proposed Algorithm

In our simulation, we have considered 60 sensor nodes to analyze the network performance. Java program is coded according to the proposed algorithm. The base station is located at (100, 100) location. Initially the all the nodes in the network will have same energy. The following figures (Fig. 4, 5, and 6) show the status of the nodes at their different rounds. Figure 4 display the initial set up and (x, y) location of all the 60 sensor nodes. They are all alive at this round of the network. The black circle represents alive node and the "x" represents a dead node.

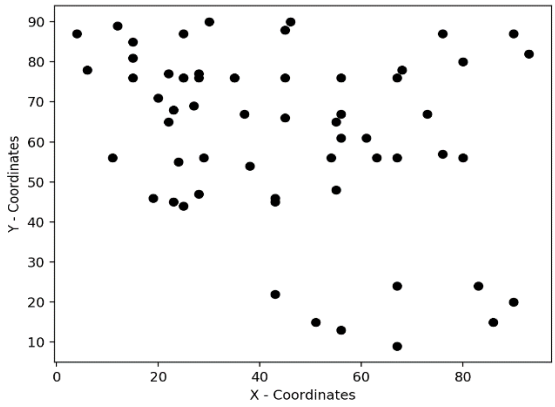

Figure 4. Nodes status at the beginning.

After the 10th rounds, we see some of the nodes are dead and most of them are still alive (Fig. 5).

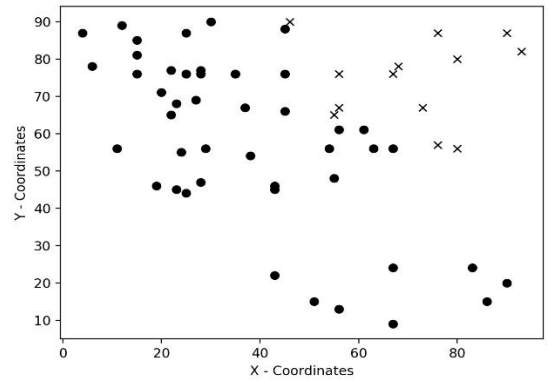

Figure 5. Nodes survival status at round 10.

After the 30th round, we found that most of the nodes are dead (Fig. 6).

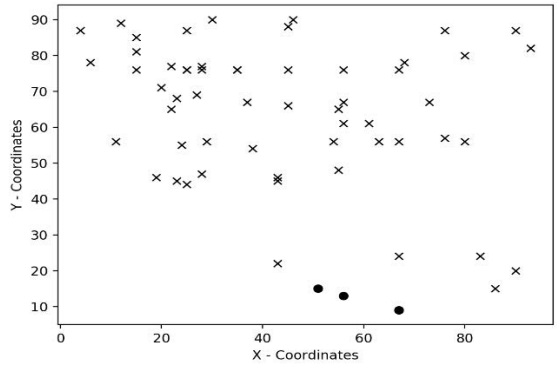

Figure 6. Nodes survival status at round 30.

Figure 7 represents the graphical representation of all the nodes at which round it dies and the graph is plotted based on the simulation results. The graph is drawn by considering all the 60 nodes on the x-axis and number of rounds they can communicate with the base station on the y-axis. For example, node number 60 dies at round 29 and node number 41 dies at round 9.

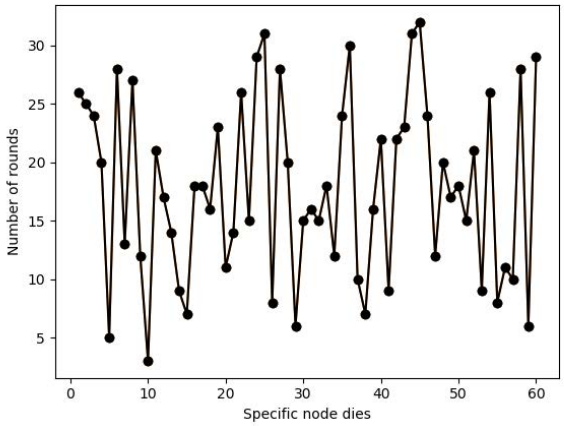

Figure 7. Nodes' survival status at a specific round.

Table 1. Node's location and status data

#	Location	Distance	Proposed	PEGASIS	#	Location	Distance	Proposed	PEGASIS
1	76,14	89.3	26	12	31	54,56	63.7	16	3
2	12,89	88.7	25	15	32	43,46	78.5	15	12
3	15,85	86.3	24	20	33	25,87	76.1	18	20
4	67,24	82.9	20	3	34	67,56	55	12	25
5	80,56	48.3	5	2	35	15,76	88.3	24	7
6	25,44	93.6	28	3	36	19,46	97.3	30	15
7	45,66	64.7	13	8	37	56,76	50.1	10	9
8	28,47	89.4	27	25	38	76,87	27.3	7	2
9	45,76	60	12	7	39	23,45	94.6	16	8
10	73,67	42.6	3	5	40	20,71	85.1	22	6
11	29,56	83.5	21	25	41	68,78	38.8	9	1
12	27,69	79.3	17	25	42	38,54	77.2	22	8
13	37,67	71.1	14	3	43	23,68	83.4	23	3
14	56,67	55	9	4	44	67,9	96.8	31	20
15	46,90	54.9	7	2	45	56,13	97.5	32	20
16	22,77	81.3	18	5	46	25,76	78.7	24	4
17	11,56	99.3	18	9	47	45,88	56.3	12	8
18	25,76	78.7	16	20	48	28,77	75.6	20	2
19	22,65	85.5	23	15	49	35,76	69.3	17	13
20	56,61	58.8	11	7	50	30,90	70.7	18	6
21	61,61	55.2	14	20	51	55,48	68.8	15	3
22	24,55	88.3	26	4	52	28,76	75.9	21	17
23	35,76	69.3	15	4	53	55,65	57	9	10
24	4,87	96.9	29	25	54	43,45	79.2	26	13
25	51,15	98.1	31	12	55	80,80	28.3	8	8
26	67,76	40.8	8	5	56	6,78	96.5	11	5
27	43,22	96.6	28	25	57	76,57	49.2	10	9
28	83,24	77.9	20	10	58	86,15	86.1	28	12
29	90,87	16.4	6	1	59	93,82	19.3	6	4
30	63,56	57.5	15	13	60	15,81	87.1	29	10

Table 1 shows the complete data of the 60 sensor nodes. The column header indicated by # represents the node number. We have a total of 60 nodes with labeled from #1 through #60.

The “Location” columns represent the (x, y) coordinates of each sensor nodes. In our simulation, we have considered that sensor nodes are not mobile, i.e. they remain in the same location until they die. For example, node number 1 is located at (x_1, y_1) = (76, 14) and node number 50 is located at (x_{50}, y_{50}) = (30, 90).

The “Distance” columns show the distance of a sensor node from the base station, i.e. how far is that node located from the base station. For example, the distance between node number 3 which is located at (x_3, y_3) = (15, 85) and base station which is located at (x, y) = (100,100) can be calculates as:

$$d = \sqrt{[(x-x_3)^2 + (y-y_3)^2]} = \sqrt{[(100-15)^2 + (100-85)^2]} = 86.3$$

The “Proposed” columns display the number of rounds at which a particular node is dying for the proposed algorithm. For example, node number 5 dies after round 5 and node number 33 dies after round 18 for the proposed algorithm.

The “PEGASIS” columns demonstrate the number of round after which a sensor node dies for the PEGASIS algorithm. For example, node number 15 dies after round 2 and node number 45 dies after round 20 for the PEGASIS algorithm.

In Table 1, we see nodes are surviving longer in the proposed algorithm compared to the PEGASIS algorithm. For example, node number 7 dies after round 13 in the proposed algorithm and it dies after 8 in the PEGASIS algorithm. Only a few cases, some of our nodes dying earlier than PEGASIS due to their location and functionality. For example, node number 34 dies after round 12 in the proposed algorithm and it dies after 25 as per the PEGASIS. If we see the overall performance, the nodes lifetime has increased in the proposed method.

C. Simulation Results

Table 2 shows the simulation output of the proposed and the PEGASIS algorithms. The first column shows the number of round in the simulation, the second column provides how many nodes survives at that round based on the proposed algorithm, and the third column displays how many nodes survives according to the PEGASIS algorithm.

Here we assume that all nodes are alive at round 0 for both algorithms. At round number 10, 45 nodes are alive according to the proposed method compared to only 24 nodes alive according to the PEGASIS method. At round 26, all nodes are dead for the PEGASIS algorithm, whereas, 10 more nodes are still surviving as per the proposed method. All nodes are dead at round 32 for the proposed method.

Table 2. Comparison of node status for the proposed and the PEGASIS

Round	Proposed	PEGASIS
0	60	60
2	60	54
4	59	43
6	54	38
8	50	30
10	45	24
12	40	20
14	37	17
16	31	15
18	27	14
20	24	9
22	19	9
24	14	9
26	10	0
28	6	0
30	3	0
32	0	0
34	0	0
36	0	0
38	0	0
40	0	0

After all the nodes in the network dies, then we can calculate the lifetime of the network based on the number of rounds the data is been communicated between nodes and the base station.

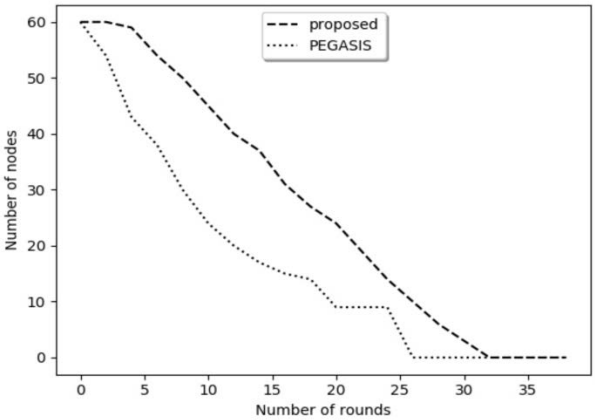

Figure 8. Network lifetime comparison between the proposed and PEGASIS algorithms.

Figure 8 is displaying the number of nodes survives versus the number of rounds at which they die. It compares between the proposed algorithm and the basic PEGASIS algorithm. As we see in the above graph, all the nodes are dead after 26 rounds of data transmission to the base station for the PEGASIS algorithm. The proposed algorithm staying a bit longer than the PEGASIS i.e., the sensor network dies at round 32. In comparing these two algorithms, we found that the proposed algorithm prolongs the overall network lifetime more than the basic PEGASIS algorithm. Also, the proposed algorithm is more energy-efficient compared to the LEACH and PEGASIS.

In Fig. 8, we have compared between the proposed algorithm and basic PEGASIS. Since PEGASIS outperforms LEACH, we did not include LEACH in the comparison.

IV. Data Visualization

One of the most important tasks of wireless sensor networks is to monitor the environment remotely. There are two main parts of the WSN applications: deployment area and remote monitoring & controlling area. The deployment area is the environment where we deploy the sensors to monitor the activities of interest such as temperature, motion, humidity, and others. In the monitoring area, we remotely collect the data from the sensors and serially feed to the computer as shown in Fig. 9. The first block showing the sensors that we deployed in the field. The second block is a RF receiver and receiving data wirelessly from the sensor field and feeding to a computer using a serial port. The third block is a computer or a decision support unit that is used to process the data and monitor the field.

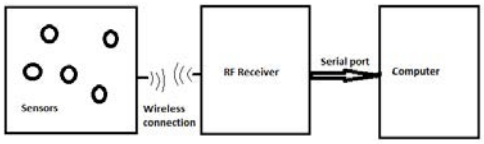

Figure 9. Schematic diagram for sensor network and data analyzer.

A. Hardware Components

In our experiments, we used sensors manufactured by the Synapse Wireless Inc. [16] which is located in Huntsville, Alabama. We used sensor with Model SM200, PART RF200P81. The RF200P91 is a reliable through-hole module that integrates with wireless networks. It has a line of sight communicate range up to 1500 feet and it can tolerate temperature ranging from -40^{o} C to +85^{o} C. It has a 4-kilobyte internal EEPROM (Electrically Erasable Programmable Read Only Memory). We deployed five of these sensors in the field to monitor temperature from the surrounding area. The left side of the Fig. 10 shows these sensors that we have used and the right side of that figure shows the wireless RF receiver. This receiver is feeding data to a computer through a serial port.

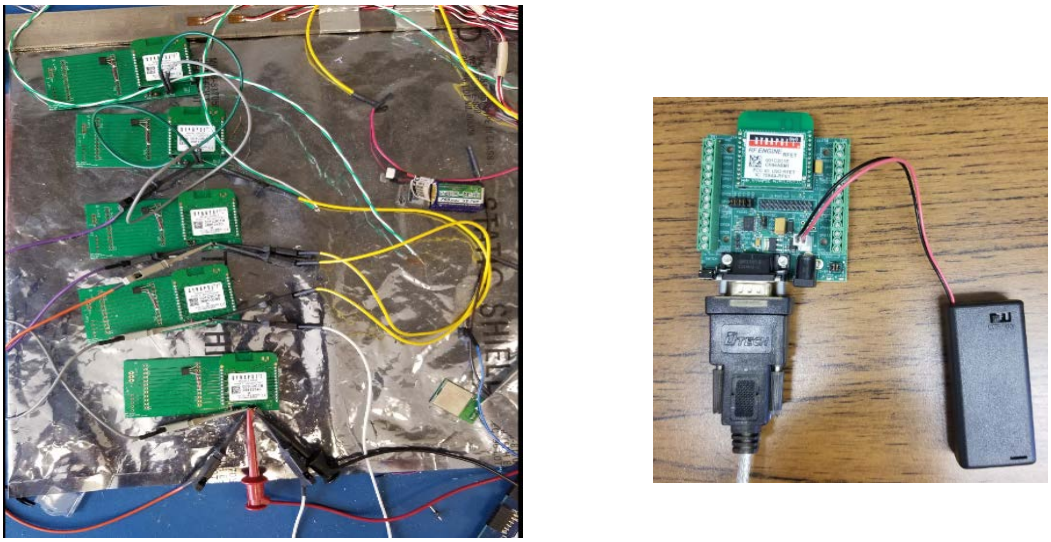

Figure 10. Sensor array (left) and RF data receiver (right).

B. Data Analysis

Sensor data visualization is achieved using the Python programming. We have used *matplolib*, which is a Python 2D plotting library for producing publication quality figures [17]. Figure 11 displays the data from five individual sensors, namely, node-0, node-1, node-2, node-3, and node-4. Due to their placement location, different sensors are providing different temperatures values in their raw format. For example, the temperature of node-0 varies from 467 to 469 in their raw format whereas, the temperature of node-2 varies from 463 to 465. In the X-axis, we are keeping only fresh 300 samples and removing the older values.

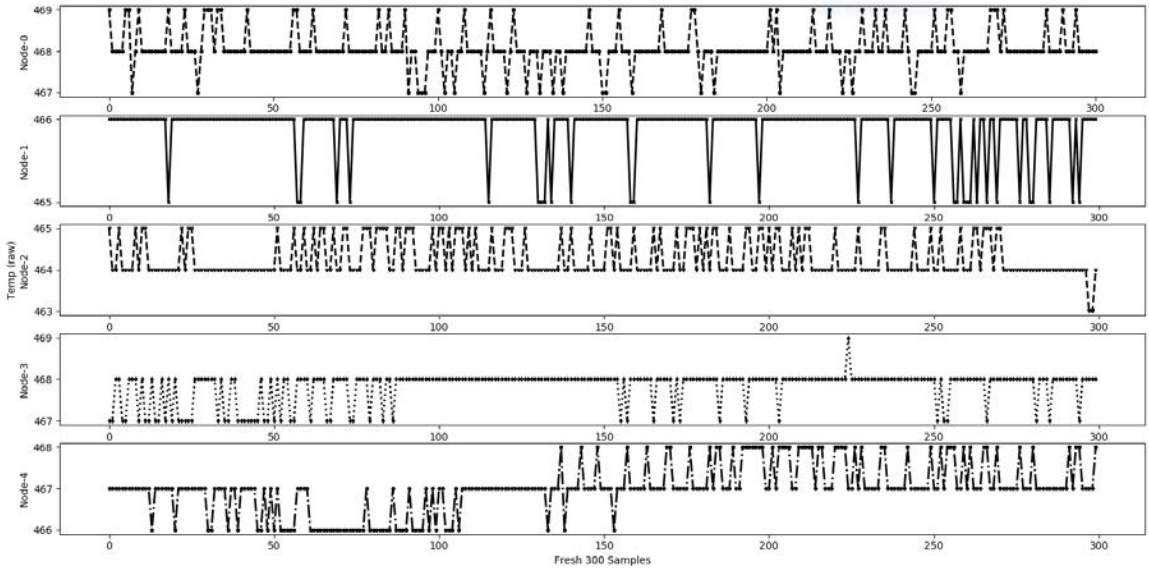

Figure 11. Sensor data display for each node separately.

Figure 12 combines all the temperatures from these five sensors into a single graph. Here the temperature is ranging from 464 to 469 in their raw format in a room environment. This figure helps us to know about the whole environment in a single view. We kept only fresh 300 samples of the temperature. Based upon the application, we can easily change the number of samples to be displayed.

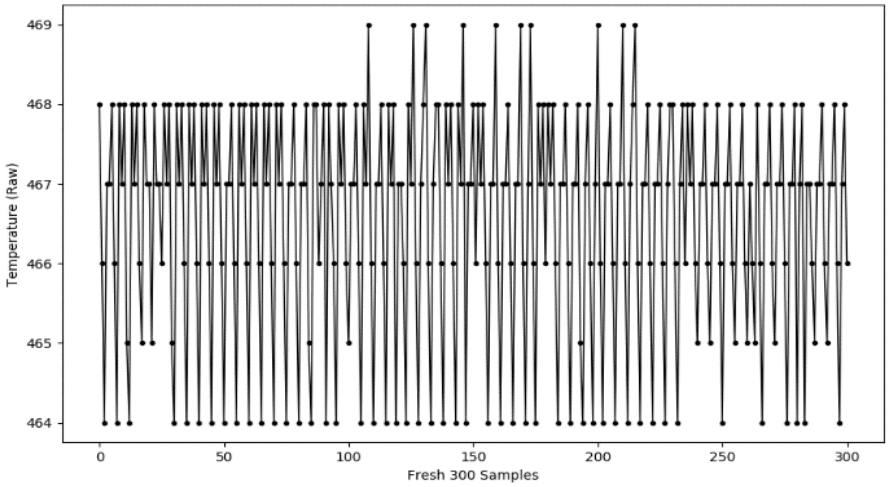

Figure 12. Sensor data display in a single graph for nodes combined.

V. Conclusion

In this paper, we describe the proposed algorithm along with the other two algorithms, namely, LEACH and PEGASIS. LEACH is a cluster based hierarchical algorithm and PEGASIS is a chain-based algorithm. Many researchers around the globe have modified both of these algorithms. In this paper, we combined the concepts of these two algorithms and proposed a modified version that compares favorably with the existing algorithms. Since the lifetime is one of the most important factors to be considered while designing the sensor networks, our proposed algorithm outperforms other two algorithms in terms of network lifetime. The proposed algorithm has an improvement of about 7% in the lifetime of the network than PEGASIS. Hence, the proposed protocol has better performance in terms of lifetime than the existing basic protocols according to the simulation results conducted in this research.

In data visualization, we have considered only five sensors. In practice, we may have hundreds of sensors. Our programs are easily upgradable to any large number of sensors.

In this research all the nodes are considered non-mobile. The locations of the nodes do not change once they are deployed. In many practical applications, these nodes are dynamic, i.e. mobile. In future, we can consider the mobility issue of sensor nodes while forming the clusters and chain. In this research, we also do not consider the network delay. As a further research, we can consider the network delay to compute network performance and energy-efficiency. Moreover, aerospace vehicles operates in an extremely harsh environments with temperature ranging from cryogenic to very high [3]. Our future research direction could include batteries that may operate adequately in these extreme environments.

Acknowledgments

The authors would like to thank NASA MSFC Faculty Fellowship program and their staff members for providing the opportunity to conduct this research. We also would like to thanks engineers and scientists at NASA MSFC ES36 group who took time and shared their thoughts and ideas on using wireless sensor network technologies in space applications.

References

[1] M. Othmana and K. Shazalib, “Wireless sensor network applications: a study in environment monitoring system,” *International Symposium on Robotics and Intelligent Sensors 2012 (IRIS 2012)*, Procedia Engineering 41 (2012), pp. 1204–1210.

[2] K. Bouabdellaha , H. Noureddine, and S. Larbi, “Using wireless sensor networks for reliable forest fires detection,” *The 3rd International Conference on Sustainable Energy Information Technology (SEIT 2013)*, Procedia Computer Science 19 (2013), pp. 794–801.

[3] W. Willson and G. Atkinson, “Wireless sensors for space applications,” *Sensors & Transducers Journal*, vol. 13, Special Issue, Dec. 2011, pp. 1-9.

[4] I. Akyildiz, W. Su, Y. Sankarasubramaniam, and E. Cayirci, “Wireless sensor networks: a survey,” Computer Networks 38 (2002) 393–422.

[5] K. Akkaya and M. Younis, “A survey on routing protocols for wireless sensor networks,” Ad Hoc Networks 3 (2005) 325–349.

[6] K. Romer and F. Mattern, “The Design Space of Wireless Sensor Networks,” *IEEE Wireless Communications*, Vol.11, Issue 6, Dec. 2004.

[7] S. Sin, M. Woo, and C.Raghavendra, “Power-aware routing in mobile ad hoc networks,” *In proceedings ACM/lEEE Mobicom'98*,1998.

[8] M. Zorzi and R. Rao, “Energy Management in Wireless Communications,” *In Proceedings 6th WINLAB Workshop on Third Generation Wireless Information Network*, Mar. 1997.

[9] W. Heinzelman, A. Chandrakasan, and H. Balakrishnan, “Energy-efficient communication protocol for wireless microsensor networks,” in the *Proceedings of the Hawaii International Conference on System Sciences*, Jan. 4-7, 2000, Maui, Hawaii.

[10] F. Xiangning and S. Yulin, “Improvement on LEACH protocol of wireless sensor network,” *in the Proceeding of the 2007 International* Conference on *Sensor Technologies and Applications (SENSORCOMM 2007)*, Valencia, Spain.

[11] M. Tong and M. Tang, “LEACH-B: An improved LEACH protocol for wireless sensor network,” *in the Proceeding of the 6th IEEE International Conference on Wireless Communications Networking and Mobile Computing (WiCOM)*, Chengdu, China, Sep. 2010.

[12] H. Shwe, A. Kumar, and P. Chong, “Building efficient multi-level wireless sensor networks with cluster-based routing protocol,” *KSII Transaction on Internet ad Information Systems*, vol. 10, no. 9, pp. 4272-4286, Sep. 2016.

[13] S. Lindsey and C. Raghavendra, “PEGASIS: power efficient gathering in sensor information systems,” *in the Proceedings of the IEEE Aerospace Conference*, Big Sky, Montana, Mar. 2002.

[14] T. Li, F. Ruan, Z. Fan, J. Wang, and J. Kim, “An Improved PEGASIS Protocol for Wireless Sensor Network,” *in the IEEE Proceeding of the 2015 3rd International Conference on Computer and Computing* Science (COMCOMS), Hanoi, Vietnam.

[15] S. Feng, B. Qi, and L. Tang, “An improved energy-efficient PEGASIS-based protocol in wireless sensor networks,”, *in the Proceeding of the IEEE 8th International Conference on Fuzzy Systems and Knowledge Discovery (FSKD)*, Shanghai, China, July 2011.

[16] Synapse Wireless, Inc. www.synapsewireless.com.

[17] Matplotlib, www.matplotlib.org.

Cognitive Work Analysis of Space Launch System Manual Steering

Joshua Shive[1]
Tennessee State University, Nashville, TN, 37209, USA

H. Charles Dischinger, Jr.[2]
Marshall Space Flight Center, Huntsville, AL, 35811, USA

This project explores human-automation coordination in manual steering of the Space Launch System (SLS). We consider a proposed implementation of manual steering known as manual command, in which the crew prescribes a desired vehicle state, such as a desired attitude, and the ascent Flight Control System acts to reduce the error between the commanded state and the vehicle's current state. We used Cognitive Work Analysis to examine how transitions between fully-automated control and manual command place different responsibilities on the crew. We performed a work domain analysis of SLS navigation during automated Core Stage flight and constructed an abstraction hierarchy of the work domain. To examine how the crew's responsibilities and information needs change during nominal and off-nominal flight conditions, we created different versions of the abstraction hierarchy with information overlaid to illustrate human-automation functions during automated flight and manually controlled flight. Cognitive Work Analysis provides a useful tool for designing and analyzing complex sociotechnical systems, as well as a means of facilitating communication across design teams. Future work will complete the remaining phases of Cognitive Work Analysis and analyze the availability of information on the existing Orion/SLS crew displays for specific manual control scenarios.

Nomenclature

CWA	=	Cognitive Work Analysis
FCS	=	Flight Control System
GN&C	=	Guidance, Navigation, and Control
ICPS	=	Interim Cryogenic Propulsion Stage
LAS	=	Launch Abort System
MECO	=	Main Engine Cut Off
NASA	=	National Aeronautics and Space Administration
PIO	=	Pilot-Involved Oscillations
RGA	=	Rate Gyro Assembly
RINU	=	Redundant Inertial Navigation Unit
SRB	=	Solid Rocket Booster
SLS	=	Space Launch System

"There will forever be disagreement over who, exactly, flies NASA ships—
the engineers on the ground, or the spacemen in the capsules." – Craig Nelson, *Rocket Men*[1]

I. Introduction

The Space Launch System (SLS), NASA's new heavy-lift vehicle, is designed to be a highly-automated system. That is, under normal (or *nominal*) flight conditions, the vehicle's systems will execute all of the required functions for launch, flight, and reentry without input from the crew or the Mission Control Center. In fact, its first

[1] Associate Professor, Department of Psychology, Tennessee State University
[2] Deputy Branch Chief, Spacecraft and Vehicle Systems, NASA Marshall Space Flight Center

scheduled flight, Exploration Mission One, will be un-crewed. However, SLS will also be used for crewed flights, with the crew in the Orion Crew Vehicle atop the SLS. During these flights, the crew, in collaboration with Mission Control, will be expected to provide manual input to the vehicle during emergency (*off-nominal*) situations. Our current project uses Cognitive Work Analysis to explore human-automation coordination during manual steering of SLS.

NASA's crewed launch vehicles, like all of its crewed systems, are required to carry a human-rating certification, which means that the vehicles meet NASA's safety standards for human health and performance.[2] The human-rating certification has three components. First, crewed systems should provide a safe environment for the crew throughout the duration of the mission (*e.g.*, with no sharp edges on exposed surfaces). Second, crewed systems should, as much as possible, allow for the crew to be rescued in the event of an emergency (Safe Recovery). For this reason, NASA develops and evaluates abort scenarios for the various phases of a mission. Finally, crewed systems should provide for human interaction with its systems "to enhance overall safety and mission success" (part of Human-Systems Integration). This requirement relates directly to the crew's ability to control the spacecraft during the mission. In particular, the human-rating requirements include the provision that "the crewed system shall provide the capability for the crew to manually control the flight path and attitude of their spacecraft, with the following exception: during the atmospheric portion of Earth ascent when structural and thermal margins have been determined to negate the benefits of manual control." This provision goes on to specify that manual control does not mean the ability to bypass the flight control system.

Manual steering has shown its utility during in-flight phases of several prominent NASA missions. During Apollo 11, Neil Armstrong activated manual control to choose a new landing site and land the lunar module on the surface of the Moon. On Apollo 13, the crew manually steered the vehicle using the Earth's terminator for visual guidance while performing an engine burn to alter their earthward trajectory on their return from lunar orbit.[3] In addition, manual steering during ascent phases has been supported on previous launch vehicles. For example, the Apollo crew were trained to fly the Saturn V during powered and coast phases of ascent in the event of an inertial measurement unit failure, although they never had to do so. Furthermore, the Space Shuttle featured a Control Stick Steering mode that would allow the Shuttle crew to manually steer the vehicle if the guidance algorithm was unable to find a guidance solution that would allow the vehicle to reach the altitude and velocity required for Main Engine Cut Off (MECO).[4]

Manual control during ascent has been controversial since the early days of the space program. Arguments for including manual control in launch vehicles can be summarized as follows. First, crew input during ascent may produce better outcomes than automated control, especially during unforeseen circumstances. For example, the crew may be able to steer the vehicle away from populated areas or keep the vehicle within structural safety margins. Furthermore, training the crew for manual control may improve the crew's insight into the vehicle's behavior during launch. In addition, when launch vehicles are unproven, it may be better to include manual control to give the crew the chance to influence the vehicle's behavior. Finally, when launch vehicles are still being designed, it is much cheaper to implement manual control than it would be to try to incorporate it into an existing design.

Arguments against manual control counter that aborting the mission might result in better outcomes than activating manual control would. Crew members steering the vehicle via manual control might increase the risk to the crew rather than decreasing it, and the human may not be able to control the system safely. Also, implementing manual control that isn't subsequently used would be costly and wasteful. Finally, backup modes and redundant hardware are typically designed to mitigate many of the failure modes for which manual control is thought to be necessary.

Manual control of SLS is a difficult problem partly because SLS, like all crewed spacecraft, is a complex sociotechnical system. That is, its operation involves the interaction of technology, the environment, and human operators. Thus, designing such a system requires a methodology that incorporates information about constraints on human behavior in considering how to design displays and controls to support users' situational awareness and decision-making.

Highly-automated systems such as SLS provide a challenge for human factors analysis techniques that begin by considering operator tasks in system operation, such as hierarchical task analysis.[5] When the system is operating normally, operators may not have any required tasks that they must perform. However, they may have significant supervisory control responsibilities.[6] Thus, it is necessary to consider human factors methods that begin with an analysis of the system and its constraints on behavior.

Cognitive Work Analysis (CWA) is well-suited for analyzing complex sociotechnical systems.[7–9] CWA methods are useful for identifying constraints on human behavior in complex systems, clarifying design requirements for new technologies, and designing interfaces that support operators' decision making.[9] Furthermore, they are useful in clarifying how different levels of automation impact different phases of the decision-making process.[12] CWA has

shown itself useful both as a tool for analyzing the design of current systems (*e.g.*, road intersections, aviation displays, manufacturing plants, neonatal units), as well as providing the foundation for the design of new interfaces that support the monitoring of complex systems.[13–16]

Our current project does not seek to resolve the manual control debate by advocating for a particular implementation of manual control on SLS. Rather, we consider how best to support the proposed implementation of manual control during SLS ascent. We begin by giving an overview of SLS, including a discussion of SLS's ascent flight control system. Next, we conduct the first step in a Cognitive Work Analysis, a work domain analysis of SLS during Core Stage flight. We discuss the resulting abstraction hierarchy, which describes automated SLS Core Stage flight. We review human factors issues in manual steering and describe manual command, a current proposal for how to implement manual steering on SLS. We create alternate versions of the abstraction hierarchy to illustrate how transitions between automated flight and manually-commanded flight produce changes in human-automation coordination. We conclude by evaluating the CWA approach and recommending further analyses to support manual command of SLS.

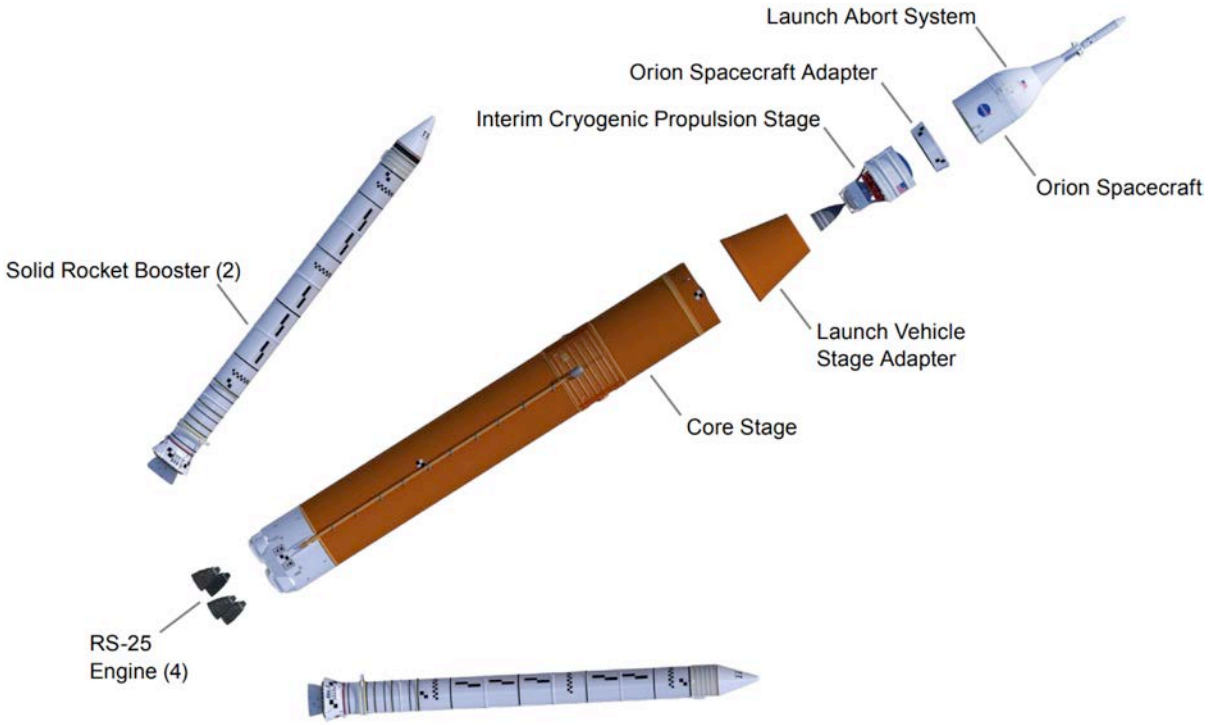

Fig 1. Space Launch System in Block 1 Configuration.

II. Overview of SLS Operations During Ascent

Exploration Mission-2, NASA's first crewed launch of the Space Launch System, will use the Block 1 configuration of SLS, shown in Figure 1. This SLS configuration features the Orion command and service modules, the Interim Cryogenic Propulsion Stage (ICPS), the Core Stage (which is powered by four RS-25 Space Shuttle Engines), and two solid rocket boosters (SRBs). This mission will involve launching Orion via the SLS and performing system checks in High Earth Orbit, followed by a trans lunar injection, moon flyby, and return to earth. Subsequent SLS flights will use different components and have different mission goals. However, the Block 1 configuration of SLS provides a good model for our analysis.

During the boost phase of ascent, which occurs during the first minutes of SLS flight, the solid rocket boosters and the Core Stage engines provide thrust to the vehicle. Manual control of SLS during the boost phase is not available, because the structural and thermal margins that the vehicle must remain within for safe operation during this period of time have been determined to be too narrow to allow for human operation and intervention. This is in line with the human-rating requirement about manual control mentioned earlier. During the boost phase, open-loop

guidance is provided by a series of commands stored in the SLS flight computer that the vehicle executes automatically at set times following liftoff.

After the solid rocket boosters separate from SLS, the Core Stage engines propel it to a specific ascent altitude at the velocity required for it to sustain a low-earth orbit. During Core Stage flight, the Flight Control System (FCS) provides closed-loop guidance. Once the vehicle has attained the desired ascent altitude and velocity, the Core Stage engines are cut off. A short time later, the ICPS and Orion crew vehicle separate from the Core Stage.

The vehicle's design provides for automated and manual aborts during both the boost phase and Core Stage phase. In particular, the Launch Abort System (LAS), which sits on top of the Orion crew vehicle, can detect whether the vehicle has exceeded the margins for safe flight and pull away from SLS to carry the crew to safety. These automated LAS aborts can occur anytime between when the SLS is sitting on the launch pad until midway through Core Stage flight. Likewise, the crew can trigger a LAS abort if they or MCC determine that one is necessary. Midway through Core Stage flight, SLS jettisons the Launch Abort System.

III. Cognitive Work Analysis of Automated Flight

To understand how crew responsibilities and information needs change during nominal and off-nominal Core Stage flight of the SLS, we performed a Cognitive Work Analysis of the vehicle. CWA involves five phases. Each phase examines various constraints on work and offers tools for analyzing workers' behavior in the system. The results of each phase of analysis feed into the next phase. In this project, we completed the first phase of CWA.

- **Work Domain Analysis** – This phase examines the constraints placed on workers by the physical, social, and cultural environment. The most common tool of analysis in this stage is the Abstraction Hierarchy, which we used in this project to examine SLS Core Stage flight.[8,17,18]
- **Cognitive Task Analysis** – This phase examines constraints that relate to the activities necessary for proper system operation. Decision ladders are issued to illustrate how information is processed by the various system actors (*e.g.*, humans, automation).
- **Strategies Analysis** – This phase examines cognitive constraints on behavior. An information flow map is often used to analyze the system at this level.
- **Social Organization and Cooperation Analysis** – In this phase, constraints arising from the ways that work can be organized in the system are analyzed, and a diagram of work organization possibilities is produced.
- **Worker Competencies Analysis** – The final stage of CWA looks at constraints based on the match between human cognitive capabilities and limitations. The Skills, Rules, and Knowledge taxonomy is used to analyze requirements for training and information support at this level.[19]

A. Method

We conducted a work domain analysis of the Space Launch System during nominal Core Stage flight. During this period, the four RS-25 Core Stage engines provide the vehicle's thrust. We chose to focus this analysis on Core Stage flight because it is the phase of flight where manual steering is allowed by the human-rating requirements and has the potential for reducing the probability that the mission will fail or the crew will be lost.

We began by reviewing existing SLS documentation, including documentation that describes the SLS flight control design.[20] We interviewed Guidance, Navigation, and Control engineers at the Marshall Space Flight Center. On the basis of the information we collected, we created the first draft of the abstraction hierarchy, which we then reviewed with the same Guidance, Navigation, and Control engineers. Finally, we revised the abstraction hierarchy based on their comments.

B. Results: Work Domain Analysis

The abstraction hierarchy describes a work domain at different degrees of abstraction, beginning with the work domain's functional purpose and ending with the physical objects that make up the work domain. Means-ends links between the levels in the abstraction hierarchy describe how the system's purposes are implemented and accomplished. The completed abstraction hierarchy provides a tool for designing a new system or analyzing an existing system. In addition, the abstraction hierarchy feeds into the second stage of Cognitive Work Analysis. Furthermore, the abstraction hierarchy can be used to generate information requirements for interfaces to support system monitoring and human-system integration. Figure 2 shows an abstraction hierarchy of the fully-automated SLS during Core Stage flight.

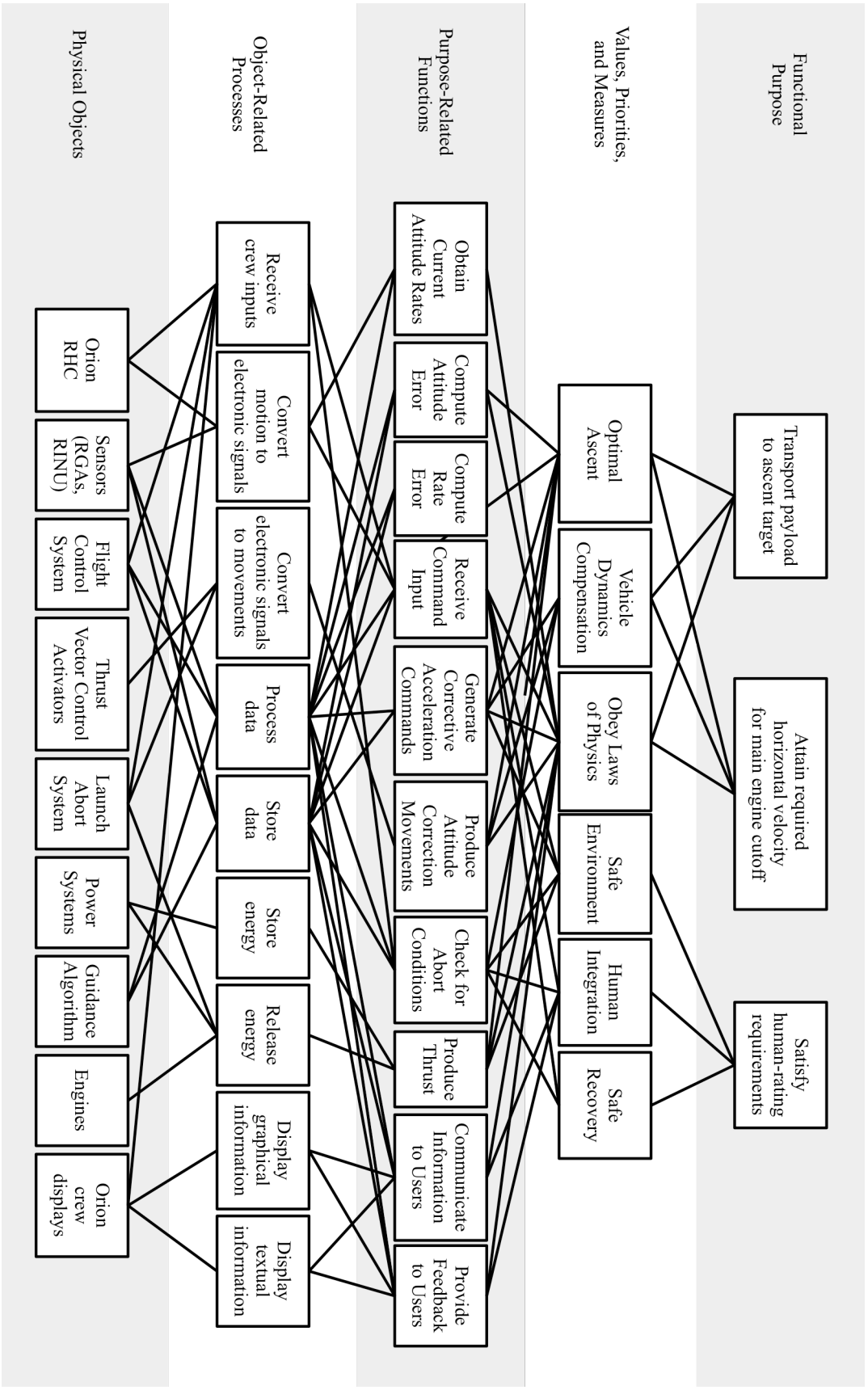

Fig 2. Abstraction Hierarchy of SLS Core Stage flight.

1. Functional Purposes

The top level of the work domain analysis describes the functional purposes of the work domain. The items at this level describe what the system is designed to do. We identified three purposes of the SLS during Core Stage flight. First, the SLS is designed to transport a payload to an ascent target. Second, it needs to attain the horizontal velocity required for Main Engine Cut Off. Finally, the SLS is designed to satisfy human-rating requirements, which exist to provide for the crew's safety.

One of the benefits of developing an abstraction hierarchy is that each level of abstraction poses questions related to system design. At the Functional Purposes level, the list of the system's purposes offers the opportunity to consider whether any of the identified purposes is at odds with another. There are a number of potential conflicts between the functional purposes of SLS Core Stage flight. For example, it may be difficult to satisfy both the requirement to transport a payload to an ascent target and the human-rating requirements. One can imagine a system that meets the first purpose but does not meet the other (for example, a system that can reach the ascent target but is too dangerous to carry crew because of the levels of acceleration it undergoes).

2. Values, Priorities, and Measures

The second level of the work domain analysis lists the criteria that define whether a system is succeeding at accomplishing its functional purposes. In our case, these can be grouped into two types. First, there are the design principles of SLS's Guidance, Navigation, and Control (GN&C) system: optimal ascent, vehicle dynamics compensation, and obeying the laws of physics. Optimal ascent refers to the goals of maximizing the system's mass-to-orbit ratio and injecting the mass into orbit while conserving as much propellant as possible. The system also needs to compensate for the effects of vehicle dynamics such as fuel slosh and vehicle flexibility, as well as obeying the laws of physics governing flight, such as conservation of mass and mass flow. The third, fourth, and fifth items at the Values, Priorities, and Measures level relate to the human-rating requirements discussed earlier. That is, the system should provide a safe environment, allow for human-systems integration, and provide for safe return via aborts.

Means-ends links connect the items at this level and the one above it. The items at the lower level describe the means by which the ends in the upper level are accomplished. For example, optimal ascent is one of the means by which transporting a payload to an ascent target is accomplished. The items at this level also pose criteria for evaluating a system design, such as "Are the criteria currently being satisfied?" and "What are the issues with satisfying them?"

3. Purpose-Related Functions

The third level of the abstraction hierarchy lists the functions associated with controlling the Space Launch System. In many cases, these functions are common to Guidance, Navigation, and Control systems.[21] The first six items form a rough outline of how the SLS GN&C system works. First, current attitude rates are obtained from rate gyro assemblies (RGAs) and the redundant inertial navigation unit (RINU). Next, the FCS calculates the error between the vehicle's current attitude and the desired attitude, as well as the angular rate error, and generates a set of corrective angular acceleration commands to reduce these error values. These commands are translated into movements of the Core Stage engines, which produce alterations in the vehicle's attitude. Other items at this level (*e.g.*, Communicating Information, Providing Feedback, and Check for Abort Conditions) relate to the human-rating requirements or describe vehicle operations outside the guidance loop (*e.g.*, Produce Thrust).

As before, the links between items at this level and the one above it indicate means-ends relationships. For example, Compute Attitude Error satisfies part of Optimal Ascent. Note that several of the items at this level are related to more than one item in the Values, Priorities, and Measures level. Note also that this level lists only functions relevant to the purposes at the top of the hierarchy. If the focus of this analysis was on another system, such as the fuel system, other functions would be listed here.

The items at this level can be used to ask several questions about the required functions for system operation. For example, what do the functions assume and require? Computing attitude error, for example, requires a way of measuring the vehicle's attitude, a way of storing a commanded attitude, and a method of quantifying the error between the current and commanded attitude. The designer can also ask whether the current design satisfies these functions and what would happen if one of the functions failed. In addition, these requirements can be used to generate descriptions of the required physical functions of the system (Level 4) that can be used to evaluate potential system components.

4. Physical Functions

The Physical Functions level of abstraction lists the processes by which the physical components of the system (Level 5) operate. The Orion rotational hand controller (RHC), for example, operates by converting physical movements into electrical signals. The links between items at this level and the one above it clarify how physical processes accomplish the purpose-related functions listed in Level 3. For example, communicating information to

users (Level 3) involves storing data, processing data, and displaying graphical or textual information (Level 4). It should be noted that systems with different physical components might accomplish the same purpose-related function using different processes (*e.g.*, receiving command input by way of a stick versus a digital user interface).

5. Physical Objects

The lowest level of the abstraction hierarchy lists the physical objects in the system. We have simplified the descriptions of these components and, in some cases, combined separate components into one unit. The links between the items in this level and the level above it relate the physical objects in the system to specific functions, processes, and capabilities that are associated with those objects.

C. Discussion: Crew Behavior During Automated Flight

The abstraction hierarchy shown in Figure 2 provides an organized description of SLS during Core Stage flight. The completed abstraction hierarchy has several uses. In the case of work situations that involve human-automation interaction, the abstraction is useful for describing how functions are allocated between humans and automation, especially when these allocations change under different operational conditions.[12]

SLS is a highly-automated system. Thus, during nominal flight conditions, the crew's role is one of supervisory control.[22] As such, the crew need to maintain situational awareness of guidance, navigation, and control and systems health. This involves scanning the Orion crew displays and comparing the values on the various displays. Figure 3 shows the abstraction hierarchy from Figure 2 with crew activities during nominal Core Stage flight indicated by black squares. As the bottom level shows, the crew interact with the Orion crew displays, which display graphical and textual information. Moving up the hierarchy, we see that their interaction with the displays allows them to view communications from the system. Human-Systems Integration is one of the Human-Rating Requirements. However, note that this interaction does not contribute to either of the first two functional purposes of the system. That is, although the crew are tasked with maintaining situational awareness of SLS operation during nominal flight, they are not taking actions either to help the vehicle reach the ascent target or attain the required horizontal velocity for Main Engine Cut Off.

IV. Manual Command of SLS During Core Stage Flight

The human-rating requirements specify that manual control should not bypass the flight control system during ascent. This requirement is supported by the results of human performance studies examining perceptual, cognitive, and motor limitations relevant to manual control. First, during launch and re-entry, astronauts experience G-loads along the x-axis (i.e., into/out of the chest or into/out of the eyeballs) as well as structural vibrations from the vehicle. G-loading and vibration may cause a number of problems with visual perception and motor performance, including increased reaction time, reduced visual acuity, increased eye movement times, and increases in subjective workload.[23].

Long vehicles are also difficult to control.[24] The lag between a control movement and the vehicle's response can lead to pilot-involved oscillations (PIO), which are instabilities in a vehicle's flight path caused by a pilot's corrective control stick movements.[25] PIOs have been responsible for a number of prominent aviation accidents. In addition, spatial disorientation, which has been a problem in aviation since the early days of flight, also provides challenges for manual steering of SLS.[26] When a pilot pulls a control stick back to "pitch-up", they expect to feel the sensation of being pressed down into their seat. However, because of the way the Core Stage engines move in response to command input, combined with the length of the vehicle, a "pitch-up" command will initially produce the sensation of heading downward. Such spatial disorientation occurs when there is a mismatch between visual input or motor responses and vestibular signals indicating the body's position or motion in space. Perceptual illusions like these can cause a pilot to produce additional corrective movements that can destabilize a vehicle's motion. Finally, SLS has internal parasitic dynamics, such as bending, wind shear, and fuel slosh, that make it difficult to control manually.[27]

Early work in engineering psychology sought to identify which tasks should be allocated to humans and which tasks should be allocated to machines. For example, humans are generally thought to be worse monitors, have a lower capacity for information, and be more error-prone. On the other hand, humans tend to be better at detecting low-intensity stimuli, exhibiting flexibility in problem-solving, and noticing patterns.[28] Thus, it has been argued, humans should be assigned tasks that fit with their strengths, while machines should be assigned the tasks at which humans are weak. Later research has noted that this approach is simplistic, in that it ignores the fact that introducing any type of automation alters the entire situation in which the human and automation work.[29] Thus, it is necessary to consider the human-automation team rather than assuming that humans and automation can do their work independently from each other.[30]

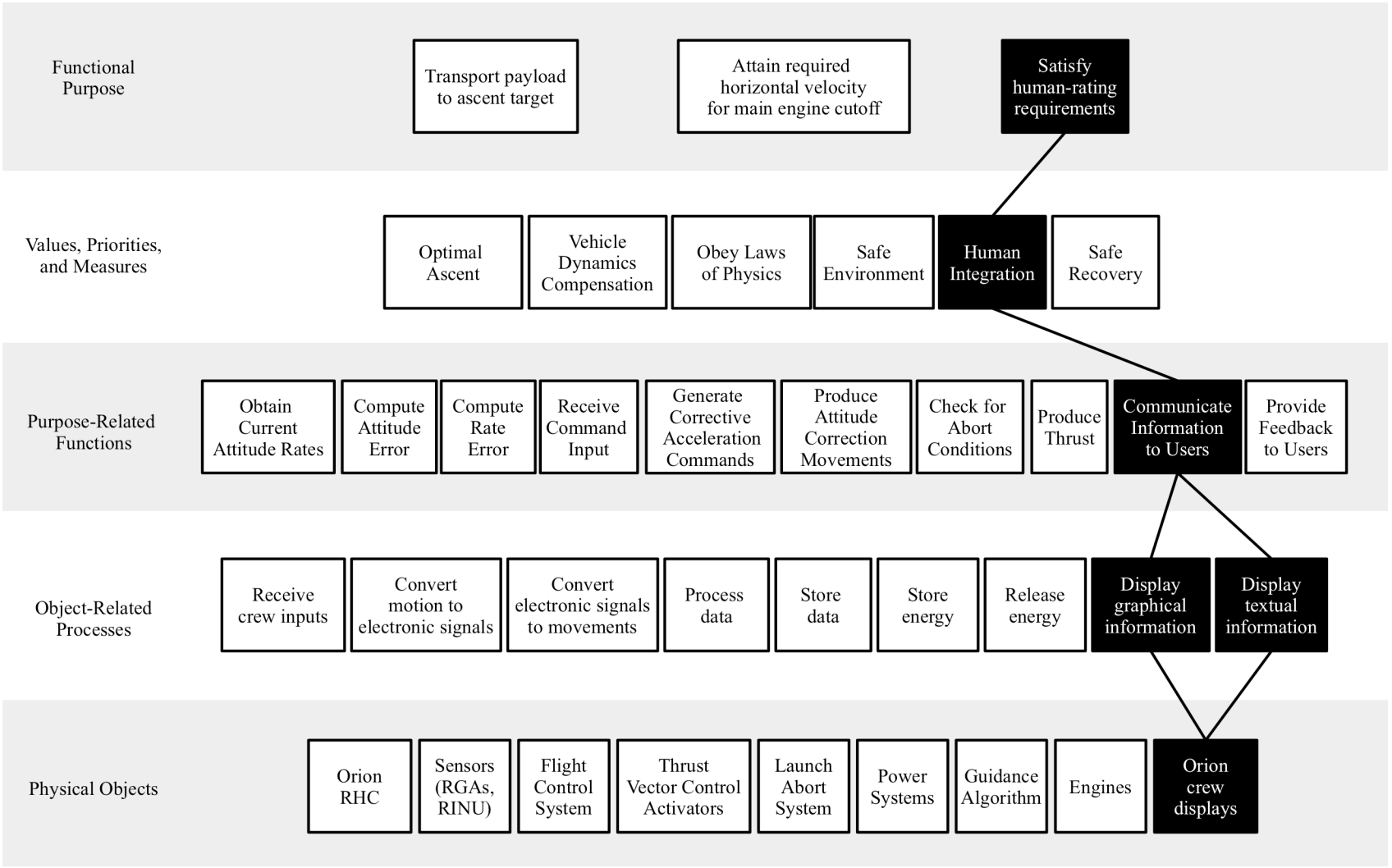

Fig 3. Abstraction hierarchy showing crew activities during nominal SLS Core Stage flight.

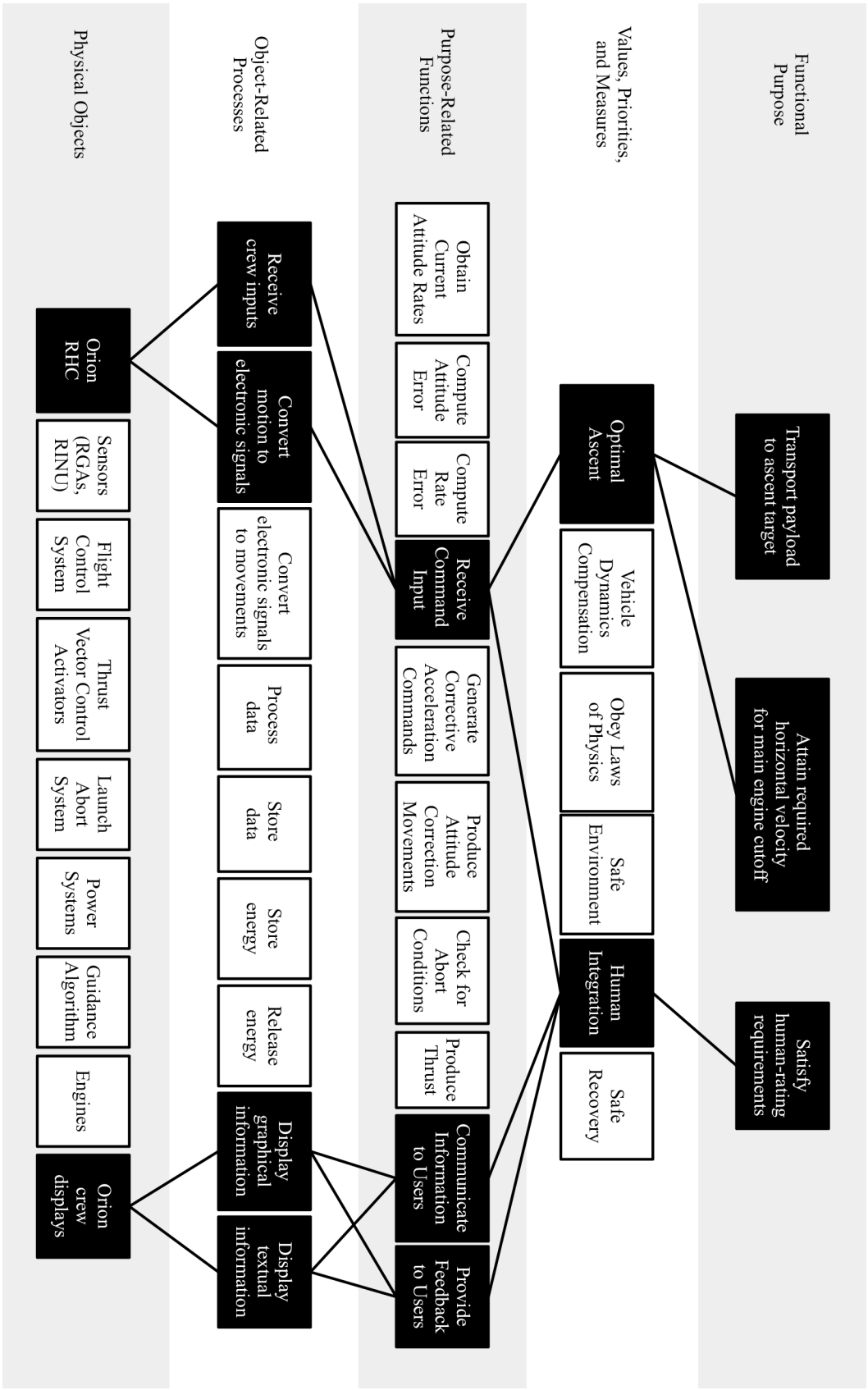

Fig 4. Abstraction Hierarchy showing crew activities during manually-commanded SLS Core Stage flight.

A. Manual Command

Guidance, Navigation, and Control engineers are recommending an implementation of manual control for SLS known as manual command. In a manual command scenario, SLS crew would use the Orion rotational hand controller (RHC) or the Orion crew displays to provide commands specifying desired flight parameters, such as vehicle attitude, attitude rate, or rate error. The Flight Control System would compare the obtained sensor data with these commanded parameters and use the resulting error values as inputs to the SLS flight control system's proportional-integral-derivative control law.[20] This control law contains elements that correct for the parasitic dynamics mentioned earlier. The flight control system would determine the required thrust vector actuator movements required to reduce the error between the vehicle's current state and the commanded state and execute those movements.

B. Abstraction Hierarchy of Manually-Commanded Flight

In order to better understand how the crew's roles change during an off-nominal phase of flight, as well as the information requirements necessary to support crew activities, we layered information on top of the existing SLS Core Stage flight abstraction hierarchy. The resulting model is shown in Figure 4. In the figure, the un-shaded boxes represent automated functions, while the shaded boxes represent functions to which the crew contribute input.

Beginning at the bottom of the hierarchy, we see that the crew's commanded input may be delivered through the Orion RHC or the Orion crew displays. The Purpose-Related Function level now shows that crew are contributing command input. In addition, crew involvement adds a required purpose-related function: providing feedback to users based on manual command input. However, note that the automation is still handling nearly all of the other purpose-related functions responsible for closed-loop guidance.

Crew input during manual command contributes to the highest levels of system operation, as shown in the abstraction hierarchy. The Values, Priorities, and Measures level indicates that crew input contributes to Optimal Ascent, which is one of the criteria for evaluating whether the system is fulfilling its functional purposes of transporting a payload to the ascent target and attaining the required horizontal velocity. Thus, the additional crew responsibilities and activities are reflected in the added capacity of the crew to influence the vehicle at all levels of its operation. In addition, the crew may have responsibilities to communicate with mission control, determine the current abort posture relative to abort trigger thresholds, and confirm which crew display indications are real. Furthermore, the crew may need to expect auto-abort, initiate manual abort, or execute proper responses per training and procedures, depending on the vehicle's current state. The wide range of possible activities during off-nominal flight highlights the importance of designing crew displays that allow the crew to quickly assess the vehicle's current state.

C. Discussion

The diversity of crew responsibilities during nominal and off-nominal situations emphasize the importance of designing crew displays that obey human factors principles.[31,32] In the fully-automated situation shown in Figure 3, the system performs without pilot input. This is equivalent to Level Ten automation in Parasuraman's and Sheridan's Levels of Automation model, where "The computer decides everything, acts autonomously, ignoring the human."[33] As mentioned before, during normal operations, this level of automation is desirable because of the narrow margins for error in the early phases of a rocket launch. However, it may have the effect of reducing the crew's situational awareness, which may impact the speed with which they can act in the event of an emergency.[34,35] Effective design of displays that offer information about the system's current and future status will be necessary for aiding crew in making timely and appropriate decisions. Furthermore, such displays will be necessary for supporting crew in the transition between automated and manual control.

The abstraction hierarchies also illustrate the complex interplay between the human and automation in the off-nominal case. While the crew provides input to the system's flight control system, the system is still responsible for calculating the deviation between the command and the current state, determining the alterations to the vehicle's attitude that will reduce the deviation, executing the physical commands that correspond to those alterations, and updating the representation of the current system state on crew displays. Thus, in addition to informing the crew about the system's current status, the displays that present information to the crew should provide adequate feedback about the results of their actions.

V. Conclusions and Recommendations

In this report, we have shown how to develop a work domain analysis of SLS Core Stage flight. Work domain analysis is only the first step in Cognitive Work Analysis. As such, it is limited to an analysis of the physical,

environmental, and cultural environment in which work is done. Other stages of CWA focus on worker activities, strategies, social organizations, and skills, rules, and knowledge, all of which place constraints on behavior. We plan to complete the additional CWA phases for SLS Core Stage flight. This will allow us to consider the information processing activities, cognitive strategies, interpersonal communication requirements, and crew training requirements necessary to support manual command of SLS.

The abstraction hierarchy was created primarily with input from Guidance, Navigation, and Control personnel. We think this was appropriate, given the high degree of automation in SLS during nominal and manually commanded flight, and we plan to continue to collaborate with those personnel in subsequent work investigating SLS manual command. However, we also plan to involve stakeholders from other NASA centers involved in the design and operation of crewed SLS flights in evaluating the work domain analysis presented in this report and completing the subsequent stages of Cognitive Work Analysis.

The work domain analyses we conducted can be used as a tool for designing new interfaces. Because the abstraction hierarchy proceeds from an analysis of a system's functional purpose, the items represented in the hierarchy represent values, functional purposes, physical functions, and physical objects that serve that purpose. Thus, they can be used to generate information requirements for ensuring that the system is operating correctly. An information availability analysis can be done in the following fashion. First, a designer can generate examples of variables that could be measured for each item in the abstraction hierarchy. For example, Safe Environment, which is one of the items in the Values, Priorities, and Measures level, could be measured in a number of ways: total acceleration, interior temperature of Orion crew vehicle, or oxygen concentration in the vehicle. For an existing display, the list of variables can be used to check whether variables related to system function are being represented on crew displays.[17] We plan to conduct information availability analyses for specific scenarios where manual command will be used and examine information availability on Orion crew displays to support crew activities during those situations. However, this information availability analysis should not be done in lieu of usability testing with crew.

This analysis has raised several open questions that still need to be addressed in implementing manual command as a manual steering option for the Space Launch System. First, given the crew display and input options (multi-function display keys, rotational hand controller), what is the optimal interface for the manual command scenario? Can manual command be implemented using the current Orion crew displays, or will additional displays need to be developed? Furthermore, how will the pilot, commander, and Mission Control Center personnel coordinate their actions during a manual command scenario?

The current work also does not address the time course of the transition between automated control and manual command of SLS. Human factors researchers have examined takeovers from automation in a variety of transportation contexts, including driving, aviation, and space operations.[36] Studies of driver performance have shown that the decreasing the length of the transition period between automated and manual control decreases the delay of driver input following the completion of the transition.[37] However, faster transitions also produce worse driving performance. A study of manual takeovers of a lunar lander showed that during mode transitions, pilots controlling the lander make fewer call-outs of vehicle parameters and take longer to notice alerts.[38] Future work should address takeover times in the automated-control-to-manual-command takeover.

Cognitive Work Analysis has potential benefits beyond facilitating the design and analysis of complex systems. In our work applying CWA methods to the analysis of SLS Core Stage flight, we have found that it can also serve as a useful tool for promoting communication between various groups of stakeholders with different technical backgrounds (*e.g.*, managers, engineers, crew office personnel). CWA methods, and the abstraction hierarchy in particular, provide a systematic framework and common language for describing the assumptions and rationales for particular design choices. These tools may facilitate increased collaboration across NASA centers in designing, implementing, and supporting systems that accomplish the dual goals of achieving mission success and crew safety.

Acknowledgments

This work was supported by a Marshall Space Flight Center Summer Faculty Fellowship grant. J. Shive and C. Dischinger wish to thank Jeb Orr, John H. Wall, and Joel Best of the Marshall Space Flight Center for offering their time and expertise in support of the project. In addition, they wish to thank Matthew Abbott of Johnson Space Center for helpful conversations regarding this research. J. Shive also wishes to thank Frank Six, Gerald Carr, and Rachael Damiani of the MSFC Summer Faculty Fellowship program for their support.

References

1 Nelson, C., *Rocket Men: the triumph and tragedy of the first Americans on the moon*, New York: Viking, 2009.

2 NASA, *NPR 8705.2C - Human-Rating Requirements for Space Systems*, 2017.

3 Lovell, J., and Kruger, J., *Lost Moon: the perilous voyage of Apollo 13*, Boston: Houghton Mifflin, 1993.

4 Sivolella, D., *To Orbit and Back Again: How the Space Shuttle Flew in Space*, New York: Springer, 2014.

5 Stanton, N. A., Salmon, P. M., Rafferty, L. A., Walker, G. H., Baber, C., and Jenkins, D. P., *Human Factors Methods: A practical guide for engineering and design, 2nd edition*, Burlington, VT: Ashgate, 2013.

6 Hobbs, A., "Unmanned Aircraft Systems," *Human Factors in Aviation*, E. Salas and D. Maurino, eds., Boston: Academic Press, 2010.

7 Vicente, K. J., *Cognitive Work Analysis*, New Jersey: Lawrence Erlbaum Associates, Inc., 1999.

8 Jenkins, D. P., Stanton, N. A., Salmon, P. M., and Walker, G. H., *Cognitive Work Analysis: Coping With Complexity*, Burlington, VT: Ashgate, 2009.

9 Naikar, N., "Cognitive work analysis: An influential legacy extending beyond human factors and engineering," *Applied Ergonomics*, vol. 59, 2017, pp. 528–540.

10 Salmon, P. M., Lenné, M. G., Read, G. J. M., Mulvihill, C. M., Cornelissen, M., Walker, G. H., Young, K. L., Stevens, N., and Stanton, N. A., "More than meets the eye: Using cognitive work analysis to identify design requirements for future rail level crossing systems," *Applied Ergonomics*, vol. 56, 2016, pp. 312–322.

11 Cornelissen, M., Salmon, P. M., Stanton, N. A., and McClure, R., "Assessing the 'system' in safe systems-based road designs: Using cognitive work analysis to evaluate intersection designs," *Accident Analysis and Prevention*, vol. 74, 2015, pp. 324–338.

12 Li, Y., and Burns, C. M., "Modeling Automation With Cognitive Work Analysis to Support Human-Automation Coordination," *Journal of Cognitive Engineering and Decision Making*, vol. 11, 2017, pp. 299–322.

13 Amelink, M. H. J., Paassen, M. M. (René) van, Mulder, M., and Flach, J. M., "Applying the Abstraction Hierarchy to the Aircraft Manual Control Task," *Proceedings of the 12th International Symposium on Aviation Psychology*, Dayton, Ohio: 2003, pp. 1–6.

14 Stanton, N. A., Mcilroy, R. C., Harvey, C., Blainey, S., Hickford, A., Preston, J. M., and Ryan, B., "Following the Cognitive Work Analysis train of thought: Exploring the constraints of modal shift to rail transport.," *Applied Ergonomics2*, vol. 56, 2013, pp. 522–540.

15 Reising, D. V, and Sanderson, P. M., "Work domain analysis of a pasteurization plant: Building an abstraction hierarchy representation," *Proceedings of the Human Factors and Ergonomics Society Annual Meeting*, 1996, pp. 293–297.

16 Vicente, K. J., "Ecological Interface Design : Progress and Challenges," *Human Factors*, vol. 44, 2002, pp. 62–78.

17 Burns, C. M., and Hajdukiewicz, J., *Ecological Interface Design*, New York: CRC Press, 2004.

18 Naikar, N., Hopcroft, R., and Moylan, A., *Work Domain Analysis : Theoretical Concepts and Methodology*, 2005. Air Operations Division Defence, Science and Technology Organisation, DSTO-TR-1665

19 McIlroy, R. C., and Stanton, N. A., "Ecological interface design two decades on: Whatever happened to the SRK taxonomy?," *IEEE Transactions on Human-Machine Systems*, vol. 45, 2015, pp. 145–163.

20 Orr, J. S., Wall, J. H., and Hall, C. E., "Space Launch System Ascent Flight Control Design," *2014 American Astronautical Society (AAS) Guidance, Navigation, and Control Conference; 2014*, 2014.

21 Taylor, T. S., *Introduction to Rocket Science and Engineering*, Boca Raton: CRC Press, 2009.

22 Sheridan, T. B., "Human Supervisory Control," *Handbook of Human Factors and Ergonomics*, G. Salvendy, ed., John Wiley & Sons, Inc., 2012, pp. 990–1015.

23 Adelstein, B. D., Beutter, B. R., Kaiser, M. K., Mccann, R. S., Stone, L. S., Anderson, M. R., Renema, F., and Paloski, W. H., "Influence of Combined Whole-Body Vibration Plus G-Loading on Visual Performance," 2008.

24 Jagacinski, R. J., "A Qualitative Look at Feedback Control Theory as a Style of Describing Behavior," *Human Factors: The Journal of Human Factors and Ergonomics Society*, vol. 19, 1977, pp. 331–347.

25 McRuer, D., Graham, D., Krendel, E., and Reisener, Jr., W., *Human Pilot Dynamics in Compensatory Systems*, Wright-Patterson Air Force Base: Technical Report AFFDL-TR-65-15.

26 Mosier, K. L., "The Human in Flight. From Kinesthetic Sense to Cognitive Sensibility," *Human Factors in Aviation*,

2010, pp. 147–173.

[27] Hanson, C. E., Miller, C. J., Wall, J. H., VanZwieten, T. S., Gilligan, E. T., Orr, J. S., Van Zwieten, T. S., Gilligan, E. T., Orr, J. S., and Wall, J. H., "Launch Vehicle Manual Steering with Adaptive Augmenting Control: In-Flight Evaluations of Adverse Interactions Using a Piloted Aircraft," *AIAA Guidance, Navigation, and Control Conference*, American Institute of Aeronautics and Astronautics, 2015, pp. 1–19.

[28] Fitts, P., *Human engineering for an effective air navigation and traffic control system*, Washington, D.C.: 1AD.

[29] Kaber, D. B., and Carolina, N., "Issues in Human – Automation Interaction Modeling : Presumptive Aspects of Frameworks of Types and Levels of Automation," *Journal of Cognitive Engineering and Decision Making*, vol. 12, 2018, pp. 7–24.

[30] Dekker, S. W. A., and Woods, D. D., "MABA-MABA or Abracadabra?," *Cognition, Technology & Work*, vol. 4, 2002, pp. 240–244.

[31] Wickens, Christopher D, Lee, J. D., and Liu, Y., Gordon Becker, S. E., *An introduction to human factors engineering*, Upper Saddle River, New Jersey: Pearson Education, Inc., 2004.

[32] Proctor, R. W., and Zandt, T. Van, *Human Factors in Simple and Complex Systems*, Boca Raton: CRC Press, 2008.

[33] Parasuraman, R., Sheridan, T. B., and Wickens, C. D., "A Model for Types and Levels of Human Interaction," *IEEE Transactions on Systems Man and Cybernetics Part A Systems and Humans*, vol. 30, 2000, pp. 286–297.

[34] Kaber, D. B., and Endsley, M. R., "The effects of level of automation and adaptive automation on human performance, situation awareness and workload in a dynamic control task," *Theoretical Issues in Ergonomics Science*, vol. 5, 2004, pp. 113–153.

[35] Kaber, D. B., and Kim, S.-H., "Understanding Cognitive Strategy With Adaptive Automation in Dual-Task Performance Using Computational Cognitive Models," *Journal of Cognitive Engineering and Decision Making*, vol. 5, 2011, pp. 309–331.

[36] Gold, C., Körber, M., Lechner, D., and Bengler, K., "Taking Over Control From Highly Automated Vehicles in Complex Traffic Situations: The Role of Traffic Density," *Human Factors*, vol. 58, Jun. 2016, pp. 642–652.

[37] Gold, C., Damböck, D., Lorenz, L., and Bengler, K., "Take over! How long does it take to get the driver back into the loop?," *Proceedings of the Human Factors and Ergonomics Society*, 2013.

[38] Hainley, C. J., Duda, K. R., Oman, C. M., and Natapoff, A., "Pilot Performance, Workload, and Situation Awareness During Lunar Landing Mode Transitions," *Journal of Spacecraft and Rockets*, vol. 50, 2013, pp. 793–801.

An Atomistic Investigation of Noncovalent Interactions in a Novel Ionic Polyimide: The Case of Density Functional Theory – Symmetry Adapted Perturbation Theory Study (DFT-SAPT)

Tomekia M. Simeon[1]
Dillard University, Department of Chemistry, New Orleans, LA 70122

Christian Thomas[2]
The University of Alabama, Department of Chemical and Biological Engineering, Tuscaloosa, AL 35487

Enrique M. Jackson[3]
NASA, Marshall Space Flight Center (MSFC), AL 35812

Jason Bara[4]
The University of Alabama, Department of Chemical and Biological Engineering, Tuscaloosa, AL 35487

and

Brittany Brown[5]
NASA, MSFC, AL, 35812

Abstract

Polyimides and polymeric ionic liquids (poly(ILs)) polymers have a range of physical, thermal, chemical and mechanical that can be easily tailor-made. Research studies suggest these polymer materials are prime candidate for additive manufacturing for spacecraft exploration. In this work, we study the interaction of noncovalent interactions in a novel polymeric ionic liquids using density functional theory methods. Our results indicate that the M06-2X-D3 calculated complexation energies agree qualitatively with the energetic ordering from DFT-SAPT calculations with an aug-cc-pVDZ basis, both for structures dominated by hydrogen-bonding and π-π stacking interactions. When the DFT-SAPT energies are decomposed into components, and we find that electrostatic interactions dominate the hydrogen- bonding interactions while dispersion makes a significant contribution to π-π stacking.

I. Introduction

Polyimides and polymeric ionic liquids (poly(ILs)) are at the forefront of advanced polymer materials. Their uniqueness involves the ability of their solvation properties to be easily tuned based on the pairing of appropriate anions and cations. From this type of functionalization arises a number of physicochemical properties, such as low vapor pressure, chemical stability at high temperatures, and miscibility with polar/nonpolar and electrolyte solvents. Furthermore, based on these properties they are receiving considerable attention based on current and potential applications in a variety of fields in the scientific community.[1-3] Wide attention in the field of additive manufacturing is of extreme interest and importance for ILs implementation, specifically 3-D printing. As of now, there are little to no polymers that are suitable for additive manufacturing use and ILs may prove to be the solution to this deficit.

[1] Assistant Professor, Dept. of Chemistry, Dillard University, New Orleans, LA 70122.
[2] Ph.D. Candidate, Dept. of Chemical & Biological Engineering, The University of Alabama, Tuscaloosa, AL 35487.
[3] Aerospace Polymeric Engineer, Materials and Process Lab, EM22, MSFC, AL 35812.
[4] Associate Professor, Dept. of Chemical & Biological Engineering, The University of Alabama, Tuscaloosa, AL 35487.
[5] Environmental Control and Life Support Engineer, Building 4755, MSFC, AL 35812.

Unlike most commercially available materials available for 3-D printing, ILs retain their robust nature while displaying the ease of processing and conductivity. This unique combination of properties is not found in conventional polyimides or other engineering polymers. This novelty is of interest to NASA-MSFC and the Agency's Mission Directorate's human exploration in additive manufacturing and modeling. For example, ionic polyimides can be extruded, made into pellets and used in 3-D printing for aerospace applications such as, valves, seals and gears.

Previous NASA summer fellows have studied in detail (properties ranging from thermal, electrical and structural) an unique class of polyimides and poly (ILs) synthesized at the University of Alabama (UA) in Professor Jason Bara's lab. At NASA-MSFC experimental findings using for example, DSC and TMA instrumentation has been studied thoroughly and well documented for over ~100 polymers. The low-cost fabrication and ease of functionalization leads to the guide of development of future materials. Notably, MSFC could have a significant market share in processing novel materials to be added to the In-Space Manufacturing and Space Launch Systems (SLS) spacecraft. As a continuation of previous research at MSFC, we ventured into now modeling these polymer "building blocks" to more rapidly identify viable ionic polyimide configurations. There is now a significant opportunity for making a major step forward in our understanding of these polymers through the use of high performance computation.

Empirical potential classical molecular dynamics calculations are now possible, and such calculations on an HPC system for a long enough time (~ 1 microsecond) to equilibrate structures that include explicit water and ions would enable us to determine useful information about polymer folding/unfolding, including both cation-anion interactions, H-bonding and π-π stacking that are found in polyimides and poly(ILs). Yet, a key issue that needs to be established is whether the proposed molecular dynamic force fields, such as CHARMM[4] are providing qualitatively accurate information about folding/unfolding in polyimides and poly(ILs) such that a correct picture of functionalization and Coulombic effects is generated. This force-field assessment activity can now be provided using electronic structure calculations based on the Density Functional Theory-Symmetry Adapted Perturbation Theory (DFT-SAPT)[5-7] approach, as is provided in the Molpro software[8].

The goal of this project is twofold: 1) to use high quality electronic structure results to determine H-bonding and π-π stacking interaction energies that can be used to calibrate for MD simulations and 2) to DFT-SAPT, which is a method that treats intermolecular interactions at a higher level than DFT, to explore these same interactions for ILs thereby calibrating the DFT results, and providing a decomposition of the energy into components that can provide insight into the description of larger polymers.

Density functional theory methods provide these capabilities and we now have higher quality DFT functionals that include dispersion effects implicitly so the quality of the interaction energy calculation is now much better than in the past. Nevertheless, DFT approximations intrinsically lack the ability to recover the $-C_6/R^6$ dependence on the London dispersion interaction energy or the interatomic/molecular distance R. Hence, clarifying the accuracy of our DFT calculations is of essential importance. In this work, we implemented Grimme's DFT-D3 method (denoted by the suffix "-D3") to provide an empirical dispersion correction for DFT,[9,10] and the results are compared with DFT-SAPT results with a large basis for ultimate determination of the quality of these methods.

Details of the structural models used to study H-bonding and π-π stacking interactions and the calculated geometric parameters are presented in Methods. The results of our structural modeling, while the DFT-SAPT results are presented and compared with DFT-D3 results. Finally in conclusions, the main findings are summarized.

II. Methods

Structural Parameters: A total of fifteen polyimides and poly(ILs) was optimized and the folded versus unfolded conformations were studied. For the purpose of this paper we focus on PMDA API ortho xylene polymer complex (Figure 1) and use it as a benchmark for future DFT-SAPT calculations. The details involving the solvation of the complex is shown in Figure 2 and the short chain of the oligomer is shown in Figure 3. A fragmentation scheme to understand the systems, is shown in Figure 4 and 5, wherein the parent molecule is broken into two **Complexes A** and **B**.

The relative contribution of π-π stacking interactions are considered in **Complex A** and the H-bonding interactions to the overall complex binding is established in **Complex B**. For these model complexes, constrained geometry optimizations at the HF/3-21G(d) level of theory have been performed to account for the addition of hydrogen atoms to take care of dangling bonds. The final geometries are then subjected to single-point calculations at the M06-2X level of theory and using DFT-D3.[9,10]

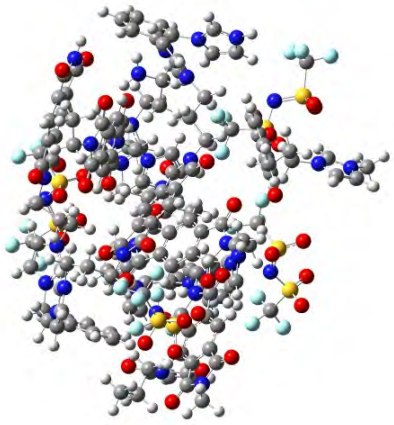

Figure 1. PMDA API ortho xylene polymer complex.

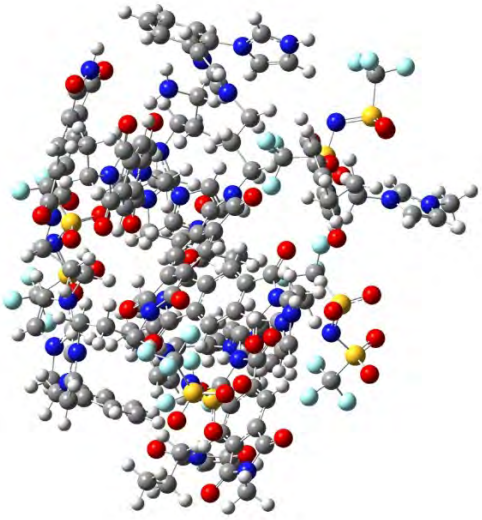

Figure 2. Optimized PMDA API ortho xylene polymer calculated demonstrating regions of π-π stacking and hydrogen-bonding interactions. The lowest-energy conformers were then geometry optimized using the PM6 semi-empirical method – including SCRF (SMD) implicit solvation using Gaussian '16.[18,1 9] The PM6 method was employed for monomer geometry optimization using the SMD solvation model, with acetonitrile as the solvent (ε = 35.688). This model includes a parameterized function to reproduce dispersion corrections.

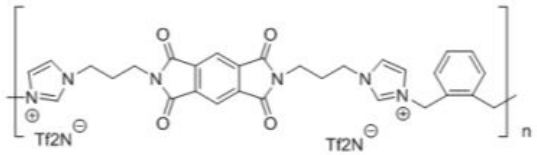

Figure 3. PMDA API ortho xylene polymer short oligomer.

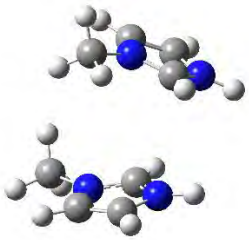

Figure 4. The fragmentation scheme for π-π stacking in PMDA API ortho xylene polymer labeled **Complex A**. A total of 15 fragments was taken from optimized globular structure and used for DFT-SAPT calculations.

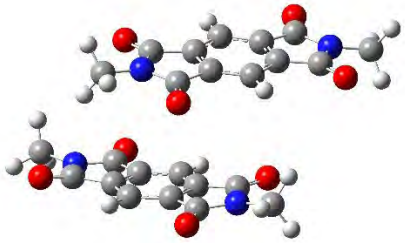

Figure 5. The fragmentation scheme for H-bonding in PMDA API ortho xylene polymer labeled **Complex B**. A total of 15 fragments was taken from optimized globular structure and used for DFT-SAPT calculations.

III. Theoretical Methods

The specific implementation of DFT-SAPT that was used is in the Molpro quantum chemistry program.[8] To the best of our knowledge no systematic study has been reported accounting for the decomposition of the intermolecular complexation energy for a polyimides and poly(ILs) employing DFT-SAPT.

The DFT-SAPT calculations were invoked using the density fitting (DF) approximation referred to as DF-DFT-SAPT. It has been demonstrated that interaction energies from this method deviate by less than 1% from corresponding DFT-SAPT results.[11] In the DF-DFT-SAPT method the DFT orbitals are used in evaluating the electrostatics and first-order exchange-repulsion corrections to the interaction energy, with the induction and dispersion contributions (along with their exchange counterparts) calculated from response functions. The asymptotically corrected PBE0(PBE0AC) exchange-correlation (xc) functional containing 25% of 'exact' exchange[12-15] along with the adiabatic local density approximation (ALDA) xc kernel was used for the monomers in this calculation.[16] The correlation consistent basis sets, both in their regular cc-pV*n*Z and (diffuse function-) aug-cc-pV*n*Z augmented variants were considered abbreviated as VDZ, aVDZ. The asymptotic correction for the PBE0AC xc potential requires knowledge of the sum of the ionization potential (IP) (called the *shift*) and the highest occupied molecular orbital (HOMO) energy; both were calculated for our complexes at the PBE0/aug-cc-pVDZ level of theory.[17]

IV. Results

SAPT provides the most rigorous approach of those that we have considered, both for evaluating ΔE and for partitioning the energy into physically defined energy components. SAPT calculations are time consuming, however the complexes considered here are small enough that such calculations can be performed, even with aug-cc-pVDZ basis sets. In SAPT the total interaction energy (E_{tot}) is naturally partitioned into electrostatics (E_{el}), effective induction (E_i), effective dispersion (E_D), and effective exchange-repulsion (E_{ex}) energies. The density functional based theory (DFT) SAPT method combines DFT with SAPT using quantities calculated from Kohn-Sham density and linear response density matrices.[64,65] Ideally, we envision our DFT-SAPT calculations serving as a benchmark for exploiting the design of future ionic complexes. In the present work, we carried out calculations involving cc-pVDZ and aug-cc-pVDZ basis sets, which we denote by VDZ and AVDZ. The calculations in this paper were done as single point calculations for two variations on the **Complex A** and **B**, in which they are minimized using M06-2X level of theory and using DFT-D3. The DFT-SAPT results for these structures are presented in Tables I and II. Note that structures **A** and **B** are both dimers (two fragments), and we have approximated the total SAPT energy by summing calculations for the two nearest neighbor dimer components.

The results in Table I show that the electrostatic interaction makes the largest contribution to complexation for **Complex B**. The decomposition of ΔE reveals the E_{el} contribution accounts to over 60-75% of the total ΔE for **Complex B**, whereas for **A** the E_{disp} contribution is dominant. This result for Complex B is expected given that the polar C-H···O moiety interacts with the charged amine. Meanwhile, the exchange-repulsion contribution is short-range and small for **Complex B**. Typically in electrostatically dominated complexes there are significant contributions from induction, however Table II shows that E_i plays a secondary role in **Complex B**.

In contrast to this, for **Complex A**, the electrostatic, exchange and induction energies are comparable in magnitude. The E_{el}/E_i ratio is 0.51 for **Complex** A compared to 2.69 for Complex **B** (using the AVDZ basis set). Note also that induction is comparable in **Complex A** and **B**. In nonpolar molecules dispersion is usually the dominant attractive force. In the present application Table II shows that dispersion is much larger for **Complex A** than for **Complex B**, and in fact dispersion is the dominant contribution to the energy of **Complex A**. The interactions associated with π-π interactions are associated with displaced-stacked geometries, such as parallel and angle-displaced geometries. The $E^{(2)}$ of **Complex A** is roughly 81% dispersion; whereas in **Complex B** dispersion makes a small contribution to 34% of the total energy. The DFT-SAPT complexation energies have only modest deviations from the estimated M06-2X-D3 complexation energies given in Table II. Indeed, for the largest basis set (AVDZ), the difference between and DFT-SAPT is 2.7 kcal/mol for **Complex A**, 3.8 kcal/mol for **Complex B**. While this agreement is not

of chemical accuracy, the level of agreement provides confidence in the use of M06-2X-D3 for empirical potential modeling of the polyimides and poly(ILs) structures.

TABLE I. First-order DF-DFT-SAPT electrostatic ($E_{el}^{(1)}$), exchange-electrostatic ($E_{ex}^{(1)}$) perturbation energies and the total energy $E^{(1)}$ (in kcal/mol) for **Complex A** and **Complex B** components.

Complex	$E_{el}^{(1)}$	$E_{Ex}^{(1)}$	$E^{(1)}$	$\delta(HF)$
A				
cc-pVDZ	-11.7	10.3	-1.05	-1.89
aug-cc-pVDZ	-9.8	9.9	0.15	-4.84
B				
cc-pVDZ	-56.5	7.2	-48.5	12.4
aug-cc-pVDZ	-54.4	7.9	-46.4	-6.76

TABLE II. Second-order DF-DFT-SAPT induction ($E_{i,0}^{(2)}$), exchange-induction ($E_{i,Ex}^{(2)}$), total induction ($E_{i}^{(2)}$), dispersion ($E_{D,0}^{(2)}$), exchange-dispersion ($E_{D,Ex}^{(2)}$), total dispersion ($E_{D}^{(2)}$), and total second-order ($E^{(2)}$) and total complexation ($E^{(1)} + E^{(2)}$) energies for **Complex A** and **Complex B** components (in kcal/mol).

Complex	$E_{i,0}^{(2)}$	$E_{i,Ex}^{(2)}$	$E_{i}^{(2)}$	$E_{D,0}^{(2)}$	$E_{D,Ex}^{(2)}$	$E_{D}^{(2)}$	$E^{(2)}$	$E^{(1)} + E^{(2)}$
A								
cc-pVDZ	-21.6	4.7	-17.1	-39.5	-0.4	-20.5	-25.3	-26.4
aug-cc-pVDZ	-25.5	4.5	-19.3	-49	0	-25.6	-32.2	-32.4
M06-2X-D3								-35.1
B								
cc-pVDZ	-26.6	0.6	-18.8	-21.6	-1.9	-13.5	-24.9	-73.1
aug-cc-pVDZ	-29.3	0.5	-20.2	-29.0	-1.6	-17.8	-30.5	-76.9
M06-2X-D3								-80.7

V. Conclusions

In this study, we have used DFT-D3 and DFT-SAPT methods to study interactions in H-bonded and π-π stacked complexes that appear in PMDA API ortho xylene polymer. The M06-2X-D3 results show reasonable quantitative agreement with DFT-SAPT, which enhances our confidence in using DFT-D3 to model the important interactions of complex ionic polymers.

The DFT-SAPT analysis reveals that electrostatics dominates the interaction for **Complex B**, while dispersion is dominant in **Complex A**. While DFT-SAPT is not scalable to significantly larger systems, this comparison provides an important benchmark for further improvements in DFT functionals that can be scaled. In addition, the comparison between the V*DZ* and AV*DZ* basis sets demonstrates it is much better for a balanced description to increase the basis to AVDZ size. With this in mind, it is clear that improved DFT methods for describing these interactions in applications to the modeling of polyimides and poly(ILs). Therefore, the functionalization of these materials chemical, conductive and mechanical properties may answer to the problem of additive manufacturing polymers.

VI. Acknowledgements

This work was conducted at the Marshall Space Flight Center. Acknowledgements are owed to Dr. Enrique Jackson, Dr. Brittany Brown, Dr. Jason Bara of the University of Alabama Tuscaloosa and Dr. Kendall Byler of the University of Alabama Huntsville.

VII. References

1. Plechkova, N.V. and Seddon, K.R. Applications of Ionic Liquids in the Chemical Industry. *Chem. Soc. Rev.* **2008**, *37*, 123–150.
2. Brandt, A.; Grasvik, J.; Hallett, J. P.; Welton, T. Deconstruction of Lignocellulosic Biomass with Ionic Liquids *Green Chem.* **2013**, *15*, 550–583.
3. MacFarlane, D.R.; Tachikawa, N.; Forsyth, M.; Pringle, J.M.; Howlett, P.C.; Elliott,G.D.; Davis, J.H.A.; Watanabe, M.; Simon, P.; Angell, C.A. Energy Applications of Ionic Liquids *Energy Environ. Sci.* **2014**, *7*, 232–250.
4. MacKerell, Jr., A.D. "Atomistic Models and Force Fields" in *Computational Biochemistry and Biophysics*, O.M. Becker, A.D. MacKerell, Jr., B. Roux, and M.Watanabe, Eds., Marcel Dekker, Inc. New York, **2001**, p. 7-38.
5.Jeziorski, B.; Moszynski, R.; Szalewicz, K. Perturbation-Theory Approach to Intermolecular Potential-Energy Surfaces of Van-Der-Waals Complexes, *Chem. Rev.* **1994**, *94*, 1887-930.
6. Misquitta, A. J.; Podeszwa, R.; Jeziorski, B.; Szalewicz, K. Intermolecular Potentials Based on Symmetry-Adapted Perturbation Theory with Dispersion Energies from Time-Dependent Density-Functional Calculations, *J. Chem. Phys.* **2005**, *123*.
7. Hesselmann, A.; Jansen, G. The Helium Dimer Potential from a Combined Density Functional Theory and Symmetry-Adapted Perturbation Theory Approach Using an Exact Exchange-Correlation Potential, *PCCP* **2003**, *5*, 5010-14.
8.Werner, H. J.; Knowles, P. J.; Knizia, G.; Manby, F. R.; Schutz, M. Molpro: A General-Purpose Quantum Chemistry Program Package, *Comp. Molec. Sci.* **2012**, *2*, 242-53.
9. Grimme, S.; Antony, J.; Ehrlich, S.; Krieg, H. A Consistent and Accurate Ab Initio Parametrization of Density Functional Dispersion Correction (Dft-D) for the 94 Elements H-Pu, *The Journal of Chemical Physics* **2010**, *132*, 154104-19.
10. Goerigk, L.; Grimme, S. A Thorough Benchmark of Density Functional Methods for General Main Group Thermochemistry, Kinetics, and Noncovalent Interactions, *PCCP* **2011**, *13*, 6670-88.
11. Hesselmann, A.; Jansen, G.; Schutz, M. Density-Functional Theory-Symmetry-Adapted Intermolecular Perturbation Theory with Density Fitting: A New Efficient Method to Study Intermolecular Interaction Energies, *J. Chem. Phys.* **2005**, *122*.
12. Hesselmann, A.; Jansen, G. First-Order Intermolecular Interaction Energies from Kohn-Sham Orbitals, *CPL* **2002**, *357*, 464-70.
13. Perdew, J. P.; Burke, K.; Ernzerhof, M. Generalized Gradient Approximation Made Simple, *Phys. Rev. Lett.* **1996**, *77*, 3865-68.
14. Adamo, C.; Barone, V. Toward Reliable Density Functional Methods without Adjustable Parameters: The Pbe0 Model, *J. Chem. Phys.* **1999**, *110*, 6158-70.
15. Gruning, M.; Gritsenko, O. V.; van Gisbergen, S. J. A.; Baerends, E. J. Shape Corrections to Exchange-Correlation Potentials by Gradient-Regulated Seamless Connection of Model Potentials for Inner and Outer Region, *J. Chem. Phys.* **2001**, *114*, 652-60.
16. Gross, E. K. U.; Dobson, J. F.; Petersilka, M. Density Functional Theory of Time-Dependent Phenomena. In *Density Functional Theory Ii*; Nalewajski, R. F., Ed.; Springer-Verlag: Berlin, **1996**; Vol. 181; pp 81-172.
17. Gruning, M.; Gritsenko, O. V.; van Gisbergen, S. J. A.; Baerends, E. J. Shape Corrections to Exchange-Correlation Potentials by Gradient-Regulated Seamless Connection of Model Potentials for Inner and Outer Region, *J. Chem. Phys.* **2001**, *114*, 652-60.

18. Kelly, C. P.; Cramer, C. J.; Truhlar, D. G. SM6: A Density Functional Theory Continuum Solvation Model for Calculating Aqueous Solvation Free Energies of Neutrals, Ions, and Solute−Water Clusters. *J. Chem. Theory Comput.* **2005**, *1*, 1133–1152.
19. 1. M. J. Frisch, G. W. Trucks, H. B. Schlegel, G. E. Scuseria, M. A. Robb, J. R. Cheeseman, G. Scalmani, V. Barone, G. A. Petersson, H. Nakatsuji, X. Li, M. Caricato, A. V. Marenich, J. Bloino, B. G. Janesko, R. Gomperts, B. Mennucci, H. P. Hratchian, J. V. , and D. J. F. Gaussian 16, Revision B.01 **2017**.

Catalyst Development for an Arc-Ignited Hydrogen Peroxide/ABS Hybrid Rocket System

Stephen A. Whitmore,[*] Christopher J. Martinez,[†] Daniel P. Merkley,[‡]
Utah State University, Logan UT, 84322-4130
and
Daniel Cavender[§]
NASA Marshall Space Flight Center, Huntsville AL, 35812

The authors have collaborated with NASA MSFC to develop key technologies for a prototype upper stage of a dedicated nano-launch vehicle. In addition to providing sufficient impulse for orbit insertion, the unique motor system also provides capability for multiple restarts; allowing operation as an orbital maneuvering thruster. The hybrid motor design uses 85%-90% hydrogen peroxide solution and 3-D printed ABS as propellants. In the original system design the peroxide catalyst bed was completely removed and a patented arc-ignition system thermally ignited the propellants. The thermal ignition system was effective but resulted in a combustion latency of approximately 1-second, reducing overall performance and allowing for significant variability in the delivered total impulse. This work investigates whether adding a small catalyst pack for ignition augmentation can eliminate or significantly reduce the observed ignition latency and improve overall system performance. The effectiveness of multiple catalytic minerals including potassium permanganate, manganese dioxide, manganese (III) oxide, and potassium nitrate were examined and compared to traditional noble-metal catalyst materials like silver or platinum. These alternative materials are significantly less expensive than noble metals. Catalytic activity test results, designs for an augmentation catbed integrated with the thermal ignition system, and preliminary unaugmented and augmented hot-fire test results are presented.

[*] Professor and Director, Propulsion Research Laboratory, Mechanical and Aerospace Engineering Department, 4130 Old Main Hill.
[†] Graduate Research Assistant, Mechanical and Aerospace Engineering Department.
[‡] Graduate Research Associate and NSTRF Graduate Fellow.
[§] Engineering Lead, Small Spacecraft & Green Propulsion Systems, ER-23.

Design of Experiment for the Measurement of Aerosol Droplet Size Distribution of Temperature-Controlled Thermally Atomized Printed Electronic Inks

Chih-Hao Wu[1] and Furman V. Thompson[2]
NASA Marshall Space Flight Center, Huntsville, AL, 35812

In-Space Manufacturing (ISM) centers around NASA's growing need and ability to produce space technologies on demand in space. As the future of long term presence in space and deep space exploration approach, fundamental questions of our dependence on earth resupply to Low Earth Orbit (LEO) remain unanswered. ISM is leading various effort to evaluate the feasibility of producing essential spares and redundant parts on demand to enable a sustainable space-based supply chain model for part resupply. Among the parts and systems being considered, Avionics form the neural network of modern day aircraft and space vehicles providing a wealth of information ranging from Guidance, Navigation, and Control (GN&C) systems to on board Environmental Control and Life Support (ECLS) systems. Recent advances in the use of Aerosol Jet Technology to print Avionics components ranging from electrical traces on a circuit board to complex transistors and sensors, raise the possibility of using such technology to reproduce or recreate electronic parts on demand with the help of custom electronics 3D printers. The challenge herein lies within the ability of such printers to generate and deposit an aerosol of electronic material utilizing processes independent of or enhanced by gravity to ensure controllably identical or improved behavior of the aerosol in an International Space Station (ISS) laboratory and on the ground. The behavior as well as the hazards and properties associated with such aerosols in a microgravity environment must be understood well in order to merit a feasible approach to utilizing them for manufacturing in space. In this report, we outline the experimental setup of a modified conventional vaping device to be used as the ideal gravity independent thermal atomization mechanism to generate aerosol. Our objective is to identify the ideal mass, density, and volume of our aerosolized droplets of ink to conclude that there exist a threshold of aerosolized ink droplet sizes that are indeed independent of the effects of gravity and remain stable after atomization. We use a Malvern Spraytec® Spray Particle Size Analyzer to perform real-time laser diffraction measurement of our ink droplets during atomization. The droplet size between conductive ink, dielectric ink and vegetable glycerin have been measured and contrasted. Furthermore, the mechanism of thermal atomization versus traditional pneumatic and ultrasonic atomization for operation in microgravity have been explored.

I. Introduction

In Additive Manufactured Avionics (AMA) development, aerosol jet printing technology demonstrated a very bright future of producing fine featured, and geometrically complexed avionics parts. Aerosol jet printing technology currently use pneumatically and ultrasonic atomization process to aerosolized the conductive ink droplet to be deposited onto the substrate terrestrially. However, these two conventional atomization process rely on gravity to function properly. With many research and develop ahead, the newly developed thermal atomization [15] shows great promising to atomize the droplet independent of gravity. The main principle behind the thermal atomization is the capillary action or wicking concept. It is the ability of the conductive nanoparticle ink of fluid to flow in the narrow spaces without the assistance of gravity. The ink then thermally boiled to be atomized into aerosol droplet. Once thermally atomized. Our objective for the project in the next step involved is to characterize the aerosolized droplets. In the process of characterizing the aerosol, one of the first task is to determine the droplet size distribution. In this report, the droplet size was determined experimentally through Malvern Spraytec® equipment. With known size of droplet and based on the existing literature, we can then predict our thermally generated droplet will be independent of gravity and therefore can suspend in the air indefinitely [17]. This scientific fact will provide avionic engineers a new perspective and advantage in designing apparatus to print electronics in space utilizing aerosol jet printing

[1] Summer Faculty Fellow, EEE Parts Packaging (ES43), NASA MSFC, Harding University.
[2] Focus Area Champion, EEE Parts Packaging (ES43), Huntsville, AL, 35812, NASA MSFC.

technology. In addition, we demonstrate the thermally generated droplet sizes measured are in the same size range of conventional pneumatic and ultrasonic atomization. Furthermore, similar liquid droplet sizes has been compared and contrasted.

II. The measurement of droplet size of thermally atomization

The Description of the device

(1) Power Supply

The power supply we use is a commercial product (SMOK OSUB 40W 1350mAh) of a conventional vaping device for the atomization process as shown in Figure 2. This is a medium size power supply marketed for average consumers. In our experiments of aerosol size measurements, we set the power usage to the maximum value of 40 watts. The power supply also has an adjustable temperature, micro USB port and OLED display for commercial vaping purposes. The power supply has dimensions of 75 mm in depth, 25 mm in height and 54.5 mm in width. The temperature range is between 200 degrees and 600 degrees Fahrenheit and the voltage range is between 0.8V to 9.0V. [15]

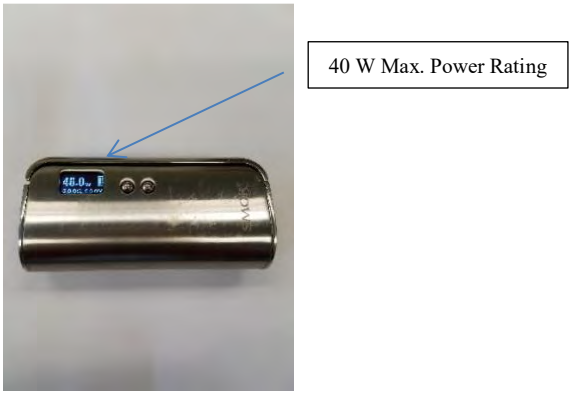

Figure 2. The Power Supply purchased for the thermal atomization process

(2) Rebuildable Dripping Atomizer (RDA)

The Vandy Vape Mesh 24 mm RDA with mesh wire was chosen for this experiment. As illustrated in Figure 3, the RDA chosen provide a 24 mm diameter dual invincible clamp style postless build deck with an open platform where custom mesh wire could be designed and built.

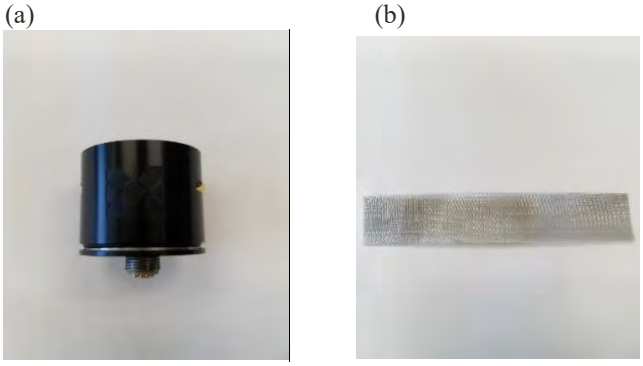

Figure 3. (a) The Mesh RDA and (b) mesh wire chosen for the thermal atomization process

The Mesh RDA was manufactured from 304 stainless steel. The unique build deck has two 11mm terminals with side mounted flathead screws to secure the mesh. Airflow enters the Mesh 24mm RDA via dual adjustable side air slots. The Mesh RDA equipped with two 9 mm drip tips, one ULTEM as well as one Doc drip tip, a 510 drip tip adapter and a bottom feed pin. As can be seen in Figure 4, we build our mesh coils using Vandy Vape mesh wires (SS316L).

Figure 4. The Internal structure of the RDA for the thermal atomization process

(3) Malvern Spraytec® System Description

Nanoparticle aerosol size measurements are critical across a range of applications such drugs delivery to the human respiratory system through automotive fuel injection system. However, aerosol present unique challenges in terms of the measurement environment and the speed of the event which must be characterized. In our experiment, we chose Malvern Spraytec® for the conductive ink and dielectric ink atomized aerosol measurements. It deliver accurate aerosol size measurement and analysis. It provide real-time, high-speed measurements to ensure the complete characterization. In addition, the system offers unparalleled sensitivity to changes in the spray size distribution. Extensive size distribution data are generated rapidly and allows for an instant understanding of the evolution of aerosol over time. The Malvern Spraytec® system measures droplet size distributions through the principle of laser diffraction. This requires the angular intensity of light scattered from aerosol to be measured as it passes through a laser beam as shown in the following Figure 5 between Collimated Optics and Fourier Lens. The recorded scattering pattern is then analyzed using an optical model to yield a size distribution. The angular range over which scattering measurements are made has been optimized within the Malvern Spraytec® to ensure polydisperse size distributions are fully resolved. Particle size calculations are then carried out using a multiple scattering algorithm.

In Specific, it provide the in-situ aerosol analysis from a robust platform as illustrated in following Figure 5. As illustrated, it composed of HeNe Laser, Collimating Optics, Fourier Lens, Detector/Data Acquisition system and Adjustable Sliding Rail.

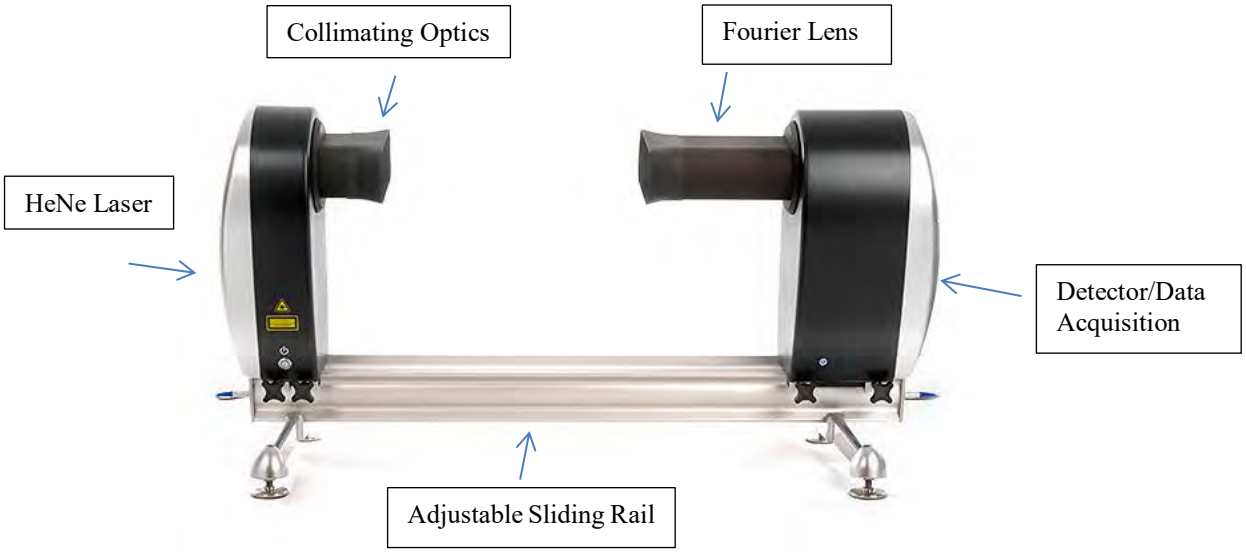

Figure 5. Malvern Spraytec® used in our experiment for the measurement of the conductive and dielectric aerosol

(4) The aerosol droplet of fluid to be atomized

We experimented with thermal atomization of conductive silver nanoparticle ink, dielectric polyimide ink and vegetable glycerin as illustrated in Figure 6 (a) (b) and (c).

(a) (b) (c)

Figure 6. (a) Novacentrix® Conductive Ink (b) Nexolve® Polyimide and (c) Vegetable Glycerin

We next generate the thermal atomization through wicking material and the heating element of the conductive ink, dielectric ink (Polyimide) and vegetable Glycerin. The wicking material we use is Ready X Wick®. This particular wicking material can withstands heat over 2200 degree Fahrenheit. The conductive ink we use is Novacentrix® Metalon® HPS 030-AE1. It is a water-based aerosol sprayable silver flake ink with viscosity between 130-180 c.P. and specific gravity of about 2.0. The silver content is 55% by weight. Figure 6 (a) shows Novacentrix® Metalon® HPS 030-AE1. The dielectric ink (Polyimide) we chose to atomize is Nexolve® CP1 Polyimide, a high performance material which has been widely used in display technology, space structures, thermal insulation and advanced composites. This material provides superior physical and electrical properties over a wide range of temperature and in a number of harsh environments. The polyimide liquid is shown in Figure 6 (b). The Nexolve® CP1 we are using is available in the form of continuous rolls, sprayable resin, castable resin, raw powder and optical film. We chose the sprayable resin with NMP solvent. Our polyimide CP1 Fluid has 6.06% solid loading and viscosity of 78 c.P. Finally, we also atomize the vegetable Glycerin as shown in Figure 6 (c) as a benchmark comparison. [15]

(5) Experimental Results

The following Table 1 illustrated the atomized aerosol droplet size of three different materials:

Novacentrix® Conductive Ink	Nexolve® Polyimide	Vegetable Glycerin
1-5 um	3-5 um	2-3 um

Table 1. Aerosol size distribution of (a) Novacentrix® Conductive Ink (b) Nexolve® Polyimide and (c) Vegetable Glycerin

III. The Comparison of Droplet Size for Three Different Atomization Processes

The Additive Manufactured Avionics (AMA) laboratory within NASA Marshall Space Flight Center (MSFC) ES 43 Electrical, Electronic and Electromechanical (EEE) parts packaging group use Optomec Aerosol Jet® Deposition System 300 (AJ 300) as shown in Figure 1. AJ 300 is capable of generating aerosol droplet that possess conductive inks to deposit onto various substrates to create functional electronic parts. Currently, there are two major conventional atomization process to create aerosol. There are pneumatic atomization process and an ultrasonic atomization process. Here we briefly report these two main atomization principles and provide the droplet size through existing literature [16]. The main reason we attempt the thermal atomization is its unique mechanism that is independent of gravity influence. As described in the introduction section, conventional pneumatic and ultrasonic atomization rely on gravity to hold the ink in the reservoir. These two conventional mechanisms cannot function under microgravity condition. However, the newly developed thermal atomization does not rely gravity to work. The wicking material draw the ink from juice well through capillary action. Once the wicking material is full of the ink, we then thermally boiled the ink through the heating element. The ink aerosolized to form the liquid droplet. The main contribution for this summer work is to design the experiment to adopt the possible droplet measurement of characterization best suited for our

application. We have identified Malvern Spracytec® to measure the droplet size experimentally. In addition, we also investigate Combustion® DMS500 as a possible measurement equipment for comparison. We started the contract negotiation with Battelle to design the experiments for the characterization of the aerosol generated. We are also in the process to have Malvern Spracytec® to perform real time measurement of aerosol droplet size distribution.

(a) A brief introduction of Pneumatic Atomization Process method and its generated droplet size

The Additive Manufactured Avionics (AMA) laboratory within NASA Marshall Space Flight Center (MSFC) ES 43 Electrical, Electronic and Electromechanical (EEE) parts packaging group Aerosol Jet® printer (AJ 300) has traditionally adopted a pneumatic atomization process. Pneumatic atomization process generate its conductive aerosol by supplying external air pressure to an atomizing reservoir. Inside the reservoir well where the conductive ink stored, the process utilized a high-speed air stream across the top of an open vertical channel of the ink. This high-speed low-pressure air stream is at the top of submerged channel where the bottom is the conductive ink reservoir. Right above of ink reservoir, the bottom condition for the air pressure and speed is just the opposite. Because the difference between the pressure, the conductive nanoparticle ink therefore is sucked up to the channel and being atomized through Bernoulli's principle. According to Aerosol Jet® User Manuel [16], the pneumatic atomization process generated the droplet size of 1-5 um.

(b) A brief Introduction of Ultrasonic Atomization Process method and its generated droplet size

The ultrasonic atomization process takes place for the AJ 300 is to agitate the conductive nanoparticle ink material to create the dimension of (3-5 um) aerosol nucleic droplet [16]. When conductive ink, such as silver nanoparticle, agitated by a few Mega Hertz range frequency value of wave will create a capillary wave. On the surface of this liquid silver nanoparticle, the crest of the mentioned capillary wave will form the aerosol droplet. This is the basic principle behind the Optomec ultrasonic atomization process.

(c) Thermal Atomization Process method and its generated droplet size

As discussed in the above, the thermal atomization aerosol droplet measurement through Malvern Spraytec provide the silver nanoparticle conductive ink of 3 um.

The following Table 2 illustrate the droplet size comparison of three different atomization mechanisms:

Pneumatic Atomization	Ultrasonic Atomization	Thermal Atomization
1-5 um	3-5 um	2-3 um

Table 2. The droplet measurement comparsion of three different atomization processes

We can conclude our novel thermal atomization aerosol droplet size is at the same ballpark as pneumatic and ultrasonic atomization. This is to state that the process itself offer the same benchmark comparison as far as the droplet size is concerned.

IV. The Mechanics of Aerosol Transmission [11]

According to [13], virsus without the associated water, mucus and pus droplet is in the size range of 0.02 um to 3 um. Bacteria is the size range of 5 um to 100 um. The fungal spores is in the size range of 1 um to 10 um. The most important factor for the virus to travel in the free air is their size and airflow pattern. The droplet size will change with time based on the environmental condition such as the humidity in the air. The humanity in the air will change the rate of the drop evaporation process and subsequently altering the size of the aerosol droplet. Based on this general observation, one can easily see why the dry air droplet evaporate quickly, reduce in size of its aerosol and fall to the ground more slowly. The changing size in droplet affect how it respond to the airflow pattern, as illustrated in Figure 7. This condition ultimately decide the rate of how quickly it could settle. Stoke's settling law determines aerosol's movement in the air. In general, it stated that a sphere falls under the opposing forces of gravity downwards and air friction upwards as illustrated in Figure 3. Knight [17] estimated the time taken for the aerosol for various diameter to fall for 3 meter. Particle of diameters 1-3 um will suspended almost infinitely. Aerosol with diameter of 10 um will

take 17 minutes to settle. Particle with diameter 20 um will take 4 minutes to settle. Aerosol with diameter 100 um will take 10 second to fall to the floor.

V. Prediction of Aerosol Behavior in Microgravity

Our measured diameter for the conductive ink aerosol is 3 um. Our measured diameter for the dielectric ink aerosol is 2.5 um. We can a conclusion that our lightweight nanoparticle aerosol of silver conductive ink will suspension in the air free of gravity effect. Furthermore, if we direct the aerosol into the substrate, it will deposit onto the substrate without bouncing off to other direction with controlled humidity condition.

VI. Conclusion

The purpose of this project was to determine the size distribution of the aerosol nuclei droplet of the conductive ink and dielectric ink of alternative approach of novel thermal atomization developed. Based on the scientific measurement under the condition where the controlled temperature (98 degree Fahrenheit and ambient air pressure of 3 psi), Malvern Spraytec® equipment provide the aerosol nuclei droplet size reading of 3 um. We conclude that aerosol nuclei under this condition will suspend in the air infinitely without the influence of gravity. This scientific fact will enable us to design the printer and new printing regime for In-Space Manufacturing (ISM) to a brand new chapter. and process with the capability to produce printable electronics in space. This capability will give NASA the potential to support the next generation avionics development. In addition, the aerosol nuclei droplet size of conventionally terrestrial pneumatic and ultrasonic atomization based deposition has been compared to see the advantage of the new noval approach of atomization process.

Acknowledgments

I graciously appreciate the opportunity to work with my mentor Furman Thompson and thank him for his excellent guidance, motivation and support. I also want to thank Jordan Rine of Eco Smoke store of Huntsville, AL for his expert opinions on the conventional vaping device selection and consultation.

References

[1]Mikheev, V. B., Brinkman, M. C., Granville, C. A., Gordan, S. M., Clark, P. I., Real-Time Measurement of Electronic Cigarette Aerosol Size Distribution and Metals Content Analysis. *Nicotine & Tobacco Research 2016, 1895-1902.* (2016).

[2]Owen, M. K., Ensor, D. S., Sparks, L. E., Airborne Particle Sizes and Sources Found In Indoor Air. *Atmospheric Environment*, Vol. 26, No. 12, pp 2149-2162. (1992).

[3]Pratte, P., Cosandey, S., Goujon-Ginglinger, C., A Scattering Methodology for Droplet Sizing of e-Cigarette Aerosol. *Inhalation Toxicology*, (28) 12 537-545. (2016).

[4]Colbeck, I., Lazaridis M., Aerosol Science: Technology and Application, Wiley, New York, 2014

[5]Sunol, F., Gonzalez-Cinca, R., Liquid Jet Breakup and Subsequent Droplet Dynamics Under Normal Gravity and in Microgravity Conditions. *Physics of Fluids 2, 077102.* (2015).

[6]Gibson, I., *Additive Manufacturing Technologies*, 2nd edition, Springer, New York, 2015.

[7]Prater, T. J., Bean, Q. A., Beshears, R. D., Rolin, T. D., Werkheiser, N. J., Ordonez, E. A., Ryan, R. M., Ledbetter, F. E., "Summary Report on Phase I Results From 3D Printing in Zero-G Technology Demonstration Mission, Volume I, NASA/TP-2016-219101, Marshall Space Flight Center, Huntsville, Alabama.

[8]Aerosol Jet and Optomec are trademark of Optomec, Inc.

[9]Monti, R., Physics of Fluid in Microgravity, Taylor and Francis, New York, 2001.

[10]Lappa, M., Fluids, Materials & Microgravity-Numerical Techniques and Insights into Physics, Elsevier, Oxford, 2004.

[11]Tang, J. W., Li, Y., Eames, I., Chan, P. K. S., Ridgway., Factors Involved in the Aerosol Transmission of Infection and Control of Ventilation in Healthcare Premises. *Journal of Hospital Infection (2006) 64, 100-114.* (2006).

[12]Snyder, M. P., Dunn, J. J., Gonzales, E. G., "Effect of Microgravity on Extrusion Based Additive Manufacturing", *American Institute of Aeronautics and Astronautics Space 2013 Conference and Exposition,* San Diego, CA. September 10-12, 2013.

[14]Meyer, M. E., "Aerosol Sampling Experiment on the International Space Station", *47th International Conference on Environmental Systems,* Charleston, SC. July 16-20, 2017.

[15]Wu, C., Thompson, F. V., "Application of Temperature-Controlled Thermal Atomization for Printing Electronics in Space", NASA/TM-2017-219848, Marshall Space Flight Center, Huntsville, Alabama.

[16]Neville, E., D'Arezzo, K., Aerosol Jet® AJ 300 User Manual, P/N 9000324. Optomec, Inc., 2016.

[17]Knight, V., Virus as agents of Airborne Contagion, *Annals of the New York Academy of Sciences, (1980); 353:147-156*. (1980).

Finite Element Analysis of Progressing Failure in Pinned Joints of Composite Panels

2018 NASA Marshall Space Flight Center Summer Faculty Fellowship Final Report

Charles Yang[1]
Wichita State University, Wichita, KS 67260

William E. Guin[2] *and* Justin R. Jackson[3]
NASA Marshall Space Flight Center, Huntsville, AL 35811

A composite Payload Attach Fitting (PAF) is being designed and fabricated at NASA Marshall Space Flight Center for the Block 1B heavy-lift Space Launch System (SLS). Functions as the primary structural interface between the payload and the body of the lunch vehicle, the PAF is a cone-shaped structure of about 25 feet in diameter, 11 feet in length, and consists of eight longitudinal segments of curved composite honeycomb sandwich panels. The PAF is connected to the payload at the forward end and to the body of the launch vehicle at the aft end by metal clevis fittings via pin-connections. The objective of this study is to investigate the effectiveness of finite element models with progressive failure analysis to predict the load carrying capacity of the pinned joints. Both two- and three-dimensional finite element models were developed in ABAQUS/Standard. User subroutines of three sets of failure criteria were implemented to capture the material nonlinearity and property degradations due to damage. Four mesh densities were used to show convergence of failure load of the models. Two pin sizes and two composite layups were included in this investigation. Comparison between finite element and experimental results was satisfactory.

Nomenclature

d = index of lamina shear damage/nonlinearity
e_m = index of matrix failure
e_f = index of matrix failure
e_{fm} = index of fiber/matrix shear failure
E_x = lamina Young's modulus in the fiber direction
E_y = lamina Young's modulus in the resin direction
E_z = lamina Young's modulus in the out-of-plane direction
G_{xy}, G_{xy}, G_{xy}, = lamina shear moduli
X_c = lamina compressive strength in the fiber direction
X_t = lamina tensile strength in the fiber direction
Y_c = lamina compressive strength in the resin direction
Y_t = lamina tensile strength in the resin direction
α = coefficient of lamina shear nonlinearity
γ_{xy}, γ_{xy}, γ_{xy}, = lamina shear strains
ν_{xy}, ν_{xy}, ν_{xy}, = Poisson's ratios
σ_x = lamina stress in the fiber direction
σ_y = lamina stress in the resin direction
σ_z = lamina stress in the out-of-plane direction

[1] Professor, Department of Aerospace Engineering, MSFC Faculty Fellow
[2] Materials Engineer, EM 42, MSFC Collaborator
[3] Materials Engineer, EM 42

I. Introduction

Advanced composites have been the "material of choice" in aerospace industries in the past decades due their high strength-to-weight ratio compared to traditional metallic materials. Research and development efforts as well as experience have gradually pushed the applications of advanced composite materials from secondary, non-essential parts such as cosmetic aircraft interior panels to primary load-carrying structures such as the all-composite fuselage of Boeing 787 and Airbus A350, just to name a few. NASA's intension to take advantage of the benefits from advanced composite materials can be seen from the Composite Crew Module (CCM) constructed from 2006 for the Constellation Program Crew Exploration Vehicle. Even though the CCM was not actually adopted for any space exploration projects, the technologies industry gained have assisted in future composites applications.

NASA's current heavy-lift Space Launch System (SLS) program is aiming at sending astronauts and/or payloads to cis-lunar space as well as to Mars and other deep-space destinations in the 2020s. Part of the new flight hardware development of the SLS program is the honeycomb sandwich composite Payload Attach Fitting (PAF). As shown in Fig. 1, the PAF is a cone-shaped structure used to connect the payload to the body of the launch vehicle. The main function of the PAF is to support the weight and inertia force during launch and deployment of the payload. Based on the current design, the forward end of the PAF is about 60 inches in diameter while the aft diameter is about 320 inches. The PAF is fabricated by automated fiber placement process and each one-eighth of the PAF is laid-up and autoclave cured individually. The eight segments are then joined with a double-lap configuration in the longitudinal direction to complete the PAF. The PAF is joined to the payload on the forward end and to the launch vehicle body on the aft end via metal fittings. Figure 2 shows the schematic of a metal clevis fitting at the forward end.

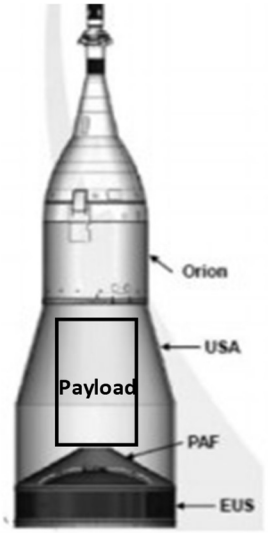

Figure 1. Location of PAF.

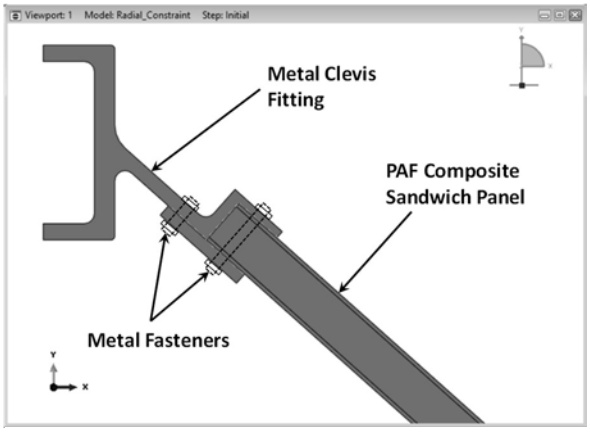

Figure 2. Metal clevis fitting.

The purpose of this study is to investigate the effectiveness of finite element models with progressive failure analysis in predicting the load carrying capacity of pinned joints of composite sandwich panels, as shown in Fig. 3. While there has not been much research work conducted on pin-bearing or bolt-bearing damage of composite honeycomb sandwich panels, pin- and bolt-bearing damage on solid composite laminates have been studied in depth [1-14]. Assume the honeycomb core in a composite sandwich panel does not take significant bearing load, the two composite facesheets of the sandwich panel are bearing all the load transferred in a pinned joint. Therefore, the pin-bearing capacity of the facesheets which are two solid composite laminates is used to determine the load carrying capacity of the pinned joints of composite honeycomb sandwich panels.

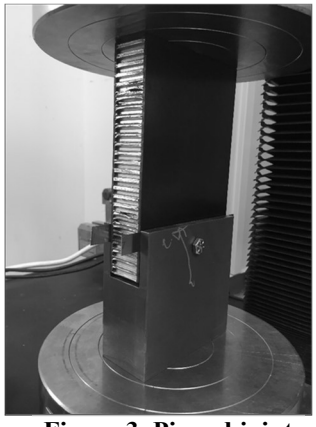

Figure 3. Pinned joint test.

Three representative works conducted by (1) Chang and Lessard in 1991 [15], (2) Riccio in 2005 [16], and (3) Olmedo and Santiuste in 2012 [17] were followed in this current study. All three researches used ABAQUS finite element user subroutines based on progressive damage models of composite laminae, including matrix tensile/compressive failure, fiber tensile/compressive failure, and fiber/matrix shearing

failure, to analyze the bearing failures and to predict the load carry capacities of pinned and bolted joints composite laminates. Shear nonlinearity was included in Chang and Lessard's and Olmedo and Santiuste's models. The failure criteria of each of these three researches are described in the next section.

II. Failure Criteria

A. Chang and Lessard (1991) [15]

Chang and Lessard investigated the strength of open-hole composite laminates using two-dimensional finite element models with progressive damage analysis. They included the nonlinear in-plane lamina shear response in the form of

$$\gamma_{xy} = \frac{\sigma_{xy}}{G_{xy}} + \alpha\sigma_{xy}^3 \tag{1}$$

where x represents the fiber direction, y represents the resin direction, and α is the nonlinear coefficient which Chang and Lessard determined to be $0.8\text{x}10^{-14}$ for T300/976 composite lamina. If this nonlinear relationship is regarded as a stress-induced degradation/damage, Chang and Lessard used four damage/failure modes to evaluate the material properties degradation of each ply of the laminate: (1) shear nonlinearity, (2) matrix tensile/compressive failure, (3) fiber/matrix shearing failure, and (4) fiber compressive/buckling failure.

(1) Shear Nonlinearity: When a damage parameter d_{xy} is introduced so that $G_{xy} = (1\text{-}d_{xy})\ G_{xy,\text{original}}$, d_{xy} can be derived as

$$d_{xy} = \frac{3\alpha G_{xy}\sigma_{xy}^2 - 2\alpha\sigma_{xy}^3/\gamma_{xy}}{1 + 3\alpha G_{xy}\sigma_{xy}^2} \tag{2}$$

(2) Matrix Failure: With the failure index e_m defined for matrix failure if greater than 1, when $\sigma_y > 0$,

$$e_m^2 = \left(\frac{\sigma_y}{Y_t}\right)^2 + \left(\frac{\sigma_{xy}}{S_{xy}}\right)^2 = \left(\frac{\sigma_y}{Y_t}\right)^2 + \frac{2\sigma_{xy}^2/G_{xy} + 3\alpha\sigma_{xy}^4}{2S_{xy}^2/G_{xy} + 3\alpha S_{xy}^4} \tag{3}$$

when $\sigma_y < 0$,

$$e_m^2 = \left(\frac{\sigma_y}{Y_c}\right)^2 + \left(\frac{\sigma_{xy}}{S_{xy}}\right)^2 = \left(\frac{\sigma_y}{Y_c}\right)^2 + \frac{2\sigma_{xy}^2/G_{xy} + 3\alpha\sigma_{xy}^4}{2S_{xy}^2/G_{xy} + 3\alpha S_{xy}^4} \tag{4}$$

where Y_t and Y_c are the tensile and compressive strengths in the resin direction, respectively, and S_{xy} is the in-plane shear strength of the lamina.

(3) Fiber/Matrix Shearing Failure: With the failure index e_{fm} defined for fiber/matrix shearing failure if greater than 1,

$$e_{fm}^2 = \left(\frac{\sigma_x}{X_c}\right)^2 + \left(\frac{\sigma_{xy}}{S_{xy}}\right)^2 = \left(\frac{\sigma_x}{X_c}\right)^2 + \frac{2\sigma_{xy}^2/G_{xy} + 3\alpha\sigma_{xy}^4}{2S_{xy}^2/G_{xy} + 3\alpha S_{xy}^4} \tag{5}$$

where X_c is the compressive strength in the fiber direction of the lamina.

(4) Fiber Compressive/Buckling Failure: With the failure index e_b defined for fiber compressive/buckling failure if greater than 1, when $\sigma_x < 0$,

$$e_b = -\frac{\sigma_x}{X_c} \tag{6}$$

Table 1 shows the degraded material properties after each of the failure criteria is met according to Chang and Lessard's study.

Table 1. Material degradation due to failure (Chang and Lessard)

Failure Mode	E_x	E_y	v_{xy}	G_{xy}
Shear Nonlinearity	E_x	E_y	v_{xy}	1
Matrix	E_x	1	0	G_{xy}
Fiber/Matrix Shearing	E_x	E_y	0	1
Fiber Compressive/Buckling	1	E_y	0	G_{xy}

B. Riccio (2005) [16]

Riccio studied the damage onset and propagation of single-lap bolted composite joints using three-dimensional finite element models with progressive damage analysis. He used the similar failure criteria as Chang and Lessard's but did not include shear nonlinearity in his damage formulation. Three failure modes were included in his ABAQUS user subroutine to determine material degradation.

(1) Matrix Failure: With the failure index e_m defined for matrix failure if greater than 1, when $\sigma_y + \sigma_z > 0$,

$$e_m^2 = \left(\frac{\sigma_y}{Y_t}\right)^2 + \left(\frac{\sigma_{xy}}{S_{xy}}\right)^2 + \left(\frac{\sigma_{yz}}{S_{yz}}\right)^2 \tag{7}$$

when $\sigma_y + \sigma_z < 0$,

$$e_m^2 = \left(\frac{\sigma_y}{Y_c}\right)^2 + \left(\frac{\sigma_{xy}}{S_{xy}}\right)^2 + \left(\frac{\sigma_{yz}}{S_{yz}}\right)^2 \tag{8}$$

where S_{yz} is the yz-plane shear strength of the lamina.

(2) Fiber Failure: With the failure index e_f defined for fiber failure if greater than 1, when $\sigma_x > 0$,

$$e_f^2 = \left(\frac{\sigma_x}{X_t}\right)^2 + \left(\frac{\sigma_{xy}}{S_{xy}}\right)^2 + \left(\frac{\sigma_{xz}}{S_{xz}}\right)^2 \tag{9}$$

when $\sigma_x < 0$,

$$e_f^2 = \left(\frac{\sigma_x}{X_c}\right)^2 \tag{10}$$

where X_t is the tensile strength in the fiber direction and S_{xz} is the xz-plane shear strength of the lamina.

(3) Fiber/Matrix Shearing Failure: With the failure index e_{fm} defined for fiber/matrix shearing failure if greater than 1, when $\sigma_x < 0$,

$$e_{fm}^2 = \left(\frac{\sigma_x}{X_c}\right)^2 + \left(\frac{\sigma_{xy}}{S_{xy}}\right)^2 + \left(\frac{\sigma_{xz}}{S_{xz}}\right)^2 \tag{11}$$

Table 2 shows the degraded material properties after each of the failure criteria is met according to Riccio's paper.

Table 2. Material degradation due to failure (Riccio)

Failure Mode	E_x	E_y	E_z	v_{xy}	v_{xz}	v_{yz}	G_{xy}	G_{xz}	G_{yz}
Matrix	E_x	kE_y	kE_z	kv_{xy}	kv_{xz}	v_{yz}	G_{xy}	G_{xz}	G_{yz}
Fiber	kE_x	E_y	E_z	v_{xy}	v_{xz}	v_{yz}	G_{xy}	G_{xz}	G_{yz}
Fiber/Matrix Shearing	E_x	E_y	E_z	v_{xy}	v_{xz}	v_{yz}	kG_{xy}	kG_{xz}	kG_{yz}

$k = 0.1$

C. Olmendo and Santiuste (2012) [17]

Olmendo and Santiuste expanded the Harshin failure criteria [18] to cover all three directions and used them to predict the failure load of bolted single-lap composite joints. Shear nonlinearity in all three directions were included in their approach. If shear nonlinearity in each direction is treated as a separate damage mode, Olmendo and Santiuste's analysis includes a total of six failure modes. Besides the three shear nonlinear modes, the other three failure modes are matrix failure, fiber failure, and fiber/matrix shearing failure.

(1) Shear Nonlinearity: Use the same damage formulation of G_{xy} in Eq. (2) for the other two shear moduli, the degraded shear moduli are $G_{xz} = (1\text{-}d_{xz})\ G_{xz,\text{original}}$ and $G_{yz} = (1\text{-}d_{yz})\ G_{yz,\text{original}}$, where d_{xz} and d_{yz} are

$$d_{xz} = \frac{3\alpha G_{xz}\sigma_{xz}^2 - 2\alpha\sigma_{xz}^3/\gamma_{xz}}{1 + 3\alpha G_{xz}\sigma_{xz}^2} \tag{12}$$

$$d_{yz} = \frac{3\alpha G_{yz}\sigma_{yz}^2 - 2\alpha\sigma_{yz}^3/\gamma_{yz}}{1 + 3\alpha G_{yz}\sigma_{yz}^2} \tag{13}$$

(2) Matrix Failure: With the failure index e_m defined for matrix failure if greater than 1, when $\sigma_y > 0$ or $\sigma_z > 0$,

$$e_m^2 = \left(\frac{\sigma_y}{Y_t}\right)^2 + \frac{2\sigma_{xy}^2/G_{xy} + 3\alpha\sigma_{xy}^4}{2S_{xy}^2/G_{xy} + 3\alpha S_{xy}^4} + \frac{2\sigma_{yz}^2/G_{yz} + 3\alpha\sigma_{yz}^4}{2S_{yz}^2/G_{yz} + 3\alpha S_{yz}^4} \tag{14}$$

or

$$e_m^2 = \left(\frac{\sigma_z}{Y_t}\right)^2 + \frac{2\sigma_{xz}^2/G_{xz} + 3\alpha\sigma_{xz}^4}{2S_{xz}^2/G_{xz} + 3\alpha S_{xz}^4} + \frac{2\sigma_{yz}^2/G_{yz} + 3\alpha\sigma_{yz}^4}{2S_{yz}^2/G_{yz} + 3\alpha S_{yz}^4} \tag{15}$$

when $\sigma_y < 0$ or $\sigma_z < 0$,

$$e_m^2 = \left(\frac{\sigma_y}{Y_c}\right)^2 + \frac{2\sigma_{xy}^2/G_{xy} + 3\alpha\sigma_{xy}^4}{2S_{xy}^2/G_{xy} + 3\alpha S_{xy}^4} + \frac{2\sigma_{yz}^2/G_{yz} + 3\alpha\sigma_{yz}^4}{2S_{yz}^2/G_{yz} + 3\alpha S_{yz}^4} \tag{16}$$

or

$$e_m^2 = \left(\frac{\sigma_z}{Y_c}\right)^2 + \frac{2\sigma_{xz}^2/G_{xz} + 3\alpha\sigma_{xz}^4}{2S_{xz}^2/G_{xz} + 3\alpha S_{xz}^4} + \frac{2\sigma_{yz}^2/G_{yz} + 3\alpha\sigma_{yz}^4}{2S_{yz}^2/G_{yz} + 3\alpha S_{yz}^4} \tag{17}$$

(3) Fiber Failure: With the failure index e_f defined for fiber failure if greater than 1, when $\sigma_x > 0$,

$$e_f^2 = \left(\frac{\sigma_x}{X_t}\right)^2 + \frac{2\sigma_{xy}^2/G_{xy} + 3\alpha\sigma_{xy}^4}{2S_{xy}^2/G_{xy} + 3\alpha S_{xy}^4} + \frac{2\sigma_{xz}^2/G_{xz} + 3\alpha\sigma_{xz}^4}{2S_{xz}^2/G_{xz} + 3\alpha S_{xz}^4} \tag{18}$$

when $\sigma_x < 0$,

$$e_f^2 = \left(\frac{\sigma_x}{X_c}\right)^2 \tag{19}$$

(4) Fiber/Matrix Shearing Failure: With the failure index e_{fm} defined for fiber/matrix shearing failure if greater than 1, when $\sigma_x < 0$,

$$e_{fm}^2 = \left(\frac{\sigma_x}{X_c}\right)^2 + \frac{2\sigma_{xy}^2/G_{xy} + 3\alpha\sigma_{xy}^4}{2S_{xy}^2/G_{xy} + 3\alpha S_{xy}^4} + \frac{2\sigma_{xz}^2/G_{xz} + 3\alpha\sigma_{xz}^4}{2S_{xz}^2/G_{xz} + 3\alpha S_{xz}^4} \tag{20}$$

Table 3 shows the degraded material properties after each of the failure criteria is met according to Olmendo and Santiuste's study.

Table 3. Material degradation due to failure (Olmendo and Santiuste)

Failure Mode	E_x	E_y	E_z	ν_{xy}	ν_{xz}	ν_{yz}	G_{xy}	G_{xz}	G_{yz}
G_{xy} Nonlinearity	E_x	E_y	E_z	ν_{xy}	ν_{xz}	ν_{yz}	1	G_{xz}	G_{yz}
G_{xz} Nonlinearity	E_x	E_y	E_z	ν_{xy}	ν_{xz}	ν_{yz}	G_{xy}	1	G_{yz}
G_{yz} Nonlinearity	E_x	E_y	E_z	ν_{xy}	ν_{xz}	ν_{yz}	G_{xy}	G_{xz}	1
Matrix	E_x	$0.4E_y$	$0.4E_z$	0	0	0	G_{xy}	G_{xz}	$0.2G_{yz}$
Fiber	$0.14E_x$	$0.4E_y$	$0.4E_z$	0	0	0	$0.25G_{xy}$	$0.25G_{xz}$	$0.2G_{yz}$
Fiber/Matrix Shearing	E_x	E_y	E_z	0	0	ν_{yz}	$0.25G_{xy}$	$0.25G_{xz}$	G_{yz}

III. Finite Element Models

A. Two-Dimensional Models

The commercial finite element software ABAQUS/Standard was used for the progressive failure analysis of this study. Four-noded, two-dimensional plane-stress reduced integration solid elasticity elements (CPS4R) were used for the models with Chang and Lessard's failure criteria. Figure 4 shows the finite element mesh of a half-model of a 4"x6" composite plate pinned with a 0.25"-diameter steel pin. The pin has an edge distance of 1". Due to symmetry, the nodes on the left edge of the laminate were applied with symmetry boundary condition which constrains the displacement in the *x*-direction. Constraint equations were applied to the nodes on the top edge of the laminate so that they have the same *y*-directional displacement to simulate the loading condition of the test setup. Surface contact was applied between the pin hole of the laminate and the steel pin. The nodes within an approximately 0.125"-diameter circle of the center of the steel pin were fixed for both *x*- and *y*-directional displacements. Elastic material property option "Lamina" was selected for the composite plies where values of E_x, E_y, ν_{xy}, G_{xy}, G_{xz}, and G_{yz} were supplied. Four field variables were added in the material property to specify the four failure modes according to Chang and Lessard's four failure criteria. Options of "User Defined Field" and "Depvar" with four dependent variables were selected so that ABAQUS will look for the user subroutine to calculate the degraded material properties. A FORTRAN user subroutine "USDFLD" was coded to calculate the four "field variables," FV1, FV2, FV3, and FV4. The field variable describing the shear nonlinearity parameter d_{xy} is a real value varying between 0 and 1. The other three field variables have integer values of either 0, no damage has occurred, or 1, damage has occurred. Load was applied by defining a downward displacement on the top nodes of the laminate. A ".inp," keywords, file of the model, was generated from ABAQUS/CAE to be executed under the command prompt because this is the only way to run ABAQUS models with a user subroutine. It should be noted that the elements in the plate portion of the model simulate one ply of the laminate. These elements were duplicated for other plies in the ".inp" file while keeping the nodes the same. As shown in Fig. 5, four mesh densities were used to test the convergence of the finite element models. The numbers of elements shown are of each ply together with the pin.

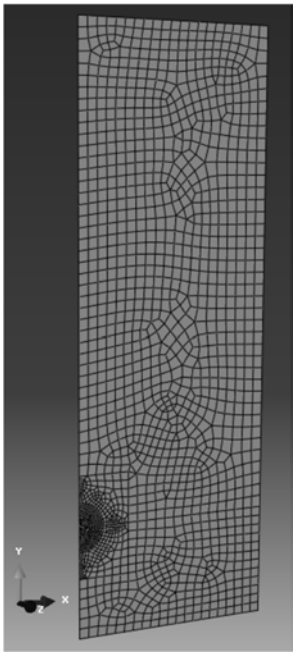

Figure 4. 2D Finite element mesh.

B. Three-Dimensional Models

Eight-noded, three-dimensional reduced integration solid elasticity elements (C3D8R) were used for the models with Riccio's and Olmedo Santiuste's failure criteria. Because the stacking sequences of the laminates are symmetric, only half thickness of the laminate was included in the finite element models. Figure 6 shows the finite element mesh of a quarter-model of a 4"x6" composite plate pinned with a 0.25"-diameter steel pin. One element was used in the thickness direction for each group of consecutive plies of the same angle. Due to symmetry, the nodes on the left edge

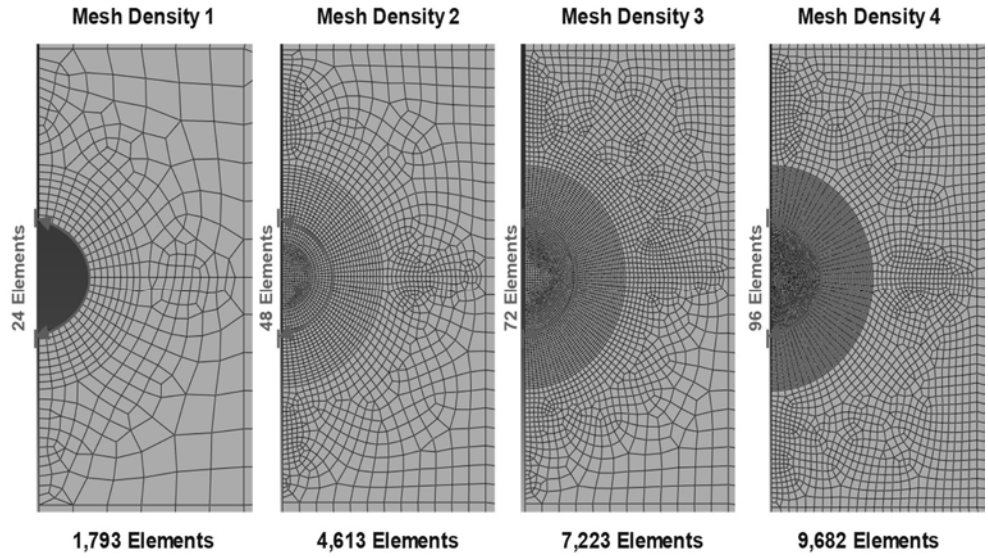

Figure 5. Finite element meshes of different densities.

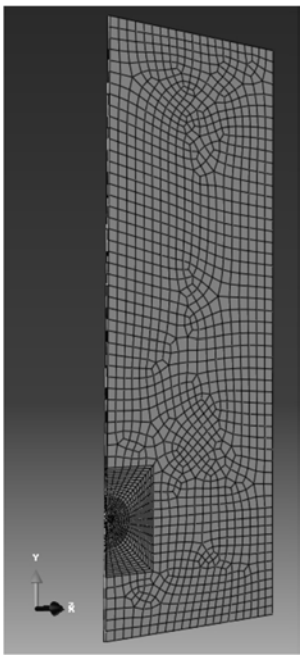

Figure 6. 3D finite element mesh.

and back face of the laminate were applied with symmetry boundary conditions which constrains the displacements in the *x*-direction and *z*-direction, respectively. Constraint equations were applied to the nodes on the upper end of the laminate so that they have the same *y*-directional displacement to simulate the loading condition of the test setup. Surface contact was applied between the pin hole of the laminate and the steel pin. The nodes within an approximately 0.125"-diameter circle of the center of the steel pin were fixed for both *x*- and *y*-directional displacements. Elastic material property option "Engineering Constants" was selected for the composite plies where values of E_x, E_y, E_z, ν_{xy}, ν_{xz}, ν_{yz}, G_{xy}, G_{xz}, and G_{yz} were supplied. Material degradation models were applied only to the elements around the pin hole on the laminate, as shown in Fig. 7, in order to reduce the computation time assuming failure will occur only within this region. Three and six field variables were added to the material property of these elements to specify the three and six failure modes for Riccio's and Olmedo and Santiuste's failure criteria, respectively. Same as the two-dimension models, options of "User Defined Field" and "Depvar" with three and six dependent variables were selected for Riccio's and Olmedo and Santiuste's failure criteria, respectively. Four mesh densities similar to the two-dimensional models were used for the three-dimensional models with five elements through the thickness.

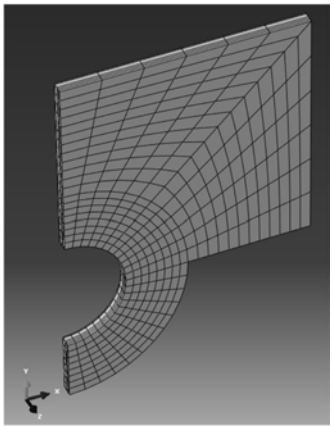

Figure 7. Elements with damage features.

IV. Results and Discussion

All material properties of the composite lamina used in the finite element models were obtained from the literature. Two compressive strength values in the fiber direction, 169 ksi and 251 ksi, were used to show how significant this property will affect the overall joint bearing capacity. Figure 8 shows the typical force history of the two-dimensional model with Chang and Lessard's failure criteria with two mesh densities. Both force histories show a significant load drop toward the end indicating complete failure of the joint. On the other hand, the 3D model of mesh density 1 in Fig. 9 shows several minor load drops before no more converged time increment can be reached at the end. In the same figure, however, the model with higher mesh density reached complete failure as a time increment was converged with a drastic load drop at the end.

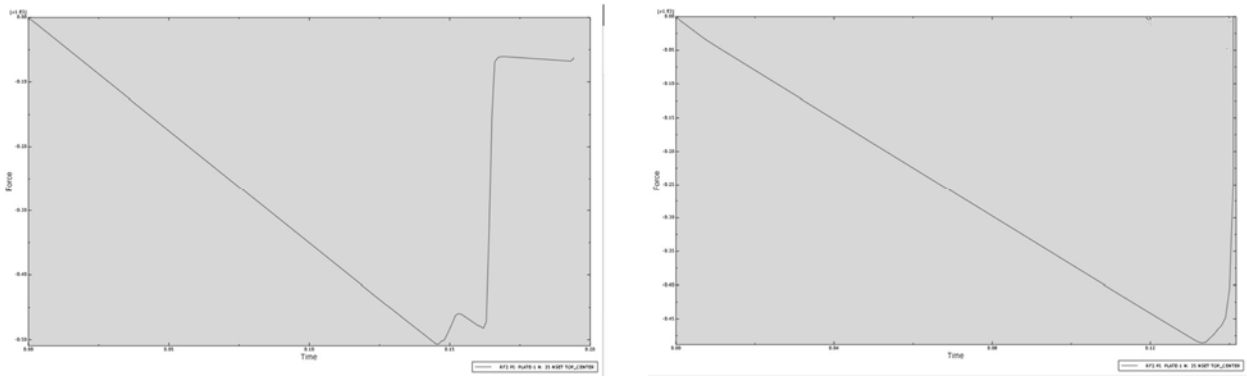

Figure 8. Force histories from 2D models of 0.25"-pin mesh densities 1 (left), and 4 (right).

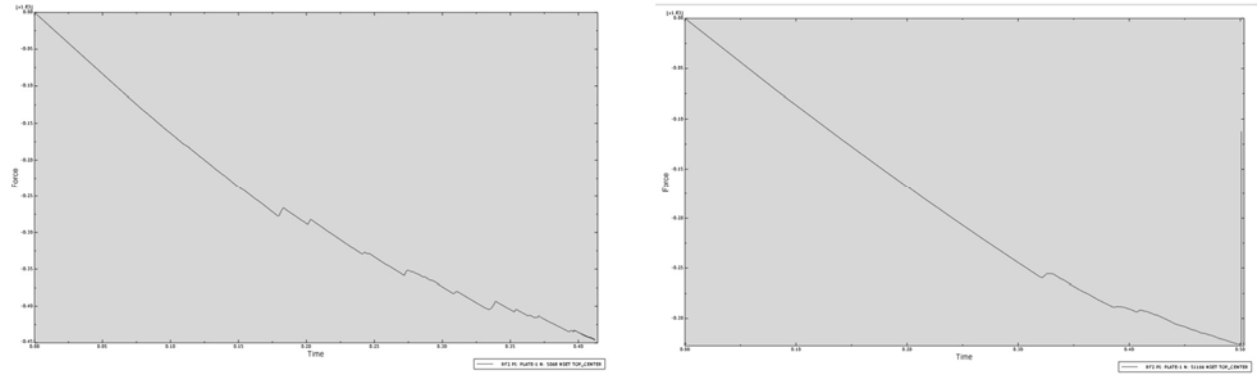

Figure 9. Force histories from 3D models of 0.25"-pin, mesh densities 1 (left), and 4 (right).

Figures 11-13 show the comparison between the predicted failure loads by the finite element models of different mesh densities and the experimental results of the three joint configurations. Figure 14 shows the comparison of each set of failure criteria. It can be seen that almost all models resulted in lower joint strengths with higher mesh densities. Among all three sets of failure criteria, Olmedo's seems to predict the failure loads most accurately with mesh density 4. Olmedo's model tends to overestimate the failure load with low mesh densities. As can be seen in Fig. 14, besides Chang and Lessard's criteria, a higher X_c value does not always result in a higher joint failure load.

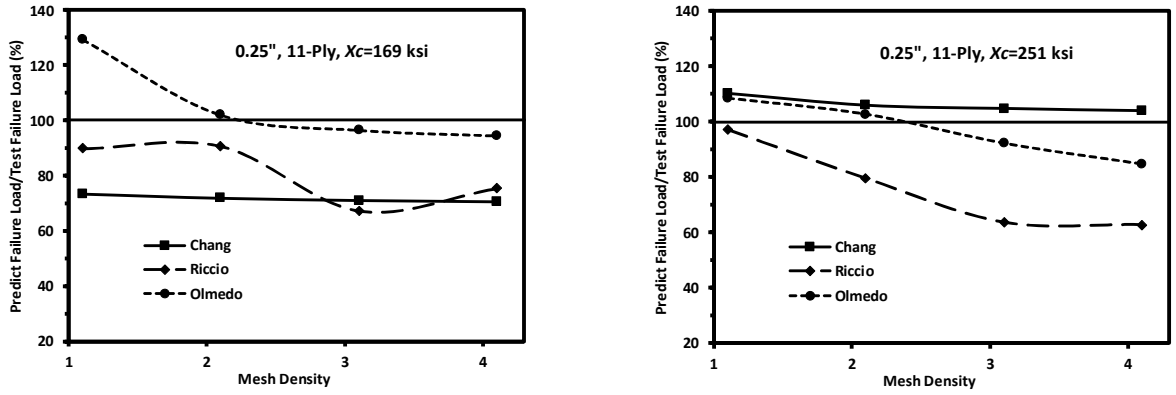

Figure 10. Comparison between FE and experimental results of 0.25"-pin 11-ply laminate.

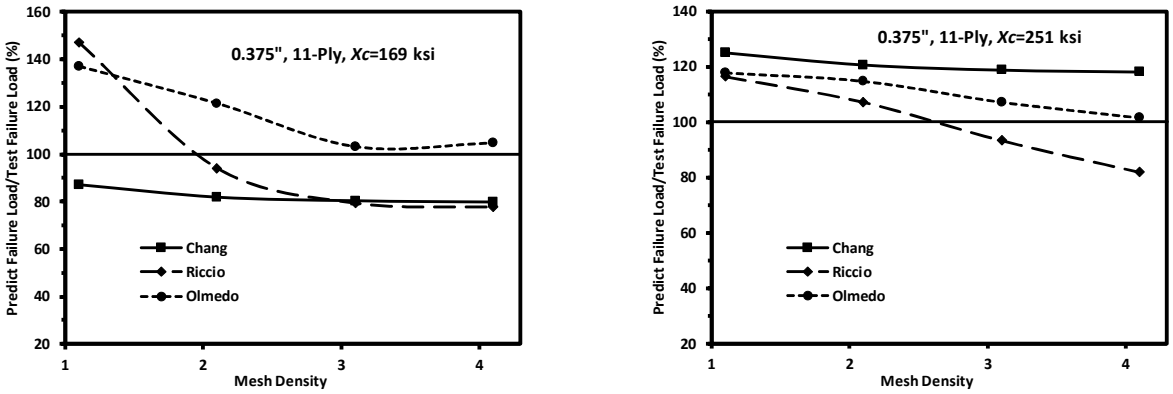

Figure 11. Comparison between FE and experimental results of 0.375"-pin 11-ply laminate.

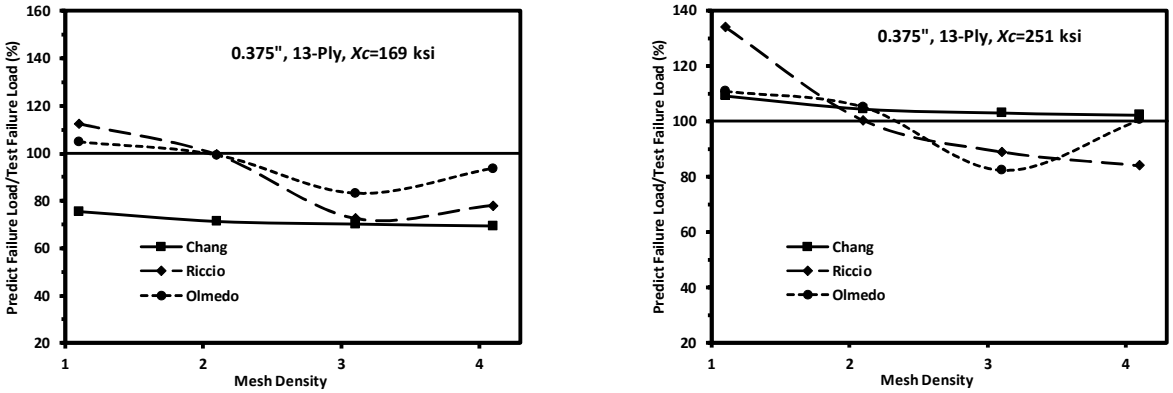

Figure 12. Comparison between FE and experimental results of 0.375"-pin 13-ply laminate.

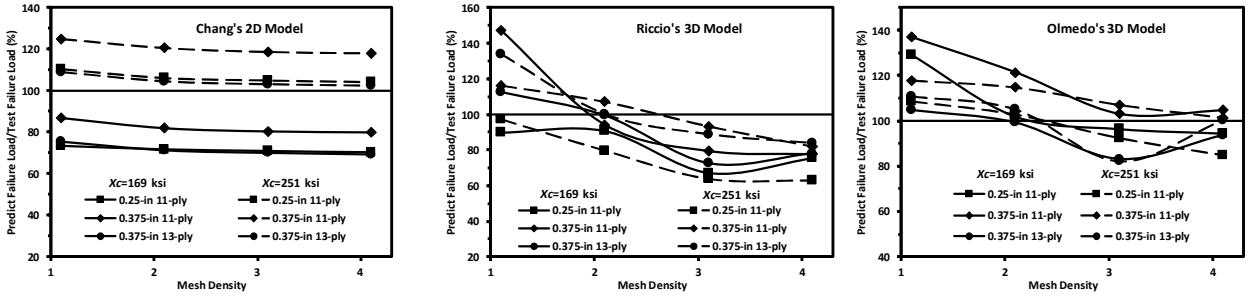

Figure 13. Results from Chang's, Riccio's, and Olmedo's models.

V. Conclusion

Three-dimensional finite element models of progressive failure analysis are believed to be the most reliable method to predict the ultimate failure loads of composite structures such as pinned composite joints. Such method has become attractive because these models can be executed on a personal computer with a reasonable runtime nowadays thanks to the increased computation power of these machines. The current study demonstrated the effectiveness of such models and compared three sets of failure criteria from the literature. Three pinned joint configurations with two pin sizes and two laminate thicknesses were used for this study. Four mesh densities were used for the finite element models with each of the three sets of failure criteria. The two-dimensional models with Chang and Lessard's failure

criteria showed a clear trend of convergence on failure loads, even though the converged results were not most accurate among the three sets of failure criteria. Riccio's failure criteria, which do not consider the shear nonlinearity of composite laminae, tend to underestimate the failure loads. Among all three sets of failure criteria, Olmedo and Santiuste's criteria seemed to provide the most accurate estimate of failure loads even though the convergence on mesh density was not monotonic. Strength values of composite plies played a significant role in failure analysis. The unidirectional laminate used in the standard tests for compressive strength in the fiber direction is well-constrained and has a short gage length to prevent buckling. However, the needed strength value in the fiber direction for the finite element models is of both compressive and "micro" or "local" buckling strength. This "micro" or "local" buckling strength of composite plies is not well defined so there is no established test method for it. The lack of reliable and appropriate strength values is the obstacle for the accuracy of three-dimensional finite element models of progressive failure analysis.

.

Acknowledgments

The first author of this report would like to express his appreciation to the Marshall Space Flight Center Faculty Fellowship Program Director, Dr. Frank Six, and all the coordinators including Dr. Gerald Karr, Rachael Damiani, Mona Miller, and Katie Hayden, for providing this unique opportunity to work with NASA researchers in a NASA environment. A special gratitude he gives to the MSFC Collaborator, Dr. William Guin. He has spent time and efforts to make this Fellowship meaningful and fruitful. Many thanks also go to Justin Jackson and Robert Wingate for their tremendous help.

References

[1]Thoppul, S. D., Finegan, J., and Gibson, R. F., "Mechanics of Mechanically Fastened Joints in Polymer–Matrix Composite Structures – A review," *Composites Science and Technology,* Vol. 69, 2009, pp. 301-329.

[2]Xiao, Y., and Ishikawa, T., "Bearing Strength and Failure Behavior of Bolted Composite Joints (part I: Experimental Investigation)," *Composites Science and Technology,* Vol. 65, 2005, pp. 1022-1031.

[3]Xiao, Y., and Ishikawa, T., "Bearing Strength and Failure Behavior of Bolted Composite Joints (part II: Modeling and Simulation)," *Composites Science and Technology,* Vol. 65, 2005, pp. 1032-1043.

[4]Camanho, P. P., and Lambert, M., "A Design Methodology for Mechanically Fastened Joints in Laminated Composite Materials," *Composites Science and Technology,* Vol. 66, 2006, pp. 3004-3020.

[5]Broughton, W. R., Crocker, L. E., and Gower, M. R. L., "Design Requirements for Bonded and Bolted Composite Structures," NPL Report MATC(A)65, January 2002.

[6]İçten, B. M., and Sayman, O., "Failure Analysis of Pin-Loaded Aluminum–Glass–Epoxy Sandwich Composite Plates," *Composites Science and Technology,* Vol. 63, 2003, pp. 727-737.

[7]Shokrieh, M. M., "Failure of Laminated Composite Pinned Connections," Master's Thesis, Dept. of Mechanical Engineering, McGill Univ., Montreal, Canada, 1991.

[8]Zhou Y., Fei, Q., and Tao, J., "Profile design of loaded pins in composite single lap joints: From circular to non-circular," *Results in Physics*, Vol. 6, 2016, pp. 471-480.

[9]Okutan, B., and Karakuzu, R., "The Failure Strength For Pin-loaded Multi-directional Fiber-glass Reinforced Epoxy Laminate," *Journal of Composite Materials*, Vol. 36, No. 24, 2002, pp. 2695-2712.

[10]Okutan, B., and Karakuzu, R., "The strength of pinned joints in laminated composites," *Composites Science and Technology,* Vol. 63, 2003, pp. 893-905.

[11]Lessard, L. B., and Shokrieh, M. M., "Two-Dimensional Modeling of Composite Pinned-Joint failure ," *Journal of Composite Materials*, Vol. 29, No. 5, 1995, pp. 671-697.

[12]Wang, H. S., Hung, C. L., and Chang, F. K., "Bearing Failure of Bolted Composite Joints. Part I: Experimental Characterization," *Journal of Composite Materials*, Vol. 30, No. 12, 1996, pp. 1284-1313.

[13]Hung, C. L. and Chang, F. K., "Bearing Failure of Bolted Composite Joints. Part II: Model and Verification," *Journal of Composite Materials*, Vol. 30, No. 12, 1996, pp. 1359-1400.

[14]Chamis, C. C., "Simplified Procedures for Designing Composite Bolted Joints," NASA Technical Memorandum 100281, 1988.

[15]Chang, F-K., and Lessard, L. B., "Damage Tolerance of Laminated Composites Containing an Open Hole and Subjected to Compressive Loadings: Part I—Analysis," *Journal of Composite Materials*, Vol. 25, No. 1, 1991, pp. 2–43.

[16]Riccio, A., "Effects of Geometrical and Material Features on Damage Onset and Propagation in Single-lap Bolted Composite Joints under Tensile Load: Part II – Numerical Studies," *Journal of Composite Materials*, Vol 39, No. 23, 2005, pp 2091–2112.

[17]Olmedo, Á. and Santiuste, C., "On the prediction of bolted single-lap composite joints," *Composite Structures*, Vol. 94, No. 6, 2012, pp. 2110–2117.

[18]Hashin, Z. "Failure Criteria for Unidirectional Fibre Composites," *Journal of Applied Mechanics*, Vol. 47, 1980, pp. 329–334.

APPENDIX A— NASA MARSHALL SPACE FLIGHT CENTER FACULTY FELLOWSHIP PROGRAM ANNOUNCEMENT

APPENDIX B—NASA MARSHALL SPACE FLIGHT CENTER FACULTY FELLOWSHIP PROGRAM DESCRIPTION

Program Description

- The Marshall Faculty Fellowship program is a residential research experience. Fellows are required to conduct their research, during the ten-week program, on-site at the Marshall Space Flight Center.
- Participants cannot receive remuneration from other entities or other programs or other university or government sources during the Faculty Fellowship 10-week period.
- An oral presentation by the Fellow to the Marshall group with which s/he has been affiliated is required, near the end of the fellowship period.
- A written final report is required at the end of the Fellowship.
- A written evaluation of the program by the Fellow is expected at the end of the Fellowship.

Eligibility

- US citizen
- Full time teaching or research appointment at accredited US university or college.
- Fellowship is awarded for one summer period, but Fellow may apply again for a second year.
- Women, under-represented minorities, and persons, with disabilities are encouraged to apply.

Selection

The applications selected to be Faculty Fellows will be chosen by the Marshall group which has been assigned the area of investigation (concentration) chosen by the applicant.

Marshall Collaborator

A Marshall Collaborator will be identified to serve as the co-investigator and day-to-day contact. At the end of the ten-week period, the Faculty Fellow and the Marshall Collaborator will prepare a white paper summarizing the summer effort, including results and recommending follow-up work.

Compensation

Stipends for Faculty Fellows are set as follows for the 10-week period:

Assistant Professors and Research Faculty	$15,000
Associate Professors	$17,000
Professors	$19,000

A relocation allowance of $1,500 will be provided to fellows who live more than fifty miles from the Marshall Center.

A travel supplement of $500 will be provided to those fellows receiving the relocation allowance.

REPORT DOCUMENTATION PAGE

Form Approved
OMB No. 0704-0188

1. REPORT DATE *(DD-MM-YYYY)*	2. REPORT TYPE	3. DATES COVERED *(From - To)*
01–11–2019	Technical Memorandum	

4. TITLE AND SUBTITLE

Marshall Space Flight Center Faculty Fellowship Program

5a. CONTRACT NUMBER

5b. GRANT NUMBER

5c. PROGRAM ELEMENT NUMBER

6. AUTHOR(S)

N.F. Six, Program Director and G. Karr, Compiler*

5d. PROJECT NUMBER

5e. TASK NUMBER

5f. WORK UNIT NUMBER

7. PERFORMING ORGANIZATION NAME(S) AND ADDRESS(ES)

George C. Marshall Space Flight Center
Huntsville, AL 35812

8. PERFORMING ORGANIZATION REPORT NUMBER

M–1490

9. SPONSORING/MONITORING AGENCY NAME(S) AND ADDRESS(ES)

National Aeronautics and Space Administration
Washington, DC 20546–0001

10. SPONSORING/MONITOR'S ACRONYM(S)

NASA

11. SPONSORING/MONITORING REPORT NUMBER

NASA/TM—2019–220139

12. DISTRIBUTION/AVAILABILITY STATEMENT

Unclassified-Unlimited
Subject Category 31
Availability: NASA STI Information Desk (757–864–9658)

13. SUPPLEMENTARY NOTES

Prepared by the Academic Affairs Office, Office of Human Capital
*The University of Alabama in Huntsville

14. ABSTRACT

The research projects conducted by the 2018 Faculty Fellows at NASA Marshall Space Flight Center included propulsion studies on cryogenic tank pressurization, transmitted torque in a cryogenic environment, condensation in presence of noncondensables, Europa Lander Deorbit Stage, and catalyst development for a hybrid rocket. Spacecraft systems research was conducted on wireless sensor networks and printed electronic inks. Vehicle Systems studies were performed on Mars ascent vehicle analysis, architecture models, and Space Launch System manual steering. Space science studies included planetary lava flow.

15. SUBJECT TERMS

wireless sensors, propulsion, green propellant, materials, 3D printing, friction stir welds, instruments, solar neutrinos, gamma-ray polarimeter, lightning

16. SECURITY CLASSIFICATION OF:			17. LIMITATION OF ABSTRACT	18. NUMBER OF PAGES	19a. NAME OF RESPONSIBLE PERSON
a. REPORT	b. ABSTRACT	c. THIS PAGE			STI Help Desk at email: help@sti.nasa.gov
U	U	U	UU	150	19b. TELEPHONE NUMBER *(Include area code)* STI Help Desk at: 757–864–9658

National Aeronautics and
Space Administration
IS02
George C. Marshall Space Flight Center
Huntsville, Alabama 35812